Appendix 1

$$40 < P_t^{\gamma} < 50\ GeV/c$$

Table 1: Selection 1. $\phi_{(\gamma,jet)} = 180^{\circ} \pm 15^{\circ}$. UA1 algorithm. $L_{int} = 3\ fb^{-1}$

P_{tCUT}^{clust}	30	20	15	10	5
P_t^{jet}	43.021	42.771	42.679	42.755	43.202
P_t^{Jet}–P_t^{jet}	0.168	0.167	0.161	0.160	0.127
$P_{t(\nu)}^{Jet}$	0.169	0.168	0.162	0.161	0.128
$R_{event}^{\nu \in Jet}$	0.033	0.033	0.033	0.033	0.027
$P_{t(\mu)}^{Jet}$	0.100	0.099	0.096	0.099	0.087
$R_{event}^{\mu \in Jet}$	0.018	0.018	0.017	0.017	0.014
P_t^{miss}	4.551	4.511	4.470	4.399	4.134
$P_{t\nu \in Jet}^{miss}$	7.054	6.942	6.843	6.777	6.576
$Nevent_{(c)}$	268902	245202	216110	146582	34146
$Nevent_{(b)}$	35719	31001	26171	17859	3145
$29 sub/all$	0.91	0.91	0.90	0.90	0.89
R_{gc}^{jet}	0.65	0.65	0.65	0.65	0.64
Entries	56532	52588	46991	34426	8421

Table 2: Selection 1. $\phi_{(\gamma,jet)} = 180^{\circ} \pm 15^{\circ}$. LUCELL algorithm. $L_{int} = 3\ fb^{-1}$

P_{tCUT}^{clust}	30	20	15	10	5
P_t^{jet}	43.253	43.000	42.949	43.026	43.408
P_t^{Jet}–P_t^{jet}	0.168	0.165	0.160	0.156	0.121
$P_{t(\nu)}^{Jet}$	0.169	0.166	0.161	0.157	0.121
$R_{event}^{\nu \in Jet}$	0.033	0.033	0.033	0.032	0.027
$P_{t(\mu)}^{Jet}$	0.103	0.100	0.098	0.093	0.094
$R_{event}^{\mu \in Jet}$	0.018	0.018	0.017	0.017	0.015
P_t^{miss}	4.556	4.510	4.474	4.382	4.104
$P_{t\nu \in Jet}^{miss}$	7.027	6.915	6.834	6.745	6.595
$Nevent_{(c)}$	309114	282493	247561	164891	36393
$Nevent_{(b)}$	38078	33585	28418	18758	3145
$29 sub/all$	0.92	0.91	0.91	0.90	0.90
R_{gc}^{jet}	0.65	0.65	0.65	0.64	0.63
Entries	54922	50723	44738	31455	7751

$$100 < P_t^{\gamma} < 120\ GeV/c$$

Table 3: Selection 1. $\phi_{(\gamma,jet)} = 180^{\circ} \pm 15^{\circ}$. UA1 algorithm. $L_{int} = 3\ fb^{-1}$

P_{tCUT}^{clust}	30	20	15	10	5
P_t^{jet}	102.627	104.675	105.575	106.329	106.917
P_t^{Jet}–P_t^{jet}	0.546	0.538	0.523	0.501	0.488
$P_{t(\nu)}^{Jet}$	0.548	0.539	0.525	0.502	0.489
$R_{event}^{\nu \in Jet}$	0.044	0.042	0.040	0.038	0.034
$P_{t(\mu)}^{Jet}$	0.258	0.249	0.234	0.228	0.216
$R_{event}^{\mu \in Jet}$	0.023	0.022	0.021	0.019	0.019
P_t^{miss}	5.166	5.139	5.102	5.053	4.913
$P_{t\nu \in Jet}^{miss}$	14.245	14.512	14.817	14.831	15.412
$Nevent_{(c)}$	15716	11502	8299	4776	927
$Nevent_{(b)}$	2570	1713	1221	665	102
$29 sub/all$	0.89	0.88	0.88	0.86	0.83
R_{gc}^{jet}	0.65	0.65	0.65	0.65	0.65
Entries	63316	48178	37512	23472	4467

Table 4: Selection 1. $\phi_{(\gamma,jet)} = 180^{\circ} \pm 15^{\circ}$. LUCELL algorithm. $L_{int} = 3\ fb^{-1}$

P_{tCUT}^{clust}	30	20	15	10	5
P_t^{jet}	103.378	105.266	106.137	106.938	107.216
P_t^{Jet}–P_t^{jet}	0.549	0.544	0.524	0.475	0.491
$P_{t(\nu)}^{Jet}$	0.552	0.546	0.525	0.477	0.492
$R_{event}^{\nu \in Jet}$	0.045	0.043	0.041	0.037	0.034
$P_{t(\mu)}^{Jet}$	0.260	0.249	0.240	0.223	0.198
$R_{event}^{\mu \in Jet}$	0.023	0.022	0.021	0.019	0.017
P_t^{miss}	5.168	5.136	5.110	5.010	4.897
$P_{t\nu \in Jet}^{miss}$	14.169	14.506	14.527	14.442	15.832
$Nevent_{(c)}$	16828	12532	9015	5083	965
$Nevent_{(b)}$	2609	1803	1272	659	96
$29 sub/all$	0.89	0.89	0.88	0.87	0.85
R_{gc}^{jet}	0.65	0.65	0.65	0.64	0.63
Entries	59683	44691	34139	20072	4019

$$200 < P_t^{\gamma} < 240\ GeV/c$$

Table 5: Selection 1. $\phi_{(\gamma,jet)} = 180° \pm 15°$. UA1 algorithm. $L_{int} = 3\ fb^{-1}$

P_{tCUT}^{clust}	30	20	15	10	5
P_t^{jet}	211.973	213.370	214.124	214.874	215.511
P_t^{Jet}–P_t^{jet}	0.886	0.874	0.823	0.768	0.639
$P_{t(\nu)}^{Jet}$	0.889	0.877	0.825	0.770	0.640
$R_{event}^{\nu \in Jet}$	0.039	0.038	0.037	0.035	0.033
$P_{t(\mu)}^{Jet}$	0.420	0.399	0.360	0.338	0.344
$R_{event}^{\mu \in Jet}$	0.020	0.019	0.019	0.017	0.016
P_t^{miss}	5.558	5.529	5.444	5.368	5.130
$P_{t\nu \in Jet}^{miss}$	24.382	24.517	23.705	23.182	20.955
$Nevent_{(c)}$	1081	753	547	317	52
$Nevent_{(b)}$	152	100	70	36	6
$29 sub/all$	0.86	0.85	0.85	0.84	0.82
R_{gc}^{jet}	0.62	0.62	0.62	0.62	0.61
Entries	52542	37741	28477	17189	3142

Table 6: Selection 1. $\phi_{(\gamma,jet)} = 180° \pm 15°$. LUCELL algorithm. $L_{int} = 3\ fb^{-1}$

P_{tCUT}^{clust}	30	20	15	10	5
P_t^{jet}	212.521	213.982	214.736	215.460	216.044
P_t^{Jet}–P_t^{jet}	0.866	0.850	0.802	0.742	0.568
$P_{t(\nu)}^{Jet}$	0.869	0.853	0.805	0.744	0.569
$R_{event}^{\nu \in Jet}$	0.038	0.037	0.036	0.034	0.028
$P_{t(\mu)}^{Jet}$	0.417	0.390	0.353	0.336	0.268
$R_{event}^{\mu \in Jet}$	0.019	0.019	0.019	0.017	0.014
P_t^{miss}	5.529	5.487	5.412	5.337	4.975
$P_{t\nu \in Jet}^{miss}$	24.076	24.016	23.622	23.102	21.347
$Nevent_{(c)}$	1012	694	487	261	44
$Nevent_{(b)}$	138	90	60	27	4
$29 sub/all$	0.86	0.85	0.84	0.83	0.80
R_{gc}^{jet}	0.66	0.65	0.65	0.65	0.64
Entries	49253	34775	25582	14562	2786

$$300 < P_t^{\gamma} < 360\ GeV/c$$

Table 7: Selection 1. $\phi_{(\gamma,jet)} = 180° \pm 15°$. UA1 algorithm. $L_{int} = 3\ fb^{-1}$

P_{tCUT}^{clust}	30	20	15	10	5
P_t^{jet}	320.158	321.502	322.289	322.869	322.911
P_t^{Jet}–P_t^{jet}	1.077	1.069	1.060	1.015	1.161
$P_{t(\nu)}^{Jet}$	1.081	1.072	1.063	1.018	1.163
$R_{event}^{\nu \in Jet}$	0.035	0.034	0.033	0.033	0.035
$P_{t(\mu)}^{Jet}$	0.515	0.506	0.476	0.448	0.433
$R_{event}^{\mu \in Jet}$	0.019	0.018	0.017	0.017	0.017
P_t^{miss}	5.764	5.721	5.692	5.572	5.691
$P_{t\nu \in Jet}^{miss}$	31.983	32.597	33.078	32.371	35.201
$Nevent_{(c)}$	172	117	84	46	8
$Nevent_{(b)}$	25	15	10	6	1
$29 sub/all$	0.84	0.83	0.82	0.80	0.78
R_{gc}^{jet}	0.62	0.62	0.62	0.62	0.61
Entries	46297	32513	24157	14318	2642

Table 8: Selection 1. $\phi_{(\gamma,jet)} = 180° \pm 15°$. LUCELL algorithm. $L_{int} = 3\ fb^{-1}$

P_{tCUT}^{clust}	30	20	15	10	5
P_t^{jet}	320.687	322.011	322.732	323.248	323.646
P_t^{Jet}–P_t^{jet}	1.072	1.061	1.055	0.983	1.052
$P_{t(\nu)}^{Jet}$	1.076	1.064	1.057	0.985	1.053
$R_{event}^{\nu \in Jet}$	0.035	0.033	0.033	0.032	0.032
$P_{t(\mu)}^{Jet}$	0.507	0.483	0.480	0.412	0.388
$R_{event}^{\mu \in Jet}$	0.018	0.018	0.017	0.016	0.013
P_t^{miss}	5.761	5.722	5.686	5.499	5.465
$P_{t\nu \in Jet}^{miss}$	32.220	33.054	33.221	31.968	34.611
$Nevent_{(c)}$	161	106	74	39	7
$Nevent_{(b)}$	22	14	9	5	1
$29 sub/all$	0.83	0.82	0.81	0.80	0.77
R_{gc}^{jet}	0.66	0.65	0.65	0.65	0.64
Entries	43320	29783	21707	12104	2334

Appendix 2 $\quad 40 < P_t^{\gamma} < 50\ GeV/c$

$P_t^{isol} < 5\ GeV/c, \quad \epsilon^{\gamma} < 7\%$

Table 1: Selection 1. $\Delta\phi_{(\gamma,jet)} = 180° \pm 180°$. UA1 algorithm.

P_{tCUT}^{clust}	30	20	15	10	5
Nevent*	2394845	1909496	1522879	982716	228466
$P_t 56$	16.9	13.9	11.8	9.6	7.2
$\Delta\phi$	13.6	10.1	8.1	6.2	4.5
P_t^{out}	13.6	11.0	9.3	7.6	5.6
$P_t^{\eta>5}$	5.0	4.9	4.8	4.7	4.5
$(P_t^{\gamma}-P_t^{part})/P_t^{\gamma}$	0.0198	0.0168	0.0116	0.0076	0.0017
$(P_t^{J}-P_t^{part})/P_t^{J}$	-0.0336	-0.0315	-0.0287	-0.0225	-0.0174
$(P_t^{\gamma}-P_t^{J})/P_t^{\gamma}$	0.0321	0.0316	0.0265	0.0198	0.0125
$P_t(O+\eta>5)/P_t^{\gamma}$	-0.0247	-0.0004	0.0054	0.0061	0.0040
$1-cos(\Delta\phi)$	0.0537	0.0289	0.0179	0.0104	0.0056
$\sigma(Db[\gamma,J])^{**}$	0.1883	0.1655	0.1485	0.1263	0.1039
$\sigma(Db[\gamma,part])^{***}$	0.1876	0.1687	0.1485	0.1237	0.0946
Entries	21321	17000	13558	8749	2034

Table 2: Selection 1. $\Delta\phi_{(\gamma,jet)} = 180° \pm 180°$. UA2 algorithm.

P_{tCUT}^{clust}	30	20	15	10	5
Nevent	1977339	1586791	1279250	821196	188703
$P_t 56$	16.9	13.9	11.9	9.7	7.4
$\Delta\phi$	13.4	9.9	8.0	6.1	4.4
P_t^{out}	13.5	10.9	9.4	7.7	5.8
$P_t^{\eta>5}$	5.0	4.9	4.8	4.7	4.5
$(P_t^{\gamma}-P_t^{part})/P_t^{\gamma}$	0.0167	0.0140	0.0090	0.0072	-0.0006
$(P_t^{J}-P_t^{part})/P_t^{J}$	-0.0460	-0.0471	-0.0482	-0.0434	-0.0398
$(P_t^{\gamma}-P_t^{J})/P_t^{\gamma}$	0.0404	0.0427	0.0415	0.0388	0.0313
$P_t(O+\eta>5)/P_t^{\gamma}$	-0.0152	0.0116	0.0207	0.0256	0.0232
$1-cos(\Delta\phi)$	0.0526	0.0281	0.0177	0.0102	0.0055
$\sigma(Db[\gamma,J])$	0.1866	0.1647	0.1478	0.1260	0.1027
$\sigma(Db[\gamma,part])$	0.1904	0.1714	0.1509	0.1277	0.0984
Entries	17604	14127	11389	7311	1680

Table 3: Selection 1. $\Delta\phi_{(\gamma,jet)} = 180° \pm 180°$. LUCELL algorithm.

P_{tCUT}^{clust}	30	20	15	10	5
Nevent	2762367	2231415	1778302	1126940	255872
$P_t 56$	16.8	14.0	11.9	9.6	7.2
$\Delta\phi$	13.4	10.2	8.2	6.3	4.6
P_t^{out}	13.5	11.1	9.5	7.7	5.6
$P_t^{\eta>5}$	5.0	4.9	4.8	4.7	4.6
$(P_t^{\gamma}-P_t^{part})/P_t^{\gamma}$	0.0226	0.0190	0.0129	0.0080	0.0005
$(P_t^{J}-P_t^{part})/P_t^{J}$	-0.0479	-0.0466	-0.0446	-0.0356	-0.0266
$(P_t^{\gamma}-P_t^{J})/P_t^{\gamma}$	0.0480	0.0471	0.0418	0.0319	0.0192
$P_t(O+\eta>5)/P_t^{\gamma}$	-0.0070	0.0147	0.0201	0.0178	0.0104
$1-cos(\Delta\phi)$	0.0517	0.0290	0.0182	0.0106	0.0059
$\sigma(Db[\gamma,J])$	0.1874	0.1673	0.1511	0.1296	0.1072
$\sigma(Db[\gamma,part])$	0.1888	0.1712	0.1502	0.1245	0.0900
Entries	24593	19866	15832	10033	2278

*Number of events (Nevent) is given in this and in the following tables for integrated luminosity $L_{int} = 3\ fb^{-1}$

** $Db[\gamma,part] \equiv (P_t^{\gamma}-P_t^{part})/P_t^{\gamma}$

*** $Db[\gamma,J] \equiv (P_t^{\gamma}-P_t^{J})/P_t^{\gamma}$

Table 4: Selection 1. $\Delta\phi_{(\gamma,jet)} = 180° \pm 15°$. UA1 algorithm.

P_{tCUT}^{clust}	30	20	15	10	5
Nevent	1607683	1473232	1292841	908583	223636
$P_t 56$	12.4	11.4	10.4	8.9	7.0
$\Delta\phi$	6.0	5.8	5.6	5.1	4.2
P_t^{out}	9.1	8.6	8.0	7.0	5.5
$P_t^{\eta>5}$	4.8	4.7	4.7	4.6	4.4
$(P_t{}^{\gamma}-P_t^{part})/P_t{}^{\gamma}$	0.0089	0.0101	0.0076	0.0057	0.0017
$(P_t{}^{J}-P_t^{part})/P_t{}^{J}$	-0.0262	-0.0260	-0.0247	-0.0202	-0.0171
$(P_t{}^{\gamma}-P_t{}^{J})/P_t{}^{\gamma}$	0.0167	0.0212	0.0197	0.0162	0.0124
$P_t(O+\eta>5)/P_t{}^{\gamma}$	0.0053	0.0102	0.0092	0.0068	0.0051
$1-cos(\Delta\phi)$	0.0081	0.0077	0.0072	0.0061	0.0043
$\sigma(Db[\gamma,J])$	0.1785	0.1589	0.1445	0.1237	0.1009
$\sigma(Db[\gamma,part])$	0.1664	0.1538	0.1401	0.1195	0.0927
Entries	14313	13116	11510	8089	1991

Table 5: Selection 1. $\Delta\phi_{(\gamma,jet)} = 180° \pm 15°$. UA2 algorithm.

P_{tCUT}^{clust}	30	20	15	10	5
Nevent	1331368	1228929	1085605	761103	184772
$P_t 56$	12.5	11.5	10.5	9.1	7.2
$\Delta\phi$	5.9	5.8	5.6	5.1	4.1
P_t^{out}	9.1	8.6	8.1	7.1	5.7
$P_t^{\eta>5}$	4.8	4.8	4.7	4.6	4.4
$(P_t{}^{\gamma}-P_t^{part})/P_t{}^{\gamma}$	0.0072	0.0081	0.0061	0.0057	-0.0004
$(P_t{}^{J}-P_t^{part})/P_t{}^{J}$	-0.0404	-0.0430	-0.0451	-0.0420	-0.0393
$(P_t{}^{\gamma}-P_t{}^{J})/P_t{}^{\gamma}$	0.0284	0.0346	0.0364	0.0364	0.0310
$P_t(O+\eta>5)/P_t{}^{\gamma}$	0.0173	0.0239	0.0261	0.0274	0.0241
$1-cos(\Delta\phi)$	0.0079	0.0076	0.0071	0.0061	0.0042
$\sigma(Db[\gamma,J])$	0.1764	0.1583	0.1443	0.1235	0.1006
$\sigma(Db[\gamma,part])$	0.1682	0.1564	0.1426	0.1229	0.0966
Entries	11853	10941	9665	6776	1645

Table 6: Selection 1. $\Delta\phi_{(\gamma,jet)} = 180° \pm 15°$. LUCELL algorithm.

P_{tCUT}^{clust}	30	20	15	10	5
Nevent	1864454	1716974	1506143	1041237	250144
$P_t 56$	12.6	11.6	10.5	8.9	6.9
$\Delta\phi$	6.1	5.9	5.7	5.1	4.2
P_t^{out}	9.3	8.8	8.2	7.2	5.6
$P_t^{\eta>5}$	4.8	4.7	4.7	4.6	4.4
$(P_t{}^{\gamma}-P_t^{part})/P_t{}^{\gamma}$	0.0114	0.0122	0.0093	0.0066	0.0005
$(P_t{}^{J}-P_t^{part})/P_t{}^{J}$	-0.0362	-0.0371	-0.0359	-0.0289	-0.0229
$(P_t{}^{\gamma}-P_t{}^{J})/P_t{}^{\gamma}$	0.0287	0.0329	0.0311	0.0248	0.0160
$P_t(O+\eta>5)/P_t{}^{\gamma}$	0.0205	0.0251	0.0238	0.0187	0.0117
$1-cos(\Delta\phi)$	0.0083	0.0079	0.0074	0.0062	0.0044
$\sigma(Db[\gamma,J])$	0.1781	0.1612	0.1473	0.1272	0.1042
$\sigma(Db[\gamma,part])$	0.1681	0.1563	0.1418	0.1210	0.0885
Entries	16599	15286	13409	9270	2227

Table 7: Selection 1. $\Delta\phi_{(\gamma,jet)} = 180° \pm 10°$. UA1 algorithm.

P_{tCUT}^{clust}	30	20	15	10	5
Nevent	1268355	1183663	1064376	787162	207236
$P_t 56$	11.3	10.4	9.6	8.3	6.7
$\Delta\phi$	4.3	4.2	4.2	4.0	3.6
P_t^{out}	8.2	7.8	7.3	6.6	5.4
$P_t^{\eta>5}$	4.7	4.7	4.7	4.5	4.3
$(P_t{}^{\gamma}-P_t^{part})/P_t{}^{\gamma}$	0.0068	0.0075	0.0058	0.0047	0.0003
$(P_t{}^{J}-P_t^{part})/P_t{}^{J}$	-0.0234	-0.0241	-0.0235	-0.0189	-0.0174
$(P_t{}^{\gamma}-P_t{}^{J})/P_t{}^{\gamma}$	0.0128	0.0170	0.0168	0.0142	0.0112
$P_t(O+\eta>5)/P_t{}^{\gamma}$	0.0055	0.0098	0.0095	0.0072	0.0052
$1-cos(\Delta\phi)$	0.0040	0.0039	0.0038	0.0036	0.0029
$\sigma(Db[\gamma,J])$	0.1734	0.1558	0.1424	0.1223	0.1002
$\sigma(Db[\gamma,part])$	0.1592	0.1469	0.1343	0.1162	0.0887
Entries	11292	10538	9476	7008	1845

Table 8: Selection 1. $\Delta\phi_{(\gamma,jet)} = 180° \pm 10°$. UA2 algorithm.

P_{tCUT}^{clust}	30	20	15	10	5
Nevent	1062466	998329	900945	662258	171405
$P_t 56$	11.4	10.6	9.8	8.5	6.9
$\Delta\phi$	4.3	4.3	4.2	4.0	3.5
P_t^{out}	8.2	7.9	7.4	6.7	5.5
$P_t^{\eta>5}$	4.7	4.7	4.7	4.5	4.3
$(P_t{}^{\gamma}-P_t^{part})/P_t{}^{\gamma}$	0.0060	0.0064	0.0049	0.0043	-0.0016
$(P_t{}^{J}-P_t^{part})/P_t{}^{J}$	-0.0386	-0.0415	-0.0442	-0.0414	-0.0379
$(P_t{}^{\gamma}-P_t{}^{J})/P_t{}^{\gamma}$	0.0263	0.0317	0.0343	0.0344	0.0285
$P_t(O+\eta>5)/P_t{}^{\gamma}$	0.0191	0.0246	0.0272	0.0278	0.0228
$1-cos(\Delta\phi)$	0.0040	0.0040	0.0039	0.0036	0.0029
$\sigma(Db[\gamma,J])$	0.1705	0.1557	0.1427	0.1221	0.0998
$\sigma(Db[\gamma,part])$	0.1621	0.1507	0.1380	0.1193	0.0938
Entries	9459	8888	8021	5896	1526

Table 9: Selection 1. $\Delta\phi_{(\gamma,jet)} = 180° \pm 10°$. LUCELL algorithm.

P_{tCUT}^{clust}	30	20	15	10	5
Nevent	1463797	1372366	1234096	901619	231498
$P_t 56$	11.5	10.6	9.8	8.4	6.6
$\Delta\phi$	4.3	4.3	4.2	4.0	3.6
P_t^{out}	8.4	8.0	7.5	6.7	5.4
$P_t^{\eta>5}$	4.7	4.7	4.7	4.5	4.3
$(P_t{}^{\gamma}-P_t^{part})/P_t{}^{\gamma}$	0.0094	0.0102	0.0082	0.0063	0.0000
$(P_t{}^{J}-P_t^{part})/P_t{}^{J}$	-0.0366	-0.0377	-0.0370	-0.0300	-0.0254
$(P_t{}^{\gamma}-P_t{}^{J})/P_t{}^{\gamma}$	0.0279	0.0319	0.0311	0.0258	0.0179
$P_t(O+\eta>5)/P_t{}^{\gamma}$	0.0204	0.0245	0.0237	0.0187	0.0119
$1-cos(\Delta\phi)$	0.0041	0.0040	0.0039	0.0036	0.0030
$\sigma(Db[\gamma,J])$	0.1729	0.1580	0.1451	0.1255	0.1028
$\sigma(Db[\gamma,part])$	0.1613	0.1499	0.1371	0.1181	0.0848
Entries	13032	12218	10987	8027	2061

Table 10: Selection 1. $\Delta\phi_{(\gamma,jet)} = 180° \pm 5°$. UA1 algorithm.

P_{tCUT}^{clust}	30	20	15	10	5
Nevent	773346	731899	667650	517698	149165
$P_t 56$	10.1	9.3	8.6	7.5	6.1
$\Delta\phi$	2.4	2.4	2.3	2.3	2.2
P_t^{out}	7.4	7.0	6.6	6.0	5.0
$P_t^{\eta>5}$	4.7	4.6	4.6	4.4	4.1
$(P_t{}^{\gamma}-P_t^{part})/P_t{}^{\gamma}$	0.0077	0.0085	0.0061	0.0042	0.0006
$(P_t{}^{J}-P_t^{part})/P_t{}^{J}$	-0.0178	-0.0185	-0.0182	-0.0161	-0.0134
$(P_t{}^{\gamma}-P_t{}^{J})/P_t{}^{\gamma}$	0.0097	0.0135	0.0125	0.0110	0.0080
$P_t(O+\eta>5)/P_t{}^{\gamma}$	0.0049	0.0087	0.0076	0.0063	0.0037
$1-cos(\Delta\phi)$	0.0012	0.0012	0.0012	0.0011	0.0010
$\sigma(Db[\gamma,J])$	0.1641	0.1490	0.1382	0.1202	0.0990
$\sigma(Db[\gamma,part])$	0.1517	0.1420	0.1292	0.1126	0.0919
Entries	6885	6516	5944	4609	1328

Table 11: Selection 1. $\Delta\phi_{(\gamma,jet)} = 180° \pm 5°$. UA2 algorithm.

P_{tCUT}^{clust}	30	20	15	10	5
Nevent	650913	619351	567120	435814	126588
$P_t 56$	10.1	9.5	8.7	7.6	6.3
$\Delta\phi$	2.4	2.4	2.4	2.3	2.2
P_t^{out}	7.3	7.0	6.7	6.1	5.1
$P_t^{\eta>5}$	4.6	4.6	4.6	4.4	4.1
$(P_t{}^{\gamma}-P_t^{part})/P_t{}^{\gamma}$	0.0067	0.0067	0.0053	0.0030	-0.0020
$(P_t{}^{J}-P_t^{part})/P_t{}^{J}$	-0.0345	-0.0368	-0.0387	-0.0392	-0.0340
$(P_t{}^{\gamma}-P_t{}^{J})/P_t{}^{\gamma}$	0.0248	0.0289	0.0306	0.0315	0.0251
$P_t(O+\eta>5)/P_t{}^{\gamma}$	0.0204	0.0244	0.0261	0.0274	0.0212
$1-cos(\Delta\phi)$	0.0012	0.0012	0.0012	0.0011	0.0011
$\sigma(Db[\gamma,J])$	0.1601	0.1479	0.1369	0.1180	0.0976
$\sigma(Db[\gamma,part])$	0.1523	0.1449	0.1327	0.1138	0.0950
Entries	5795	5514	5049	3880	1127

Table 12: Selection 1. $\Delta\phi_{(\gamma,jet)} = 180° \pm 5°$. LUCELL algorithm.

P_{tCUT}^{clust}	30	20	15	10	5
Nevent	884209	840515	767954	590596	166688
$P_t 56$	10.2	9.5	8.7	7.6	5.9
$\Delta\phi$	2.4	2.4	2.4	2.3	2.3
P_t^{out}	7.5	7.2	6.8	6.1	5.0
$P_t^{\eta>5}$	4.7	4.6	4.6	4.5	4.1
$(P_t{}^{\gamma}-P_t^{part})/P_t{}^{\gamma}$	0.0087	0.0097	0.0069	0.0050	-0.0002
$(P_t{}^{J}-P_t^{part})/P_t{}^{J}$	-0.0316	-0.0326	-0.0322	-0.0273	-0.0216
$(P_t{}^{\gamma}-P_t{}^{J})/P_t{}^{\gamma}$	0.0238	0.0273	0.0257	0.0220	0.0144
$P_t(O+\eta>5)/P_t{}^{\gamma}$	0.0190	0.0224	0.0208	0.0171	0.0104
$1-cos(\Delta\phi)$	0.0012	0.0012	0.0012	0.0011	0.0011
$\sigma(Db[\gamma,J])$	0.1632	0.1514	0.1410	0.1234	0.1009
$\sigma(Db[\gamma,part])$	0.1522	0.1419	0.1302	0.1145	0.0854
Entries	7872	7483	6837	5258	1484

Table 13: Selection 2. $\Delta\phi_{(\gamma,jet)} = 180^\circ \pm 15^\circ, \epsilon^{jet} < 8\%$. UA1 algorithm.

P_{tCUT}^{clust}	30	20	15	10	5
Nevent	1058535	986086	887017	657316	182525
$P_t 56$	11.6	10.6	9.8	8.5	6.8
$\Delta\phi$	5.8	5.7	5.5	5.0	4.1
P_t^{out}	8.9	8.3	7.7	6.8	5.4
$P_t^{\eta>5}$	4.7	4.7	4.7	4.5	4.4
$(P_t{}^{\gamma}-P_t^{part})/P_t{}^{\gamma}$	-0.0075	-0.0052	-0.0052	-0.0041	-0.0039
$(P_t{}^{J}-P_t^{part})/P_t{}^{J}$	-0.0018	-0.0059	-0.0074	-0.0082	-0.0113
$(P_t{}^{\gamma}-P_t{}^{J})/P_t{}^{\gamma}$	-0.0215	-0.0117	-0.0085	-0.0041	0.0015
$P_t(O+\eta>5)/P_t{}^{\gamma}$	-0.0324	-0.0223	-0.0187	-0.0131	-0.0058
$1-cos(\Delta\phi)$	0.0077	0.0074	0.0070	0.0059	0.0042
$\sigma(Db[\gamma,J])$	0.1787	0.1562	0.1410	0.1196	0.0992
$\sigma(Db[\gamma,part])$	0.1527	0.1397	0.1281	0.1101	0.0873
Entries	9424	8779	7897	5852	1625

Table 14: Selection 2. $\Delta\phi_{(\gamma,jet)} = 180^\circ \pm 15^\circ, \epsilon^{jet} < 6\%$. UA2 algorithm.

P_{tCUT}^{clust}	30	20	15	10	5
Nevent	566334	530391	474903	352134	105584
$P_t 56$	11.5	10.6	9.6	8.3	6.7
$\Delta\phi$	5.7	5.6	5.4	4.9	4.0
P_t^{out}	8.8	8.2	7.7	6.7	5.4
$P_t^{\eta>5}$	4.7	4.7	4.6	4.5	4.3
$(P_t{}^{\gamma}-P_t^{part})/P_t{}^{\gamma}$	-0.0180	-0.0157	-0.0139	-0.0105	-0.0125
$(P_t{}^{J}-P_t^{part})/P_t{}^{J}$	-0.0154	-0.0210	-0.0249	-0.0282	-0.0322
$(P_t{}^{\gamma}-P_t{}^{J})/P_t{}^{\gamma}$	-0.0187	-0.0075	-0.0001	0.0094	0.0140
$P_t(O+\eta>5)/P_t{}^{\gamma}$	-0.0290	-0.0175	-0.0098	0.0007	0.0073
$1-cos(\Delta\phi)$	0.0075	0.0072	0.0068	0.0057	0.0040
$\sigma(Db[\gamma,J])$	0.1805	0.1582	0.1417	0.1184	0.0963
$\sigma(Db[\gamma,part])$	0.1509	0.1389	0.1264	0.1055	0.0857
Entries	5042	4722	4228	3135	940

Table 15: Selection 2. $\Delta\phi_{(\gamma,jet)} = 180^\circ \pm 15^\circ, \epsilon^{jet} < 8\%$. LUCELL algorithm.

P_{tCUT}^{clust}	30	20	15	10	5
Nevent	1207812	1128624	1016076	749421	208921
$P_t 56$	11.6	10.6	9.8	8.4	6.8
$\Delta\phi$	5.9	5.7	5.5	5.0	4.2
P_t^{out}	8.9	8.3	7.8	6.9	5.5
$P_t^{\eta>5}$	4.7	4.7	4.7	4.6	4.4
$(P_t{}^{\gamma}-P_t^{part})/P_t{}^{\gamma}$	-0.0074	-0.0050	-0.0054	-0.0045	-0.0034
$(P_t{}^{J}-P_t^{part})/P_t{}^{J}$	-0.0138	-0.0174	-0.0192	-0.0189	-0.0184
$(P_t{}^{\gamma}-P_t{}^{J})/P_t{}^{\gamma}$	-0.0095	-0.0009	0.0023	0.0053	0.0084
$P_t(O+\eta>5)/P_t{}^{\gamma}$	-0.0207	-0.0118	-0.0083	-0.0040	0.0012
$1-cos(\Delta\phi)$	0.0079	0.0075	0.0071	0.0060	0.0043
$\sigma(Db[\gamma,J])$	0.1774	0.1581	0.1428	0.1225	0.1017
$\sigma(Db[\gamma,part])$	0.1519	0.1395	0.1266	0.1100	0.0861
Entries	10753	10048	9046	6672	1860

Table 16: Selection 3. $\Delta\phi_{(\gamma,jet)} = 180^\circ \pm 15^\circ, \epsilon^{jet} < 8\%$. UA1 algorithm.

P_{tCUT}^{clust}	30	20	15	10	5
Nevent	465468	436825	391559	289906	85927
$P_t 56$	11.4	10.5	9.6	8.3	6.7
$\Delta\phi$	5.7	5.5	5.3	4.9	4.0
P_t^{out}	8.8	8.2	7.7	6.7	5.3
$P_t^{\eta>5}$	4.7	4.7	4.7	4.6	4.4
$(P_t{}^{\gamma}-P_t^{part})/P_t{}^{\gamma}$	-0.0188	-0.0163	-0.0148	-0.0109	-0.0114
$(P_t{}^{J}-P_t^{part})/P_t{}^{J}$	0.0117	0.0067	0.0030	0.0000	-0.0052
$(P_t{}^{\gamma}-P_t{}^{J})/P_t{}^{\gamma}$	-0.0460	-0.0351	-0.0278	-0.0182	-0.0109
$P_t(O+\eta>5)/P_t{}^{\gamma}$	-0.0561	-0.0449	-0.0374	-0.0268	-0.0179
$1-cos(\Delta\phi)$	0.0073	0.0070	0.0066	0.0056	0.0041
$\sigma(Db[\gamma,J])$	0.1788	0.1573	0.1404	0.1172	0.0966
$\sigma(Db[\gamma,part])$	0.1516	0.1386	0.1269	0.1066	0.0884
Entries	4144	3889	3486	2581	765

Table 17: Selection 3. $\Delta\phi_{(\gamma,jet)} = 180^\circ \pm 15^\circ, \epsilon^{jet} < 6\%$. UA2 algorithm.

P_{tCUT}^{clust}	30	20	15	10	5
Nevent	465468	436825	391559	289906	85927
$P_t 56$	11.4	10.5	9.6	8.3	6.7
$\Delta\phi$	5.7	5.5	5.4	4.9	4.0
P_t^{out}	8.7	8.2	7.6	6.7	5.3
$P_t^{\eta>5}$	4.7	4.7	4.7	4.6	4.4
$(P_t{}^{\gamma}-P_t^{part})/P_t{}^{\gamma}$	-0.0188	-0.0163	-0.0148	-0.0109	-0.0114
$(P_t{}^{J}-P_t^{part})/P_t{}^{J}$	-0.0161	-0.0214	-0.0252	-0.0280	-0.0313
$(P_t{}^{\gamma}-P_t{}^{J})/P_t{}^{\gamma}$	-0.0184	-0.0075	-0.0003	0.0088	0.0144
$P_t(O+\eta>5)/P_t{}^{\gamma}$	-0.0285	-0.0173	-0.0099	0.0003	0.0074
$1-cos(\Delta\phi)$	0.0074	0.0071	0.0067	0.0057	0.0041
$\sigma(Db[\gamma,J])$	0.1789	0.1571	0.1404	0.1174	0.0962
$\sigma(Db[\gamma,part])$	0.1516	0.1386	0.1269	0.1066	0.0884
Entries	4144	3889	3486	2581	765

Table 18: Selection 3. $\Delta\phi_{(\gamma,jet)} = 180^\circ \pm 15^\circ, \epsilon^{jet} < 8\%$. LUCELL algorithm.

P_{tCUT}^{clust}	30	20	15	10	5
Nevent	465468	436825	391559	289906	85927
$P_t 56$	11.4	10.5	9.6	8.3	6.7
$\Delta\phi$	5.7	5.6	5.4	4.9	4.0
P_t^{out}	8.8	8.2	7.7	6.7	5.3
$P_t^{\eta>5}$	4.7	4.7	4.7	4.6	4.4
$(P_t{}^{\gamma}-P_t^{part})/P_t{}^{\gamma}$	-0.0188	-0.0163	-0.0148	-0.0109	-0.0114
$(P_t{}^{J}-P_t^{part})/P_t{}^{J}$	0.0041	-0.0010	-0.0047	-0.0076	-0.0110
$(P_t{}^{\gamma}-P_t{}^{J})/P_t{}^{\gamma}$	-0.0384	-0.0276	-0.0205	-0.0110	-0.0053
$P_t(O+\eta>5)/P_t{}^{\gamma}$	-0.0485	-0.0374	-0.0301	-0.0196	-0.0123
$1-cos(\Delta\phi)$	0.0074	0.0071	0.0067	0.0057	0.0041
$\sigma(Db[\gamma,J])$	0.1789	0.1577	0.1414	0.1184	0.0976
$\sigma(Db[\gamma,part])$	0.1516	0.1386	0.1269	0.1066	0.0884
Entries	4144	3889	3486	2581	765

Table 19: Selection 3. $\Delta\phi_{(\gamma,jet)} = 180^\circ \pm 15^\circ, \epsilon^{jet} < 8\%$. UA1 algorithm.

P_{tCUT}^{clust}	30	20	15	10	5
Nevent	1011471	945313	850512	629460	172529
$P_t 56$	11.5	10.5	9.7	8.4	6.7
$\Delta\phi$	5.8	5.7	5.5	5.0	4.1
${P_t}^{out}$	8.8	8.3	7.7	6.8	5.4
${P_t}^{\eta>5}$	4.7	4.7	4.7	4.6	4.4
$({P_t}^{\gamma}-{P_t}^{part})/{P_t}^{\gamma}$	-0.0085	-0.0060	-0.0060	-0.0045	-0.0034
$({P_t}^{J}-{P_t}^{part})/{P_t}^{J}$	-0.0024	-0.0060	-0.0076	-0.0085	-0.0107
$({P_t}^{\gamma}-{P_t}^{J})/{P_t}^{\gamma}$	-0.0214	-0.0123	-0.0088	-0.0042	0.0017
$P_t(O+\eta>5)/{P_t}^{\gamma}$	-0.0323	-0.0229	-0.0191	-0.0132	-0.0056
$1 - cos(\Delta\phi)$	0.0077	0.0074	0.0069	0.0059	0.0043
$\sigma(Db[\gamma, J])$	0.1767	0.1561	0.1407	0.1198	0.0992
$\sigma(Db[\gamma, part])$	0.1519	0.1393	0.1273	0.1097	0.0868
Entries	9005	8416	7572	5604	1536

Table 20: Selection 3. $\Delta\phi_{(\gamma,jet)} = 180^\circ \pm 15^\circ, \epsilon^{jet} < 8\%$. LUCELL algorithm.

P_{tCUT}^{clust}	30	20	15	10	5
Nevent	1011471	945313	850512	629460	172529
$P_t 56$	11.5	10.5	9.7	8.4	6.7
hline $\Delta\phi$	5.8	5.7	5.5	5.0	4.1
${P_t}^{out}$	8.8	8.3	7.8	6.9	5.5
${P_t}^{\eta>5}$	4.7	4.7	4.7	4.6	4.4
$({P_t}^{\gamma}-{P_t}^{part})/{P_t}^{\gamma}$	-0.0085	-0.0060	-0.0060	-0.0045	-0.0034
$({P_t}^{J}-{P_t}^{part})/{P_t}^{J}$	-0.0086	-0.0124	-0.0140	-0.0146	-0.0155
$({P_t}^{\gamma}-{P_t}^{J})/{P_t}^{\gamma}$	-0.0153	-0.0062	-0.0028	0.0016	0.0062
$P_t(O+\eta>5)/{P_t}^{\gamma}$	-0.0263	-0.0168	-0.0132	-0.0075	-0.0012
$1 - cos(\Delta\phi)$	0.0077	0.0074	0.0070	0.0060	0.0043
$\sigma(Db[\gamma, J])$	0.1765	0.1563	0.1414	0.1206	0.1002
$\sigma(Db[\gamma, part])$	0.1519	0.1393	0.1273	0.1097	0.0868
Entries	9005	8416	7572	5604	1536

Appendix 3 $\quad 100 < P_t{}^{\gamma} < 120\ GeV/c$

$P_t{}^{isol} < 5\ GeV/c, \quad \epsilon^{\gamma} < 7\%$

Table 1: Selection 1. $\Delta\phi_{(\gamma,jet)} = 180° \pm 180°$. UA1 algorithm.

P_{tCUT}^{clust}	30	20	15	10	5
Nevent*	112470	79818	59678	35069	6739
$P_t 56$	22.2	17.0	14.4	11.9	9.6
$\Delta\phi$	6.1	4.4	3.7	2.8	2.2
$P_t{}^{out}$	17.4	12.8	10.5	8.2	5.7
$P_t{}^{\eta>5}$	5.9	5.7	5.7	5.5	5.3
$(P_t{}^{\gamma}-P_t{}^{part})/P_t{}^{\gamma}$	0.0141	0.0062	0.0043	0.0035	0.0051
$(P_t{}^{J}-P_t{}^{part})/P_t{}^{J}$	-0.0566	-0.0309	-0.0225	-0.0133	-0.0057
$(P_t{}^{\gamma}-P_t{}^{J})/P_t{}^{\gamma}$	0.0496	0.0265	0.0186	0.0104	0.0063
$P_t(O+\eta>5)/P_t{}^{\gamma}$	0.0341	0.0164	0.0103	0.0040	0.0019
$1-cos(\Delta\phi)$	0.0107	0.0053	0.0036	0.0021	0.0014
$\sigma(Db[\gamma,J])^{**}$	0.1423	0.1068	0.0909	0.0765	0.0611
$\sigma(Db[\gamma,part])^{***}$	0.1287	0.0997	0.0873	0.0761	0.0742
Entries	17591	12484	9334	5485	1054

Table 2: Selection 1. $\Delta\phi_{(\gamma,jet)} = 180° \pm 180°$. UA2 algorithm.

P_{tCUT}^{clust}	30	20	15	10	5
Nevent	106857	77830	59333	35127	6803
$P_t 56$	22.7	18.0	15.5	13.0	10.6
$\Delta\phi$	6.0	4.4	3.6	2.8	2.1
$P_t{}^{out}$	17.0	12.7	10.6	8.2	6.0
$P_t{}^{\eta>5}$	5.8	5.6	5.6	5.5	5.0
$(P_t{}^{\gamma}-P_t{}^{part})/P_t{}^{\gamma}$	0.0154	0.0091	0.0075	0.0070	0.0073
$(P_t{}^{J}-P_t{}^{part})/P_t{}^{J}$	-0.0523	-0.0320	-0.0259	-0.0174	-0.0083
$(P_t{}^{\gamma}-P_t{}^{J})/P_t{}^{\gamma}$	0.0485	0.0307	0.0249	0.0181	0.0125
$P_t(O+\eta>5)/P_t{}^{\gamma}$	0.0336	0.0210	0.0170	0.0122	0.0092
$1-cos(\Delta\phi)$	0.0103	0.0052	0.0035	0.0021	0.0013
$\sigma(Db[\gamma,J])$	0.1369	0.1042	0.0902	0.0755	0.0541
$\sigma(Db[\gamma,part])$	0.1349	0.1107	0.1003	0.0911	0.0846
Entries	16713	12173	9280	5494	1064

Table 3: Selection 1. $\Delta\phi_{(\gamma,jet)} = 180° \pm 180°$. LUCELL algorithm.

P_{tCUT}^{clust}	30	20	15	10	5
Nevent	119459	86813	64710	37320	6912
$P_t 56$	21.6	17.0	14.3	11.5	8.8
$\Delta\phi$	5.9	4.5	3.7	2.9	2.2
$P_t{}^{out}$	17.0	13.0	10.7	8.3	5.7
$P_t{}^{\eta>5}$	5.9	5.7	5.7	5.6	5.3
$(P_t{}^{\gamma}-P_t{}^{part})/P_t{}^{\gamma}$	0.0128	0.0060	0.0029	0.0020	0.0019
$(P_t{}^{J}-P_t{}^{part})/P_t{}^{J}$	-0.0586	-0.0363	-0.0284	-0.0189	-0.0112
$(P_t{}^{\gamma}-P_t{}^{J})/P_t{}^{\gamma}$	0.0513	0.0313	0.0227	0.0142	0.0082
$P_t(O+\eta>5)/P_t{}^{\gamma}$	0.0364	0.0212	0.0144	0.0076	0.0037
$1-cos(\Delta\phi)$	0.0100	0.0054	0.0037	0.0022	0.0014
$\sigma(Db[\gamma,J])$	0.1378	0.1073	0.0915	0.0774	0.0620
$\sigma(Db[\gamma,part])$	0.1246	0.0986	0.0832	0.0706	0.0621
Entries	18684	13578	10121	5837	1081

*Number of events (Nevent) is given in this and in the following tables for integrated luminosity $L_{int} = 3\ fb^{-1}$

** $Db[\gamma,part] \equiv (P_t{}^{\gamma}-P_t{}^{part})/P_t{}^{\gamma}$

*** $Db[\gamma,J] \equiv (P_t{}^{\gamma}-P_t{}^{J})/P_t{}^{\gamma}$

Table 4: Selection 1. $\Delta\phi_{(\gamma,jet)} = 180° \pm 15°$. UA1 algorithm.

P_{tCUT}^{clust}	30	20	15	10	5
Nevent	103705	78015	59211	35018	6726
$P_t 56$	20.3	16.5	14.2	11.8	9.5
$\Delta\phi$	4.9	4.1	3.6	2.8	2.2
${P_t}^{out}$	15.5	12.3	10.4	8.1	5.7
${P_t}^{\eta>5}$	5.7	5.7	5.6	5.5	5.2
$({P_t}^{\gamma}-{P_t}^{part})/{P_t}^{\gamma}$	0.0119	0.0058	0.0039	0.0034	0.0050
$({P_t}^{J}-{P_t}^{part})/{P_t}^{J}$	-0.0488	-0.0297	-0.0222	-0.0132	-0.0056
$({P_t}^{\gamma}-{P_t}^{J})/{P_t}^{\gamma}$	0.0428	0.0251	0.0181	0.0103	0.0061
$P_t(O+\eta>5)/{P_t}^{\gamma}$	0.0322	0.0161	0.0102	0.0040	0.0018
$1-cos(\Delta\phi)$	0.0058	0.0042	0.0032	0.0020	0.0012
$\sigma(Db[\gamma,J])$	0.1352	0.1055	0.0903	0.0764	0.0609
$\sigma(Db[\gamma,part])$	0.1225	0.0985	0.0866	0.0761	0.0742
Entries	16220	12202	9261	5477	1052

Table 5: Selection 1. $\Delta\phi_{(\gamma,jet)} = 180° \pm 15°$. UA2 algorithm.

P_{tCUT}^{clust}	30	20	15	10	5
Nevent	98910	76187	58898	35095	6790
$P_t 56$	20.9	17.5	15.4	13.0	10.5
$\Delta\phi$	4.8	4.1	3.5	2.8	2.1
${P_t}^{out}$	15.1	12.3	10.4	8.2	6.0
${P_t}^{\eta>5}$	5.6	5.6	5.5	5.4	4.9
$({P_t}^{\gamma}-{P_t}^{part})/{P_t}^{\gamma}$	0.0126	0.0088	0.0072	0.0070	0.0072
$({P_t}^{J}-{P_t}^{part})/{P_t}^{J}$	-0.0458	-0.0308	-0.0254	-0.0173	-0.0081
$({P_t}^{\gamma}-{P_t}^{J})/{P_t}^{\gamma}$	0.0418	0.0295	0.0243	0.0180	0.0123
$P_t(O+\eta>5)/{P_t}^{\gamma}$	0.0317	0.0209	0.0168	0.0122	0.0092
$1-cos(\Delta\phi)$	0.0057	0.0042	0.0032	0.0020	0.0011
$\sigma(Db[\gamma,J])$	0.1298	0.1028	0.0896	0.0754	0.0539
$\sigma(Db[\gamma,part])$	0.1283	0.1097	0.0998	0.0911	0.0846
Entries	15470	11916	9212	5489	1062

Table 6: Selection 1. $\Delta\phi_{(\gamma,jet)} = 180° \pm 15°$. LUCELL algorithm.

P_{tCUT}^{clust}	30	20	15	10	5
Nevent	111064	84869	64192	37269	6899
$P_t 56$	20.0	16.5	14.1	11.5	8.7
$\Delta\phi$	4.9	4.2	3.6	2.9	2.2
${P_t}^{out}$	15.4	12.5	10.5	8.2	5.7
${P_t}^{\eta>5}$	5.7	5.7	5.6	5.6	5.3
$({P_t}^{\gamma}-{P_t}^{part})/{P_t}^{\gamma}$	0.0107	0.0056	0.0025	0.0019	0.0018
$({P_t}^{J}-{P_t}^{part})/{P_t}^{J}$	-0.0522	-0.0351	-0.0279	-0.0189	-0.0111
$({P_t}^{\gamma}-{P_t}^{J})/{P_t}^{\gamma}$	0.0454	0.0300	0.0221	0.0141	0.0080
$P_t(O+\eta>5)/{P_t}^{\gamma}$	0.0348	0.0210	0.0142	0.0076	0.0037
$1-cos(\Delta\phi)$	0.0058	0.0044	0.0033	0.0021	0.0012
$\sigma(Db[\gamma,J])$	0.1317	0.1061	0.0909	0.0774	0.0619
$\sigma(Db[\gamma,part])$	0.1193	0.0974	0.0825	0.0707	0.0621
Entries	17371	13274	10040	5829	1079

Table 7: Selection 1. $\Delta\phi_{(\gamma,jet)} = 180° \pm 10°$. UA1 algorithm.

P_{tCUT}^{clust}	30	20	15	10	5
Nevent	90854	72676	56955	34545	6681
$P_t 56$	18.7	15.7	13.7	11.7	9.4
$\Delta\phi$	3.8	3.5	3.2	2.7	2.1
P_t^{out}	13.8	11.5	9.9	8.0	5.7
$P_t^{\eta>5}$	5.7	5.6	5.6	5.4	5.1
$(P_t{}^{\gamma}-P_t^{part})/P_t{}^{\gamma}$	0.0098	0.0047	0.0033	0.0033	0.0051
$(P_t{}^{J}-P_t^{part})/P_t{}^{J}$	-0.0440	-0.0280	-0.0211	-0.0123	-0.0051
$(P_t{}^{\gamma}-P_t{}^{J})/P_t{}^{\gamma}$	0.0375	0.0229	0.0168	0.0096	0.0057
$P_t(O+\eta>5)/P_t{}^{\gamma}$	0.0295	0.0153	0.0097	0.0036	0.0016
$1-cos(\Delta\phi)$	0.0033	0.0029	0.0025	0.0018	0.0011
$\sigma(Db[\gamma,J])$	0.1307	0.1028	0.0886	0.0751	0.0607
$\sigma(Db[\gamma,part])$	0.1172	0.0953	0.0845	0.0760	0.0744
Entries	14210	11367	8908	5403	1045

Table 8: Selection 1. $\Delta\phi_{(\gamma,jet)} = 180° \pm 10°$. UA2 algorithm.

P_{tCUT}^{clust}	30	20	15	10	5
Nevent	86691	70976	56667	34654	6771
$P_t 56$	19.3	16.6	14.8	12.9	10.5
$\Delta\phi$	3.8	3.5	3.2	2.7	2.0
P_t^{out}	13.5	11.4	10.0	8.1	5.9
$P_t^{\eta>5}$	5.6	5.5	5.4	5.4	4.9
$(P_t{}^{\gamma}-P_t^{part})/P_t{}^{\gamma}$	0.0107	0.0078	0.0064	0.0066	0.0072
$(P_t{}^{J}-P_t^{part})/P_t{}^{J}$	-0.0416	-0.0290	-0.0243	-0.0167	-0.0081
$(P_t{}^{\gamma}-P_t{}^{J})/P_t{}^{\gamma}$	0.0371	0.0273	0.0228	0.0173	0.0122
$P_t(O+\eta>5)/P_t{}^{\gamma}$	0.0296	0.0202	0.0162	0.0119	0.0092
$1-cos(\Delta\phi)$	0.0033	0.0029	0.0025	0.0018	0.0011
$\sigma(Db[\gamma,J])$	0.1255	0.1005	0.0875	0.0740	0.0539
$\sigma(Db[\gamma,part])$	0.1233	0.1070	0.0978	0.0907	0.0847
Entries	13559	11101	8863	5420	1059

Table 9: Selection 1. $\Delta\phi_{(\gamma,jet)} = 180° \pm 10°$. LUCELL algorithm.

P_{tCUT}^{clust}	30	20	15	10	5
Nevent	97401	78757	61539	36770	6860
$P_t 56$	18.5	15.6	13.5	11.3	8.6
$\Delta\phi$	3.8	3.6	3.3	2.7	2.1
P_t^{out}	13.7	11.6	10.0	8.1	5.7
$P_t^{\eta>5}$	5.7	5.6	5.6	5.5	5.2
$(P_t{}^{\gamma}-P_t^{part})/P_t{}^{\gamma}$	0.0085	0.0043	0.0018	0.0017	0.0019
$(P_t{}^{J}-P_t^{part})/P_t{}^{J}$	-0.0481	-0.0338	-0.0270	-0.0182	-0.0107
$(P_t{}^{\gamma}-P_t{}^{J})/P_t{}^{\gamma}$	0.0405	0.0278	0.0207	0.0135	0.0078
$P_t(O+\eta>5)/P_t{}^{\gamma}$	0.0324	0.0202	0.0137	0.0073	0.0036
$1-cos(\Delta\phi)$	0.0034	0.0030	0.0025	0.0018	0.0011
$\sigma(Db[\gamma,J])$	0.1277	0.1038	0.0891	0.0762	0.0618
$\sigma(Db[\gamma,part])$	0.1139	0.0938	0.0799	0.0701	0.0622
Entries	15234	12318	9625	5751	1073

Table 10: Selection 1. $\Delta\phi_{(\gamma,jet)} = 180° \pm 5°$. UA1 algorithm.

P_{tCUT}^{clust}	30	20	15	10	5
Nevent	62165	52901	44180	29545	6253
P_t56	16.4	13.9	12.4	10.8	9.0
$\Delta\phi$	2.2	2.2	2.2	2.0	1.8
P_t^{out}	11.5	9.6	8.5	7.3	5.5
$P_t^{\eta>5}$	5.5	5.4	5.4	5.2	4.8
$(P_t^{\gamma}-P_t^{part})/P_t^{\gamma}$	0.0072	0.0043	0.0029	0.0030	0.0046
$(P_t^{J}-P_t^{part})/P_t^{J}$	-0.0363	-0.0226	-0.0169	-0.0096	-0.0024
$(P_t^{\gamma}-P_t^{J})/P_t^{\gamma}$	0.0293	0.0185	0.0133	0.0076	0.0038
$P_t(O+\eta>5)/P_t^{\gamma}$	0.0240	0.0133	0.0084	0.0030	0.0005
$1-cos(\Delta\phi)$	0.0011	0.0011	0.0010	0.0009	0.0008
$\sigma(Db[\gamma,J])$	0.1234	0.0971	0.0839	0.0710	0.0558
$\sigma(Db[\gamma,part])$	0.1094	0.0915	0.0824	0.0760	0.0743
Entries	9723	8274	6910	4621	978

Table 11: Selection 1. $\Delta\phi_{(\gamma,jet)} = 180° \pm 5°$. UA2 algorithm.

P_{tCUT}^{clust}	30	20	15	10	5
Nevent	60094	52095	44122	29718	6342
P_t56	17.0	14.8	13.5	12.0	10.2
$\Delta\phi$	2.2	2.2	2.1	2.0	1.7
P_t^{out}	11.2	9.6	8.6	7.4	5.7
$P_t^{\eta>5}$	5.5	5.4	5.3	5.2	4.6
$(P_t^{\gamma}-P_t^{part})/P_t^{\gamma}$	0.0071	0.0060	0.0053	0.0063	0.0075
$(P_t^{J}-P_t^{part})/P_t^{J}$	-0.0364	-0.0253	-0.0206	-0.0141	-0.0047
$(P_t^{\gamma}-P_t^{J})/P_t^{\gamma}$	0.0303	0.0229	0.0191	0.0153	0.0104
$P_t(O+\eta>5)/P_t^{\gamma}$	0.0253	0.0180	0.0145	0.0112	0.0085
$1-cos(\Delta\phi)$	0.0011	0.0010	0.0010	0.0009	0.0007
$\sigma(Db[\gamma,J])$	0.1176	0.0949	0.0832	0.0707	0.0488
$\sigma(Db[\gamma,part])$	0.1135	0.1007	0.0950	0.0896	0.0860
Entries	9399	8148	6901	4648	992

Table 12: Selection 1. $\Delta\phi_{(\gamma,jet)} = 180° \pm 5°$. LUCELL algorithm.

P_{tCUT}^{clust}	30	20	15	10	5
Nevent	66392	56807	47434	31233	6419
P_t56	16.1	13.8	12.2	10.4	8.1
$\Delta\phi$	2.3	2.2	2.2	2.0	1.8
P_t^{out}	11.4	9.7	8.6	7.3	5.4
$P_t^{\eta>5}$	5.5	5.4	5.4	5.3	4.9
$(P_t^{\gamma}-P_t^{part})/P_t^{\gamma}$	0.0061	0.0032	0.0010	0.0013	0.0008
$(P_t^{J}-P_t^{part})/P_t^{J}$	-0.0413	-0.0284	-0.0229	-0.0150	-0.0083
$(P_t^{\gamma}-P_t^{J})/P_t^{\gamma}$	0.0335	0.0228	0.0170	0.0111	0.0054
$P_t(O+\eta>5)/P_t^{\gamma}$	0.0281	0.0177	0.0122	0.0065	0.0021
$1-cos(\Delta\phi)$	0.0011	0.0011	0.0010	0.0009	0.0007
$\sigma(Db[\gamma,J])$	0.1208	0.0978	0.0848	0.0718	0.0567
$\sigma(Db[\gamma,part])$	0.1061	0.0884	0.0766	0.0687	0.0608
Entries	10384	8885	7419	4885	1004

Table 13: Selection 2. $\Delta\phi_{(\gamma,jet)} = 180^\circ \pm 15^\circ, \epsilon^{jet} < 4\%$. UA1 algorithm.

P_{tCUT}^{clust}	30	20	15	10	5
Nevent	62459	50305	40331	25536	5639
$P_t 56$	18.0	15.0	13.1	10.9	8.8
$\Delta\phi$	4.6	3.9	3.4	2.7	2.1
P_t^{out}	13.8	11.5	9.9	7.9	5.6
$P_t^{\eta>5}$	5.5	5.5	5.4	5.3	5.0
$(P_t{}^{\gamma}-P_t^{part})/P_t{}^{\gamma}$	-0.0028	-0.0045	-0.0037	-0.0016	0.0005
$(P_t{}^{J}-P_t^{part})/P_t{}^{J}$	-0.0173	-0.0132	-0.0106	-0.0058	-0.0033
$(P_t{}^{\gamma}-P_t{}^{J})/P_t{}^{\gamma}$	0.0055	0.0025	0.0021	0.0005	0.0014
$P_t(O+\eta>5)/P_t{}^{\gamma}$	-0.0035	-0.0049	-0.0042	-0.0045	-0.0018
$1-cos(\Delta\phi)$	0.0052	0.0039	0.0030	0.0019	0.0012
$\sigma(Db[\gamma,J])$	0.1166	0.0943	0.0801	0.0677	0.0527
$\sigma(Db[\gamma,part])$	0.1014	0.0821	0.0716	0.0646	0.0614
Entries	9769	7868	6308	3994	882

Table 14: Selection 2. $\Delta\phi_{(\gamma,jet)} = 180^\circ \pm 15^\circ, \epsilon^{jet} < 4\%$. UA2 algorithm.

P_{tCUT}^{clust}	30	20	15	10	5
Nevent	57313	46347	37384	23624	5192
$P_t 56$	18.3	15.4	13.5	11.2	8.9
$\Delta\phi$	4.6	3.9	3.4	2.7	2.1
P_t^{out}	13.8	11.5	10.0	7.9	5.8
$P_t^{\eta>5}$	5.4	5.4	5.3	5.2	4.8
$(P_t{}^{\gamma}-P_t^{part})/P_t{}^{\gamma}$	-0.0027	-0.0033	-0.0031	-0.0013	0.0020
$(P_t{}^{J}-P_t^{part})/P_t{}^{J}$	-0.0243	-0.0215	-0.0194	-0.0154	-0.0088
$(P_t{}^{\gamma}-P_t{}^{J})/P_t{}^{\gamma}$	0.0130	0.0120	0.0114	0.0104	0.0091
$P_t(O+\eta>5)/P_t{}^{\gamma}$	0.0044	0.0049	0.0054	0.0058	0.0070
$1-cos(\Delta\phi)$	0.0053	0.0039	0.0030	0.0019	0.0011
$\sigma(Db[\gamma,J])$	0.1138	0.0931	0.0799	0.0668	0.0467
$\sigma(Db[\gamma,part])$	0.1067	0.0886	0.0771	0.0688	0.0663
Entries	8964	7249	5847	3695	812

Table 15: Selection 2. $\Delta\phi_{(\gamma,jet)} = 180^\circ \pm 15^\circ, \epsilon^{jet} < 4\%$. LUCELL algorithm.

P_{tCUT}^{clust}	30	20	15	10	5
Nevent	67159	54461	43515	27467	5978
$P_t 56$	17.8	14.9	13.0	10.7	8.3
$\Delta\phi$	4.6	4.0	3.5	2.8	2.1
P_t^{out}	13.8	11.6	9.9	7.9	5.6
$P_t^{\eta>5}$	5.6	5.5	5.4	5.4	5.0
$(P_t{}^{\gamma}-P_t^{part})/P_t{}^{\gamma}$	-0.0031	-0.0048	-0.0045	-0.0027	-0.0017
$(P_t{}^{J}-P_t^{part})/P_t{}^{J}$	-0.0223	-0.0177	-0.0146	-0.0098	-0.0073
$(P_t{}^{\gamma}-P_t{}^{J})/P_t{}^{\gamma}$	0.0099	0.0063	0.0051	0.0032	0.0030
$P_t(O+\eta>5)/P_t{}^{\gamma}$	0.0010	-0.0010	-0.0011	-0.0018	0.0000
$1-cos(\Delta\phi)$	0.0053	0.0040	0.0031	0.0020	0.0012
$\sigma(Db[\gamma,J])$	0.1154	0.0947	0.0805	0.0679	0.0525
$\sigma(Db[\gamma,part])$	0.0979	0.0791	0.0678	0.0594	0.0512
Entries	10504	8518	6806	4296	935

Table 16: Selection 3. $\Delta\phi_{(\gamma,jet)} = 180^\circ \pm 15^\circ, \epsilon^{jet} < 4\%$. UA1 algorithm.

P_{tCUT}^{clust}	30	20	15	10	5
Nevent	45478	37102	29743	18855	3945
$P_t 56$	17.5	14.9	12.9	10.8	8.4
$\Delta\phi$	4.5	3.9	3.4	2.7	2.1
P_t^{out}	13.5	11.4	9.9	7.9	5.7
$P_t^{\eta>5}$	5.5	5.4	5.3	5.2	4.8
$(P_t{}^{\gamma}-P_t^{part})/P_t{}^{\gamma}$	-0.0039	-0.0049	-0.0045	-0.0025	-0.0004
$(P_t{}^{J}-P_t^{part})/P_t{}^{J}$	-0.0136	-0.0117	-0.0094	-0.0047	-0.0006
$(P_t{}^{\gamma}-P_t{}^{J})/P_t{}^{\gamma}$	0.0019	0.0010	0.0005	-0.0010	-0.0012
$P_t(O+\eta>5)/P_t{}^{\gamma}$	-0.0066	-0.0061	-0.0055	-0.0058	-0.0036
$1-cos(\Delta\phi)$	0.0050	0.0038	0.0030	0.0019	0.0011
$\sigma(Db[\gamma,J])$	0.1112	0.0930	0.0793	0.0661	0.0459
$\sigma(Db[\gamma,part])$	0.1003	0.0816	0.0700	0.0615	0.0559
Entries	7113	5803	4652	2949	617

Table 17: Selection 3. $\Delta\phi_{(\gamma,jet)} = 180^\circ \pm 15^\circ, \epsilon^{jet} < 4\%$. UA2 algorithm.

P_{tCUT}^{clust}	30	20	15	10	5
Nevent	45478	37102	29743	18855	3945
$P_t 56$	17.5	14.9	12.9	10.8	8.4
$\Delta\phi$	4.5	3.9	3.4	2.7	2.1
P_t^{out}	13.5	11.5	9.9	7.9	5.8
$P_t^{\eta>5}$	5.5	5.4	5.3	5.2	4.8
$(P_t{}^{\gamma}-P_t^{part})/P_t{}^{\gamma}$	-0.0039	-0.0049	-0.0045	-0.0025	-0.0004
$(P_t{}^{J}-P_t^{part})/P_t{}^{J}$	-0.0253	-0.0231	-0.0208	-0.0157	-0.0104
$(P_t{}^{\gamma}-P_t{}^{J})/P_t{}^{\gamma}$	0.0129	0.0119	0.0114	0.0097	0.0084
$P_t(O+\eta>5)/P_t{}^{\gamma}$	0.0044	0.0048	0.0054	0.0049	0.0060
$1-cos(\Delta\phi)$	0.0050	0.0038	0.0030	0.0019	0.0011
$\sigma(Db[\gamma,J])$	0.1115	0.0932	0.0797	0.0665	0.0466
$\sigma(Db[\gamma,part])$	0.1003	0.0816	0.0700	0.0615	0.0559
Entries	7113	5803	4652	2949	617

Table 18: Selection 3. $\Delta\phi_{(\gamma,jet)} = 180^\circ \pm 15^\circ, \epsilon^{jet} < 4\%$. LUCELL algorithm.

P_{tCUT}^{clust}	30	20	15	10	5
Nevent	45478	37102	29743	18855	3945
$P_t 56$	17.5	14.9	12.9	10.8	8.4
$\Delta\phi$	4.5	3.9	3.4	2.7	2.1
P_t^{out}	13.5	11.5	9.9	7.9	5.7
$P_t^{\eta>5}$	5.5	5.4	5.3	5.2	4.8
$(P_t{}^{\gamma}-P_t^{part})/P_t{}^{\gamma}$	-0.0039	-0.0049	-0.0045	-0.0025	-0.0004
$(P_t{}^{J}-P_t^{part})/P_t{}^{J}$	-0.0178	-0.0156	-0.0127	-0.0075	-0.0024
$(P_t{}^{\gamma}-P_t{}^{J})/P_t{}^{\gamma}$	0.0058	0.0046	0.0037	0.0017	0.0007
$P_t(O+\eta>5)/P_t{}^{\gamma}$	-0.0027	-0.0025	-0.0023	-0.0031	-0.0017
$1-cos(\Delta\phi)$	0.0051	0.0038	0.0030	0.0019	0.0011
$\sigma(Db[\gamma,J])$	0.1121	0.0938	0.0798	0.0664	0.0462
$\sigma(Db[\gamma,part])$	0.1003	0.0816	0.0700	0.0615	0.0559
Entries	7113	5803	4652	2949	617

Appendix 4 $\quad 200 < P_t{}^{\gamma} < 240\ GeV/c$

$P_t{}^{isol} < 5\ GeV/c, \quad \epsilon^{\gamma} < 7\%$

Table 1: Selection 1. $\Delta\phi_{(\gamma,jet)} = 180° \pm 180°$. UA1 algorithm.

P_{tCUT}^{clust}	30	20	15	10	5
Nevent*	8543	5624	3971	2142	351
P_t56	23.6	18.1	15.2	12.3	8.9
$\Delta\phi$	3.2	2.4	2.0	1.6	1.2
$P_t{}^{out}$	19.0	14.0	11.4	8.7	6.2
$P_t{}^{\eta>5}$	6.9	6.8	6.7	6.6	5.9
$(P_t{}^{\gamma}-P_t{}^{part})/P_t{}^{\gamma}$	-0.0004	-0.0021	-0.0018	-0.0007	-0.0022
$(P_t{}^{J}-P_t{}^{part})/P_t{}^{J}$	-0.0331	-0.0236	-0.0188	-0.0141	-0.0124
$(P_t{}^{\gamma}-P_t{}^{J})/P_t{}^{\gamma}$	0.0257	0.0168	0.0132	0.0103	0.0078
$P_t(O+\eta>5)/P_t{}^{\gamma}$	0.0229	0.0153	0.0122	0.0097	0.0075
$1-cos(\Delta\phi)$	0.0028	0.0015	0.0010	0.0006	0.0004
$\sigma(Db[\gamma,J])^{**}$	0.0835	0.0661	0.0577	0.0504	0.0425
$\sigma(Db[\gamma,part])^{***}$	0.0744	0.0589	0.0526	0.0488	0.0306
Entries	22331	14701	10381	5599	917

Table 2: Selection 1. $\Delta\phi_{(\gamma,jet)} = 180° \pm 180°$. UA2 algorithm.

P_{tCUT}^{clust}	30	20	15	10	5
Nevent	9359	6712	4988	2828	522
P_t56	27.0	22.5	19.9	17.3	12.9
$\Delta\phi$	3.0	2.3	2.0	1.5	1.2
$P_t{}^{out}$	17.2	13.3	11.0	8.5	5.9
$P_t{}^{\eta>5}$	6.8	6.6	6.5	6.4	6.0
$(P_t{}^{\gamma}-P_t{}^{part})/P_t{}^{\gamma}$	0.0055	0.0049	0.0057	0.0073	0.0051
$(P_t{}^{J}-P_t{}^{part})/P_t{}^{J}$	-0.0090	-0.0055	-0.0034	-0.0003	-0.0019
$(P_t{}^{\gamma}-P_t{}^{J})/P_t{}^{\gamma}$	0.0093	0.0066	0.0059	0.0052	0.0049
$P_t(O+\eta>5)/P_t{}^{\gamma}$	0.0068	0.0052	0.0049	0.0046	0.0046
$1-cos(\Delta\phi)$	0.0025	0.0015	0.0010	0.0006	0.0004
$\sigma(Db[\gamma,J])$	0.0769	0.0630	0.0556	0.0473	0.0413
$\sigma(Db[\gamma,part])$	0.0962	0.0874	0.0845	0.0848	0.0668
Entries	24463	17544	13038	7393	1365

Table 3: Selection 1. $\Delta\phi_{(\gamma,jet)} = 180° \pm 180°$. LUCELL algorithm.

P_{tCUT}^{clust}	30	20	15	10	5
Nevent	9491	6772	4908	2717	471
P_t56	23.8	19.3	16.4	13.2	9.3
$\Delta\phi$	3.0	2.4	2.0	1.6	1.2
$P_t{}^{out}$	17.4	13.6	11.1	8.6	5.8
$P_t{}^{\eta>5}$	7.0	6.9	6.8	6.6	6.1
$(P_t{}^{\gamma}-P_t{}^{part})/P_t{}^{\gamma}$	0.0013	0.0004	0.0009	0.0008	-0.0018
$(P_t{}^{J}-P_t{}^{part})/P_t{}^{J}$	-0.0167	-0.0119	-0.0085	-0.0052	-0.0058
$(P_t{}^{\gamma}-P_t{}^{J})/P_t{}^{\gamma}$	0.0123	0.0078	0.0057	0.0033	0.0016
$P_t(O+\eta>5)/P_t{}^{\gamma}$	0.0099	0.0063	0.0046	0.0027	0.0013
$1-cos(\Delta\phi)$	0.0025	0.0015	0.0010	0.0006	0.0004
$\sigma(Db[\gamma,J])$	0.0786	0.0662	0.0586	0.0500	0.0434
$\sigma(Db[\gamma,part])$	0.0792	0.0683	0.0630	0.0557	0.0303
Entries	24809	17702	12829	7101	1231

*Number of events (Nevent) is given in this and in the following tables for integrated luminosity $L_{int} = 3\ fb^{-1}$

** $Db[\gamma,part] \equiv (P_t{}^{\gamma}-P_t{}^{part})/P_t{}^{\gamma}$

*** $Db[\gamma,J] \equiv (P_t{}^{\gamma}-P_t{}^{J})/P_t{}^{\gamma}$

Table 4: Selection 1. $\Delta\phi_{(\gamma,jet)} = 180° \pm 15°$. UA1 algorithm.

P_{tCUT}^{clust}	30	20	15	10	5
Nevent	8515	5623	3971	2142	351
$P_t 56$	23.5	18.1	15.2	12.3	8.9
$\Delta\phi$	3.2	2.4	2.0	1.6	1.2
${P_t}^{out}$	18.9	14.0	11.4	8.7	6.2
${P_t}^{\eta>5}$	6.9	6.8	6.7	6.6	5.9
$({P_t}^{\gamma}-{P_t}^{part})/{P_t}^{\gamma}$	-0.0005	-0.0021	-0.0018	-0.0007	-0.0022
$({P_t}^{J}-{P_t}^{part})/{P_t}^{J}$	-0.0328	-0.0234	-0.0188	-0.0141	-0.0124
$({P_t}^{\gamma}-{P_t}^{J})/{P_t}^{\gamma}$	0.0254	0.0167	0.0132	0.0103	0.0078
$P_t(O+\eta>5)/{P_t}^{\gamma}$	0.0228	0.0153	0.0122	0.0097	0.0075
$1-cos(\Delta\phi)$	0.0026	0.0015	0.0010	0.0006	0.0004
$\sigma(Db[\gamma,J])$	0.0832	0.0659	0.0577	0.0504	0.0425
$\sigma(Db[\gamma,part])$	0.0743	0.0589	0.0526	0.0488	0.0306
Entries	22258	14697	10381	5599	917

Table 5: Selection 1. $\Delta\phi_{(\gamma,jet)} = 180° \pm 15°$. UA2 algorithm.

P_{tCUT}^{clust}	30	20	15	10	5
Nevent	9338	6711	4988	2828	522
$P_t 56$	26.9	22.5	19.9	17.3	12.9
$\Delta\phi$	3.0	2.3	2.0	1.5	1.2
${P_t}^{out}$	17.1	13.3	11.0	8.5	5.9
${P_t}^{\eta>5}$	6.8	6.6	6.5	6.4	6.0
$({P_t}^{\gamma}-{P_t}^{part})/{P_t}^{\gamma}$	0.0054	0.0049	0.0057	0.0073	0.0051
$({P_t}^{J}-{P_t}^{part})/{P_t}^{J}$	-0.0089	-0.0054	-0.0034	-0.0003	-0.0019
$({P_t}^{\gamma}-{P_t}^{J})/{P_t}^{\gamma}$	0.0092	0.0066	0.0059	0.0052	0.0049
$P_t(O+\eta>5)/{P_t}^{\gamma}$	0.0068	0.0052	0.0049	0.0046	0.0046
$1-cos(\Delta\phi)$	0.0024	0.0014	0.0010	0.0006	0.0004
$\sigma(Db[\gamma,J])$	0.0767	0.0628	0.0556	0.0473	0.0413
$\sigma(Db[\gamma,part])$	0.0961	0.0874	0.0845	0.0848	0.0668
Entries	24410	17541	13038	7393	1365

Table 6: Selection 1. $\Delta\phi_{(\gamma,jet)} = 180° \pm 15°$. LUCELL algorithm.

P_{tCUT}^{clust}	30	20	15	10	5
Nevent	9473	6770	4908	2717	471
$P_t 56$	23.8	19.3	16.4	13.2	9.3
$\Delta\phi$	3.0	2.4	2.0	1.6	1.2
${P_t}^{out}$	17.3	13.5	11.1	8.6	5.8
${P_t}^{\eta>5}$	6.9	6.9	6.8	6.6	6.1
$({P_t}^{\gamma}-{P_t}^{part})/{P_t}^{\gamma}$	0.0013	0.0004	0.0009	0.0008	-0.0018
$({P_t}^{J}-{P_t}^{part})/{P_t}^{J}$	-0.0166	-0.0118	-0.0085	-0.0052	-0.0058
$({P_t}^{\gamma}-{P_t}^{J})/{P_t}^{\gamma}$	0.0122	0.0077	0.0057	0.0033	0.0016
$P_t(O+\eta>5)/{P_t}^{\gamma}$	0.0099	0.0063	0.0046	0.0027	0.0013
$1-cos(\Delta\phi)$	0.0024	0.0015	0.0010	0.0006	0.0004
$\sigma(Db[\gamma,J])$	0.0784	0.0660	0.0586	0.0500	0.0434
$\sigma(Db[\gamma,part])$	0.0791	0.0683	0.0630	0.0557	0.0303
Entries	24763	17697	12829	7101	1231

Table 7: Selection 1. $\Delta\phi_{(\gamma,jet)} = 180° \pm 10°$. UA1 algorithm.

P_{tCUT}^{clust}	30	20	15	10	5
Nevent	8285	5590	3965	2141	351
$P_t 56$	22.8	18.0	15.2	12.3	8.9
$\Delta\phi$	2.9	2.3	2.0	1.6	1.2
${P_t}^{out}$	18.1	13.8	11.3	8.7	6.2
${P_t}^{\eta>5}$	6.8	6.7	6.7	6.6	5.9
$({P_t}^{\gamma}-{P_t}^{part})/{P_t}^{\gamma}$	-0.0006	-0.0021	-0.0018	-0.0006	-0.0022
$({P_t}^{J}-{P_t}^{part})/{P_t}^{J}$	-0.0319	-0.0233	-0.0188	-0.0141	-0.0124
$({P_t}^{\gamma}-{P_t}^{J})/{P_t}^{\gamma}$	0.0246	0.0166	0.0132	0.0103	0.0078
$P_t(O+\eta>5)/{P_t}^{\gamma}$	0.0225	0.0153	0.0122	0.0097	0.0075
$1-cos(\Delta\phi)$	0.0021	0.0014	0.0010	0.0006	0.0004
$\sigma(Db[\gamma,J])$	0.0821	0.0658	0.0577	0.0504	0.0425
$\sigma(Db[\gamma,part])$	0.0736	0.0588	0.0526	0.0488	0.0306
Entries	21657	14613	10363	5597	917

Table 8: Selection 1. $\Delta\phi_{(\gamma,jet)} = 180° \pm 10°$. UA2 algorithm.

P_{tCUT}^{clust}	30	20	15	10	5
Nevent	9130	6676	4980	2827	522
$P_t 56$	26.3	22.3	19.8	17.3	12.9
$\Delta\phi$	2.8	2.3	1.9	1.5	1.2
${P_t}^{out}$	16.5	13.1	11.0	8.5	5.9
${P_t}^{\eta>5}$	6.7	6.6	6.5	6.4	6.0
$({P_t}^{\gamma}-{P_t}^{part})/{P_t}^{\gamma}$	0.0052	0.0048	0.0055	0.0072	0.0051
$({P_t}^{J}-{P_t}^{part})/{P_t}^{J}$	-0.0084	-0.0053	-0.0035	-0.0004	-0.0019
$({P_t}^{\gamma}-{P_t}^{J})/{P_t}^{\gamma}$	0.0086	0.0064	0.0059	0.0052	0.0049
$P_t(O+\eta>5)/{P_t}^{\gamma}$	0.0066	0.0051	0.0049	0.0046	0.0046
$1-cos(\Delta\phi)$	0.0020	0.0014	0.0010	0.0006	0.0004
$\sigma(Db[\gamma,J])$	0.0758	0.0626	0.0555	0.0473	0.0413
$\sigma(Db[\gamma,part])$	0.0951	0.0868	0.0836	0.0844	0.0668
Entries	23866	17451	13017	7390	1365

Table 9: Selection 1. $\Delta\phi_{(\gamma,jet)} = 180° \pm 10°$. LUCELL algorithm.

P_{tCUT}^{clust}	30	20	15	10	5
Nevent	9272	6731	4901	2716	471
$P_t 56$	23.2	19.2	16.3	13.2	9.3
$\Delta\phi$	2.8	2.3	2.0	1.6	1.2
${P_t}^{out}$	16.7	13.4	11.1	8.6	5.8
${P_t}^{\eta>5}$	6.9	6.8	6.8	6.6	6.1
$({P_t}^{\gamma}-{P_t}^{part})/{P_t}^{\gamma}$	0.0012	0.0003	0.0009	0.0009	-0.0018
$({P_t}^{J}-{P_t}^{part})/{P_t}^{J}$	-0.0159	-0.0116	-0.0084	-0.0052	-0.0058
$({P_t}^{\gamma}-{P_t}^{J})/{P_t}^{\gamma}$	0.0117	0.0075	0.0056	0.0033	0.0016
$P_t(O+\eta>5)/{P_t}^{\gamma}$	0.0097	0.0062	0.0047	0.0027	0.0013
$1-cos(\Delta\phi)$	0.0020	0.0014	0.0010	0.0006	0.0004
$\sigma(Db[\gamma,J])$	0.0777	0.0657	0.0586	0.0500	0.0434
$\sigma(Db[\gamma,part])$	0.0786	0.0679	0.0630	0.0557	0.0303
Entries	24237	17594	12810	7099	1231

Table 10: Selection 1. $\Delta\phi_{(\gamma,jet)} = 180° \pm 5°$. UA1 algorithm.

P_{tCUT}^{clust}	30	20	15	10	5
Nevent	6750	5017	3746	2098	349
$P_t 56$	20.4	16.8	14.5	12.1	8.8
$\Delta\phi$	2.0	1.9	1.7	1.5	1.2
P_t^{out}	15.4	12.5	10.7	8.6	6.2
$P_t^{\eta>5}$	6.7	6.6	6.6	6.5	5.8
$(P_t{}^{\gamma}-P_t^{part})/P_t{}^{\gamma}$	-0.0009	-0.0021	-0.0019	-0.0006	-0.0022
$(P_t{}^{J}-P_t^{part})/P_t{}^{J}$	-0.0294	-0.0222	-0.0183	-0.0139	-0.0124
$(P_t{}^{\gamma}-P_t{}^{J})/P_t{}^{\gamma}$	0.0223	0.0156	0.0127	0.0102	0.0078
$P_t(O+\eta>5)/P_t{}^{\gamma}$	0.0214	0.0148	0.0121	0.0097	0.0075
$1-cos(\Delta\phi)$	0.0009	0.0008	0.0007	0.0005	0.0003
$\sigma(Db[\gamma,J])$	0.0789	0.0647	0.0570	0.0501	0.0425
$\sigma(Db[\gamma,part])$	0.0695	0.0569	0.0516	0.0489	0.0307
Entries	17643	13114	9793	5483	911

Table 11: Selection 1. $\Delta\phi_{(\gamma,jet)} = 180° \pm 5°$. UA2 algorithm.

P_{tCUT}^{clust}	30	20	15	10	5
Nevent	7552	6018	4706	2775	519
$P_t 56$	24.1	21.2	19.2	17.1	12.8
$\Delta\phi$	2.0	1.8	1.7	1.5	1.1
P_t^{out}	13.9	11.8	10.3	8.3	5.9
$P_t^{\eta>5}$	6.6	6.5	6.4	6.3	5.9
$(P_t{}^{\gamma}-P_t^{part})/P_t{}^{\gamma}$	0.0057	0.0051	0.0058	0.0074	0.0051
$(P_t{}^{J}-P_t^{part})/P_t{}^{J}$	-0.0063	-0.0043	-0.0029	-0.0001	-0.0018
$(P_t{}^{\gamma}-P_t{}^{J})/P_t{}^{\gamma}$	0.0073	0.0059	0.0056	0.0051	0.0049
$P_t(O+\eta>5)/P_t{}^{\gamma}$	0.0065	0.0052	0.0050	0.0047	0.0046
$1-cos(\Delta\phi)$	0.0009	0.0008	0.0007	0.0005	0.0003
$\sigma(Db[\gamma,J])$	0.0728	0.0613	0.0544	0.0466	0.0414
$\sigma(Db[\gamma,part])$	0.0932	0.0863	0.0838	0.0849	0.0670
Entries	19741	15731	12300	7254	1357

Table 12: Selection 1. $\Delta\phi_{(\gamma,jet)} = 180° \pm 5°$. LUCELL algorithm.

P_{tCUT}^{clust}	30	20	15	10	5
Nevent	7671	6036	4618	2660	469
$P_t 56$	21.1	17.9	15.6	12.9	9.2
$\Delta\phi$	2.0	1.9	1.7	1.5	1.2
P_t^{out}	14.2	12.1	10.4	8.4	5.8
$P_t^{\eta>5}$	6.8	6.7	6.6	6.5	6.1
$(P_t{}^{\gamma}-P_t^{part})/P_t{}^{\gamma}$	0.0013	0.0005	0.0007	0.0009	-0.0018
$(P_t{}^{J}-P_t^{part})/P_t{}^{J}$	-0.0139	-0.0105	-0.0079	-0.0050	-0.0058
$(P_t{}^{\gamma}-P_t{}^{J})/P_t{}^{\gamma}$	0.0100	0.0068	0.0051	0.0033	0.0016
$P_t(O+\eta>5)/P_t{}^{\gamma}$	0.0092	0.0061	0.0045	0.0028	0.0013
$1-cos(\Delta\phi)$	0.0009	0.0008	0.0007	0.0005	0.0003
$\sigma(Db[\gamma,J])$	0.0750	0.0642	0.0573	0.0495	0.0435
$\sigma(Db[\gamma,part])$	0.0762	0.0668	0.0616	0.0560	0.0304
Entries	20051	15779	12071	6952	1225

Table 13: Selection 2. $\Delta\phi_{(\gamma,jet)} = 180^\circ \pm 15^\circ,\ \epsilon^{jet} < 3\%$. UA1 algorithm.

$P_{t\,CUT}^{clust}$	30	20	15	10	5
Nevent	7615	5317	3869	2132	351
$P_t 56$	22.7	17.8	15.1	12.3	8.9
$\Delta\phi$	3.1	2.4	2.0	1.6	1.2
P_t^{out}	17.8	13.6	11.2	8.7	6.2
$P_t^{\eta>5}$	6.8	6.7	6.6	6.6	5.9
$(P_t^\gamma - P_t^{part})/P_t^\gamma$	-0.0032	-0.0034	-0.0024	-0.0008	-0.0022
$(P_t^J - P_t^{part})/P_t^J$	-0.0253	-0.0207	-0.0175	-0.0139	-0.0124
$(P_t^\gamma - P_t^J)/P_t^\gamma$	0.0167	0.0134	0.0118	0.0100	0.0078
$P_t(O+\eta>5)/P_t^\gamma$	0.0142	0.0120	0.0108	0.0094	0.0075
$1 - cos(\Delta\phi)$	0.0025	0.0015	0.0010	0.0006	0.0004
$\sigma(Db[\gamma, J])$	0.0774	0.0627	0.0550	0.0498	0.0425
$\sigma(Db[\gamma, part])$	0.0705	0.0568	0.0517	0.0486	0.0306
Entries	19906	13898	10113	5573	917

Table 14: Selection 2. $\Delta\phi_{(\gamma,jet)} = 180^\circ \pm 15^\circ,\ \epsilon^{jet} < 3\%$. UA2 algorithm.

$P_{t\,CUT}^{clust}$	30	20	15	10	5
Nevent	8047	5900	4447	2562	484
$P_t 56$	24.4	20.1	17.5	14.9	11.5
$\Delta\phi$	3.0	2.3	1.9	1.5	1.2
P_t^{out}	16.7	13.0	10.9	8.4	5.9
$P_t^{\eta>5}$	6.7	6.6	6.5	6.4	5.9
$(P_t^\gamma - P_t^{part})/P_t^\gamma$	0.0002	0.0007	0.0019	0.0038	0.0030
$(P_t^J - P_t^{part})/P_t^J$	-0.0100	-0.0081	-0.0065	-0.0040	-0.0040
$(P_t^\gamma - P_t^J)/P_t^\gamma$	0.0056	0.0052	0.0054	0.0053	0.0049
$P_t(O+\eta>5)/P_t^\gamma$	0.0033	0.0038	0.0044	0.0047	0.0046
$1 - cos(\Delta\phi)$	0.0024	0.0014	0.0010	0.0006	0.0004
$\sigma(Db[\gamma, J])$	0.0737	0.0611	0.0539	0.0472	0.0413
$\sigma(Db[\gamma, part])$	0.0831	0.0745	0.0715	0.0709	0.0570
Entries	21035	15423	11624	6697	1264

Table 15: Selection 2. $\Delta\phi_{(\gamma,jet)} = 180^\circ \pm 15^\circ,\ \epsilon^{jet} < 3\%$. LUCELL algorithm.

$P_{t\,CUT}^{clust}$	30	20	15	10	5
Nevent	8487	6294	4706	2684	471
$P_t 56$	22.8	18.7	16.0	13.1	9.3
$\Delta\phi$	2.9	2.4	2.0	1.6	1.2
P_t^{out}	16.5	13.1	10.9	8.5	5.8
$P_t^{\eta>5}$	6.8	6.8	6.7	6.6	6.1
$(P_t^\gamma - P_t^{part})/P_t^\gamma$	-0.0015	-0.0014	-0.0004	0.0005	-0.0018
$(P_t^J - P_t^{part})/P_t^J$	-0.0110	-0.0089	-0.0074	-0.0048	-0.0058
$(P_t^\gamma - P_t^J)/P_t^\gamma$	0.0050	0.0039	0.0038	0.0028	0.0016
$P_t(O+\eta>5)/P_t^\gamma$	0.0027	0.0025	0.0028	0.0022	0.0013
$1 - cos(\Delta\phi)$	0.0023	0.0015	0.0010	0.0006	0.0004
$\sigma(Db[\gamma, J])$	0.0735	0.0623	0.0559	0.0488	0.0434
$\sigma(Db[\gamma, part])$	0.0742	0.0648	0.0609	0.0550	0.0303
Entries	22185	16453	12301	7017	1231

Table 16: Selection 3. $\Delta\phi_{(\gamma,jet)} = 180^\circ \pm 15^\circ,\ \epsilon^{jet} < 3\%$. UA1 algorithm.

P_{tCUT}^{clust}	30	20	15	10	5
Nevent	5746	4207	3067	1686	284
$P_t 56$	21.9	17.9	15.2	12.4	8.8
$\Delta\phi$	2.9	2.3	2.0	1.5	1.2
P_t^{out}	16.9	13.5	11.2	8.7	6.1
$P_t^{\eta>5}$	6.7	6.6	6.6	6.5	5.9
$(P_t{}^{\gamma}-P_t^{part})/P_t{}^{\gamma}$	-0.0033	-0.0033	-0.0022	-0.0004	-0.0019
$(P_t{}^{J}-P_t^{part})/P_t{}^{J}$	-0.0237	-0.0197	-0.0166	-0.0132	-0.0128
$(P_t{}^{\gamma}-P_t{}^{J})/P_t{}^{\gamma}$	0.0156	0.0126	0.0113	0.0099	0.0079
$P_t(O+\eta>5)/P_t{}^{\gamma}$	0.0133	0.0112	0.0103	0.0093	0.0076
$1-cos(\Delta\phi)$	0.0023	0.0014	0.0010	0.0006	0.0004
$\sigma(Db[\gamma,J])$	0.0742	0.0625	0.0547	0.0495	0.0449
$\sigma(Db[\gamma,part])$	0.0686	0.0593	0.0545	0.0516	0.0298
Entries	15019	10997	8016	4407	742

Table 17: Selection 3. $\Delta\phi_{(\gamma,jet)} = 180^\circ \pm 15^\circ,\ \epsilon^{jet} < 3\%$. UA2 algorithm.

P_{tCUT}^{clust}	30	20	15	10	5
Nevent	5746	4207	3067	1686	284
$P_t 56$	21.9	17.9	15.2	12.4	8.8
$\Delta\phi$	2.9	2.3	1.9	1.5	1.2
P_t^{out}	16.2	13.0	10.8	8.4	6.0
$P_t^{\eta>5}$	6.7	6.6	6.6	6.5	5.9
$(P_t{}^{\gamma}-P_t^{part})/P_t{}^{\gamma}$	-0.0033	-0.0033	-0.0022	-0.0004	-0.0019
$(P_t{}^{J}-P_t^{part})/P_t{}^{J}$	-0.0134	-0.0120	-0.0110	-0.0091	-0.0107
$(P_t{}^{\gamma}-P_t{}^{J})/P_t{}^{\gamma}$	0.0059	0.0053	0.0058	0.0059	0.0058
$P_t(O+\eta>5)/P_t{}^{\gamma}$	0.0038	0.0039	0.0048	0.0053	0.0055
$1-cos(\Delta\phi)$	0.0022	0.0014	0.0010	0.0006	0.0004
$\sigma(Db[\gamma,J])$	0.0719	0.0612	0.0544	0.0494	0.0453
$\sigma(Db[\gamma,part])$	0.0686	0.0593	0.0545	0.0516	0.0298
Entries	15019	10997	8016	4407	742

Table 18: Selection 3. $\Delta\phi_{(\gamma,jet)} = 180^\circ \pm 15^\circ,\ \epsilon^{jet} < 3\%$. LUCELL algorithm.

P_{tCUT}^{clust}	30	20	15	10	5
Nevent	5746	4207	3067	1686	284
$P_t 56$	21.9	17.9	15.2	12.4	8.8
$\Delta\phi$	2.9	2.3	1.9	1.5	1.2
P_t^{out}	16.2	13.0	10.8	8.3	5.9
$P_t^{\eta>5}$	6.7	6.6	6.6	6.5	5.9
$(P_t{}^{\gamma}-P_t^{part})/P_t{}^{\gamma}$	-0.0033	-0.0033	-0.0022	-0.0004	-0.0019
$(P_t{}^{J}-P_t^{part})/P_t{}^{J}$	-0.0095	-0.0078	-0.0064	-0.0044	-0.0058
$(P_t{}^{\gamma}-P_t{}^{J})/P_t{}^{\gamma}$	0.0022	0.0012	0.0014	0.0013	0.0012
$P_t(O+\eta>5)/P_t{}^{\gamma}$	0.0000	-0.0002	0.0004	0.0007	0.0009
$1-cos(\Delta\phi)$	0.0022	0.0014	0.0010	0.0006	0.0004
$\sigma(Db[\gamma,J])$	0.0717	0.0610	0.0541	0.0490	0.0446
$\sigma(Db[\gamma,part])$	0.0686	0.0593	0.0545	0.0516	0.0298
Entries	15019	10997	8016	4407	742

Appendix 5 $\quad 300 < P_t{}^{\gamma} < 360\ GeV/c$

$P_t{}^{isol} < 5\ GeV/c, \quad \epsilon^{\gamma} < 7\%$

Table 1: Selection 1. $\Delta\phi_{(\gamma,jet)} = 180° \pm 180°$. UA1 algorithm.

P_{tCUT}^{clust}	30	20	15	10	5
Nevent*	1710	1108	779	413	67
P_t56	25.1	19.4	16.3	13.1	9.7
$\Delta\phi$	2.3	1.7	1.5	1.2	1.0
$P_t{}^{out}$	19.5	14.3	11.6	8.8	6.0
$P_t{}^{\eta>5}$	8.4	8.3	8.1	8.0	8.4
$(P_t{}^{\gamma}–P_t{}^{part})/P_t{}^{\gamma}$	-0.0016	-0.0019	-0.0024	-0.0020	0.0004
$(P_t{}^{J}–P_t{}^{part})/P_t{}^{J}$	-0.0251	-0.0191	-0.0159	-0.0131	-0.0141
$(P_t{}^{\gamma} - P_t{}^{J})/P_t{}^{\gamma}$	0.0192	0.0141	0.0112	0.0091	0.0113
$P_t(O+\eta>5)/P_t{}^{\gamma}$	0.0179	0.0133	0.0106	0.0087	0.0111
$1 - cos(\Delta\phi)$	0.0014	0.0008	0.0005	0.0004	0.0002
$\sigma(Db[\gamma, J])^{**}$	0.0626	0.0520	0.0449	0.0400	0.0453
$\sigma(Db[\gamma, part])^{***}$	0.0578	0.0476	0.0406	0.0343	0.0379
Entries	18994	12308	8653	4591	747

Table 2: Selection 1. $\Delta\phi_{(\gamma,jet)} = 180° \pm 180°$. UA2 algorithm.

P_{tCUT}^{clust}	30	20	15	10	5
Nevent	1971	1399	1034	584	107
P_t56	30.6	25.8	23.0	19.9	15.3
$\Delta\phi$	2.1	1.7	1.4	1.2	0.9
$P_t{}^{out}$	17.5	13.4	11.1	8.6	5.9
$P_t{}^{\eta>5}$	8.2	8.1	7.9	7.7	8.2
$(P_t{}^{\gamma}–P_t{}^{part})/P_t{}^{\gamma}$	0.0049	0.0047	0.0043	0.0040	0.0022
$(P_t{}^{J}–P_t{}^{part})/P_t{}^{J}$	-0.0071	-0.0056	-0.0047	-0.0040	-0.0102
$(P_t{}^{\gamma} - P_t{}^{J})/P_t{}^{\gamma}$	0.0087	0.0075	0.0068	0.0063	0.0096
$P_t(O+\eta>5)/P_t{}^{\gamma}$	0.0075	0.0068	0.0063	0.0060	0.0094
$1 - cos(\Delta\phi)$	0.0012	0.0007	0.0005	0.0003	0.0002
$\sigma(Db[\gamma, J])$	0.0585	0.0501	0.0441	0.0384	0.0434
$\sigma(Db[\gamma, part])$	0.0859	0.0804	0.0761	0.0712	0.0589
Entries	21891	15537	11481	6484	1187

Table 3: Selection 1. $\Delta\phi_{(\gamma,jet)} = 180° \pm 180°$. LUCELL algorithm.

P_{tCUT}^{clust}	30	20	15	10	5
Nevent	1901	1336	959	522	90
P_t56	25.5	20.9	17.8	14.1	10.2
$\Delta\phi$	2.2	1.7	1.5	1.2	1.0
$P_t{}^{out}$	17.9	13.9	11.4	8.6	5.8
$P_t{}^{\eta>5}$	8.5	8.5	8.3	8.2	8.3
$(P_t{}^{\gamma}–P_t{}^{part})/P_t{}^{\gamma}$	-0.0001	-0.0001	-0.0001	-0.0005	0.0011
$(P_t{}^{J}–P_t{}^{part})/P_t{}^{J}$	-0.0156	-0.0126	-0.0100	-0.0086	-0.0076
$(P_t{}^{\gamma} - P_t{}^{J})/P_t{}^{\gamma}$	0.0114	0.0089	0.0070	0.0056	0.0063
$P_t(O+\eta>5)/P_t{}^{\gamma}$	0.0102	0.0082	0.0065	0.0053	0.0060
$1 - cos(\Delta\phi)$	0.0012	0.0008	0.0005	0.0004	0.0002
$\sigma(Db[\gamma, J])$	0.0616	0.0538	0.0479	0.0431	0.0409
$\sigma(Db[\gamma, part])$	0.0625	0.0556	0.0518	0.0432	0.0463
Entries	21116	14836	10646	5797	999

*Number of events (Nevent) is given in this and in the following tables for integrated luminosity $L_{int} = 3\ fb^{-1}$

** $Db[\gamma, part] \equiv (P_t{}^{\gamma}–P_t{}^{part})/P_t{}^{\gamma}$

*** $Db[\gamma, J] \equiv (P_t{}^{\gamma} - P_t{}^{J})/P_t{}^{\gamma}$

Table 4: Selection 1. $\Delta\phi_{(\gamma,jet)} = 180° \pm 15°$. UA1 algorithm.

P_{tCUT}^{clust}	30	20	15	10	5
Nevent	1710	1108	779	413	67
$P_t 56$	25.1	19.4	16.3	13.1	9.7
$\Delta\phi$	2.3	1.7	1.5	1.2	1.0
P_t^{out}	19.5	14.3	11.6	8.8	6.0
$P_t^{\eta>5}$	8.4	8.3	8.1	8.0	8.4
$(P_t{}^{\gamma}-P_t^{part})/P_t{}^{\gamma}$	-0.0016	-0.0019	-0.0024	-0.0020	0.0004
$(P_t{}^{J}-P_t^{part})/P_t{}^{J}$	-0.0251	-0.0191	-0.0159	-0.0131	-0.0141
$(P_t{}^{\gamma}-P_t{}^{J})/P_t{}^{\gamma}$	0.0192	0.0141	0.0112	0.0091	0.0113
$P_t(O{+}\eta{>}5)/P_t{}^{\gamma}$	0.0179	0.0133	0.0106	0.0087	0.0111
$1-cos(\Delta\phi)$	0.0014	0.0008	0.0005	0.0004	0.0002
$\sigma(Db[\gamma,J])$	0.0626	0.0520	0.0449	0.0400	0.0453
$\sigma(Db[\gamma,part])$	0.0578	0.0476	0.0406	0.0343	0.0379
Entries	18994	12308	8653	4591	747

Table 5: Selection 1. $\Delta\phi_{(\gamma,jet)} = 180° \pm 15°$. UA2 algorithm.

P_{tCUT}^{clust}	30	20	15	10	5
Nevent	1971	1399	1034	584	107
$P_t 56$	30.6	25.8	23.0	19.9	15.3
$\Delta\phi$	2.1	1.7	1.4	1.2	0.9
P_t^{out}	17.5	13.4	11.1	8.6	5.9
$P_t^{\eta>5}$	8.2	8.1	7.9	7.7	8.2
$(P_t{}^{\gamma}-P_t^{part})/P_t{}^{\gamma}$	0.0049	0.0047	0.0043	0.0040	0.0022
$(P_t{}^{J}-P_t^{part})/P_t{}^{J}$	-0.0071	-0.0056	-0.0047	-0.0040	-0.0102
$(P_t{}^{\gamma}-P_t{}^{J})/P_t{}^{\gamma}$	0.0087	0.0075	0.0068	0.0063	0.0096
$P_t(O{+}\eta{>}5)/P_t{}^{\gamma}$	0.0075	0.0068	0.0063	0.0060	0.0094
$1-cos(\Delta\phi)$	0.0012	0.0007	0.0005	0.0003	0.0002
$\sigma(Db[\gamma,J])$	0.0585	0.0501	0.0441	0.0384	0.0434
$\sigma(Db[\gamma,part])$	0.0859	0.0804	0.0761	0.0712	0.0589
Entries	21890	15537	11481	6484	1187

Table 6: Selection 1. $\Delta\phi_{(\gamma,jet)} = 180° \pm 15°$. LUCELL algorithm.

P_{tCUT}^{clust}	30	20	15	10	5
Nevent	1901	1336	959	522	90
$P_t 56$	25.5	20.9	17.8	14.1	10.2
$\Delta\phi$	2.2	1.7	1.5	1.2	1.0
P_t^{out}	17.9	13.9	11.4	8.6	5.8
$P_t^{\eta>5}$	8.5	8.5	8.3	8.2	8.3
$(P_t{}^{\gamma}-P_t^{part})/P_t{}^{\gamma}$	-0.0001	-0.0001	-0.0001	-0.0005	0.0011
$(P_t{}^{J}-P_t^{part})/P_t{}^{J}$	-0.0156	-0.0126	-0.0100	-0.0086	-0.0076
$(P_t{}^{\gamma}-P_t{}^{J})/P_t{}^{\gamma}$	0.0114	0.0089	0.0070	0.0056	0.0063
$P_t(O{+}\eta{>}5)/P_t{}^{\gamma}$	0.0102	0.0082	0.0065	0.0053	0.0060
$1-cos(\Delta\phi)$	0.0012	0.0008	0.0005	0.0004	0.0002
$\sigma(Db[\gamma,J])$	0.0616	0.0538	0.0479	0.0431	0.0409
$\sigma(Db[\gamma,part])$	0.0625	0.0556	0.0518	0.0432	0.0463
Entries	21116	14836	10646	5797	999

Table 7: Selection 1. $\Delta\phi_{(\gamma,jet)} = 180° \pm 10°$. UA1 algorithm.

P_{tCUT}^{clust}	30	20	15	10	5
Nevent	1705	1108	779	413	67
$P_t 56$	25.0	19.4	16.3	13.1	9.7
$\Delta\phi$	2.2	1.7	1.5	1.2	1.0
P_t^{out}	19.3	14.3	11.6	8.8	6.0
$P_t^{\eta>5}$	8.4	8.3	8.1	8.0	8.4
$(P_t{}^{\gamma}-P_t^{part})/P_t{}^{\gamma}$	-0.0016	-0.0019	-0.0024	-0.0020	0.0004
$(P_t{}^{J}-P_t^{part})/P_t{}^{J}$	-0.0250	-0.0191	-0.0159	-0.0131	-0.0141
$(P_t{}^{\gamma}-P_t{}^{J})/P_t{}^{\gamma}$	0.0192	0.0141	0.0112	0.0091	0.0113
$P_t(O{+}\eta{>}5)/P_t{}^{\gamma}$	0.0179	0.0133	0.0106	0.0087	0.0111
$1-cos(\Delta\phi)$	0.0013	0.0008	0.0005	0.0004	0.0002
$\sigma(Db[\gamma,J])$	0.0625	0.0520	0.0449	0.0400	0.0453
$\sigma(Db[\gamma,part])$	0.0577	0.0476	0.0406	0.0343	0.0379
Entries	18931	12304	8653	4591	747

Table 8: Selection 1. $\Delta\phi_{(\gamma,jet)} = 180° \pm 10°$. UA2 algorithm.

P_{tCUT}^{clust}	30	20	15	10	5
Nevent	1966	1399	1034	584	107
$P_t 56$	30.5	25.8	23.0	19.9	15.3
$\Delta\phi$	2.1	1.7	1.4	1.2	0.9
P_t^{out}	17.4	13.4	11.1	8.6	5.9
$P_t^{\eta>5}$	8.2	8.1	7.9	7.7	8.2
$(P_t{}^{\gamma}-P_t^{part})/P_t{}^{\gamma}$	0.0049	0.0047	0.0043	0.0040	0.0022
$(P_t{}^{J}-P_t^{part})/P_t{}^{J}$	-0.0071	-0.0056	-0.0047	-0.0040	-0.0102
$(P_t{}^{\gamma}-P_t{}^{J})/P_t{}^{\gamma}$	0.0086	0.0075	0.0068	0.0063	0.0096
$P_t(O{+}\eta{>}5)/P_t{}^{\gamma}$	0.0075	0.0068	0.0063	0.0060	0.0094
$1-cos(\Delta\phi)$	0.0012	0.0007	0.0005	0.0003	0.0002
$\sigma(Db[\gamma,J])$	0.0584	0.0501	0.0441	0.0384	0.0434
$\sigma(Db[\gamma,part])$	0.0858	0.0804	0.0761	0.0712	0.0589
Entries	21838	15533	11481	6484	1187

Table 9: Selection 1. $\Delta\phi_{(\gamma,jet)} = 180° \pm 10°$. LUCELL algorithm.

P_{tCUT}^{clust}	30	20	15	10	5
Nevent	1898	1336	959	522	90
$P_t 56$	25.5	20.9	17.8	14.1	10.2
$\Delta\phi$	2.1	1.7	1.5	1.2	1.0
P_t^{out}	17.8	13.9	11.4	8.6	5.8
$P_t^{\eta>5}$	8.5	8.5	8.3	8.2	8.3
$(P_t{}^{\gamma}-P_t^{part})/P_t{}^{\gamma}$	0.0000	-0.0001	-0.0001	-0.0005	0.0011
$(P_t{}^{J}-P_t^{part})/P_t{}^{J}$	-0.0156	-0.0125	-0.0100	-0.0086	-0.0076
$(P_t{}^{\gamma}-P_t{}^{J})/P_t{}^{\gamma}$	0.0114	0.0089	0.0070	0.0056	0.0063
$P_t(O{+}\eta{>}5)/P_t{}^{\gamma}$	0.0102	0.0082	0.0065	0.0053	0.0060
$1-cos(\Delta\phi)$	0.0012	0.0008	0.0005	0.0004	0.0002
$\sigma(Db[\gamma,J])$	0.0616	0.0538	0.0479	0.0431	0.0409
$\sigma(Db[\gamma,part])$	0.0624	0.0556	0.0518	0.0432	0.0463
Entries	21082	14832	10646	5797	999

Table 10: Selection 1. $\Delta\phi_{(\gamma,jet)} = 180° \pm 5°$. UA1 algorithm.

P_{tCUT}^{clust}	30	20	15	10	5
Nevent	1552	1072	770	412	67
P_t56	23.4	18.9	16.1	13.0	9.7
$\Delta\phi$	1.8	1.6	1.4	1.2	1.0
P_t^{out}	17.5	13.7	11.4	8.8	6.0
$P_t^{\eta>5}$	8.3	8.2	8.0	7.9	8.4
$(P_t{}^{\gamma}-P_t^{part})/P_t{}^{\gamma}$	-0.0017	-0.0018	-0.0024	-0.0019	0.0004
$(P_t{}^{J}-P_t^{part})/P_t{}^{J}$	-0.0240	-0.0188	-0.0158	-0.0130	-0.0141
$(P_t{}^{\gamma}-P_t{}^{J})/P_t{}^{\gamma}$	0.0183	0.0138	0.0110	0.0090	0.0113
$P_t(O+\eta>5)/P_t{}^{\gamma}$	0.0175	0.0132	0.0105	0.0087	0.0111
$1-cos(\Delta\phi)$	0.0008	0.0006	0.0005	0.0003	0.0002
$\sigma(Db[\gamma,J])$	0.0613	0.0513	0.0446	0.0398	0.0453
$\sigma(Db[\gamma,part])$	0.0568	0.0470	0.0401	0.0343	0.0379
Entries	17236	11910	8547	4579	747

Table 11: Selection 1. $\Delta\phi_{(\gamma,jet)} = 180° \pm 5°$. UA2 algorithm.

P_{tCUT}^{clust}	30	20	15	10	5
Nevent	1814	1358	1022	582	107
P_t56	29.0	25.3	22.8	19.9	15.3
$\Delta\phi$	1.7	1.5	1.4	1.1	0.9
P_t^{out}	15.8	12.9	10.9	8.6	5.9
$P_t^{\eta>5}$	8.1	7.9	7.8	7.6	8.2
$(P_t{}^{\gamma}-P_t^{part})/P_t{}^{\gamma}$	0.0048	0.0048	0.0043	0.0041	0.0022
$(P_t{}^{J}-P_t^{part})/P_t{}^{J}$	-0.0062	-0.0050	-0.0043	-0.0038	-0.0102
$(P_t{}^{\gamma}-P_t{}^{J})/P_t{}^{\gamma}$	0.0079	0.0072	0.0066	0.0062	0.0096
$P_t(O+\eta>5)/P_t{}^{\gamma}$	0.0071	0.0066	0.0061	0.0059	0.0094
$1-cos(\Delta\phi)$	0.0007	0.0006	0.0005	0.0003	0.0002
$\sigma(Db[\gamma,J])$	0.0569	0.0489	0.0436	0.0380	0.0434
$\sigma(Db[\gamma,part])$	0.0849	0.0803	0.0762	0.0712	0.0589
Entries	20142	15078	11349	6465	1187

Table 12: Selection 1. $\Delta\phi_{(\gamma,jet)} = 180° \pm 5°$. LUCELL algorithm.

P_{tCUT}^{clust}	30	20	15	10	5
Nevent	1750	1290	946	521	90
P_t56	24.1	20.3	17.6	14.1	10.2
$\Delta\phi$	1.8	1.6	1.4	1.2	1.0
P_t^{out}	16.2	13.3	11.2	8.6	5.8
$P_t^{\eta>5}$	8.4	8.3	8.2	8.2	8.3
$(P_t{}^{\gamma}-P_t^{part})/P_t{}^{\gamma}$	-0.0001	-0.0001	-0.0002	-0.0004	0.0011
$(P_t{}^{J}-P_t^{part})/P_t{}^{J}$	-0.0147	-0.0121	-0.0098	-0.0085	-0.0076
$(P_t{}^{\gamma}-P_t{}^{J})/P_t{}^{\gamma}$	0.0106	0.0086	0.0069	0.0056	0.0063
$P_t(O+\eta>5)/P_t{}^{\gamma}$	0.0098	0.0080	0.0064	0.0052	0.0060
$1-cos(\Delta\phi)$	0.0007	0.0006	0.0005	0.0003	0.0002
$\sigma(Db[\gamma,J])$	0.0603	0.0528	0.0474	0.0428	0.0409
$\sigma(Db[\gamma,part])$	0.0618	0.0553	0.0515	0.0432	0.0463
Entries	19435	14329	10511	5782	999

Table 13: Selection 2. $\Delta\phi_{(\gamma,jet)} = 180^\circ \pm 15^\circ,\ \epsilon^{jet} < 3\%$ UA1 algorithm.

$P_{t\,CUT}^{clust}$	30	20	15	10	5
Nevent	1644	1097	777	413	67
$P_t 56$	24.8	19.4	16.3	13.1	9.7
$\Delta\phi$	2.2	1.7	1.5	1.2	1.0
P_t^{out}	19.0	14.2	11.6	8.8	6.0
$P_t^{\eta>5}$	8.3	8.2	8.1	8.0	8.4
$(P_t{}^{\gamma}-P_t^{part})/P_t{}^{\gamma}$	-0.0022	-0.0020	-0.0024	-0.0020	0.0004
$(P_t{}^{J}-P_t^{part})/P_t{}^{J}$	-0.0227	-0.0184	-0.0158	-0.0131	-0.0141
$(P_t{}^{\gamma}-P_t{}^{J})/P_t{}^{\gamma}$	0.0166	0.0134	0.0111	0.0091	0.0113
$P_t(O{+}\eta{>}5)/P_t{}^{\gamma}$	0.0153	0.0126	0.0105	0.0087	0.0111
$1-cos(\Delta\phi)$	0.0013	0.0008	0.0005	0.0004	0.0002
$\sigma(Db[\gamma,J])$	0.0608	0.0512	0.0449	0.0400	0.0453
$\sigma(Db[\gamma,part])$	0.0576	0.0477	0.0406	0.0343	0.0379
Entries	18259	12188	8634	4591	747

Table 14: Selection 2. $\Delta\phi_{(\gamma,jet)} = 180^\circ \pm 15^\circ,\ \epsilon^{jet} < 3\%$ UA2 algorithm.

$P_{t\,CUT}^{clust}$	30	20	15	10	5
Nevent	1781	1279	951	538	99
$P_t 56$	27.6	22.9	20.3	17.6	13.2
$\Delta\phi$	2.1	1.7	1.4	1.2	0.9
P_t^{out}	17.3	13.4	11.1	8.6	5.9
$P_t^{\eta>5}$	8.2	8.1	7.9	7.7	8.3
$(P_t{}^{\gamma}-P_t^{part})/P_t{}^{\gamma}$	0.0018	0.0017	0.0019	0.0025	0.0018
$(P_t{}^{J}-P_t^{part})/P_t{}^{J}$	-0.0090	-0.0083	-0.0071	-0.0058	-0.0109
$(P_t{}^{\gamma}-P_t{}^{J})/P_t{}^{\gamma}$	0.0077	0.0073	0.0068	0.0064	0.0098
$P_t(O{+}\eta{>}5)/P_t{}^{\gamma}$	0.0065	0.0065	0.0063	0.0061	0.0096
$1-cos(\Delta\phi)$	0.0012	0.0007	0.0005	0.0003	0.0002
$\sigma(Db[\gamma,J])$	0.0576	0.0495	0.0440	0.0390	0.0443
$\sigma(Db[\gamma,part])$	0.0756	0.0682	0.0659	0.0633	0.0528
Entries	19774	14200	10562	5979	1100

Table 15: Selection 2. $\Delta\phi_{(\gamma,jet)} = 180^\circ \pm 15^\circ,\ \epsilon^{jet} < 3\%$. LUCELL algorithm.

$P_{t\,CUT}^{clust}$	30	20	15	10	5
Nevent	1815	1310	953	522	90
$P_t 56$	25.0	20.7	17.7	14.1	10.2
$\Delta\phi$	2.1	1.7	1.5	1.2	1.0
P_t^{out}	17.4	13.8	11.4	8.6	5.8
$P_t^{\eta>5}$	8.5	8.4	8.3	8.2	8.3
$(P_t{}^{\gamma}-P_t^{part})/P_t{}^{\gamma}$	-0.0009	-0.0004	-0.0002	-0.0005	0.0011
$(P_t{}^{J}-P_t^{part})/P_t{}^{J}$	-0.0133	-0.0115	-0.0096	-0.0082	-0.0076
$(P_t{}^{\gamma}-P_t{}^{J})/P_t{}^{\gamma}$	0.0086	0.0078	0.0067	0.0055	0.0063
$P_t(O{+}\eta{>}5)/P_t{}^{\gamma}$	0.0074	0.0070	0.0061	0.0051	0.0060
$1-cos(\Delta\phi)$	0.0012	0.0008	0.0005	0.0004	0.0002
$\sigma(Db[\gamma,J])$	0.0595	0.0525	0.0474	0.0422	0.0409
$\sigma(Db[\gamma,part])$	0.0609	0.0549	0.0519	0.0433	0.0463
Entries	20154	14546	10581	5792	999

Table 16: Selection 3. $\Delta\phi_{(\gamma,jet)} = 180^\circ \pm 15^\circ,\ \epsilon^{jet} < 3\%$. UA1 algorithm.

P_{tCUT}^{clust}	30	20	15	10	5
Nevent	1239	873	622	334	56
$P_t 56$	23.7	19.4	16.4	13.2	9.4
$\Delta\phi$	2.1	1.7	1.5	1.2	1.0
P_t^{out}	18.0	14.2	11.6	8.8	6.0
$P_t^{\eta>5}$	8.3	8.3	8.1	8.1	8.5
$(P_t{}^{\gamma}-P_t^{part})/P_t{}^{\gamma}$	-0.0024	-0.0021	-0.0024	-0.0018	0.0003
$(P_t{}^{J}-P_t^{part})/P_t{}^{J}$	-0.0220	-0.0186	-0.0159	-0.0135	-0.0150
$(P_t{}^{\gamma}-P_t{}^{J})/P_t{}^{\gamma}$	0.0158	0.0134	0.0111	0.0095	0.0119
$P_t(O{+}\eta{>}5)/P_t{}^{\gamma}$	0.0146	0.0126	0.0105	0.0091	0.0116
$1-cos(\Delta\phi)$	0.0012	0.0008	0.0005	0.0004	0.0002
$\sigma(Db[\gamma,J])$	0.0593	0.0521	0.0458	0.0416	0.0470
$\sigma(Db[\gamma,part])$	0.0561	0.0481	0.0420	0.0365	0.0379
Entries	13756	9694	6905	3709	622

Table 17: Selection 3. $\Delta\phi_{(\gamma,jet)} = 180^\circ \pm 15^\circ,\ \epsilon^{jet} < 3\%$. UA2 algorithm.

P_{tCUT}^{clust}	30	20	15	10	5
Nevent	1239	873	622	334	56
$P_t 56$	23.7	19.4	16.4	13.2	9.4
$\Delta\phi$	2.1	1.7	1.5	1.2	1.0
P_t^{out}	17.0	13.5	11.2	8.6	5.9
$P_t^{\eta>5}$	8.3	8.3	8.1	8.1	8.5
$(P_t{}^{\gamma}-P_t^{part})/P_t{}^{\gamma}$	-0.0024	-0.0021	-0.0024	-0.0018	0.0003
$(P_t{}^{J}-P_t^{part})/P_t{}^{J}$	-0.0138	-0.0130	-0.0119	-0.0109	-0.0133
$(P_t{}^{\gamma}-P_t{}^{J})/P_t{}^{\gamma}$	0.0080	0.0079	0.0072	0.0069	0.0102
$P_t(O{+}\eta{>}5)/P_t{}^{\gamma}$	0.0069	0.0072	0.0067	0.0065	0.0100
$1-cos(\Delta\phi)$	0.0011	0.0008	0.0005	0.0003	0.0002
$\sigma(Db[\gamma,J])$	0.0575	0.0511	0.0453	0.0414	0.0470
$\sigma(Db[\gamma,part])$	0.0561	0.0481	0.0420	0.0365	0.0379
Entries	13756	9694	6905	3709	622

Table 18: Selection 3. $\Delta\phi_{(\gamma,jet)} = 180^\circ \pm 15^\circ,\ \epsilon^{jet} < 3\%$. LUCELL algorithm.

P_{tCUT}^{clust}	30	20	15	10	5
Nevent	1239	873	622	334	56
$P_t 56$	23.7	19.4	16.4	13.2	9.4
$\Delta\phi$	2.1	1.7	1.5	1.2	1.0
P_t^{out}	17.1	13.5	11.2	8.5	5.8
$P_t^{\eta>5}$	8.3	8.3	8.1	8.1	8.5
$(P_t{}^{\gamma}-P_t^{part})/P_t{}^{\gamma}$	-0.0024	-0.0021	-0.0024	-0.0018	0.0003
$(P_t{}^{J}-P_t^{part})/P_t{}^{J}$	-0.0120	-0.0106	-0.0092	-0.0079	-0.0105
$(P_t{}^{\gamma}-P_t{}^{J})/P_t{}^{\gamma}$	0.0064	0.0057	0.0045	0.0040	0.0075
$P_t(O{+}\eta{>}5)/P_t{}^{\gamma}$	0.0052	0.0049	0.0040	0.0036	0.0073
$1-cos(\Delta\phi)$	0.0012	0.0008	0.0005	0.0003	0.0002
$\sigma(Db[\gamma,J])$	0.0575	0.0511	0.0453	0.0413	0.0468
$\sigma(Db[\gamma,part])$	0.0561	0.0481	0.0420	0.0365	0.0379
Entries	13756	9694	6905	3709	622

Appendix 6

$$\hat{p}_{\perp}^{\,min} = 40\ GeV/c$$
$$P_t^{isol} < 2\ GeV/c, \quad \epsilon^{\tilde{\gamma}} < 5\%, \quad \Delta\phi = 15^{\circ}$$

Table 1: Number of events per $L_{int} = 3\ fb^{-1}$

$P_{t\ cut}^{\ clust}$ (GeV/c)	$P_{t\ cut}^{\ out}$ (GeV/c)					
	5	10	15	20	30	1000
5	529000	894000	929000	931000	931000	931000
10	1406000	3045000	3676000	3839000	3874000	3876000
15	1625000	3823000	5086000	5588000	5735000	5741000
20	1694000	4116000	5685000	6465000	6814000	6846000
30	1754000	4323000	6109000	7122000	7852000	8076000

Table 2: S/B

$P_{t\ cut}^{\ clust}$ (GeV/c)	$P_{t\ cut}^{\ out}$ (GeV/c)					
	5	10	15	20	30	1000
5	11.0± 3.0	8.3± 1.6	8.0± 1.5	8.0± 1.5	8.0± 1.5	8.0± 1.5
10	6.6± 0.9	5.6± 0.5	5.2± 0.4	5.0± 0.4	5.0± 0.4	5.1± 0.4
15	5.5± 0.7	4.9± 0.4	4.4± 0.3	4.2± 0.3	4.1± 0.3	4.1± 0.2
20	5.3± 0.6	4.4± 0.3	3.9± 0.2	3.7± 0.2	3.5± 0.2	3.5± 0.2
30	5.0± 0.6	3.9± 0.3	3.4± 0.2	3.2± 0.2	3.0± 0.1	2.9± 0.1

Table 3: $\langle F \rangle,\ F = (P_t{}^{\tilde{\gamma}} - P_t{}^{Jet})/P_t{}^{\tilde{\gamma}}$

$P_{t\ cut}^{\ clust}$ (GeV/c)	$P_{t\ cut}^{\ out}$ (GeV/c)					
	5	10	15	20	30	1000
5	0.007	0.008	0.008	0.008	0.008	0.008
10	0.003	0.009	0.012	0.013	0.013	0.013
15	0.005	0.011	0.018	0.020	0.022	0.022
20	0.005	0.012	0.020	0.024	0.026	0.027
30	0.005	0.011	0.021	0.024	0.029	0.031

Table 4: $\sigma(F),\ F = (P_t{}^{\tilde{\gamma}} - P_t{}^{Jet})/P_t{}^{\tilde{\gamma}}$

$P_{t\ cut}^{\ clust}$ (GeV/c)	$P_{t\ cut}^{\ out}$ (GeV/c)					
	5	10	15	20	30	1000
5	0.063	0.075	0.079	0.079	0.079	0.079
10	0.068	0.085	0.097	0.102	0.104	0.104
15	0.070	0.090	0.109	0.123	0.129	0.130
20	0.070	0.092	0.113	0.133	0.145	0.147
30	0.071	0.093	0.117	0.140	0.159	0.163

$$\hat{p}_{\perp}^{\,min} = 100\ GeV/c$$
$$P_t^{\,isol} < 2\ GeV/c, \quad \epsilon^{\tilde{\gamma}} < 5\%, \quad \Delta\phi = 15^{\circ}$$

Table 5: Number of events per $L_{int} = 3\ fb^{-1}$

${P_t}_{cut}^{clust}$ (GeV/c)	${P_t}_{cut}^{out}$ (GeV/c)					
	5	10	15	20	30	1000
5	14100	24700	27100	27400	27400	27600
10	38100	82900	104400	111200	114100	114300
15	45400	107100	147700	169500	184400	185400
20	47600	115400	167700	202300	235800	243000
30	49400	122100	181900	229700	296000	330000

Table 6: S/B

${P_t}_{cut}^{clust}$ (GeV/c)	${P_t}_{cut}^{out}$ (GeV/c)					
	5	10	15	20	30	1000
5	48.6± 28.9	38.8± 15.9	36.4± 13.8	36.7± 13.9	36.7± 13.9	33.5± 12.2
10	22.6± 4.0	22.6± 4.0	19.7± 3.0	18.7± 2.7	17.9± 2.5	17.7± 2.5
15	19.9± 4.6	17.3± 2.5	14.7± 1.7	14.1± 1.5	13.1± 1.3	13.0± 1.3
20	16.9± 3.6	14.6± 1.9	12.0± 1.2	11.2± 1.0	9.6± 0.7	9.4± 0.7
30	16.2± 3.3	12.6± 1.5	10.4± 0.9	8.7± 0.7	7.1± 0.5	6.5± 0.4

Table 7: $\langle F \rangle$, $F = ({P_t}^{\tilde{\gamma}} - {P_t}^{Jet})/{P_t}^{\tilde{\gamma}}$

${P_t}_{cut}^{clust}$ (GeV/c)	${P_t}_{cut}^{out}$ (GeV/c)					
	5	10	15	20	30	1000
5	0.002	0.001	0.003	0.004	0.004	0.005
10	0.002	0.003	0.005	0.007	0.008	0.008
15	0.001	0.003	0.005	0.009	0.013	0.013
20	0.002	0.003	0.006	0.010	0.016	0.018
30	0.002	0.003	0.005	0.011	0.018	0.027

Table 8: $\sigma(F)$, $F = ({P_t}^{\tilde{\gamma}} - {P_t}^{Jet})/{P_t}^{\tilde{\gamma}}$

${P_t}_{cut}^{clust}$ (GeV/c)	${P_t}_{cut}^{out}$ (GeV/c)					
	5	10	15	20	30	1000
5	0.028	0.035	0.038	0.038	0.039	0.039
10	0.028	0.038	0.046	0.049	0.052	0.052
15	0.029	0.041	0.051	0.057	0.065	0.066
20	0.030	0.042	0.053	0.062	0.075	0.080
30	0.030	0.043	0.055	0.067	0.087	0.101

$$\hat{p}_{\perp}^{\,min} = 200\ GeV/c$$
$$P_t^{\,isol} < 2\ GeV/c, \quad \epsilon^{\tilde{\gamma}} < 5\%, \quad \Delta\phi = 15^{\circ}$$

Table 9: Number of events per $L_{int} = 3\ fb^{-1}$

$P_{t\ cut}^{\ clust}$	$P_{t\ cut}^{\ out}\ (GeV/c)$					
(GeV/c)	5	10	15	20	30	1000
5	620	1220	1330	1360	1360	1380
10	1660	4100	5220	5700	5820	5840
15	2080	5420	7880	9310	10160	10290
20	2230	5960	9020	11240	13230	13840
30	2310	6290	9770	12590	16570	19510

Table 10: S/B

$P_{t\ cut}^{\ clust}$	$P_{t\ cut}^{\ out}\ (GeV/c)$					
(GeV/c)	5	10	15	20	30	1000
5	179±166	114± 61	102± 50	104± 51	104± 51	104± 51
10	42.9± 12.4	43.5± 8.6	44.2± 7.6	38.7± 6.0	39.5± 6.1	39.5± 6.1
15	42.1± 11.2	42.8± 7.1	39.9± 5.3	31.5± 3.5	28.4± 2.9	28.3± 2.9
20	31.2± 7.0	36.1± 5.3	29.7± 3.3	24.7± 2.3	20.7± 1.6	19.4± 1.5
30	30.2± 6.6	28.6± 3.7	23.2± 2.2	19.3± 1.5	15.8± 1.0	13.6± 0.8

Table 11: $\langle F \rangle,\ F = (P_t{}^{\tilde{\gamma}} - P_t{}^{Jet})/P_t{}^{\tilde{\gamma}}$

(GeV/c)	5	10	15	20	30	1000
5	0.003	0.002	0.003	0.003	0.003	0.004
10	0.001	0.003	0.004	0.005	0.005	0.005
15	0.001	0.003	0.005	0.007	0.007	0.008
20	0.001	0.003	0.005	0.007	0.008	0.009
30	0.001	0.003	0.005	0.007	0.009	0.014

Table 12: $\sigma(F),\ F = (P_t{}^{\tilde{\gamma}} - P_t{}^{Jet})/P_t{}^{\tilde{\gamma}}$

$P_{t\ cut}^{\ clust}$	$P_{t\ cut}^{\ out}\ (GeV/c)$					
(GeV/c)	5	10	15	20	30	1000
5	0.014	0.017	0.019	0.020	0.022	0.024
10	0.015	0.019	0.023	0.025	0.027	0.027
15	0.015	0.020	0.025	0.029	0.033	0.035
20	0.015	0.021	0.026	0.031	0.038	0.042
30	0.015	0.021	0.027	0.033	0.043	0.054

$$\hat{p}_\perp^{min} = 40\ GeV/c$$
$$P_t^{isol} < 2\ GeV/c,\ \ \epsilon^{\tilde{\gamma}} < 5\%,\ \ \Delta\phi = 15^\circ,\ \ \epsilon^{jet} < 5\%$$

Table 13: Number of events per $L_{int} = 300\ pb^{-1}$

$P_{t\ cut}^{clust}$ (GeV/c)	$P_{t\ cut}^{out}$ (GeV/c)					
	5	10	15	20	30	1000
5	347000	594000	617000	617000	617000	617000
10	810000	1721000	2031000	2106000	2120000	2120000
15	900000	2053000	2640000	2880000	2940000	2942000
20	929000	2158000	2865000	3220000	3360000	3367000
30	944000	2220000	2994000	3455000	3781000	3875000

Table 14: S/B

$P_{t\ cut}^{clust}$ (GeV/c)	$P_{t\ cut}^{out}$ (GeV/c)					
	5	10	15	20	30	1000
5	12.5± 4.4	10.2± 2.6	9.5± 2.3	9.5± 2.3	9.5± 2.3	9.5± 2.3
10	8.8± 1.8	7.1± 0.9	6.9± 0.8	6.5± 0.7	6.5± 0.7	6.5± 0.7
15	7.7± 1.4	6.7± 0.8	6.2± 0.6	5.7± 0.5	5.6± 0.5	5.6± 0.5
20	7.8± 1.4	6.2± 0.7	5.7± 0.5	5.2± 0.5	5.0± 0.4	4.9± 0.4
30	7.7± 1.4	5.7± 0.6	5.1± 0.5	4.6± 0.4	4.2± 0.3	4.0± 0.3

Table 15: $\langle F \rangle,\ F = ({P_t}^{\tilde{\gamma}} - {P_t}^{Jet})/{P_t}^{\tilde{\gamma}}$

$P_{t\ cut}^{clust}$ (GeV/c)	$P_{t\ cut}^{out}$ (GeV/c)					
	5	10	15	20	30	1000
5	0.005	0.003	0.002	0.002	0.002	0.002
10	-0.001	-0.004	-0.007	-0.009	-0.010	-0.010
15	-0.001	-0.004	-0.008	-0.011	-0.012	-0.013
20	0.000	-0.003	-0.007	-0.010	-0.014	-0.015
30	-0.001	-0.004	-0.007	-0.011	-0.015	-0.020

Table 16: $\sigma(F),\ F = ({P_t}^{\tilde{\gamma}} - {P_t}^{Jet})/{P_t}^{\tilde{\gamma}}$

$P_{t\ cut}^{clust}$ (GeV/c)	$P_{t\ cut}^{out}$ (GeV/c)					
	5	10	15	20	30	1000
5	0.063	0.072	0.075	0.075	0.075	0.075
10	0.068	0.079	0.087	0.093	0.094	0.094
15	0.068	0.083	0.096	0.111	0.115	0.115
20	0.067	0.084	0.100	0.120	0.129	0.129
30	0.067	0.085	0.102	0.126	0.145	0.149

$$\hat{p}_{\perp}^{\,min} = 100\ GeV/c$$
$$P_t^{isol} < 2\ GeV/c,\ \ \epsilon^{\tilde{\gamma}} < 5\%,\ \ \Delta\phi = 15^{\circ},\ \ \epsilon^{jet} < 5\%$$

Table 17: Number of events per $L_{int} = 3\ fb^{-1}$

$P_{t\ cut}^{clust}$ (GeV/c)	$P_{t\ cut}^{\ out}$ (GeV/c)					
	5	10	15	20	30	1000
5	14100	24100	26100	26400	26400	26500
10	36900	78900	98300	103700	106300	106400
15	43200	99600	134800	152400	163700	164400
20	45000	106400	150700	177700	202500	207100
30	46200	111200	161300	197500	245500	264800

Table 18: S/B

$P_{t\ cut}^{clust}$ (GeV/c)	$P_{t\ cut}^{\ out}$ (GeV/c)					
	5	10	15	20	30	1000
5	48.4± 28.8	47.4± 21.4	42.5± 17.5	42.8± 17.6	42.8± 17.6	38.4± 15.1
10	24.1± 4.4	24.1± 4.4	21.0± 3.4	20.3± 3.1	19.1± 2.8	18.9± 2.8
15	21.7± 5.3	18.9± 2.9	16.5± 2.0	16.1± 1.9	15.0± 1.6	14.9± 1.6
20	18.4± 4.1	16.3± 2.3	13.7± 1.5	13.2± 1.3	11.1± 1.0	11.0± 1.0
30	17.8± 3.9	14.6± 1.9	12.3± 1.3	10.6± 0.9	8.4± 0.6	7.9± 0.5

Table 19: $\langle F \rangle,\ F = (P_t{}^{\tilde{\gamma}} - P_t{}^{Jet})/P_t{}^{\tilde{\gamma}}$

$P_{t\ cut}^{clust}$ (GeV/c)	$P_{t\ cut}^{\ out}$ (GeV/c)					
	5	10	15	20	30	1000
5	0.002	0.001	0.002	0.003	0.003	0.003
10	0.002	0.002	0.004	0.005	0.006	0.006
15	0.001	0.002	0.002	0.005	0.007	0.007
20	0.001	0.002	0.003	0.005	0.008	0.008
30	0.001	0.001	0.001	0.005	0.007	0.008

Table 20: $\sigma(F),\ F = (P_t{}^{\tilde{\gamma}} - P_t{}^{Jet})/P_t{}^{\tilde{\gamma}}$

$P_{t\ cut}^{clust}$ (GeV/c)	$P_{t\ cut}^{\ out}$ (GeV/c)					
	5	10	15	20	30	1000
5	0.028	0.035	0.037	0.037	0.038	0.038
10	0.029	0.037	0.044	0.047	0.050	0.050
15	0.029	0.040	0.048	0.055	0.061	0.062
20	0.030	0.041	0.050	0.059	0.070	0.073
30	0.030	0.041	0.053	0.064	0.081	0.091

$$\hat{p}_\perp^{\,min} = 200\ GeV/c$$
$$P_t^{\,isol} < 2\ GeV/c,\ \ \epsilon^{\tilde{\gamma}} < 5\%,\ \ \Delta\phi = 15^\circ,\ \epsilon^{jet} < 5\%$$

Table 21: Number of events per $L_{int} = 3\ fb^{-1}$

$P_{t\ cut}^{\ clust}$	$P_{t\ cut}^{\ out}\ (GeV/c)$					
(GeV/c)	5	10	15	20	30	1000
5	620	1220	1330	1360	1360	1380
10	1660	4080	5200	5670	5780	5800
15	2070	5380	7770	9150	9960	10070
20	2210	5890	8840	10930	12770	13280
30	2280	6180	9480	12080	15600	17980

Table 22: S/B

$P_{t\ cut}^{\ clust}$	$P_{t\ cut}^{\ out}\ (GeV/c)$					
(GeV/c)	5	10	15	20	30	1000
5	179±166	114± 61	102± 50	104± 51	104± 51	104± 51
10	42.9± 12.4	43.4± 8.6	43.1± 7.5	39.1± 6.1	39.9± 6.2	39.9± 6.2
15	42.1± 11.2	42.5± 7.0	40.5± 5.5	32.1± 3.6	28.7± 3.0	28.5± 2.9
20	33.1± 7.7	36.8± 5.5	31.0± 3.5	25.4± 2.4	21.3± 1.7	19.9± 1.5
30	31.9± 7.2	30.9± 4.2	24.8± 2.5	20.5± 1.7	16.6± 1.1	14.5± 0.9

Table 23: $\langle F \rangle,\ F = (P_t{}^{\tilde{\gamma}} - P_t{}^{Jet})/P_t{}^{\tilde{\gamma}}$

(GeV/c)	5	10	15	20	30	1000
5	0.003	0.002	0.003	0.003	0.003	0.004
10	0.001	0.003	0.004	0.004	0.005	0.005
15	0.001	0.003	0.005	0.006	0.006	0.007
20	0.001	0.003	0.004	0.006	0.007	0.007
30	0.001	0.002	0.004	0.006	0.007	0.009

Table 24: $\sigma(F),\ F = (P_t{}^{\tilde{\gamma}} - P_t{}^{Jet})/P_t{}^{\tilde{\gamma}}$

$P_{t\ cut}^{\ clust}$	$P_{t\ cut}^{\ out}\ (GeV/c)$					
(GeV/c)	5	10	15	20	30	1000
5	0.014	0.017	0.019	0.020	0.022	0.024
10	0.015	0.019	0.023	0.025	0.026	0.027
15	0.015	0.020	0.025	0.029	0.033	0.034
20	0.015	0.021	0.026	0.031	0.037	0.040
30	0.015	0.021	0.027	0.032	0.042	0.050

On the application of "$\gamma + jet$" events for setting the absolute jet energy scale and determining the gluon distribution at the LHC .

D.V. Bandurin, V.F. Konoplyanikov, N.B. Skachkov

Joint Institute for Nuclear Research, Dubna, Russia

Abstract

We study the impact of new set of cuts, proposed in our previous works, on the improvement of accuracy of the jet energy calibration with "$pp \to \gamma + Jet + X$" process at LHC. Monte Carlo events produced by the PYTHIA 5.7 generator are used for this aim. The selection criteria for "$\gamma + jet$" event samples that would provide a good balance of $P_t{}^{\gamma}$ with $P_t{}^{jet}$ and would allow to reduce the background are described. The distributions of these events over $P_t{}^{\gamma}$ and η^{jet} are presented. The features of "$\gamma + jet$" events in the barrel region of the CMS detector ($|\eta^{jet}| < 1.4$) are exposed. The efficiency of the cuts used for background suppression is demonstrated.

It is shown that the samples of "$\gamma + jet$" events, gained with the cuts for the jet energy calibration, may have enough statistics for determining the gluon distribution inside a proton in the region of $x \geq 2 \cdot 10^{-4}$ and of Q^2 by two orders higher than that studied at HERA.

Contents

1. INTRODUCTION.

Setting an absolute energy scale for a jet, detected mostly by hadronic and electromagnetic calorimeters (HCAL and ECAL), is an important task for any of pp and $p\bar{p}$ collider experiments (see e.g. [1–8]).

The main goal of this work is to demonstrate the efficiency of the selection criteria for "$pp \to \gamma + Jet + X$" events (we shall use in what follows the abreviation "$\gamma + jet$" for them) that we proposed in [9]–[17] and which application may improve the precision of the jet transverse momentum determination (i.e. of ${P_t}^{Jet}$) based on assigning a photon ${P_t}^{\gamma}$ to a signal produced by a jet. This note summarises the results of our preliminary publications [9]–[17] [1] and includes some modifications connected with the use of jetfinders [2]. Here we shall present the results of our analysis of "$\gamma + jet$" events generated by using PYTHIA 5.7 [20]. The results of background suppression study in the framework of the GEANT [21] based detector simulation package CMSIM [22] are also included [23],[24]. Further development based on the CMSIM simulation of the detector response will be presented in our next papers.

We consider here the case of the LHC luminosity $L = 10^{33}\ cm^{-2}s^{-1}$. It will be shown below that this value is quite sufficient for selecting the event samples of a large enough volume even after an application of much more restrictive new cuts as well as of new physical variables introduced in [9]–[17]. Our aim is to select the samples of topologically clean "$\gamma + jet$" events with a good balance of ${P_t}^{\gamma}$ and ${P_t}^{Jet}$ and to use them for further modeling of the jet energy calibration procedure within packages based on the full GEANT simulation like CMSIM, for example. In this way one can estimate a jet energy calibration accuracy that can be achieved with the proposed cuts in the experiment.

Section 2 is a short introduction into the physics connected with the discussed problem. General features of "$\gamma + jet$" processes at LHC energy are presented here. We review the possible sources of the ${P_t}^{\gamma}$ and ${P_t}^{Jet}$ disbalance and the ways of selecting those events where this disbalance has a minimal value on the particle level of simulation (we follow here the terminology of [1]).

In Section 3.1 the definitions are given for the transverse momenta of different physical objects that we have introduced in [9]–[15] as the quantities that have a meaning of a part of "$\gamma + jet$" event and that we suppose to be important for studying the physics connected with a jet calibration procedure. These values of transverse momenta enter into the P_t-balance equation that reflects the total P_t conservation law for the pp-collision event as a whole.

Section 3.2 describes the criteria we have chosen to select "$\gamma + jet$" events for the jet energy calibration procedure. The "cluster" (or mini–jet) suppression criterion (P_{tCUT}^{clust}) which was formulated in an evident form in our previous publications [9]–[16] is used here. [3] (Its important impact on the selection of events with a good balance of ${P_t}^{\gamma}$ and ${P_t}^{Jet}$ will be illustrated in Sections 5–8.) These clusters have a physical meaning of a part of another new experimentally measurable quantity, introduced in [9]–[16] for the first time, namely, the sum of $\vec{P}_t$ of those

[1] The analogous work on application of methods developed in [9]–[17] for a case of Tevatron energies and D0 detector geometry was recently fulfiled [18].

[2] In contrast with [11] – [15], here we use the geometry of the CMS detector as given in CMSJET [19] and the corresponding UA1 and UA2 jetfinders of this program (in addition to the LUCELL jetfinder from PYTHIA) with their default values of parameters (the only change is that we have increased the cone radius in the UA1 jetfinder from $R_{jet} = 0.5$ to $R_{jet} = 0.7$). The minijets or clusters additional to the hard jet (of ${P_t}^{jet} \geq 30\ GeV/c$) are found by the program LUCELL in all events here.

[3] The analogous third jet cut threshold E_T^3 (varying from 20 to 8 GeV) was used in [25] for improving a single jet energy resolution in di-jet events.

particles that are *out* of the "$\gamma + jet$" system (denoted as ${P_t}^{out}$) and are detectable in the whole pseudorapidity η region covered by the detector ($|\eta| < 5.0$ for CMS). The vector and scalar forms of the total P_t balance equation, used for the pp-event as a whole, are given in Sections 3.1 and 3.2 respectively.

Another new thing is a use of a new physical object, proposed also in [9]–[16] and named an "isolated jet". This jet is contained in the cone of radius $R = 0.7$ in the $\eta - \phi$ space and it does not have any noticeable P_t activity in some ring around. The width of this ring is taken to be of $\Delta R = 0.26$ (or, approximately, of the width of 3 calorimeter towers). In other words, we will select a class of events having a total P_t activity inside the ring around this "isolated jet" within $3 - 8\%$ of jet P_t. (It will be shown in Sections 7, 8 and Appendices 2–5 that the number of events with such a clean topological structure would not be small at LHC energy.)

Section 4 is devoted to the estimation of the size of the non-detectable neutrino contribution to ${P_t}^{Jet}$. The correlation of the upper cut value, imposed onto ${P_t}^{miss}$, with the mean value of P_t of neutrinos belonging to the jet P_t, i.e. $\langle P_{t(\nu)}^{Jet} \rangle$, is considered. The detailed results of this section are presented in the tables of Appendix 1. These tables also include the ratios of the "gluonic events" $qg \rightarrow q + \gamma$ containing the information about the gluon distribution inside a proton. In the same tables the expected number of events (at $L_{int} = 3\ fb^{-1}$) having charm (c) and beauty (b) quarks in the initial state of the gluonic subprocess are also given.

Since the jet energy calibration is rather a practical than an academic task, in all the following sections we present the rates obtained with the cuts varying from strict to weak because their choice would be a matter of step-by-step statistics collection during the data taking.

Section 5 includes the results of studying the dependence of the initial state radiation (ISR) P_t-spectrum on the cut imposed on the clusters P_t (P_{tCUT}^{clust}) and on the angle between the transverse momenta vectors of a jet and a photon. We also present the rates for three different types of "$\gamma + jet$" events, in which jet fits completely in one definite region of the hadronic calorimeter: (1) in the Barrel (HB) with $|\eta| < 1.4$; or (2) in the Endcap (HE) with $1.4 < |\eta| < 3.0$ or, (3) finally, in the Forward (HF) with $3.0 < |\eta| < 5.0$.

Starting with Section 6 our analysis is concentrated on the "$\gamma + 1\ jet$" events having a jet entirely contained (on the particle level) of simulation within the central calorimeter region. The dependence on P_{tCUT}^{clust} of spectra of different physical variables [4] (and among them of those appearing in the P_t balance equation of event as a whole), as well as the dependence on it of the spatial distribution of P_t activity inside a jet, as well as outside it, are shown in Figs. 9–16.

The dependence of the number of events (for $L_{int} = 3\ fb^{-1}$) on P_{tCUT}^{clust} as well as the dependence on it of the fractional disbalance $({P_t}^{\gamma} - {P_t}^{Jet})/{P_t}^{\gamma}$ is studied in Section 7. The details of this study are presented in the tables of Appendices 2–5 that together with the corresponding Figs. 17–23 can serve to justify the variables and cuts introduced in Section 3. Figs. 18–23 as well as Tables 13–18 of Appendices 2 – 5 demonstrate the influence of the jet isolation criterion. The impact of P_{tCUT}^{out} on the fractional $({P_t}^{\gamma} - {P_t}^{Jet})/{P_t}^{\gamma}$ disbalance is shown in Figs. 24 and 25.

In Section 8 we present the estimation of the efficiency of background suppression (that was one of the main guidelines to establish the selection rules proposed in Section 3) for different numerical values of cuts. Justification of some of these cuts introduced in Section 3 for background suppression, based on the GEANT simulation with the CMSIM package, is given in [23].

The importance of the simultaneous use of the above-mentioned new parameters P_{tCUT}^{clust} and P_{tCUT}^{out} and also of the "isolated jet" criterion for background suppression (as well as for

[4] mostly those that have a strong influence on the ${P_t}^{\gamma} - {P_t}^{Jet}$ balance in an event.

improving the value of the $P_t{}^{\gamma}$ and $P_t{}^{Jet}$ balance) is demonstrated in Tables 14–22 of Section 8, in Fig.33 and in the tables of Appendix 6 that show the dependence of selected events on P_{tCUT}^{clust} and P_{tCUT}^{out} for various $P_t{}^{\gamma}$ intervals. The tables of Appendix 6 include the fractional disbalance values $(P_t{}^{\gamma} - P_t{}^{Jet})/P_t{}^{\gamma}$ that are found with an additional (as compared with tables of Appendix 2–5) account of the $P_t{}^{out}$ cut. In this sense the tables of Appendix 6 contain the final (as they include the background contribution) and *first main* result of our study of the problem of setting the absolute scale of the jet energy at the particle level defined by generation with PYTHIA.

In Section 9 we show the tables and some plots that demonstrate a possible influence of the intrinsic transverse parton momentum k_t parameter variation (including, as an illustration, some extreme k_t values) on the $P_t{}^{\gamma} - P_t{}^{Jet}$ disbalance.

Section 10 contains the *second main* result of our study of "$\gamma + jet$" events at the LHC energy [16] . Here we investigate the possibility of using the same sample of the topologically clean "$\gamma + jet$" events, obtained with the described cuts, for determining the gluon distribution in a proton (see also [54], [66]– [70]). The kinematic plot presented here shows what a region of x and Q^2 variables (namely: $2 \cdot 10^{-4} \leq x \leq 1.0$ and $1.6 \cdot 10^3 \leq Q^2 \leq 8 \cdot 10^4$ $(GeV/c)^2$) can be covered at LHC energies, with a sufficient number of events for this aim. The comparison with the kinematic regions covered by other experiments where parton distributions were studied is also shown in the same plot (see Fig. 35). It is also seen that at the LHC it would be possible to move to the values of Q^2 by about two orders higher than those that are reached at HERA.

About the Summary. We tried to write it in a way allowing a dedicated reader, who is interested in result rather than in method, to pass directly to it just after this sentence.

Since the results presented here were obtained with the PYTHIA simulation, we are planning to carry out analogous estimations with another event generator like HERWIG, for example, in subsequent papers.

2. GENERALITIES OF THE "$\gamma + jet$" PROCESS.

The useful variables are introduced for studying the effects of the initial and final state radiation on the $P_t{}^{\gamma}$ and $P_t{}^{Jet}$ balance basing on the simulation in the framework of PYTHIA. Other effects of non-perturbative nature like primordial parton k_t effect, parton-to-jet hadronization that may also lead to $P_t{}^{\gamma} - P_t{}^{Jet}$ disbalance within the physical models used in PYTHIA are also discussed.

2.1 Leading order picture.

The idea of setting of the absolute scale for a jet energy (and of hadronic calorimeter (HCAL) calibration) by means of the physical process "$pp(\bar{p}) \rightarrow \gamma + jet + X$" was realized many times in different experiments (see [1–8] and references therein). It is based on the parton picture where two partons ($q\bar{q}$ or qg), supposed to be moving in different colliding nucleons with zero transverse momenta (with respect to the beam line), produce a photon called the "direct photon". This process is described by the leading order (LO) Feynman diagrams shown in Fig. 1 (for the explanation of the numeration of lines see Section 2.2) for the "Compton-like" subprocess (ISUB=29 in PYTHIA)

$$qg \rightarrow q + \gamma \qquad (1a)$$

and for the "annihilation" subprocess (ISUB=14)

$$q\overline{q} \rightarrow g + \gamma. \qquad (1b)$$

In a case when initial partons have zero transverse momenta the P_t of the final state "γ+parton" system produced in $2 \rightarrow 2$ fundamental parton interactions (1) and (2) should be also equal to

zero, i.e. the following P_t balance equation for photon and final parton should take place

$$\vec{P}_t^{\,\gamma+part} = \vec{P}_t^{\,\gamma} + \vec{P}_t^{\,part} = 0. \tag{2}$$

Thus, one may expect that the transverse momentum of the jet produced by the final state parton (q or g), having $\vec{P}_t^{\,part} = -\vec{P}_t^{\,\gamma}$, will be close in magnitude, with a reasonable precision, to the transverse momentum of the final state photon, i.e. $\vec{P}_t^{\,Jet} \approx -\vec{P}_t^{\,\gamma}$.

It allows the absolute jet energy scale to be determined (and the HCAL to be calibrated) in the experiments with a well-calibrated electromagnetic calorimeter (ECAL). To put it simpler, one can assign to the part of the jet transverse energy E_t^{Jet} deposited in the HCAL the value of the difference between the values of the transverse energy deposited in the ECAL in the photon direction (i.e. E_t^{γ}) and the transverse energy deposited in the ECAL in the jet direction.

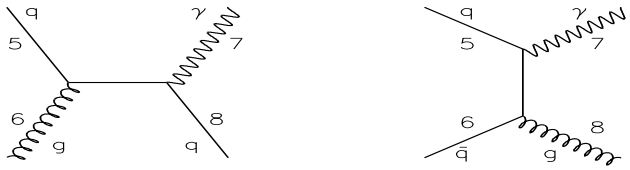

Fig. 1: Some of the leading order Feynman diagrams for direct photon production.

2.2 Initial state radiation.

Since we believe in the perturbation theory, the leading order (LO) picture described above is expected to be dominant and to determine the main contribution to the cross section. The Next-to-Leading Order (NLO) approximation (see some of the NLO diagrams in Figs. 2 and 4) introduces some deviations from a rather straightforward LO-motivated idea of jet energy calibration. A gluon radiated in the initial state (ISR), as it is seen from Fig. 2, can have its own non-zero transverse momentum $P_t^{gluon} \equiv P_t^{ISR} \neq 0$ and thus the total transverse momenta of 2 partons that appear in the initial state of fundamental $2 \to 2$ QCD subprocesses (1a) and (1b) should not be equal to zero any more. As a result of the transverse momentum conservation there should arise a disbalance between the transverse momenta of a photon P_t^{γ} and of a parton P_t^{part} produced in the fundamental $2 \to 2$ process $5 + 6 \to 7 + 8$ shown in Fig. 2 (and in Fig. 3) and thus, finally, the disbalance between P_t^{γ} and P_t of a jet produced by this parton may appear.

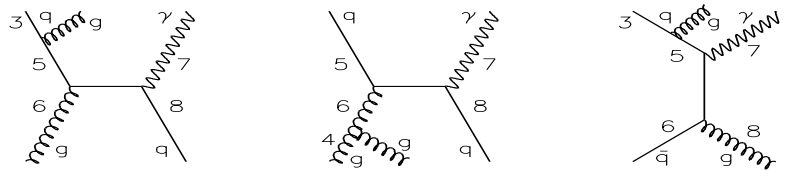

Fig. 2: Some of Feynman diagrams of direct photon production including gluon radiation in the initial state.

Following [9]–[15] and also [18] we choose the modulus of the vector sum of the transverse momentum vectors $\vec{P}_t^{\,5}$ and $\vec{P}_t^{\,6}$ of the incoming into $2 \to 2$ fundamental QCD subprocesses $5 + 6 \to 7 + 8$ partons (lines 5 and 6 in Fig. 2) and the sum of their modulus as two quantitative measures

$$P_t^{5+6} = |\vec{P}_t^{\,5} + \vec{P}_t^{\,6}|, \qquad P_t 56 = |P_t^{\,5}| + |P_t^{\,6}| \tag{3}$$

to estimate the P_t disbalance caused by ISR [5]. The modulus of the vector sum

[5]The variable $P_t^{\,5+6}$ was used in analysis in [9]–[11].

$$P_t^{\gamma+Jet} = |\vec{P}_t^{\,\gamma} + \vec{P}_t^{\,Jet}| \tag{4}$$

was also used as an estimator of the final state P_t disbalance in the "$\gamma + jet$" system in [11]–[15].

The numerical notations in the Feynman diagrams (shown in Figs. 1 and 2) and in formula (3) are chosen to be in correspondence with those used in the PYTHIA event listing for description of the parton–parton subprocess displayed schematically in Fig. 3. The "ISR" block describes the initial state radiation process that can take place before the fundamental hard $2 \to 2$ process.

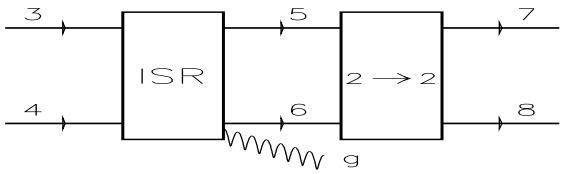

Fig. 3: PYTHIA "diagram" of $2 \to 2$ process (5+6→7+8) following the block (3+4→5+6) of initial state radiation (ISR), drawn here to illustrate the PYTHIA event listing information.

2.3 Final state radiation.

Let us consider fundamental subprocesses in which there is no initial state radiation but instead final state radiation (FSR) takes place. These subprocesses are described in the quantum field theory by the NLO diagrams like those shown in Fig. 4. It is clear that appearance of an extra gluon leg in the final state may lead to appearance of two (or more) jets or an intense jet and a weaker jet (mini-jet or cluster) in an event as it happens in the case of ISR described above. So, to suppress FSR (manifesting itself as some extra jets or clusters) the same tools as for reducing ISR should be used. But due to a usage in PYTHIA of the string model of fragmentation, which has a non-perturbartive nature, it is much more difficult to deduce (basing on the PYTHIA event listing information) the variables (analogous to (3) and (4)) to describe the final state disbalance between P_t of a jet and P_t^{γ}. That is why, keeping in mind a close analogy of the physical pictures of ISR and FSR (see Figs. 2 and 4), we shall concentrate in the following sections on studing of the initial state radiation supposing that the methods of its reduction should be also usful for suppression of FSR.

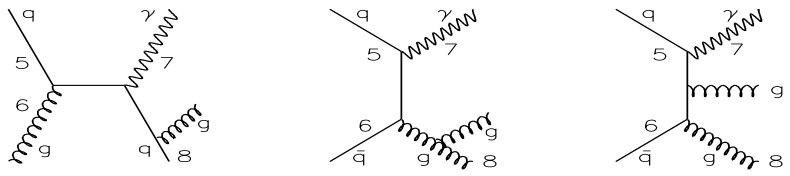

Fig. 4: Some of Feynman diagrams of direct photon production including gluon radiation in the final state.

2.4 Primordial parton k_t effect.

Now after considering the disbalance sources connected with the perturbative corrections to the leading order diagrams let us mention the physical effects of the non-perturbative nature. Thus, a possible non-zero value of the intrinsic transverse parton velocity inside a colliding proton may be another source of the P_t^{γ} and P_t^{part} disbalance in the final state. This effect at the present stage of theoretical understanding of soft physics can be described mainly in a phenomenological way. Its reasonable value is supposed to lead to the following limit on the value of intrinsic transverse

momentum $k_t \leq 1.0\ GeV/c$ of a parton. It should be noted that sometimes in the literature the total effect of ISR and of the intrinsic parton transverse momentum is denoted by a common symbol "k_t". Here we follow the approach and the phenomenological model used in PYTHIA where these two sources of the ${P_t}^{\gamma}$ and ${P_t}^{Jet}$ disbalance, having different nature, perturbative and non-perturbative ones, can be switched on separately by different keys (MSTP(61) for ISR and PARP(91), PARP(93), MSTP(91) for intrinsic parton transverse momentum k_t). In what follows we shall keep the value of k_t mainly to be fixed by the PYTHIA default value $\langle k_t \rangle = 0.44\, GeV/c$. The dependence of the disbalance between ${P_t}^{\gamma}$ and ${P_t}^{Jet}$ on a possible variation of k_t will be discussed in detail in Section 9. The general conclusion from there is that any variation of k_t within reasonable boundaries (as well as slightly beyond them) does not produce a large effect in the case when the initial state radiation is switched on. The latter makes a dominant contribution.

2.5 Parton-to-jet hadronization.

Another non-perturbative effect that leads to the ${P_t}^{\gamma} - {P_t}^{Jet}$ disbalance is connected with hadronization (or fragmentation into hadrons) of the parton produced in the fundamental $2 \rightarrow 2$ subprocess into a jet. The hadronization of the parton into a jet is described in PYTHIA within the Lund string fragmentation model. The mean values of the fractional ${P_t}^{Jet} - {P_t}^{parton}$ disbalance will be presented in the tables of Appendices 2 – 5 for three different jetfinders. As it will be shown in Section 7 (see also tables of Appendices 2–5) the hadronization effect contribution into ${P_t}^{\gamma} - {P_t}^{Jet}$ disbalance may be approximately of the same size as that of ISR.

3. CHOICE OF MEASURABLE PHYSICAL VARIABLES FOR THE "$\gamma + jet$" PROCESS AND THE CUTS FOR BACKGROUND REDUCTION.

The classification of different physical objects that participate in "$\gamma + jet$" events and that may give a noticeable contribution into the total P_t-balance in the event as a whole is done.

Two new physical observables, namely, P_t of a cluster and P_t of all detectable particles beyond "$\gamma + jet$" system, as well as the definion of isolated jet, proposed for studying ${P_t}^{\gamma} - {P_t}^{Jet}$ disbalance in [9]–[15], are discussed.

The selection cuts that would be imposed onto the physical observables of "$\gamma + jet$" events are presented.

The P_t-balance equation for the event as a whole is written in scalar form that allow to express the ${P_t}^{\gamma} - {P_t}^{Jet}$ disbalance in terms of the considered physical variables.

Apart from (1a) and (1b), other QCD subprocesses with large cross sections, by orders of magnitude larger than the cross sections of (1a) and (1b), can also lead to high P_t photons and jets in final state. So, we face the problem of selecting signal "$\gamma + jet$" events from a large QCD background. Here we shall discuss the choice of physical variables that would be useful, under some cuts on their values, for separation of the desirable processes with direct photon ("γ^{dir}") from the background events. The possible "$\gamma^{dir}-$candidate" may originate from the π^0, η, ω and K_s^0 meson decays [23], [24] or may be caused by a bremsstrahlung photon or by an electron (see Section 8).

We take the CMS ECAL size to be limited by $|\eta| \leq 2.61$ and the HCAL to consist of the Barrel (HB), Endcap (HE) and Forward (HF) parts and to be limited by $|\eta| \leq 5.0$, where $\eta = -ln\ (tan\ (\theta/2))$ is a pseudorapidity defined in terms of a polar angle θ counted from the beam line. In the plane transverse to the beam line the azimuthal angle ϕ defines the directions of $\vec{P}_t^{\,Jet}$ and $\vec{P}_t^{\,\gamma}$.

3.1 Measurable physical observables and the P_t vector balance equation.

In $pp \to \gamma + Jet + X$ events we are going to study the main physical object will be a high P_t jet to be detected in the $|\eta| < 5.0$ region and a direct photon registered by the ECAL up to $|\eta| < 2.61$. In these events there will be a set of particles mainly caused by beam remnants, i.e. by spectator parton fragments, that are flying mostly in the direction of a non-instrumented volume ($|\eta| > 5.0$) in the detector. Let us denote the total transverse momentum of these non-observable particles (i) as

$$\sum_{i \in |\eta| > 5.0} \vec{P}_t^{\,i} \equiv \vec{P}_t^{\,|\eta| > 5.0}. \tag{5}$$

Among the particles with $|\eta| < 5.0$ there may also be neutrinos. We shall denote their total momentum as

$$\sum_{i \in |\eta| < 5.0} \vec{P}_{t(\nu)}^{\,i} \equiv \vec{P}_{t(\nu)}. \tag{6}$$

The sum of the transverse momenta of these two kinds of non-detectable particles will be denoted as $P_t^{\,miss}$ [6]:

$$\vec{P}_t^{\,miss} = \vec{P}_{t(\nu)} + \vec{P}_t^{\,|\eta| > 5.0}. \tag{7}$$

A high-energy jet may also contain neutrinos that may carry part of the total jet energy and of $P_t^{\,Jet}$. The average values of these neutrino parts can be estimated from simulation.

We shall separate from the total jet transverse momentum $\vec{P}_t^{\,Jet}$ the part that can be measured in the detector, i.e. in the ECAL+HCAL calorimeter system and in the muon system. Let us denote this detectable part as $\vec{P}_t^{\,jet}$ (small "j"!). So, we shall present the total jet transverse momentum $\vec{P}_t^{\,Jet}$ as a sum of three parts:

1. $\vec{P}_{t(\nu)}^{\,Jet}$, containing the contribution of neutrinos that belong to the jet, i.e. a non-detectable part of a jet P_t (i - neutrino):

$$\vec{P}_{t(\nu)}^{\,Jet} = \sum_{i \in Jet} \vec{P}_{t(\nu)}^{\,i}. \tag{8}$$

2. $\vec{P}_{t(\mu)}^{\,Jet}$, containing the contribution of jet muons to $\vec{P}_t^{\,Jet}$ (i - muon):

$$\vec{P}_{t(\mu)}^{\,Jet} = \sum_{i \in Jet} \vec{P}_{t(\mu)}^{\,i}. \tag{9}$$

These muons make a weak signal in the calorimeter but their energy can be measured, in principle, in the muon or muon+tracker systems (in the region of $|\eta| < 2.4$ in the case of CMS geometry). Due to the absence of the muon system and the tracker beyond the $|\eta| < 2.4$ region, there exists a part of $P_t^{\,Jet}$ caused by muons with $|\eta| > 2.4$. We denote this part as $P_{t(\mu,|\eta|>2.4)}^{Jet}$. It can be considered, in some sense, as the analogue of $P_{t(\nu)}^{Jet}$ since the only trace of its presence would be weak MIP signals in calorimeter towers.

As for both points 1 and 2 above, let us say in advance that the estimation of the average values of the neutrino and muon contributions to $P_t^{\,Jet}$ (see Section 4 and Tables 1–8 of Appendix 1) has shown that they are quite small: about 0.35%–0.50% of $\langle P_t^{\,Jet} \rangle_{all}$ is due to neutrinos and

[6] This value is a part of true missing P_t in an experiment that includes the detector effects (see [1, 2]).

about 0.25% of $\langle {P_t}^{Jet} \rangle_{all}$ to muons, where "all" means averaging over all events including those without neutrinos in jets. So, they together may cause approximately about 0.6% of ${P_t}^{\gamma}$ and ${P_t}^{Jet}$ disbalance if muon signal is lost.

3. And finally, as we have mentioned before, we use $\vec{P}_t^{\,jet}$ to denote the part of $\vec{P}_t^{\,Jet}$ which includes all detectable particles of the jet [7] , i.e. the sum of P_t of jet particles that may produce a signal in the calorimeter and muon system (calo=ECAL+HCAL signal)

$$\vec{P}_t^{\,jet} = \vec{P}_{t(calo)}^{\,Jet} + \vec{P}_{t(\mu)}^{\,Jet}, \quad |\eta^{\mu}| < 2.4. \tag{10}$$

Thus, in a general case we can write for any η values:

$$\vec{P}_t^{\,Jet} = \vec{P}_t^{\,jet} + \vec{P}_{t(\nu)}^{\,Jet} + \vec{P}_{t(\mu,|\eta^{\mu}|>2.4)}^{\,Jet}. \tag{11}$$

In the case of $pp \to \gamma + Jet + X$ events the particles detected in the $|\eta| < 5.0$ region may originate from the fundamental subprocesses (1a) and (1b) corresponding to LO diagrams shown in Fig. 1, as well as from the processes corresponding to NLO diagrams (like those in Figs. 2, 4 that include ISR and FSR), and also from the "underlying" event [1], of course.

As was already mentioned in Section 2, the final states of fundamental subprocesses (1a) and (1b) may contain additional jets due to the ISR and final state radiation (FSR) caused by the higher order QCD corrections to the LO Feynman diagrams shown in Fig. 2 and Fig. 4. To understand and then to realize the jet energy calibration procedure, we need to use the event generator to find the criteria for selection of events with a good balance of $\vec{P}_t^{\,\gamma}$ with the $\vec{P}_t^{\,jet}$ part measurable in the detector. It means that to make a reasonable simulation of the calibration procedure, we need to have a selected sample of generated events having a small ${P_t}^{miss}$ (see Section 4) contribution and use it as a model. We also have to find a way to select events without additional jets or with jets suppressed down to the level of mini-jets or clusters having very small P_t.

So, for any event we separate the particles in the $|\eta| < 5.0$ region into two subsystems. The first one consists of the particles belonging to the "$\gamma + Jet$" system (here "Jet" denotes the jet with the highest $P_t \geq 30\ GeV/c$) having the total transverse momentum $\vec{P}_t^{\,\gamma+Jet}$ (large "Jet", see (11)). The second subsystem involves all other (O) particles beyond the "$\gamma + Jet$" system in the region, covered by the detector, i.e. $|\eta| < 5.0$. Let us mention that the value of $\vec{P}_t^{\,\gamma+Jet}$ may be different from the value of observable:

$$\vec{P}_t^{\,\gamma+jet} = \vec{P}_t^{\,\gamma} + \vec{P}_t^{\,jet} \quad (\text{small "jet''}), \tag{12}$$

in the case of non-detectable particles presence in a jet. The total transverse momentum of this O-system is denoted as ${P_t}^{O}$ and it is a sum of P_t of additional mini-jets (or clusters) and P_t of single hadrons, photons and leptons in the $|\eta| < 5.0$ region. Since a part of neutrinos are also present among these leptons, the difference of $\vec{P}_{t(\nu)}$ and $\vec{P}_{t(\nu)}^{\,Jet}$ gives us the transverse momentum

$$\vec{P}_{t(\nu)}^{\,O} = \vec{P}_{t(\nu)} - \vec{P}_{t(\nu)}^{\,Jet} \quad |\eta^{\nu}| < 5.0, \tag{13}$$

carried out by the neutrinos that do not belong to the jet but are contained in the $|\eta| < 5.0$ region.

[7] We shall consider the issue of charged particles contribution with small P_t into the total jet P_t while discussing the results of the full GEANT simulation (with account of the magnetic field effect) in our forthcoming papers.

We denote by $\vec{P}_t^{\,out}$ a part of $\vec{P}_t^{\,O}$ that can be measured, in principle, in the detector. Thus, $\vec{P}_t^{\,out}$ is a sum of P_t of other mini-jets or, generally, clusters (with $P_t^{\,clust}$ smaller than $P_t^{\,Jet}$) and P_t of single hadrons (h), photons (γ) and electrons (e) with $|\eta| < 5.0$ and muons (μ) with $|\eta^\mu| < 2.4$ that are out of the "$\gamma + jet$" system. For simplicity these mini-jets and clusters will be called "clusters" [8]. So, for our "$\gamma + jet$" events $\vec{P}_t^{\,out}$ is the following sum (all $\{h,\ \gamma,\ e,\ \mu\} \notin$ Jet):

$$\vec{P}_t^{\,out} = \vec{P}_t^{\,clust} + \vec{P}_{t(h)}^{\,sing} + \vec{P}_{t(\gamma)}^{\,nondir} + \vec{P}_{t(e)} + \vec{P}_{t(\mu,|\eta^\mu|<2.4)}^{\,O}; \quad |\eta| < 5.0. \tag{14}$$

And thus, finally, we have:

$$\vec{P}_t^{\,O} = \vec{P}_t^{\,out} + \vec{P}_{t(\nu)}^{\,O} + \vec{P}_{t(\mu,|\eta^\mu|>2.4)}^{\,O}. \tag{15}$$

With these notations we come to the following vector form [11] of the P_t- conservation law for the "$\gamma + Jet$" event (where γ is a direct photon) as a whole (supposing that the jet and the photon are contained in the corresponding detectable regions):

$$\vec{P}_t^{\,\gamma} + \vec{P}_t^{\,Jet} + \vec{P}_t^{\,O} + \vec{P}_t^{\,|\eta|>5.0} = 0 \tag{16}$$

with last three terms defined correspondingly by (11), (15) and (5) respectively.

3.2 Definition of selection cuts for physical variables and the scalar form of the P_t balance equation.

1. We shall select the events with one jet and one "γ^{dir}-candidate" (in what follows we shall designate it as γ and call the "photon" for brevity and only in Section 8, devoted to the backgrounds, we shall denote γ^{dir}-candidate by $\tilde{\gamma}$) with

$$P_t^{\,\gamma} \geq 40\ GeV/c \quad \text{and} \quad P_t^{\,Jet} \geq 30\ GeV/c. \tag{17}$$

The ECAL signal can be considered as a candidate for a direct photon if it fits inside the 5×5 ECAL crystal cell window having a cell with the highest P_t γ/e in the center ([29]).

For most of our applications in Sections 4, 5 and 6 mainly the PYTHIA jetfinding algorithm LUCELL will be used. The jet cone radius R in the $\eta - \phi$ space, counted from the "jet initiator cell (ic)", is taken to be $R_{ic} = ((\Delta\eta)^2 + (\Delta\phi)^2)^{1/2} = 0.7$. Below in Section 6 we shall also consider the jet radius counted from the center of gravity (gc) of the jet, i.e. R_{gc}. Comparison with the UA1 and UA2 jetfinding algorithms (taken from the CMSJET program of fast simulation [19]) is presented in Sections 6 and 7.

2. To suppress the contribution of background processes, i.e. to select mostly the events with "isolated" direct photons and to discard the events with fake "photons" (that may originate as γ^{dir}-candidates from meson decays, for instance), we restrict:

a) the value of the scalar sum of P_t of hadrons and other particles surrounding a "photon" within a cone of $R_{isol}^{\gamma} = ((\Delta\eta)^2 + (\Delta\phi)^2)^{1/2} = 0.7$ ("absolute isolation cut") [9]

$$\sum_{i \in R} P_t^{\,i} \equiv P_t^{\,isol} \leq P_{tCUT}^{isol}; \tag{18}$$

b) the value of a fraction ("fractional isolation cut")

[8] As was already mentioned in Introduction, these clusters are found by the LUCELL jetfinder with the same value of the cone radius as for jets: $R^{clust} = R^{jet} = 0.7$.

[9] We have found that S/B ratio with $R_{isol}^{\gamma} = 0.7$ is in about 1.5 times better than with $R_{isol}^{\gamma} = 0.4$ what is accompanied by only 10% of additional loss of the number of signal events.

$$\sum_{i\in R} P_t{}^i/P_t{}^\gamma \equiv \epsilon^\gamma \leq \epsilon^\gamma_{CUT}. \tag{19}$$

3. To be consistent with the application condition of the NLO formulae, one should avoid an infrared dangerous region and take care of P_t population in the region close to a γ^{dir}-candidate (see [26], [27]). In accordance with [26] and [27], we also restrict the scalar sum of P_t of particles around a "photon" within a cone of a smaller radius $R^\gamma_{singl} = 0.2$.

Due to this cut,

$$\sum_{i\in R^\gamma_{singl}} P_t{}^i \equiv P_t{}^{singl} \leq 2\ GeV/c \quad (i \neq\ \gamma^{dir}), \tag{20}$$

an "isolated" photon with high P_t also becomes a "single" one within an area of 8 calorimeter towers (of size 0.087×0.087 according to CMS geometry) which surround the tower fired by it, i.e. a tower with the highest P_t (an analog of the 3×3 tower window algorithm).

4. We accept only the events having no charged tracks (particles) with $P_t > 1\ GeV/c$ within the $R = 0.4$ cone around the γ^{dir}-candidate.

5. We also consider the structure of every event with the photon candidate at a more precise level of the 5×5 crystal cell window with a cell size of 0.0175×0.0175. To suppress the background events with photons resulting from π^0, η, ω and K^0_S meson decays, we require the absence of a high P_t hadron in the tower containing the γ^{dir}-candidate:

$$P_t{}^{hadr} \leq 5\ GeV/c. \tag{21}$$

At the PYTHIA level of simulation this cut may effectively take into account the imposing of an upper cut on the HCAL signal in the towers behind the ECAL tower fired by the direct photon (see Section 8 for details). We can not reduce this value down to, for example, 2-3 GeV/c, because a hadron with P_t below 2-3 GeV/c deposits with high probability most of its energy in ECAL and may not reveal itself in HCAL. The value 5 GeV/c is chosen with account of possible loss of hadron energy in ECAL (see [23]).

6. We select the events with the vector $\vec{P}_t{}^{Jet}$ being "back-to-back" to the vector $\vec{P}_t{}^{\gamma}$ (in the plane transverse to the beam line) within $\Delta\phi$ defined by the equation:

$$\phi_{(\gamma,\ jet)} = 180^\circ \pm \Delta\phi, \tag{22}$$

where $\phi_{(\gamma,\ jet)}$ is the angle between the $P_t{}^\gamma$ and $P_t{}^{Jet}$ vectors: $\vec{P}_t{}^{\gamma}\vec{P}_t{}^{Jet} = P_t{}^\gamma P_t{}^{Jet} \cdot cos(\phi_{(\gamma,\ jet)})$, $P_t{}^\gamma = |\vec{P}_t{}^{\gamma}|$, $P_t{}^{Jet} = |\vec{P}_t{}^{Jet}|$. The cases $\Delta\phi \leq 15^\circ, 10^\circ, 5^\circ$ (see Figs. 25,27,29 of Section 8) are considered in this paper (5° is, approximately, one CMS HCAL tower size in ϕ).

7. The initial and final state radiations (ISR and FSR) manifest themselves most clearly as some final state mini-jets or clusters activity. To suppress it, we impose a new cut condition that was not formulated in an evident form in previous experiments: we choose the "$\gamma + jet$" events that do not have any other jet-like or cluster high P_t activity by selecting the events with the values of $P_t{}^{clust}$ (the cluster cone $R_{clust}(\eta,\phi) = 0.7$), being lower than some threshold P^{clust}_{tCUT} value [25], i.e. we select the events with

$$P_t{}^{clust} \leq P^{clust}_{tCUT} \tag{23}$$

($P^{clust}_{tCUT} = 15, 10, 5\ GeV/c$ are most effective as will be shown in Sections 6–8). Here, in contrast to [11]–[15], the clusters are found by one and the same jetfinder LUCELL while three different jetfinders UA1, UA2 and LUCELL are used to find the "leading jet" (i.e. with $P_t{}^{Jet} \geq 30\ GeV/c$) in the event.

8. Now we pass to another new quantity (proposed also for the first time in [11]–[15]) that can be measured at the experiment. We limit the value of the modulus of the vector sum of $\vec{P}_t$ of all particles, except those of the "$\gamma + jet$" system, that fit into the region $|\eta| < 5.0$ covered by the ECAL and HCAL, i.e., we limit the signal in the cells "beyond the jet and photon" region, i.e. $i \notin Jet, \gamma - dir$, by the following cut:

$$\left| \sum_{i \notin Jet, \gamma - dir} \vec{P}_t{}^i \right| \equiv P_t{}^{out} \leq P_{tCUT}^{out}, \;\; |\eta^i| < 5.0. \tag{24}$$

The importance of P_{tCUT}^{out} and P_{tCUT}^{clust} for selection of events with a good balance of $P_t{}^{\gamma}$ and $P_t{}^{Jet}$ and for the background reduction will be demonstrated in Sections 7 and 8.

Below the set of selection cuts 1 – 8 will be referred to as "Selection 1". The last two of them, 7 and 8, are new criteria [11] not used in previous experiments.

9. In addition to them one more new object, introduced in [11] – [15] and named an "isolated jet", will be used in our analysis,i.e. we shall require the presence of a "clean enough" (in the sense of a limited P_t activity) region inside the ring of $\Delta R = 0.26$ width (or approximately of a size of three calorimeter towers) around the jet. Following this picture, we restrict the ratio of the scalar sum of transverse momenta of particles belonging to this ring, i.e.

$$P_t{}^{ring}/P_t{}^{jet} \equiv \epsilon^{jet} \leq \epsilon_0^{jet}, \quad \text{where} \quad P_t{}^{ring} = \sum_{i \in 0.7 < R < 1.0} |\vec{P}_t{}^i|. \tag{25}$$

(ϵ_0^{jet} is chosen to be $3 - 8\%$, see Sections 7 and 8).

The set of cuts 1 – 9 will be called in what follows "Selection 2".

10. In the following we shall consider also "Selection 3" where we shall keep only those events in which one and the same jet is found simultaneously by every of three jetfinders used here: UA1, UA2 and LUCELL (i.e. up to a good accuracy having the same values of $P_t{}^{Jet}$, R_{gc}^{jet} and $\Delta\phi$). For these jets (and also clusters in the same event) we require the following conditions:

$$P_t{}^{Jet} > 30\ GeV/c, \qquad P_t{}^{clust} < P_{tCUT}^{clust}, \qquad \Delta\phi < 15^{\circ}(10^{\circ},\ 5^{\circ}), \qquad \epsilon^{jet} \leq 3 - 8\% \tag{26}$$

The exact values of the cut parameters P_{tCUT}^{isol}, ϵ_{CUT}^{γ}, ϵ^{jet}, P_{tCUT}^{clust}, P_{tCUT}^{out} will be specified below, since they may be different, for instance, for various $P_t{}^{\gamma}$ intervals (being looser for higher $P_t{}^{\gamma}$).

11. As we have already mentioned in Section 3.1, one can expect reasonable results of the jet energy calibration procedure modeling and subsequent practical realization only if one uses a set of selected events with small $P_t{}^{miss}$. So, we also use the following cut:

$$P_t{}^{miss} \;\leq P_{tCUT}^{miss}. \tag{27}$$

For this reason we shall study in the next Section 4 the influence of $P_t{}^{miss}$ parameter on the selection of events with a reduced value of the total sum of neutrino contribution into $P_t{}^{Jet}$, i.e. $P_{t(\nu)}^{Jet}$. The aim of the event selection with small $P_{t(\nu)}^{Jet}$ is quite obvious: we need a set of events with a reduced $P_t{}^{Jet}$ uncertainty due to a possible presence of a non-detectable particle contribution to a jet [10].

To conclude this section, let us write the basic P_t-balance equation (16) of the previous section with the notations introduced here in the form more suitable to present the final results.

[10] In Section 8 we also underline the importance of this cut for reduction of $e^{\pm}$ events contribution to the background to the signal $\gamma^{dir} + jet$ events.

For this purpose we shall write equation (16) in the following scalar form (see also [11], [18]):

$$\frac{P_t^{\gamma} - P_t^{Jet}}{P_t^{\gamma}} = (1 - cos\Delta\phi) + P_t(O{+}\eta > 5.0)/P_t^{\gamma}, \tag{28}$$

where $P_t(O{+}\eta > 5.0) \equiv (\vec{P}_t^{\,O} + \vec{P}_t^{\,|\eta|>5.0)}) \cdot \vec{n}^{Jet}$ with $\vec{n}^{Jet} = \vec{P}_t^{\,Jet}/P_t^{Jet}$.

As will be shown in Section 7, the first term on the right-hand side of equation (28), i.e. $(1 - cos\Delta\phi)$ is negligibly small in a case of Selection 1, as compared with the second term and tends to decrease fast with growing P_t^{Jet}. So, in this case the main contribution to the P_t disbalance in the "$\gamma + jet$" system is caused by the term $P_t(O{+}\eta > 5.0)/P_t^{\gamma}$.

4. ESTIMATION OF A NON-DETECTABLE PART OF P_t^{Jet}.

The contribution to P_t^{jet} from neutrino ($P_{t(\nu)}^{Jet}$) is estimated. It is shown that a cut imposed onto the value of P_t^{miss} allows to select events with a negligibly small averaged value of $\langle P_{t(\nu)}^{Jet}\rangle_{all\ events}$. The values of the corresponding neutrino corrections to a measurable quantity $\vec{P}_t^{\,jet}$ are given in the tables of Appendix 1. The estimations of the number of events with charm and beauty quarks in different intervals of P_t^{Jet} as well as the averaged values of jet radius and the ratios of "gluonic process" (1a) are also included there.

In Section 3.1 we have separated the transverse momentum of a jet, i.e. P_t^{Jet}, into two parts, a detectable P_t^{jet} and a non-measurable ($P_t^{Jet} - P_t^{jet}$), consisting of $P_{t(\nu)}^{Jet}$ and $P_{t(\mu,|\eta|>2.4)}^{Jet}$ (see (11). In the same way, according to equation (15), we divided the transverse momentum P_t^{O} of "other particles" that are "out" of a jet and a direct photon system into a detectable part P_t^{out} and a non-measurable part consisting of the sum of $P_{t(\nu)}^{O}$ and $P_{t(\mu,|\eta|>2.4)}^{O}$.

We shall estimate here what part of P_t^{Jet} may be carried out by non-detectable particles [11]. For this aim we shall use the bank of the signal "$\gamma + jet$" events, i.e. caused by subprocesses (1a) and (1b), generated for three P_t^{γ} intervals: $40 < P_t^{\gamma} < 50$, $100 < P_t^{\gamma} < 120$ and $300 < P_t^{\gamma} < 360\ GeV/c$ and selected with restrictions (17) – (24) (Selection 1) and the following cut values:

$$P_{tCUT}^{isol} = 5\ GeV/c,\ \ \epsilon_{CUT}^{\gamma} = 7\%,\ \ \Delta\phi < 15^{\circ},\ \ P_{tCUT}^{clust} = 30\ GeV/c. \tag{29}$$

Here the cut $P_{tCUT}^{clust} = 30\ GeV/c$ has the meaning of a very weak restriction on mini-jets or clusters activity. No restriction was imposed on the P_t^{out} value. The results of analysis of these events are presented in Fig. 5.

The first row of Fig. 5 contains P_t^{miss} spectra of the "$\gamma + jet$" events for different P_t^{γ} intervals which demonstrate (to a good accuracy) their practical independence of P_t^{γ}.

In the second row of Fig. 5 we present the spectra of P_t^{miss} for those events (denoted as $P_{t(\nu)}^{Jet} > 0$) which contain jets having neutrinos with a non-zero $P_{t(\nu)}^{Jet}$ component of P_t^{Jet}. From these figures the dependence of the P_t^{miss} spectrum on the direct photon P_t^{γ} (approximately equal to P_t^{Jet}) is clearly seen: the spectrum tails as well as the mean values shift to a large P_t^{miss} region with growing P_t^{Jet}. (At the same time the peak position remains in the region of $P_t^{miss} < 5\ GeV/c$.) Comparison of the number of entries in the second row plots of Fig. 5 with those in the first row allows the conclusion that the part of events with the jet having the non-zero neutrinos contribution ($P_{t(\nu)}^{Jet} > 0$) has practically the same size of about 3.3% in all P_t^{γ} (or P_t^{Jet}) intervals.

[11] First we shall consider the case of switched-off decays of $\pi^{\pm}$ and $K^{\pm}$ mesons (according to the PYTHIA default agreement $\pi^{\pm}$ and $K^{\pm}$ mesons are stable).

The same spectra of $P_t{}^{miss}$ for events with $P_{t(\nu)}^{Jet} > 0$ show how many of these events shall remain after imposing a cut on $P_t{}^{miss}$ (defined by (7)) in every $P_t{}^{\gamma}$ interval.(As it will be shown in Section 8 P_{tCUT}^{miss} cut also reduces the contribution to background from the decay subprocesses $q\,g \to q' + W^{\pm}$ and $q\,\bar{q}' \to g + W^{\pm}$ with the subsequent decays $W^{\pm} \to e^{\pm}\nu$ that lead to a substantial $P_t{}^{miss}$ value and are the main source of electrons $e^{\pm}$ that may appear as direct photon candidates.)

The important thing is that such a reduction of the number of events with $P_{t(\nu)}^{Jet} > 0$ leads to reduction of the mean value of the $P_{t(\nu)}^{Jet}$, i.e. the value averaged over all collected events $\langle P_{t(\nu)}^{Jet}\rangle_{all\ events}$, in every $P_t{}^{\gamma}$ interval.

This value, found from PYTHIA generation, may serve as a model correction Δ_ν and it has to be estimated for proper determination of the total $P_t{}^{Jet}$. So, due to practical coincidence of directions of vectors of these terms we can write $P_t{}^{Jet} = P_t{}^{jet} + \Delta_\nu + \Delta_\mu$, ($|\eta^\mu| > 2.4$) where $\Delta_\nu = \langle P_{t(\nu)}^{Jet}\rangle_{all\ events}$ and $\Delta_\mu = \langle P_{t(\mu,|\eta^\mu|>2.4)}^{Jet}\rangle_{all\ events}$. (As we plan to use in this paper only events with jets belonging to Barell part of calorimeter, Δ_μ is not so important for our analysis.)

The effect of imposing a general P_{tCUT}^{miss} in each event of our sample is shown in the third row of Fig. 5. The upper cut $P_{tCUT}^{miss} = 1000\ GeV/c$, as is seen from the comparison with the second row pictures, means the absence of any upper limit for $P_{t(\nu)}^{Jet}$. The most important illustrative fact that in the absence of any restriction on $P_t{}^{miss}$ the total neutrino P_t inside the jet averaged over all events can be as large as $P_{t(\nu)}^{Jet} \approx 1\ GeV/c$ at $P_t{}^{\gamma} \geq 300\ GeV/c$ comes from the right-hand plot of the third row in Fig. 5. From the comparison of the plots in the second row with the corresponding plots in the third row [12] we see that the first essential cut $P_{tCUT}^{miss} = 20\ GeV/c$ reduces the number of entries for the first $40 < P_t{}^{\gamma} < 50\ GeV/c$ interval by less than 0.4% and the mean value of $P_{t(\nu)}^{Jet}$ by less than 10%. A more restrictive cut $P_{tCUT}^{miss} = 5\ GeV/c$ reduces the value of $\langle P_{t(\nu)}^{Jet}\rangle$ by a factor of three and leads to an approximate twofold drop of the number of events.

From the right-hand plots in Fig. 5 we see that for the $300 < P_t{}^{\gamma} < 360\ GeV/c$ interval the number of events with jets containing neutrinos (second row) is about 3.3% (Entries=3001) of the total number of the generated "$\gamma + jet$" events (Entries=89986, see first row). A very restrictive P_{tCUT}^{miss}=5 GeV/c cut leads to the reduction factor of about 50 for $\langle P_{t(\nu)}^{Jet}\rangle$($\equiv$Mean) and to about 30% reduction of the number of events. As is seen from the plot in the bottom right-hand corner of Fig. 5, the $P_{t(\nu)}^{Jet}$ spectrum for the remaining events (Entries=57475) finishes at $P_{t(\nu)}^{Jet} = 10\ GeV/c$ and sharply peaks (log scale!) at $P_{t(\nu)}^{Jet} = 0$. The averaged value of $P_{t(\nu)}^{Jet}$ under this peak is equal to 0.022 GeV/c. So, with this cut P_{tCUT}^{miss}=5 GeV/c the neutrinos make a negligible contribution to $P_t{}^{Jet}$. At the same time we see that a moderate cut $P_{tCUT}^{miss} = 10\ GeV/c$ in the $300 < P_t{}^{Jet} < 360\ GeV/c$ interval strongly reduces (by a factor of 20) the mean value of $P_{t(\nu)}^{Jet}$ (from $1\ GeV/c$ to $\langle P_{t(\nu)}^{Jet}\rangle = 0.046\ GeV/c$) at about less than 10% reduction of the number of events in this $P_t{}^{Jet}$ (or $P_t{}^{\gamma}$) interval.

In the $100 < P_t{}^{Jet} < 120\ GeV/c$ interval, as we see from the third row of Fig. 5, the same cut $P_{tCUT}^{miss} = 10\ GeV/c$ reduces the mean value of $P_{t(\nu)}^{Jet}$ by a factor of 5 (from $0.5\ GeV/c$ to $\langle P_{t(\nu)}^{Jet}\rangle = 0.09\ GeV/c$) with 10% reduction of the total number of events.

It should be noted that in the $40 < P_t{}^{Jet} < 50\ GeV/c$ interval, which is less dangerous from the point of view of the neutrino P_t content in a jet, we have already a very small mean value of

[12] This row includes the values of P_{tCUT}^{miss} and the corresponding number of entries remained after imposing P_{tCUT}^{miss}, as well as the mean value of $\langle P_{t(\nu)}^{Jet}\rangle$ (i.e. averaged over the number of the remaining entries) denoted as "Mean".

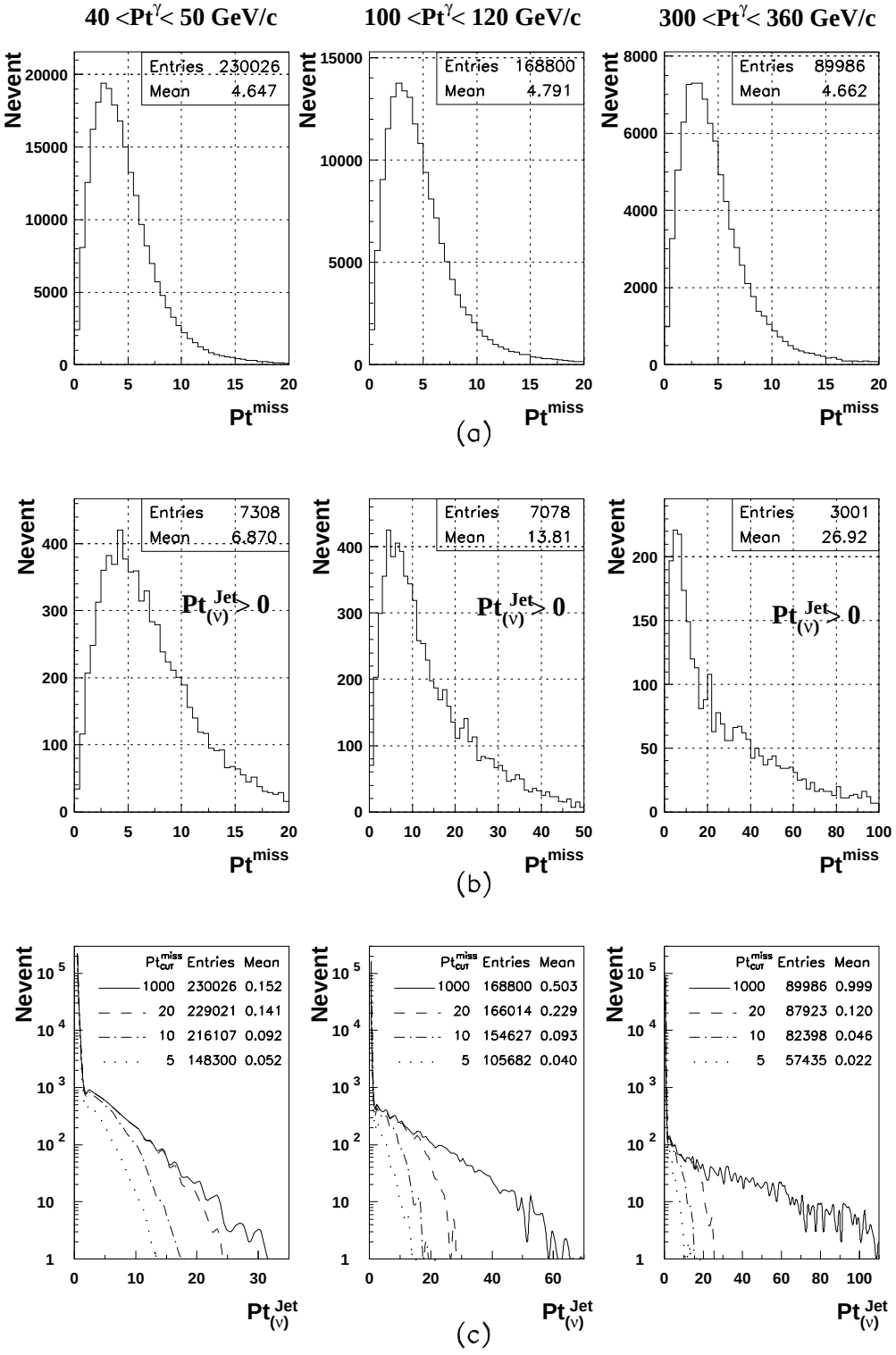

Fig. 5: a) $P_t{}^{miss}$ spectra in all events; b) $P_t{}^{miss}$ spectra in events having jets with non-zero P_t neutrinos, i.e. $P_{t(\nu)}^{Jet} > 0$; c) $P_{t(\nu)}^{Jet}$ spectra behaviour for different values of P_{tCUT}^{miss} values in various $P_t{}^{Jet} (\approx P_t{}^{\gamma})$ intervals. $P_{tCUT}^{clust} = 30\, GeV/c$.

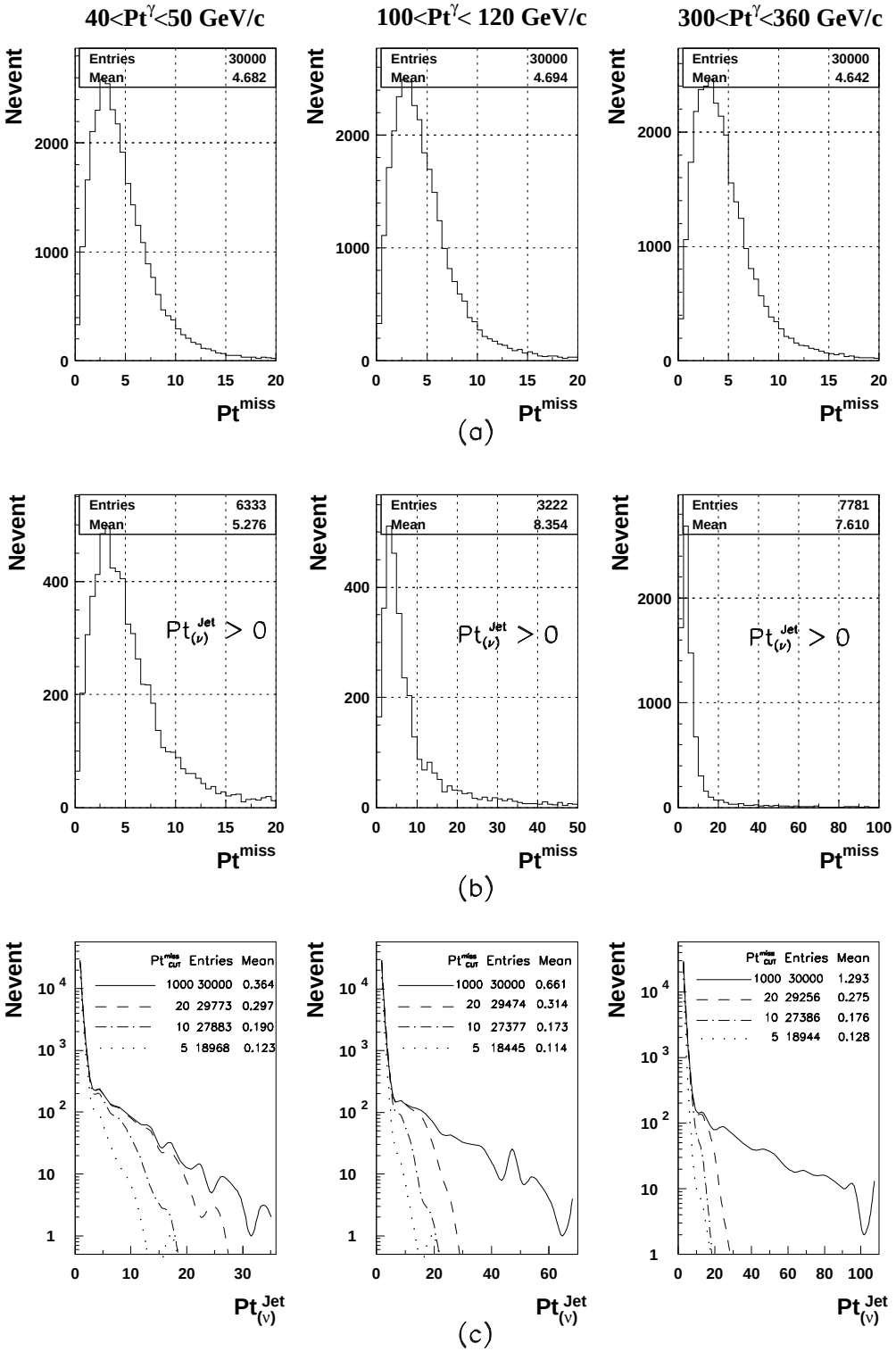

Fig. 6: $K^{\pm}, \pi^{\pm}-$decays are allowed inside the solenoid of $R = 129\ cm$ and $L = 317\ cm$. a) ${P_t}^{miss}$ spectra in all events with ; b) ${P_t}^{miss}$ spectra in events having jets with non-zero P_t neutrinos, i.e. $P_{t(\nu)}^{Jet} > 0$; c) $P_{t(\nu)}^{Jet}$ spectra behaviour for different values of P_{tCUT}^{miss} values in various ${P_t}^{Jet} (\approx {P_t}^{\gamma})$ intervals. $P_{tCUT}^{clust} = 30\ GeV/c$.

$\langle P_{t(\nu)}^{Jet} \rangle$ equal to $0.152\ GeV/c$ even without imposing any P_{tCUT}^{miss}.

The analogous (to neutrino) situation holds for the $P_{t(\mu)}^{Jet}$ contribution (as they originate mostly from the same decays).

The detailed information about the values of non-detectable $P_{t(\nu)}^{Jet}$ averaged over all events (no cut on P_t^{miss} was used) as well as about mean P_t values of muons belonging to jets $\langle P_{t(\mu)}^{Jet} \rangle$ is presented in Tables 1–8 of Appendix 1 for the sample of events with jets that are entirely contained in the barrel region of the HCAL ($|\eta^{jet}| < 1.4$, "HB-events", see Section 6 and [11]) and found by UA1 and LUCELL jetfinders. In these tables the ratio of the number of events with non-zero $P_{t(\nu)}^{Jet}$ to the total number of events is denoted by $R_{event}^{\nu \in Jet}$ and the ratio of the number of events with non-zero $P_{t(\mu)}^{Jet}$ to the total number of events is denoted by $R_{event}^{\mu \in Jet}$.

The quantity P_t^{miss} in events with $P_{t(\nu)}^{Jet} > 0$ is denoted in these tables as $P_{t\nu \in Jet}^{miss}$ and is given there for four $P_t{}^{\gamma}$ intervals ($40 < P_t{}^{\gamma} < 50$, $100 < P_t{}^{\gamma} < 120$, $200 < P_t{}^{\gamma} < 240$ and $300 < P_t{}^{\gamma} < 360\ GeV/c$) and for other P_{tCUT}^{clust} values ($P_{tCUT}^{clust} = 20, 15, 10, 5\ GeV/c$) complementary to $P_{tCUT}^{clust} = 30\ GeV/c$ used for plots [13] of Fig. 5. From Tables 1, 2 we see that the averaged value of P_t^{miss} calculated by using only the events with $P_{t(\nu)}^{Jet} > 0$, i.e. $\langle P_{t\nu \in Jet}^{miss} \rangle$, is about 6.6 – 7.0 GeV/c for the $40 < P_t{}^{\gamma} < 50\ GeV/c$ interval. It increases to about 32 GeV/c for the $300 < P_t{}^{\gamma} < 360\ GeV/c$ interval (see Tables 7, 8).

It should be noted that the averaged values of the modulus of $P_{t(\nu)}^{Jet}$ (see formula (8)) presented in the third lines of Tables 1–8 from Appendix 1 coincide with the averaged values of the difference $\langle P_t{}^{Jet} - P_t{}^{jet} \rangle \equiv \Delta_\nu$ (see Section 3.2 and second lines of Tables 1–8) to three digits, i.e. $< P_{t(\nu)}^{Jet} > = \Delta_\nu$. This is because the $\vec{P}_t{}^{Jet}$ and $\vec{P}_t{}^{jet}$ vectors are practically collinear and because we consider here the "HB-events" in which all jet muons are supposed to be also detected by the barrel muon system.

We underline that the $\langle P_{t_\nu}^{Jet} \rangle$ value estimated in Tables 1–8 has a meaning of the correction Δ_ν that should be added to $P_t{}^{jet}$ in order to take into account the P_t carried away by non-detectable particles, i.e. for a case of "HB" events when jet fits into Barrel and jet muons are measurebale, we have: $\langle P_t{}^{Jet} \rangle = \langle P_t{}^{jet} \rangle + \Delta_\nu$. It should be noted that latter on in Section 8 when we shall discuss the Pt balance of photon and jet we shall present in the tables of Appenicies 2-5 the values of $P_t{}^{Jet}$ just obtained from the values of $P_t{}^{jet}$ by adding of this correction. Here in Appendix 1 we present the values of these corrections calculated without an application of P_{tCUT}^{miss}, as the aim of these tables consists in part in showing of typical values $P_t{}^{miss}$.

Let us mention also that Tables 1–8 contain an additional information on the numbers of "$\gamma + jet$" events with jets produced by c and b quarks, i.e. $Nevent_{(c)}$ and $Nevent_{(b)}$ (see also [11, 16, 67, 70]), given for the integrated luminosity $L_{int} = 3\ fb^{-1}$ for different $P_t{}^{Jet} (\approx P_t{}^{\gamma})$ intervals. They also show the ratio ("$29 sub/all$") of the number of events caused by gluonic subprocess (1a) to the number of events due to the sum of subprocesses (1a) and (1b) and averaged jet radii $< R_{jet} >$.

It was already mentioned in the Introduction that we are planning to carry out a more detailed analysis based on the GEANT package. To have an idea of what changes can be expected, we shall consider now the case with allowed $K^{\pm}$ and $\pi^{\pm}$ decays (as the main source of neutrinos and muons). The averaged values of $P_{t(\nu)}^{Jet}$ for different $P_t{}^{\gamma}$-intervals with switched on $K^{\pm}, \pi^{\pm}$ decays are given in Fig. 6 with the same meaning of all notations as in Fig. 5. Here $K^{\pm}$ and $\pi^{\pm}$ decays are allowed inside the solenoid volume with the barrel radius $R_B = 129\ cm$ and the distance from the interaction vertex to End-cap along the z-axis $L = 317\ cm$ (CMS geometry).

From the first row of Fig. 6 we see that in a case of allowed $K^{\pm}, \pi^{\pm}$ decays the $P_t{}^{miss}$ spectrum and the position of the mean value of $P_t{}^{miss}$ for all events practically does not change

[13] Please, note that the values of $P_t{}^{miss}$ and $P_{t\nu \in Jet}^{miss}$ in the plots of Fig. 5 are slightly different from those of Appendix 1 as the former were found for events in the whole $|\eta| < 5$ region.

with growing ${P_t}^{Jet} (\approx {P_t}^{\gamma})$ in complete analogy to the first rows in Fig. 5.

At the same time the tail of ${P_t}^{miss}$ spectra for events that contain neutrinos in the jet (second row of Fig. 6) changes quite noticeably. It should be noted that the number of such events grows to $20 - 25\%$ as compared with 3% in the case considered in Fig. 5, but the mean values of ${P_t}^{miss}$ do not grow so much with ${P_t}^{\gamma}$, as is seen in Fig. 5. Now we compare the third row pictures in Figs. 5 and 6. We see that in Fig. 6 the mean value of $P_{t(\nu)}^{Jet}$ carried away by neutrinos of the jet grows from $\langle P_{t(\nu)}^{Jet} \rangle \approx 0.36\ GeV/c$ for $40 < {P_t}^{\gamma} < 50\ GeV/c$ to $\langle P_{t(\nu)}^{Jet} \rangle \approx 1.3\ GeV/c$ for $300 < {P_t}^{\gamma} < 360\ GeV/c$, i.e. its contribution into ${P_t}^{Jet}$ varies as $1\% \rightarrow 0.4\%$. From the same pictures of Fig. 6 we see that the first essential cut $P_{tCUT}^{miss} = 20\ GeV/c$ would reduce the contribution of neutrinos to ${P_t}^{Jet}$ to $\langle P_{t(\nu)}^{Jet} \rangle \approx 0.3\ GeV/c$ in all ${P_t}^{Jet}$ intervals, while the cut $P_{tCUT}^{miss} = 10\ GeV/c$ would lead to $\langle P_{t(\nu)}^{Jet} \rangle \approx 0.20\ GeV/c$ (which is at least twice larger than analogous values in Fig. 5 but still is quite acceptable) with only $\approx 8\%$ reduction of the number of events.

5. EVENT RATES FOR DIFFERENT ${P_t}^{\gamma}$ AND ${\eta}^{Jet}$ INTERVALS.

The number of "$\gamma + jet$" events distribution over ${P_t}^{\gamma}$ and ${\eta}^{\gamma}$ is studied here. It is found that in each interval of the $\Delta {P_t}^{\gamma} = 10\ GeV/c$ width the rates decrease by a factor more than 2. The number of events with jets which transverse momentum are completely (or with 5% accuracy) contained in HB, HE and HF regions are presented in Tables 9–12 for integrated luminosity $L_{\ int} = 3\ fb^{-1}$.

5.1 Dependence of distribution of the number of events on the "back-to-back" angle $\phi_{(\gamma,\ jet)}$ and on ${P_t}^{ISR}$.

The definitions of the physical variables introduced in Sections 2 and 3 allow to study a possible way to select the events with a good ${P_t}^{\gamma}$ and ${P_t}^{Jet}$ balance. Here we shall be interested to get (by help of PYTHIA generator and the theoretical models therein) an idea about the form of the spectrum of the variable $P_t 56$ (which is approximately proportional to ${P_t}^{ISR}$ up to the value of intrinsic parton transverse momentum k_t inside a proton) at different values of ${P_t}^{\gamma}$. For this aim four samples of "$\gamma + jet$" events were generated by using PYTHIA with 2 QCD subprocesses (1a) and (1b) being included simultaneously. In what follows we shall call these events as "signal events". The generations were done with the values of the PYTHIA parameter CKIN(3)($\equiv \hat{p}_{\perp}^{min}$) equal to 20, 50, 100, 150 GeV/c in order to cover four ${P_t}^{\gamma}$ intervals: 40–50, 100–120, 200–240, 300–360 GeV/c, respectively. Each sample in these ${P_t}^{\gamma}$ intervals had a size of $5 \cdot 10^6$ events. The cross sections for the two subprocesses were found to be as given in Table 1.

Table 1: The cross sections (in $microbarn$) of the $qg \rightarrow q + \gamma$ and $q\overline{q} \rightarrow g + \gamma$ subprocesses for four ${P_t}^{\gamma}$ intervals.

Subprocess type	${P_t}^{\gamma}$ interval (GeV/c)			
	40 – 50	100 – 120	200 – 240	300 – 360
$qg \rightarrow q + \gamma$	$1.19 \cdot 10^{-1}$	$6.70 \cdot 10^{-3}$	$6.09 \cdot 10^{-4}$	$1.36 \cdot 10^{-4}$
$q\overline{q} \rightarrow g + \gamma$	$0.10 \cdot 10^{-1}$	$0.69 \cdot 10^{-3}$	$0.77 \cdot 10^{-4}$	$0.20 \cdot 10^{-4}$
Total	$1.29 \cdot 10^{-1}$	$7.39 \cdot 10^{-3}$	$6.86 \cdot 10^{-4}$	$1.56 \cdot 10^{-4}$

For our analysis we used "Selection 1" (formulae (17)–(24)) defined in Sections 3.2 and the values of cut parameters (29).

In Tables 2, 3 and 5, 6 we present $P_t 56$ spectra for two most illustrative cases of ${P_t}^{\gamma}$ intervals $40 < {P_t}^{\gamma} < 50\ GeV/c$ (Tables 2 and 5) and $200 < {P_t}^{\gamma} < 240\ GeV/c$ (Tables 3 and 6). The

distributions of the number of events for the integrated luminosity $L_{int} = 3\, fb^{-1}$ in different $P_t 56$ intervals ($\langle k_t \rangle$ was taken to be fixed at the PYTHIA default value, i.e. $\langle k_t \rangle = 0.44\, GeV/c$) and for different "back-to-back" angle intervals $\phi_{(\gamma,\, jet)} = 180^\circ \pm \Delta\phi$ ($\Delta\phi \leq 15^\circ$, 10° and 5° as well as without any restriction on $\Delta\phi$, i.e. for the whole ϕ interval $\Delta\phi \leq 180^\circ$) [14] are given there. The LUCELL jetfinder was used for determination of jets and clusters [15]. Tables 2 and 3 correspond to ${P_t}^{clust} < 30\, GeV/c$ and serve as an illustration since it is rather a weak cut condition, while Tables 5 and 6 correspond to a more restrictive selection cut $P_{tCUT}^{clust} = 5\, GeV/c$ (which leads to about twofold reduction of the number of events for $\Delta\phi \leq 15^\circ$; see summarizing Tables 4 and 7).

First, from the last summary lines of Tables 2, 3 and 5, 6 we can make a general conclusion about the $\Delta\phi$-dependence of the event spectrum. Thus, in the case of weak restriction ${P_t}^{clust} < 30\ GeV/c$ we can see from Table 2 that for the $40 \leq {P_t}^{\gamma} \leq 50\ GeV/c$ interval about 66% of events are concentrated in the $\Delta\phi < 15^\circ$ range, while 32% of events are in the $\Delta\phi < 5^\circ$ range. At the same time the analogous summary line of Table 3 shows us that for higher ${P_t}^{\gamma}$ interval $200 \leq {P_t}^{\gamma} \leq 240\, GeV/c$ the $P_t 56$ spectrum for the same restriction ${P_t}^{clust} < 30\ GeV/c$ moves (as compared with low ${P_t}^{\gamma}$ intervals) to the small $\Delta\phi$ region: more than 99% of events have $\Delta\phi < 15^\circ$ and 79% of them have $\Delta\phi < 5^\circ$.

A tendency of distributions of the number of signal "$\gamma + jet$" events to be very rapidly concentrated in a rather narrow back-to-back angle interval $\Delta\phi < 15^\circ$ as ${P_t}^{\gamma}$ grows becomes more distinct with a more restrictive cut $P_{tCUT}^{clust} = 5\, GeV/c$ (see Tables 5, 6 and 7). From the last summary line of Table 5 we see for this cut that in the case of $40 \leq {P_t}^{\gamma} \leq 50\, GeV/c$ more than 97% of the events have $\Delta\phi < 15^\circ$, while 68% of them are in the $\Delta\phi < 5^\circ$ range. For $200 \leq {P_t}^{\gamma} \leq 240\, GeV/c$ (see Table 6) more than 99% of the events subject to the cut $P_{tCUT}^{clust} = 5\ GeV/c$ have $\Delta\phi < 5^\circ$. It means that while suppressing cluster or mini-jet activity by imposing $P_{tCUT}^{clust} = 5\ GeV/c$ we can select the sample of events with a clean "back-to-back" (within 15°) topology of γ and jet orientation. (Unfortunately, as it will be discussed below basing on the information from Tables 5 and 6, it does not mean that this cut allows to suppress completely the ISR). [16].

So, one can conclude that PYTHIA simulation predicts that at LHC energies most of the "$\gamma + jet$" events (more than 66%) may have the vectors $\vec{P}_t^{\,\gamma}$ and $\vec{P}_t^{\,jet}$ being back-to-back within $\Delta\phi < 15^\circ$ after imposing $P_{tCUT}^{clust} = 20\ GeV/c$. The cut $P_{tCUT}^{clust} = 5\ GeV/c$ significantly improves [17] this tendency.

It is worth mentioning that this picture reflects the predictions of one of the generators based on the approximate LO values for the cross section. It may change if the next-to-leading order or soft physics [18] effects are included.

The other lines of Tables 2, 3 and 5, 6 contain the information about the $P_t 56$ spectrum or, up to intrinsic transverse parton momentum $\langle k_t \rangle = 0.44\ GeV/c$, about ${P_t}^{ISR}$ spectrum).

From Tables 2 and 3 one can see that in the case when there are no restrictions on ${P_t}^{clust}$ the $P_t 56$ spectrum becomes a bit wider for larger values of ${P_t}^{\gamma}$.

At the same time, one can conclude from the comparison of Table 2 with Table 5 that for

[14] The value $\Delta\phi = 5^\circ$ approximately coincides with one CMS HCAL tower size in the ϕ-plane.

[15] More details connected with UA1 and UA2 jetfinders application can be found in Section 7 and Appendices 2–5 for a jet contained in CC region.

[16] See also the event spectra over ${P_t}^{clust}$ in Fig. 7 of the following Section 6.

[17] An increase in ${P_t}^{\gamma}$ produces the same effect, as is seen from comparison of Tables 2 and 3 and will be demonstrated in more detail in Section 6 and Appendices 2–5.

[18] We thank E. Pilon and J. Ph. Jouliet for the information about new LHC data on this subject and for clarifying the importance of NLO corrections and soft physics effects.

Table 2: Number of events dependence on P_t56 and $\Delta\phi$ for $40 \leq Pt^{\gamma} \leq 50\,GeV/c$ and $P_{tCUT}^{clust} = 20\,GeV/c$ for L_{int}=3fb^{-1}.

P_t56 (GeV/c)	$\Delta\phi_{max}$			
	180°	15°	10°	5°
0 – 5	1103772	1049690	1006627	849706
5 – 10	1646004	1564393	1403529	812304
10 – 15	1331589	1122473	771060	380122
15 – 20	992374	568279	365329	179767
20 – 25	725537	282135	183406	91113
25 – 30	559350	169186	112308	58395
30 – 40	911942	265961	178048	89867
40 – 50	388950	94112	62068	31000
50 – 100	91248	19442	12973	6234
100 – 300	34	0	0	0
300 – 500	0	0	0	0
0 – 500	7750799	5135671	4095348	2498507

Table 3: Number of events dependence on P_t56 and $\Delta\phi$ for $200 \leq Pt^{\gamma} \leq 240\,GeV/c$ and $P_{tCUT}^{clust} = 20\,GeV/c$ for L_{int}=3fb^{-1}.

P_t56 (GeV/c)	$\Delta\phi_{max}$			
	180°	15°	10°	5°
0 – 5	1429	1429	1427	1380
5 – 10	3266	3266	3264	3150
10 – 15	3205	3205	3200	3069
15 – 20	2827	2827	2819	2618
20 – 25	2409	2408	2393	1918
25 – 30	2006	2006	1982	1300
30 – 40	2608	2605	2533	1411
40 – 50	1237	1230	1067	586
50 – 100	1066	1018	842	536
100 – 300	313	307	293	221
300 – 500	0	0	0	0
0 – 500	20366	20301	19820	16189

Table 4: Number of events dependence on $\Delta\phi_{max}$ and on $P_t{}^{\gamma}$ for $L_{int} = 3\ fb^{-1}$. $P_{tCUT}^{clust} = 20\ GeV/c$ (summary).

$P_t{}^{\gamma}$ (GeV/c)	$\Delta\phi_{max}$			
	180°	15°	10°	5°
40 – 50	7750799	5135671	4095348	2498507
100 – 120	323766	297323	258691	176308
200 – 240	20366	20301	19820	16189
300 – 360	3638	3638	3627	3323

Table 5: Number of events dependence on P_t56 and $\Delta\phi$ for $40 \leq Pt^{\gamma} \leq 50\,GeV/c$ and $P_{tCUT}^{clust} = 5\,GeV/c$ for L_{int}=3fb^{-1}.

P_t56 (GeV/c)	$\Delta\phi_{max}$			
	180°	15°	10°	5°
0 – 5	331522	331321	329876	295759
5 – 10	319153	318581	299960	187089
10 – 15	88603	82586	60537	32335
15 – 20	21244	15327	11663	6924
20 – 25	8101	5681	4639	2992
25 – 30	4739	3395	2823	1949
30 – 40	3495	2790	2555	1714
40 – 50	1647	1277	1042	471
50 – 100	101	67	67	67
100 – 500	0	0	0	0
0 – 500	778606	761026	713161	529299

Table 6: Number of events dependence on P_t56 and $\Delta\phi$ for $200 \leq Pt^{\gamma} \leq 240\,GeV/c$ and $P_{tCUT}^{clust} = 5\,GeV/c$ for L_{int}=3fb^{-1}.

P_t56 (GeV/c)	$\Delta\phi_{max}$			
	180°	15°	10°	5°
0 - 5	369	369	369	369
5 - 10	563	563	563	562
10 - 15	217	217	217	217
15 - 20	56	56	56	56
20 - 25	20	20	20	18
25 - 30	9	9	9	7
30 - 40	7	7	7	6
40 - 50	6	6	6	5
50 - 100	10	10	10	10
100 - 300	8	8	8	8
300 - 500	0	0	0	0
0 - 500	1264	1264	1264	1257

Table 7: Number of events dependence on $\Delta\phi_{max}$ and on $P_t{}^{\gamma}$ for $L_{int} = 3\ fb^{-1}$. $P_{tCUT}^{clust} = 5\,GeV/c$ (summary).

$P_t{}^{\gamma}$ (GeV/c)	$\Delta\phi_{max}$			
	180°	15°	10°	5°
40 – 50	778606	761026	713161	529299
100 – 120	22170	22143	22038	20786
200 – 240	1264	1264	1264	1257
300 – 360	212	212	212	212

lower P_t^{γ} intervals the width of the most populated part of the P_t56 (or P_t^{ISR}) spectrum reduces two-fold with restricting P_{tCUT}^{clust}. So, for $\Delta\phi_{max} = 15^{\circ}$ we see that it drops from $0 < P_t56 < 25\ GeV/c$ for $P_{tCUT}^{clust} = 20\ GeV/c$ to a narrower interval of $0 < P_t56 < 10\,GeV/c$ for the $P_{tCUT}^{clust} = 5\,GeV/c$. At higher P_t^{γ} intervals (Tables 3 and 6) for the same value $\Delta\phi_{max} = 15^{\circ}$ the reduction factor of the P_t56 spectrum width (from the $0 < P_t56 < 50\ GeV/c$ interval for $P_{tCUT}^{clust} = 20\,GeV/c$ to the $0 < P_t56 < 15\ GeV/c$ interval for $P_{tCUT}^{clust} = 5\ GeV/c$) is more than two. But the tails of P_t^{ISR} spectra still remain to be quite long in a case of high P_t^{γ} intervals.

Thus, we can summarize that the PYTHIA generator predicts an increase in the P_t^{ISR} spectrum with growing P_t^{γ} (compare Tables 2 and 3), but this increase can be reduced by imposing a restrictive cut on P_t^{clust} (for more details see Sections 6 and 7).

So, the P_t56 spectra presented in Tables 2, 3 and 4, 5 show PYTHIA prediction that the ISR effect is a large one at LHC energies. Its P_t spectrum continues at least up to $P_t56 = 15\ GeV/c$ in the case of P_t^{γ} (or P_t^{jet}) $\approx 200\ GeV/c$ (and up to higher values as P_t^{γ} grows) even for $P_{tCUT}^{clust} = 5\ GeV/c$. It cannot be completely suppressed by $\Delta\phi$ and P_t^{clust} cuts alone. (In Section 8 the effect of the additional P_{tCUT}^{out} will be discussed) Therefore we prefer to use the P_t balance equation for the event as a whole (see equations (16) and (28) of Sections 3.1 and 3.2), i.e. an equation that takes into account the ISR and FSR effects, rather than balance equation (2) for fundamental processes (1a) and (1b) as discussed in Section 2.1. (In Section 6 we shall study a behavior of each term that enter equation (28) in order to find the criteria that would allow to select events with a good balance of P_t^{γ} and P_t^{Jet}).

Since the last lines in Tables 2, 3 and 5, 6 contain an illustrative information on $\Delta\phi$ dependence of the total number of events, we add also the summarizing Tables 4 and 7. They include more P_t^{γ} intervals and contain analogous numbers of events that can be collected in different $\Delta\phi$ intervals for two different P_t^{clust} cuts at $L_{int} = 3\,fb^{-1}$.

5.2 P_t^{γ} and η^{γ} dependence of event rates.

Here we shall present the number of events for different P_t^{γ} and η^{γ} intervals as predicted by PYTHIA simulation with weak cuts defined mostly by (29) with only change of P_{tCUT}^{clust} value from 30 to 10 GeV/c. The lines of Table 8 correspond to P_t^{γ} intervals and the columns to η^{γ} intervals. The last column of this table contains the total number of events (at $L_{int} = 3\,fb^{-1}$) in the whole ECAL η^{γ}-region $|\eta^{\gamma}| < 2.61$ for a given P_t^{γ} interval. We see that the number of events decreases fast with growing P_t^{γ} (by more than 50% for each subsequent interval). For the fixed P_t^{γ} interval the dependence on η^{γ} is given in lines of Table 8 and illustrated by Fig. 7.

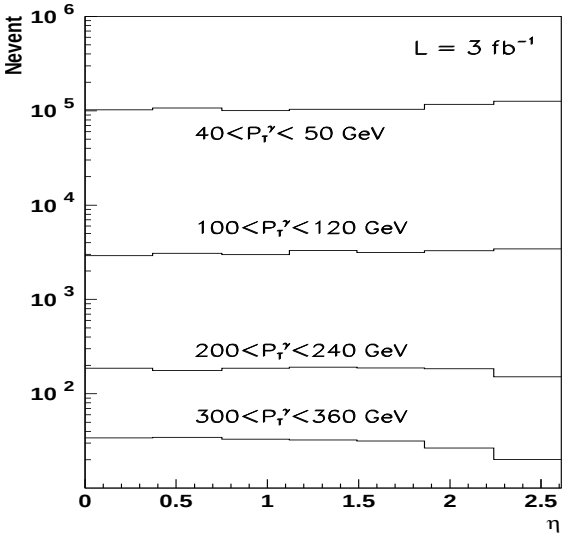

Fig. 7: η-dependence of rates for different P_t^{γ} intervals.

5.3 Estimation of "$\gamma + jet$" event rates for different calorimeter regions.

Since a jet is a wide-spread object, the η^{jet} dependence of rates for different P_t^{γ} intervals will be presented in a different way than in Section 5.2. Namely, Tables 9–12 include the rates of events

Table 8: Rates for $L_{int} = 3\ fb^{-1}$ for different ${P_t}^{\gamma}$ and η^{γ} intervals ($P_{tCUT}^{clust} = 5\,GeV/c$ and $\Delta\phi \leq 15°$).

P_t^{γ}	η^{γ} intervals							all η^{γ}
(GeV/c)	0.0-0.4	0.4-0.7	0.7-1.1	1.1-1.5	1.5-1.9	1.9-2.2	2.2-2.6	0.0-2.6
40 – 50	102656	107148	100668	103903	103499	116674	126546	761027
50 – 60	43905	41729	41074	45085	42974	47640	50310	312697
60 – 70	18153	18326	19190	20435	20816	19432	23650	140005
70 – 80	9848	10211	9963	10166	9951	11397	10447	71984
80 – 90	5287	5921	5104	5823	5385	6067	5923	39509
90 – 100	2899	3033	3033	3326	3119	3265	3558	22234
100 – 120	2908	3091	2995	3305	3133	3282	3429	22143
120 – 140	1336	1359	1189	1346	1326	1499	1471	9525
140 – 160	624	643	626	674	706	614	668	4555
160 – 200	561	469	557	555	519	555	557	3774
200 – 240	187	176	186	192	187	185	151	1264
240 – 300	103	98	98	98	100	92	74	665
300 – 360	34	34	33	32	31	27	20	212
40 – 360	188517	192274	184734	194957	191761	210742	226819	1389484

($L_{int} = 3\ fb^{-1}$) for different η^{jet} intervals, covered by the barrel, endcap and forward (HB, HE and HF) parts of the calorimeter and for different ${P_t}^{\gamma} (\approx {P_t}^{jet})$ intervals. The selection cuts are as those of Section 3.2 specified by the following values of the cut parameters:

$$P_{tCUT}^{isol} = 5\ GeV/c; \quad \epsilon_{CUT}^{\gamma} = 7\%; \quad \Delta\phi < 15°; \quad P_{tCUT}^{clust} = 5\ GeV/c. \tag{30}$$

No restrictions on other parameters are used. The first columns of these tables HB give the number of events with the jets (found by the LUCELL jetfinding algorithm of PYTHIA), all particles of which are comprised (at the particle level of simulation) entirely (100%) in the HB part and there is a 0% sharing of ${P_t}^{jet}$ (${\Delta P_t}^{jet} = 0$) between the HB and the neighboring HE part of the calorimeter. The second columns of the tables $HB + HE$ contain the number of events in which P_t of the jet is shared between the HB and HE regions. The same sequence of restriction conditions takes place in the next columns. Thus, the HE and HF columns include the number of events with jets entirely contained in these regions, while the $HE + HF$ column gives the number of events where the jet covers both the HE and HF regions. From these tables we can see what number of events can, in principle, most suitable for the precise jet energy absolute scale setting, carried out separately for the HB, HE and HF parts of the calorimeter in different ${P_t}^{\gamma}$ intervals.

Less restrictive conditions, when up to 10% of the jet P_t are allowed to be shared between the HB, HE and HF parts of the calorimeter, are given in Tables 10 and 12. Tables 9 and 10 correspond to the case of Selection 1. Tables 11 and 12 contain the number of events collected with Selection 2 criteria (defined in Section 3.2), i.e. they include only the events with "isolated jets" satisfying the isolation criterion $\epsilon^{jet} < 2\%$. A reduction factor of 4 for the number of events can be found by comparing those tables with Tables 9, 10. This is the cost of passing to Selection 2.

$Nevent_{(c)}$ and $Nevent_{(b)}$ (given for the integrated luminosity $L_{int} = 3\ fb^{-1}$) for different ${P_t}^{Jet} (\approx {P_t}^{\gamma})$ intervals $40-50, 100-120, 200-240$ and $300-360\ GeV/c$ are contained in Tables 1–12 of

Table 9 corresponds to the most restrictive selection $\Delta {P_t}^{jet} = 0$ and gives the number of events most suitable for jet energy calibration. From its last summarising line we see that for the entire interval $40 < {P_t}^{\gamma} < 360\ GeV/c$ PYTHIA predicts around half a million events for HB and a quarter of a million events for HE per month of continuous data taking at low LHC luminosity, while for HF the expected value is 75 000 events per month.

Table 9: Selection 1. $\Delta {P_t}^{jet} / {P_t}^{jet} = 0.00$

${P_t}^{\gamma}$	HB	HB+HE	HE	HE+HF	HF
40 – 50	260259	211356	141759	102299	45354
50 – 60	108827	89126	55975	41553	17216
60 – 70	49585	40076	25172	18153	7019
70 – 80	25506	20897	12881	9679	3021
80 – 90	14083	11720	7529	4873	1304
90 – 100	7261	7054	4142	2924	853
100 – 120	7703	6913	4013	2926	588
120 – 140	3372	2977	1805	1164	207
140 – 160	1650	1481	865	509	50
160 – 200	1493	1137	708	396	40
200 – 240	503	406	242	107	6
240 – 300	287	215	122	40	1
300 – 360	96	73	35	8	0
40 – 360	480538	393378	255266	184642	75660

Table 10: Selection 1. $\Delta {P_t}^{jet} / {P_t}^{jet} \leq 0.10$

${P_t}^{\gamma}$	HB	HB+HE	HE	HE+HF	HF
40 – 50	341043	55160	263629	26653	74534
50 – 60	144955	20396	108765	9300	29281
60 – 70	65525	8541	49412	3907	12621
70 – 80	34155	4093	25918	1957	5860
80 – 90	19224	1961	14741	804	2778
90 – 100	10258	1304	8394	536	1742
100 – 120	10859	1043	8357	545	1338
120 – 140	4618	509	3675	178	546
140 – 160	2325	222	1751	90	168
160 – 200	1971	147	1458	52	147
200 – 240	685	61	472	20	26
240 – 300	383	32	234	7	9
300 – 360	129	10	72	1	0
40 – 360	636418	93480	486788	44052	129050

One should keep in mind that the last columns in Tables 9–12 cannot be taken as the final result here because we have not defined the meaning of sharing ${P_t}^{jet}$ between the HF regions and the region with $|\eta| > 5$, i.e. close to a "beam-pipe" region. More accurate estimation can be done here by finding events with jets in a wider region than the HF volume restricted by $3 < |\eta^{HF}| < 5$ and by calculating the number of events in which jets are entirely contained in HF. An additional information on the number of "HB-events" (i.e. events, corresponding to HB column of Table 11) with jets produced by c and b quarks in gluonic subprocess (1a), i.e.

Table 11: Selection 2. $\Delta {P_t}^{jet}/{P_t}^{jet} = 0.00,\ \epsilon^{jet} < 2\%$.

${P_t}^{\gamma}$	HB	HB+HE	HE	HE+HF	HF
40 – 50	46972	32954	26114	16208	10041
50 – 60	23717	18911	13448	8367	5047
60 – 70	14384	9751	7469	4703	2386
70 – 80	8546	6733	4627	2960	1206
80 – 90	5653	4386	3107	1925	573
90 – 100	3326	3119	1900	1377	390
100 – 120	4157	3435	2271	1467	324
120 – 140	2183	1786	1185	710	134
140 – 160	1175	1005	635	362	31
160 – 200	1179	905	565	314	25
200 – 240	442	353	212	97	5
240 – 300	273	200	116	37	1
300 – 360	94	71	35	7	0
40 – 360	112111	83617	61686	38535	20163

Table 12: Selection 2. $\Delta {P_t}^{jet}/{P_t}^{jet} \leq 0.10,\ \epsilon^{jet} < 2\%$.

${P_t}^{\gamma}$	HB	HB+HE	HE	HE+HF	HF
40 – 50	60113	7986	45388	3909	14894
50 – 60	31495	3631	25134	1971	7259
60 – 70	18326	2248	13139	968	4011
70 – 80	11385	1243	8741	573	2132
80 – 90	7614	633	5957	292	1145
90 – 100	4544	536	3886	280	865
100 – 120	5771	481	4434	278	689
120 – 140	2909	272	2370	94	352
140 – 160	1648	138	1246	65	111
160 – 200	1560	113	1162	38	115
200 – 240	600	53	416	17	23
240 – 300	362	30	220	6	8
300 – 360	126	10	71	1	0
40 – 360	146468	17374	112177	8492	31603

Appendix 1 [19]. The ratio ("$29sub/all$") of the number of events caused by gluonic subprocess (1a) $(= 29sub)$, summed over quark flavours, to the number of events due to the sum of subprocesses (1a) and (1b) $(= all)$, also averaged over all quark flavours, is also shown there.

6. FEATURES OF "$\gamma + jet$" EVENTS IN THE CENTRAL CALORIMETER REGION.

The influence of P_{tCUT}^{clust} parameter (defining the upper limit on P_t of clusters or mini-jets in the event) on the variables characterizing the $P_t{}^{\gamma} - P_t{}^{Jet}$ balance as well as on the P_t distribution in jets and out of them is studied.

In this section we shall study the specific sample of events considered in the previous section that may be most suitable for the jet energy calibration in the HB region, with jets entirely (100%) contained in this region, i.e. having 0% sharing of $P_t{}^{jet}$ (at the PYTHIA particle level of simulation) with HE. *Below we shall call them "HB-events"*. The $P_t{}^{\gamma}$ spectrum for this particular set of events for $P_t^{clust} = 5\ GeV/c$ was presented in the second column (HB) of Table 9. Here we shall use three different jetfinders, namely, LUCELL from PYTHIA and UA1 and UA2 from CMSJET [19]. The P_t^{clust} distributions for generated events found by the all three jetfinders in two $P_t{}^{\gamma}$ intervals, $40 < P_t{}^{\gamma} < 50\ GeV/c$ and $300 < P_t{}^{\gamma} < 360\, GeV/c$, are shown in Fig. 8 for $P_{tCUT}^{clust} = 30\ GeV/c$. It is interesting to note an evident similarity of the P_t^{clust} spectra with $P_t 56$ spectra (for $\Delta\phi \leq 15°$) shown in Tables 2 and 3 (see also Figs. 9, 10), what support our intuitive picture of ISR and cluster connection described in Section 2.2.

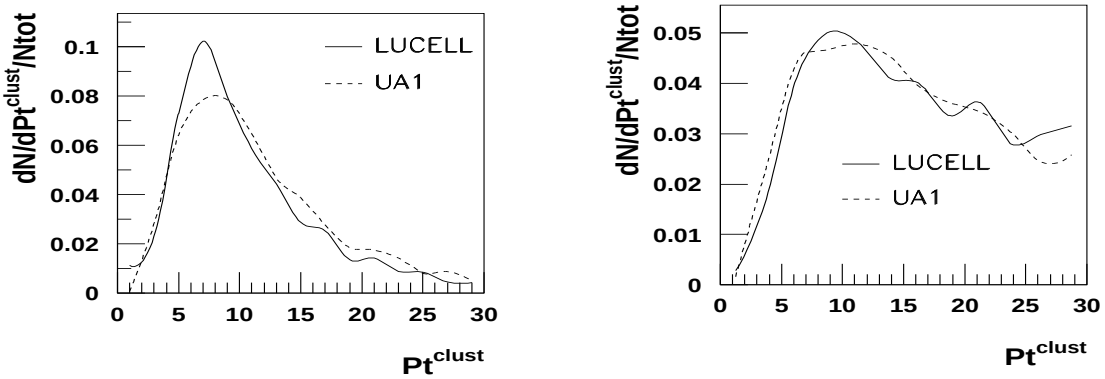

(a) (b)

Fig. 8: P_t^{clust} distribution in "$\gamma + jet$" events from two $P_t{}^{\gamma}$ intervals: (a) $40 < P_t{}^{\gamma} < 50\, GeV/c$ and (b) $300 < P_t{}^{\gamma} < 360\, GeV/c$ with the same cut $P_{tCUT}^{clust} = 30\ GeV/c$ ($\Delta\phi \leq 15°$).

6.1 Influence of the P_{tCUT}^{clust} parameter on the photon and jet P_t balance and on the initial state radiation suppression.

Here we shall study in more detail correlation of P_t^{clust} with P_t^{ISR} mentioned above. The averaged value of intrinsic parton transverse momentum will be fixed at $\langle k_t \rangle = 0.44\ GeV/c$ [20].

The banks of 1-jet "$\gamma + jet$" events gained from the results of PYTHIA generation of $5 \cdot 10^6$ signal "$\gamma + jet$" events in each of four $P_t{}^{\gamma}$ intervals (40 – 50, 100 – 120, 200 – 240, 300 – 360 GeV/c) [21] will be used here. The observables defined in Sections 3.1 and 3.2 will be restricted here by Selection 1 cuts (17) – (24) of Section 3.2 and the cut parameters defined by (29).

[19] Analogous estimations were done in [16, 54],[66]–[70].

[20] The influence of possible $\langle k_t \rangle$ variation on the $P_t{}^{\gamma} - P_t{}^{Jet}$ balance is discussed in Section 9. See also [11]–[15].

[21] they were discussed in Section 5

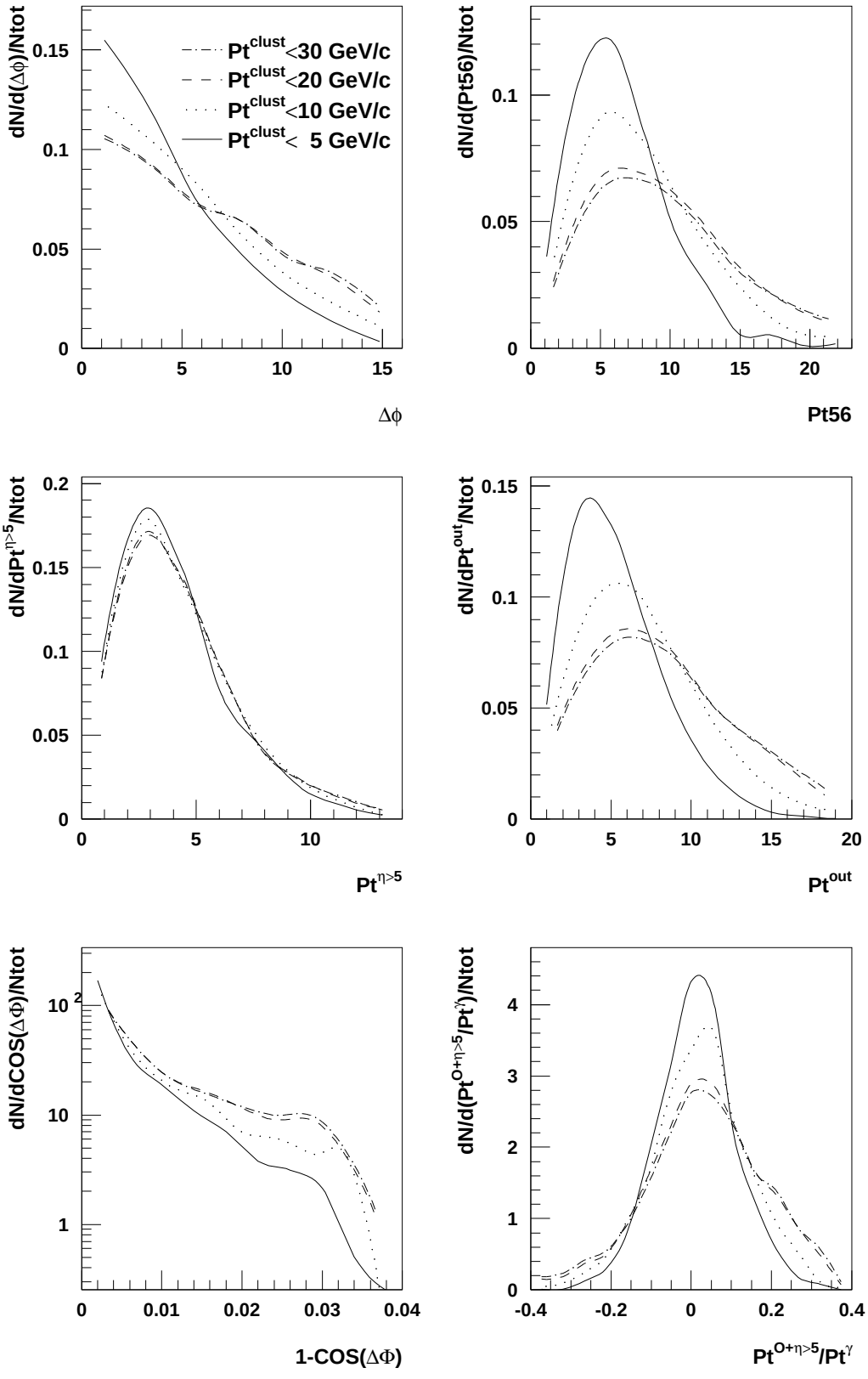

Fig. 9: LUCELL algorithm, $\Delta\phi < 15°$, $40 < P_t{}^{\gamma} < 50\,GeV/c$. Selection 1.

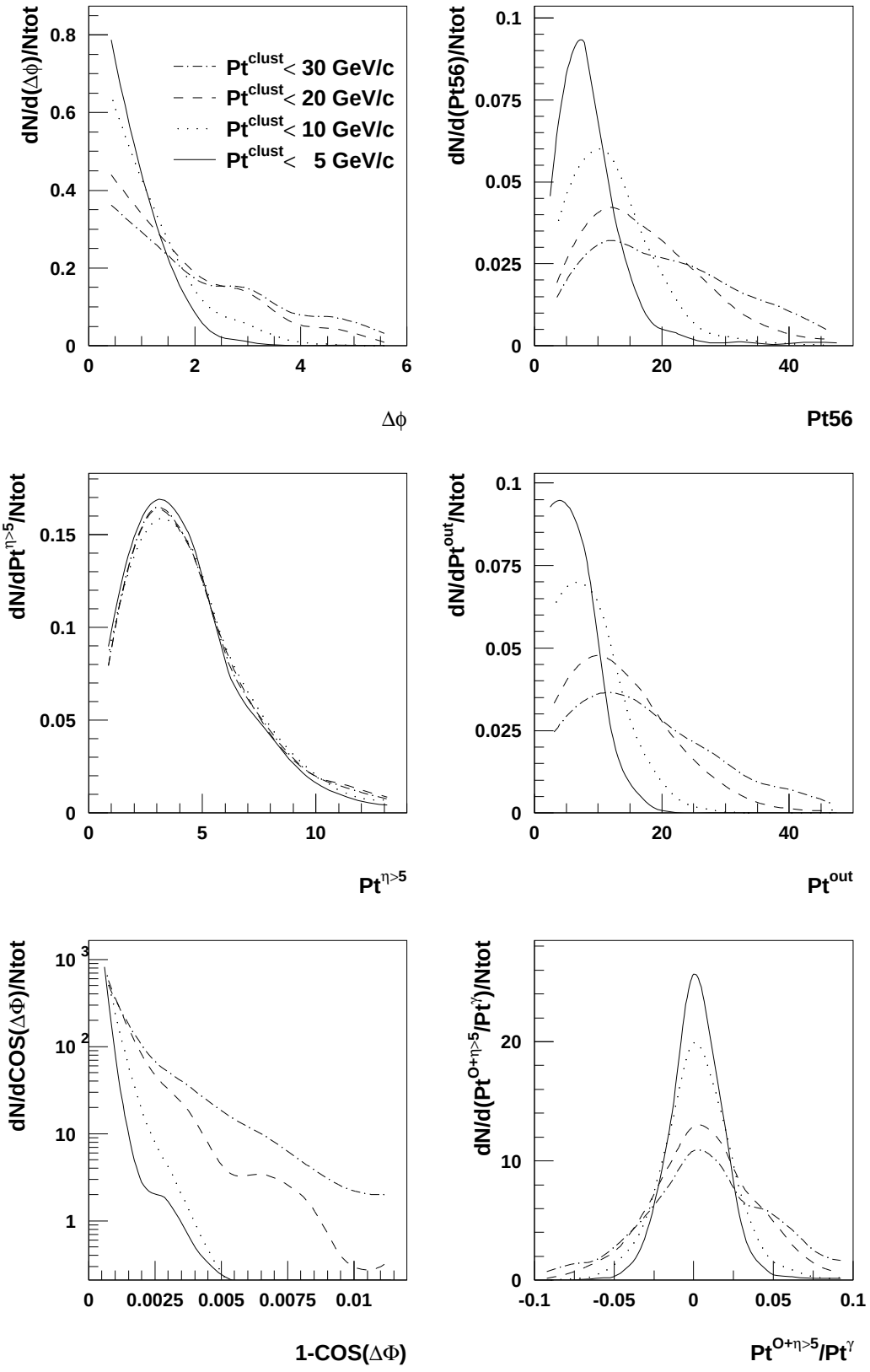

Fig. 10: LUCELL algorithm, $\Delta\phi < 15°$, $300 < P_t{}^{\gamma} < 360\, GeV/c$. Selection 1.

We have chosen from them two extreme ${P_t}^{\gamma}$ intervals to illustrate the influence of the P_{tCUT}^{clust} parameter on the distributions of physical variables, that enter the balance equation (28). These distributions are shown in Fig. 9 ($40 < {P_t}^{\gamma} < 50\,GeV/c$) and Fig. 10 ($300 < {P_t}^{\gamma} < 360\,GeV/c$).

In these figures, in addition to three variables P_t56, ${P_t}^{\eta>5.0}$, ${P_t}^{out}$, already explained in Sections 2.2, 3.1 and 3.2, we present distributions of two other variables, $P_t(O{+}\eta > 5.0)$ and $(1 - cos\Delta\phi)$, which define the right-hand side of equation (28). The distribution of the γ-jet back-to-back angle $\Delta\phi$ (see (22)) is also presented in Figs. 9 and 10.

The ISR describing variable P_t56 (defined by formula (3)) and both components of the experimentally observable disbalance measure $({P_t}^{\gamma}{-}{P_t}^{Jet})/{P_t}^{\gamma}$ (see (28)) as a sum of $(1{-}cos\Delta\phi)$ and $P_t(O{+}\eta > 5.0)/{P_t}^{\gamma}$, as well as two others, ${P_t}^{out}$ and $\Delta\phi$, show a tendency, to become smaller (the mean values and the widths) with the restriction of the upper limit on the ${P_t}^{clust}$ value (see Figs. 9, 10). It means that the jet energy calibration precision may increase with decreasing P_{tCUT}^{clust}, which justifies the intuitive choice of this new variable in Section 3. The origin of this improvement becomes clear from the P_t56 density plot, which demonstrates the decrease of P_t56 (or ${P_t}^{ISR}$) values with decrease of P_{tCUT}^{clust}.

Comparison of Fig. 9 (for $40 < {P_t}^{\gamma} < 50\,GeV/c$) and Fig. 10 (for $300 < {P_t}^{\gamma} < 360\,GeV/c$) also shows that the values of $\Delta\phi$ as a degree of back-to-backness of the photon and jet P_t vectors in the ϕ-plane decreases with increasing ${P_t}^{\gamma}$. At the same time ${P_t}^{out}$ and ${P_t}^{ISR}(= P_t56)$ distributions become slightly wider. It is also seen that the ${P_t}^{\eta>5.0}$ distribution practically does not depend on ${P_t}^{\gamma}$ and ${P_t}^{clust}$ [22].

It should be mentioned that the results presented in Figs. 9 and 10 were obtained with the LUCELL jetfinder of PYTHIA [23].

6.2 Jetfinders and the P_t structure of jets in the $\eta - \phi$ space.

In order to understand well the calibration procedure of "$\gamma + jet$" events, it is useful to keep control over some principal characteristics of internal jet structure as well as over the size of P_t activity in the space around jets.

Let us define the coordinates of jet center of gravity in the $\eta - \phi$ space (according to the PYTHIA's LUCELL subroutine definitions):

$$\eta_{gc} = \left(\sum_{i=1}^{NC} \eta_i {P_t}^i\right) / \left(\sum_{i=1}^{NC} {P_t}^i\right); \quad \phi_{gc} = \left(\sum_{i=1}^{NC} \phi_i {P_t}^i\right) / \left(\sum_{i=1}^{NC} {P_t}^i\right) \tag{31}$$

The sum in formulae (31) runs over jet cells whose total number is denoted by NC.

The left-hand columns of Figs. 11 and 12 present distributions over a distance, denoted as $R_{gc}^{jet}(\eta,\phi)$, between the center of a most remote (mr) cell of the jet and the jet center of gravity (η_{gc}, ϕ_{gc}) in HB-events for the intervals $40 < {P_t}^{\gamma} < 50\,GeV/c$ and $300 < {P_t}^{\gamma} < 360\,GeV/c$ respectively, i.e.

$$R_{gc}^{jet}(\eta,\phi) = ((\eta_{mr} - \eta_{gc})^2 + (\phi_{mr} - \phi_{gc})^2)^{1/2}, \tag{32}$$

where (η_{mr}, ϕ_{mr}) are the coordinates of the center of most remote cell of the jet.

We choose according to Section 3.2 the jet radius counted from the initiator cell (ic) to be restricted by $R_{ic}^{jet} = 0.7$ for the LUCELL and UA1 jetfinders while its value is not limitted for UA2 algorithm.

[22] see also Appendices 2–5

[23] The results obtained with all jetfinders and ${P_t}^{\gamma} - {P_t}^{Jet}$ balance will be discussed in Section 7 in more detail.

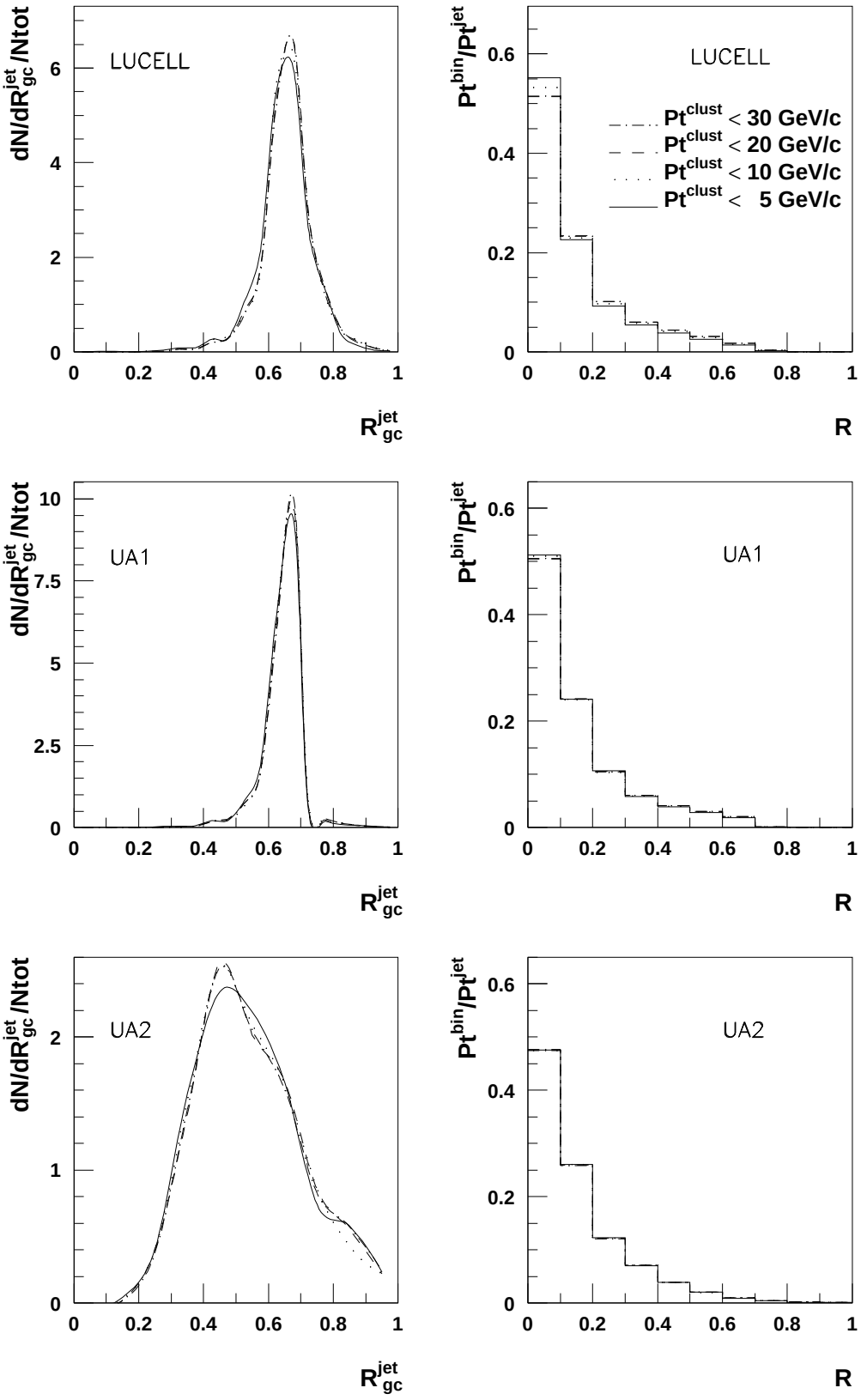

Fig. 11: LUCELL, UA1 and UA2 algorithms, $\Delta\phi < 15°$, $40 < P_t{}^{\gamma} < 50\,GeV/c$. Selection 1.

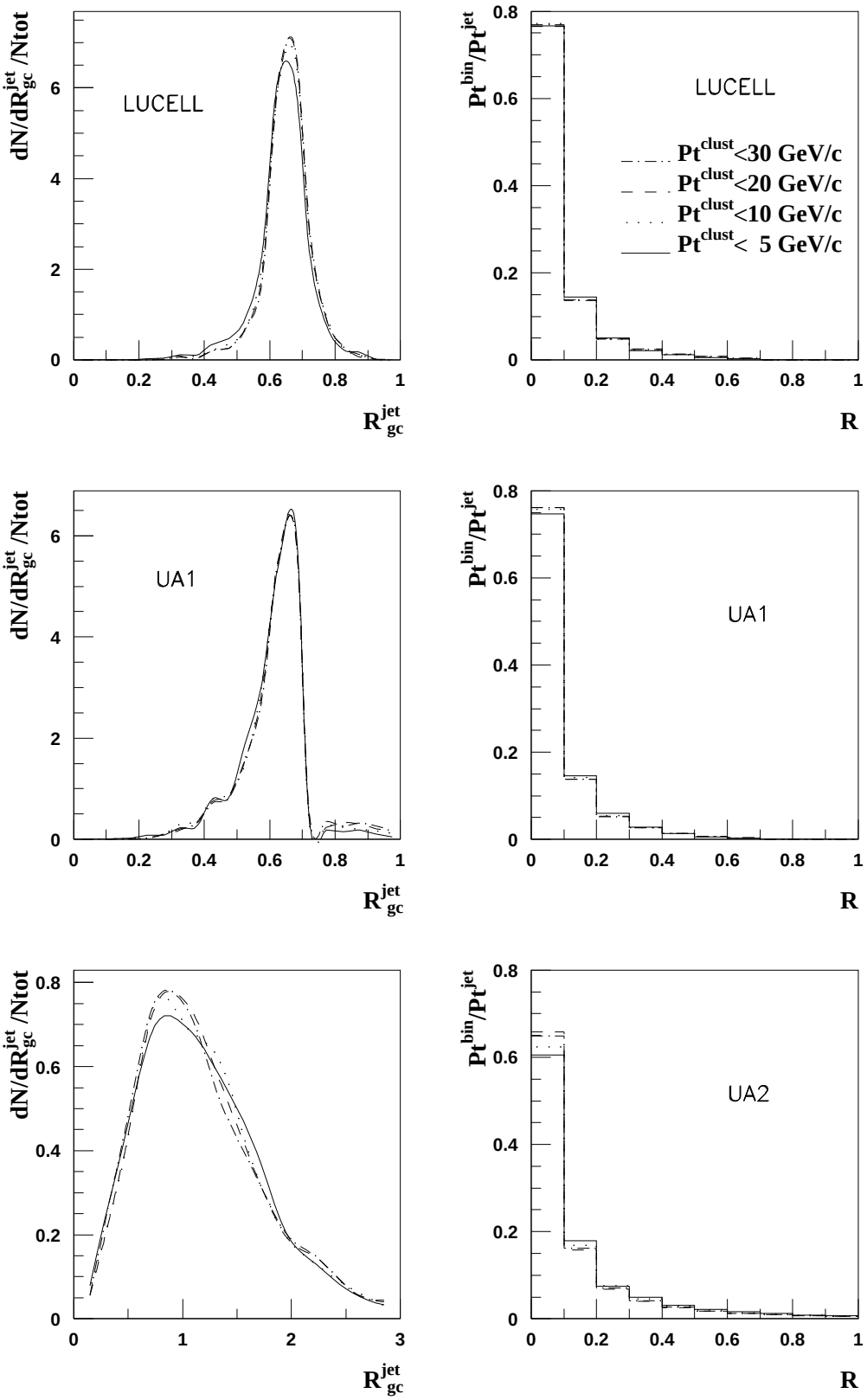

Fig. 12: LUCELL, UA1 and UA2 algorithms, $\Delta\phi < 15°$, $300 < P_t{}^{\gamma} < 360\, GeV/c$. Selection 1.

From the left-hand side plots in Figs. 11 and 12 we see that UA1 and LUCELL jetfinders give close R_{gc}^{jet} distributions.

The detailed information about the averaged jet radii for four ${P_t}^{\gamma}$ intervals is presented in the tables of Appendix 1 [24].

Now let us consider how the transverse momentum is distributed inside a jet. Let us divide the jet radius $R^{jet}(\eta,\phi) \equiv R$ into a set of ΔR bins and calculate the vector sums of cells P_t in each ΔR_{bin} ring. Normalized to ${P_t}^{Jet}$, the modulus of this vector sum, denoted by ${P_t}^{bin}$, would give the value that tells us what portion of a total ${P_t}^{Jet}$ is contained in the ring of size ΔR_{bin}. Its variation with the distance R counted from the center of gravity of the jet is shown in the right-hand columns of Figs. 11 and 12.

From these figures we can conclude that the LUCELL, UA1 and UA2 jetfinders irrespective of their internal ways of jet radius calculations, lead to more or less similar structure of P_t density in the central part inside a jet.

6.3 P_t distribution inside and outside of a jet.

Now let us see how the volume outside the jet, (i.e. calorimeter cells outside the jet cone) may be populated by P_t in these HB "$\gamma + jet$" events. For this purpose we calculate a vector sum $\vec{P}_t^{\,sum}$ of individual transverse momenta of $\Delta\eta \times \Delta\phi$ cells included by a jetfinder into a jet and of cells in a larger volume that surrounds a jet. In the latter case this procedure can be viewed as straightforward enlarging of the jet radius in the $\eta - \phi$ space. The figures that show the ratio ${P_t}^{sum}/{P_t}^{\gamma}$ as a function of the distance $R(\eta,\phi)$ counted from the jet gravity center towards its boundary and further into space outside the jet are shown in the left-hand columns of Figs. 13 and 14 for two different ${P_t}^{\gamma}$ intervals ($40 < {P_t}^{\gamma} < 50\ GeV/c$ in Fig. 13 and the $300 < {P_t}^{\gamma} < 360\ GeV/c$ in Fig. 14 intervals) in the case when all jet particles are kept in the jet.

From these figures we see that the space surrounding the jet is in general far from being an empty in the case of "$\gamma + jet$" events considered here. We also see that an average value of the total ${P_t}^{sum}$ increases with increasing volume around the jet and it exceeds ${P_t}^{\gamma}$ at $R = 0.7 - 0.8$ when all particles are included in the jet (see Figs. 13 and 14).

From the right-hand columns of Figs. 13 and 14 we see that when all particles are included in the jet, the disbalance measure (the analog of (4))

$$ {P_t}^{\gamma+sum} = \left|\vec{P}_t^{\,\gamma} + \vec{P}_t^{\,sum}\right| \tag{33} $$

achieves its minimum at $R \approx 0.7 - 0.8$ for all three jetfinding algorithms [25].

The value of ${P_t}^{\gamma+sum}$ continues to grow rapidly with increasing R after the point $R = 0.7 - 0.8$ for $40 < {P_t}^{\gamma} < 50\ GeV/c$ (see Figs. 13, 15), while for higher ${P_t}^{\gamma}$ (see Figs. 14, 16 for the $300 < {P_t}^{\gamma} < 360\ GeV/c$ interval) the ratio ${P_t}^{sum}/{P_t}^{\gamma}$ and the disbalance measure ${P_t}^{\gamma+sum}$ increase more slowly with increasing R after the point $R = 0.7 - 0.8$. This means that at higher ${P_t}^{\gamma}$ (or ${P_t}^{Jet}$) the topology of "$\gamma + jet$" events becomes more pronounced and we get a clearer picture of an "isolated" jet. This feature clarifies the motivation of introducing by us the "Selection 2" criteria in Section 3.2 (see point 9) for selection of events with "isolated jets".

[24] They show weak dependence of the jet radius on ${P_t}^{Jet} (\approx {P_t}^{\gamma})$ for all algorithms.

[25] This value is denoted as "${P_t}^{\gamma} + {P_t}^{sum}$" in Figs. 13–16.

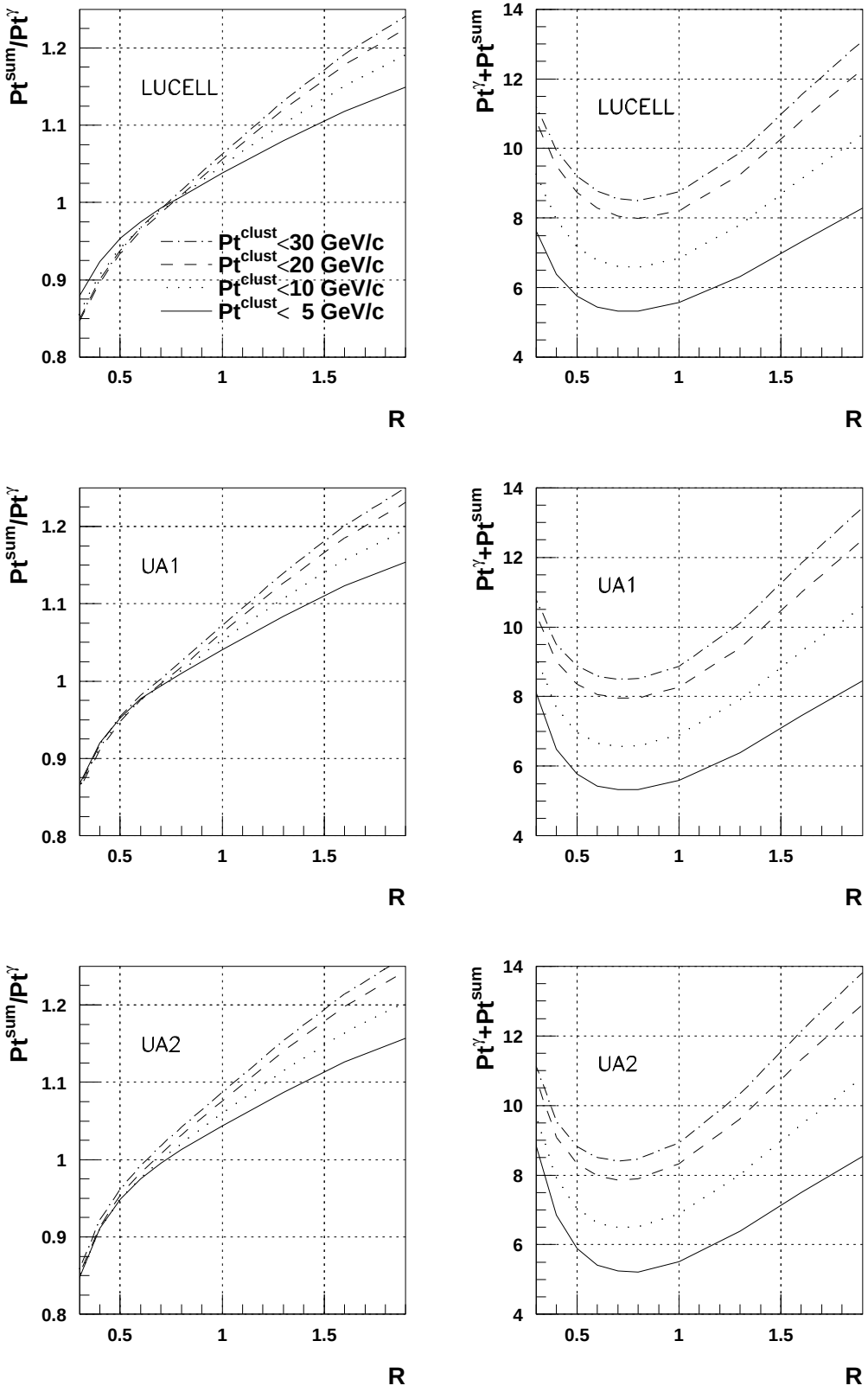

Fig. 13: LUCELL, UA1 and UA2 algorithms, $\Delta\phi < 15°$, $40 < P_t{}^{\gamma} < 50\,GeV/c$ (without account of magnetic field effect).

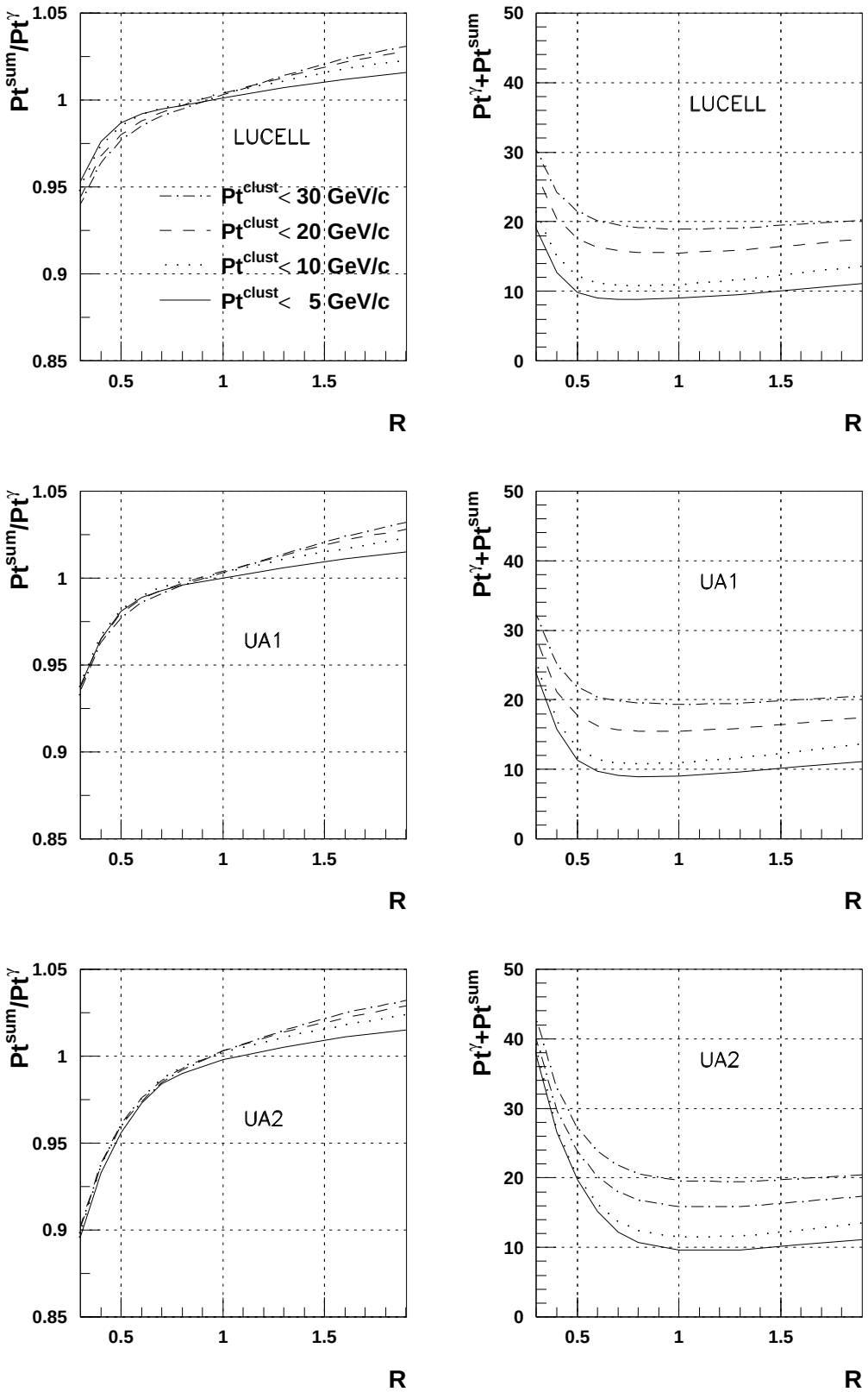

Fig. 14: LUCELL, UA1 and UA2 algorithms, $\Delta\phi < 15°$, $300 < P_t{}^{\gamma} < 360\,GeV/c$ (without account of magnetic field effect).

7. DEPENDENCE OF THE P_t-DISBALANCE IN THE "$\gamma + jet$" SYSTEM ON P_{tCUT}^{clust} and P_{tCUT}^{out} PARAMETERS.

It is shown that with Selection 2 one can collect (at the particle level) a sufficient number of events with the value of a fractional $(P_t{}^{\gamma}–P_t{}^{Jet})/P_t{}^{\gamma}$ disbalance better than 1%. The number of events (at $L_{int} = 3\ fb^{-1}$) together with other characteristics of "$\gamma + jet$" events are presented in tables of Appendices 2–5 for interval $40 < P_t{}^{\gamma} < 360\ GeV/c$. They show a possibility to define jet energy scale at low luminosity in few months.

In the previous sections we have introduced physical variables for studying "$\gamma + jet$" events (Section 3) and discussed what cuts for them may lead to a decrease in the disbalance of $P_t{}^{\gamma}$ and $P_t{}^{Jet}$ (Sections 5, 6). One can make these cuts to be tighter if more events would be collected during data taking.

Here we shall study in detail the dependence of the P_t disbalance in the "$\gamma + jet$" system on P_{tCUT}^{clust} and P_{tCUT}^{out} values. For this aim we shall use the same samples of events as in Section 5 that were generated by using PYTHIA with 2 QCD subprocesses (1a) and (1b) and collected to cover four $P_t{}^{\gamma}$ intervals: $40-50, 100-120, 200-240, 300-360\ GeV/c$. These events were selected with

$$P_t{}^{\gamma} \geq 40\ GeV/c, \quad P_t{}^{jet} \geq 30\ GeV/c \tag{34}$$

and with the use of the set of cut parameters defined by (29).

The dependence of the number of events that can be gained with Selection 1 and the above-mentioned set of cut parameters on the value of P_{tCUT}^{clust} is shown for the case of $\Delta\phi \leq 15^{\circ}$ and for four $P_t{}^{\gamma}$ intervals in Fig. 16 and in Fig. 18 for Selection 2 and in Fig. 20 for Selection 3. Each of these plots is accompanied at the same page by four additional plots (Figs. 17,19,21) that show the dependence of the fractional disbalance $(P_t{}^{\gamma}–P_t{}^{Jet})/P_t{}^{\gamma}$ on P_{tCUT}^{clust} in different $P_t{}^{\gamma}$ intervals. The dependence of this ratio is presented for three different jetfinders LUCEL, UA1 and UA2 used to determine a jet in the same event. It is worth mentioning that in contrast to UA1 and LUCELL algorithms that use a fixed value of jet radius $R^{jet}(=0.7)$, the value of R^{jet} is not restricted directly for UA2 [26] and, thus, it may take different values (see [12] and R values in Appendices 1). The differences in the results of these three jetfinders application were discussed in Section 6.2 and in [18] (see also Appendices 1–5).

The normalized event distributions over $(P_t{}^{\gamma} - P_t{}^{Jet})/P_t{}^{\gamma}$ for two most illustrative $P_t{}^{\gamma}$ intervals $40 < P_t{}^{\gamma} < 50$ and $300 < P_t{}^{\gamma} < 360\ GeV/c$ are shown for a case of $\Delta\phi \leq 15^{\circ}$ in Fig. 15 in different plots for three jetfinders. These plots demonstrate the dependence of the mean square deviations on P_{tCUT}^{clust} value, not shown in Fig. 17. From the comparison of Figs. 17, 19 and 21 (see also Appendices 2–5) one can easily see that passing from Selection 1 to Selection 2 and 3 allows to select events with a better balance of $P_t{}^{\gamma}$ and $P_t{}^{Jet}$ (about 1% and better) on the PYTHIA particle level. It is also seen that in events with "isolated jets" there is no such a strong dependence on P_{tCUT}^{clust} value in the events with $P_t{}^{\gamma} > 100\ GeV/c$.

More details on P_{tCUT}^{clust} dependence of different important features of "$\gamma + jet$" events (as predicted by PYTHIA. i.e. without account of detector effects) are presented in tables of Appendices 2 – 5. They include the information about a topology of events and mean values of most important variables that characterize $P_t{}^{\gamma} - P_t{}^{Jet}$ disbalance [27]. This information can be

[26] The only radii defining in UA2 algorithm are cone radius for preclusters search ($= 0.4$) and cone radius for subsequent precluster dressing ($= 0.3$) (see [19]).

[27] Please note that the information about averaged values of jet radius as well as $P_t{}^{miss}$ and non-detectable content of a jet is included in the tables of Appendix 1 for the same $P_t{}^{\gamma}$ intervals.

useful as a model guideline while performing jet energy calibration procedure and also serve for fine tuning of PYTHIA paramters while comparing its predictions with the collected data.

Appendix 2 contains the tables for events with ${P_t}^{\gamma}$ varying from 40 to $50\ GeV/c$. In these tables we present the values of interest found with the UA1, UA2 and LUCELL jetfinders [28] for three different Selections mentioned in Section 3.2. Each page corresponds to a definite value of $\Delta\phi$ (see (22)) as a measure of deviation from the absolute back-to-back orientation of two $\vec{P}_t^{\,\gamma}$ and $\vec{P}_t^{\,Jet}$ vectors.

So, Tables 1 – 3 on the first page of each of Appendices 2–5 correspond to $\Delta\phi < 180°$, i.e. to the case when no restriction on the back-to-back $\Delta\phi$ angle is applied. Tables 4–6 on the second page correspond to $\Delta\phi < 15°$. The third and fourth pages correspond to $\Delta\phi < 10°$ and $\Delta\phi < 5°$ respectively.

The first four pages of each Appendix contain information about variables that characterize the ${P_t}^{\gamma}$ – ${P_t}^{Jet}$ balance for Selection 1, i.e. when only cuts (17)–(24) of Section 3.2 are used.

On the fifth page of each of Appendices 2–5 we present Tables 13–15 that correspond to Selection 2 described in Section 3.2 for the cut $\Delta\phi < 15°$. Selection 2 differs from Selection 1 presented in Tables 1 – 12 by addition of cut (25). It allows one to select events with the "isolated jet", i.e. events with the total P_t activity in the $\Delta R = 0.3$ ring around the jet not exceeding $3-8\%$ of jet P_t. We have limited $\epsilon^{jet} \leq 8\%$ for $40 < {P_t}^{\gamma} < 50$ with a gradual change to $\epsilon^{jet} \leq 3\%$ for ${P_t}^{\gamma} \geq 200\ GeV/c$. The best result for UA2 in the case of $40 < {P_t}^{\gamma} < 50$ is obtained with a stricter cut $\epsilon^{jet} \leq 6\%$ (as its radius is larger) instead of the cut $\epsilon^{jet} \leq 8\%$ chosen for UA1 and LUCELL algorithms [29]. The results obtained with Selection 3 [30] are given on the sixth page of Appendices 2–5.

The columns in Tables 1 – 18 correspond to five different values $P_{tCUT}^{clust} = 30,\ 20,\ 15, 10$ and $5\ GeV/c$. The upper lines of Tables 1 – 15 in Appendices 2–5 contain the expected numbers N_{event} of "HB events" (i.e. "$\gamma + jet$" events in which the jet is entirely fitted (at the particle level!) into the barrel region of the HCAL; see Section 5)) for the integrated luminosity $L_{int} = 3\ fb^{-1}$.

In the next four lines of the tables we put the values of $P_t 56$, $\Delta\phi$, ${P_t}^{out}$ and ${P_t}^{|\eta|>5.0}$ defined by formulae (3), (22), (24) and (5) respectively and averaged over the events selected with a chosen P_{tCUT}^{clust} value.

From the tables we see that the values of $P_t 56$, $\Delta\phi$, ${P_t}^{out}$ decrease fast with decreasing P_{tCUT}^{clust}, while the averaged values of ${P_t}^{|\eta|>5.0}$ show very weak dependence on it (practically constant) [31].

The following three lines (from 6-th to 8-th) present the average values of the variables $({P_t}^{\gamma} - {P_t}^{part})/{P_t}^{\gamma}$, $({P_t}^{J} - {P_t}^{part})/{P_t}^{J}$, $({P_t}^{\gamma} - {P_t}^{J})/{P_t}^{\gamma}$ (here J≡Jet), the first and the third of which serve as the measures of the P_t disbalance in the "$\gamma + parton$" and "$\gamma + Jet$" systems while the second one has a meaning of the measure of the parton-to-hadrons (Jet) fragmentation effect.

The 9-th and 10-th lines include the averaged values of $P_t(O+\eta > 5.0)/{P_t}^{\gamma}$ and $(1 - cos(\Delta\phi))$ quantities that appear on the right-hand side of equation (28), a scalar variant of vector equation (16) for the total transverse momentum conservation in a physical event.

The value of $\langle 1 - cos(\Delta\phi)\rangle$ is smaller than the value of $\langle P_t(O+\eta > 5.0)/{P_t}^{\gamma}\rangle$ in the case

[28] the first two are taken from CMSJET fast Monte Carlo program [19]

[29] In [11] – [15] the Selection 2 criterion was considered with a more severe cut $\epsilon^{jet} \leq 2\%$.

[30] Selection 3 (see Section 3.2, point 10) leaves only those events in which jets are found simultaneously by UA1, UA2 and LUCELL jetfinders i.e. events with jets having up to a good accuracy equal coordinates of the center of gravity, ${P_t}^{jet}$ and $\phi_{(\gamma,\ jet)}$.

[31] Compare also with Figs. 9 and 10.

of Selection 1 with the cut $\Delta\phi < 15^\circ$ and tends to decrease faster with growing energy (compare Figs. 9 and 10). So, we can conclude that the main contribution into the P_t disbalance in the "$\gamma + jet$" system, as defined by equation (28), in the case of Selection 1 comes from the term $P_t(O+\eta > 5.0)/{P_t}^\gamma$, while in Selections 2 and 3 the contribution of $\langle P_t(O+\eta > 5.0)/{P_t}^\gamma\rangle$ reduces with growing ${P_t}^{clust}$ to the level of that of $\langle 1 - cos(\Delta\phi)\rangle$ and even to smaller values.

We have estimated separately the contributuions of these two terms $\vec{P_t}^{\,O} \cdot \vec{n}^{Jet}$ and $\vec{P_t}^{\,|\eta|>5.0} \cdot \vec{n}^{Jet}$ (with $\vec{n}^{Jet} = \vec{P_t}^{\,Jet}/{P_t}^{Jet}$, see (28)) that enter $P_t(O+\eta > 5.0)$. Firstly from tables it is easily seen that ${P_t}^{|\eta|>5.0}$ has practically the same value in all ${P_t}^\gamma$ intervals and it does not depend neither on $\Delta\phi$ nor on ${P_t}^{clust}$ values being equal approximately to $5\ GeV/c$. At the same time the contribution of its projection $\vec{P_t}^{\,|\eta|>5.0} \cdot \vec{n}^{Jet}$ shows a dependence on ${P_t}^{clust}$, $\Delta\phi$ and ${P_t}^\gamma$ (being of order of $\approx 0.1 - 0.2\ GeV/c$ for ${P_t}^{clust} < 20\ GeV/c$ and $\Delta\phi < 15^\circ$). The value of the fraction $\vec{P_t}^{\,|\eta|>5.0} \cdot \vec{n}^{Jet}/{P_t}^\gamma$ for $P_{tCUT}^{clust} = 10\ GeV/c$ and $\Delta\phi < 15^\circ$ is 0.006 at $40 < {P_t}^\gamma < 50\ GeV/c$ and decreases to 0.002 at $100 < {P_t}^\gamma < 120\ GeV/c$. Among these two terms the first one, $\vec{P_t}^{\,O} \cdot \vec{n}^{Jet}$, is a measurable one (its value can be found from the numbers in lines with $P_t(O+\eta > 5.0)$). Below in this section the cuts on the value of ${P_t}^{out}$ is applied to select events with better ${P_t}^\gamma$ and ${P_t}^{Jet}$ balance. Let us emphasize that it is a prediction of PYTHIA. The second term may be reduced in the experiment by imposing a cut on ${P_t}^{miss}$ (see corresponding spectra in Figs. 5, 6 of Section 4) as ${P_t}^{|\eta|>5.0}$ is a part of it.

The following two lines contain the averaged values of the standard deviations $\sigma(Db[\gamma, J])$ and $\sigma(Db[\gamma, part])$ of $({P_t}^\gamma - {P_t}^J)/{P_t}^\gamma (\equiv Db[\gamma, J])$ and $({P_t}^\gamma - {P_t}^{part})/{P_t}^\gamma (\equiv Db[\gamma, part])$ respectively. These two variables drop as one goes from ${P_t}^{clust} = 30\ GeV/c$ to ${P_t}^{clust} = 5\ GeV/c$ for all ${P_t}^\gamma$ intervals and for all jetfinding algorithms.

The last lines of the tables present the number of generated events (i.e. entries) left after cuts.

Two features are clearly seen from these tables:

(1) *parton-photon* fractional disbalance $({P_t}^\gamma - {P_t}^{part})/{P_t}^\gamma$ in events, being averaged over number of events selected with $P_{tCUT}^{clust} = 20\ GeV/c$ and $\Delta\phi < 15^\circ$, does not exceed 1% and it has mainly positive sign in Selection 1;

(2) *parton-to-jet* hadronization/fragmentation effect $({P_t}^J - {P_t}^{part})/{P_t}^J$. (that includes partially also FSR) can be. It always has a negative value. It means that a jet does not receive some part of the parent parton transverse momentum ${P_t}^{part}$. It is seen that in the case of Selection 1 this effect gives a larger contribution into ${P_t}^\gamma$ and ${P_t}^{Jet}$ disbalance than the contribution from *parton-photon* disbalance even after application of $P_{tCUT}^{clust} = 10\ GeV/c$.

(3) due to different signs these two effects partially compensate each other.

In a case of Selection 1 we see from Appendices 3–5 that for ${P_t}^\gamma > 50 GeV/c$ the decrease in P_{tCUT}^{clust} leads also to a decrease in the $({P_t}^\gamma - {P_t}^J)/{P_t}^\gamma$ ratio, i.e. we select the events that can be lead to more precise level of jet energy calibration accuracy. For instance, in the case of $100 < {P_t}^\gamma < 120\ GeV/c$ the mean value of $({P_t}^\gamma - {P_t}^J)/{P_t}^\gamma$ drops from $4.3-4.5\%$ to $1.0-1.8\%$ (see Tables 4 – 6 of Appendix 3 and Figs. 16, 17) and in the case of $200 < {P_t}^\gamma < 240\ GeV/c$ the mean value of this variable drops from $1.5 - 1.6\%$ to less than $0.5 - 0.8\%$ (see Tables 4 – 6 of Appendix 4). A worse situation is seen for the $40 < {P_t}^\gamma < 50\ GeV/c$ interval, where the disbalance changes, i.e. for LUCELL algorithm, as $2.9 \rightarrow 2.5\%$ unless to we pass to stricter Selection 2. At the same time a reduction of ${P_t}^{clust}$ leads to a reduction of $Db[\gamma, J]$. Fig. 15 serves for accumulation and illustration of the information about the ${P_t}^\gamma - {P_t}^{Jet}$ disbalnce variation with P_{tCUT}^{clust}.

After imposing the jet isolation requirement (see Tables 13–15 of Appendices 2–5) we observe that starting with $P_t^{\gamma} = 100\ GeV/c$ the mean values of P_t^{γ} and P_t^{Jet} disbalance, i.e. $(P_t^{\gamma} - P_t^{J})/P_t^{\gamma}$, are contained inside the 1% window (at particle level) for any P_t^{clust}. In the $40 < P_t^{\gamma} < 50\ GeV/c$ interval, where we have enough events even after passing to Selection 2, we see that P_{tCUT}^{clust} works more effectively [32]. Thus, $P_{tCUT}^{clust} = 20\ GeV/c$ allows $(P_t^{\gamma} - P_t^{J})/P_t^{\gamma}$ to be reduced to less than 1.5% while a stricter cut $P_{tCUT}^{clust} = 10\ GeV/c$ makes it less than 1%. The Selection 2 criterion (by $P_{tCUT}^{clust} = 10\ GeV/c$ for instance) leaves quite a sufficient number of events: about 350–750 thousand for different jetfinders (the lower value correspond to UA2 algorithm) for the $40 < P_t^{\gamma} < 50\ GeV/c$ interval and about 25 thousand for the $100 < P_t^{\gamma} < 120\ GeV/c$ interval (see Tables 13 – 15 of Appendices 2, 3 and Figs. 18, 19) at $L_{int} = 3\ fb^{-1}$.

Thus, to summarize the results presented in tables of Appendices 2–5, we want to underline that:
(I) for all Selections the reduction of P_{tCUT}^{clust} leads to lower values of mean square deviations of the photon-parton $Db[\gamma, part]$ and of photon-jet $Db[\gamma, J]$ balances;
(II) after imposing the jet isolation requirement (see Tables 13–15 of Appendices 2–5) the mean values of P_t^{γ} and P_t^{Jet} disbalance, i.e. $(P_t^{\gamma} - P_t^{J})/P_t^{\gamma}$, for all P_t^{γ} intervals are contained inside the 1% window for any $P_t^{clust} \leq 10\ GeV/c$.

The Selection 2 (with $P_{tCUT}^{clust} = 10\ GeV/c$, for instance) leaves after its application the following number of events with jets *entirely contained* (see Section 5) *in the HB region* (at $L_{int} = 3\ fb^{-1}$) :
(1) about 350 000 – 750 000 for $40 < P_t^{\gamma} < 50\ GeV/c$,
(2) about 25 000 for $100 < P_t^{\gamma} < 120\ GeV/c$,
(3) about 2000 for $200 < P_t^{\gamma} < 240\ GeV/c$ and
(4) about 500 for the $300 < P_t^{\gamma} < 360\ GeV/c$.

For intervals with $P_t^{\gamma} \geq 100\ GeV/c$ these numbers can be three times higher even with larger values of P_{tCUT}^{clust}.

The analogous results for Selection 3 are presented in Tables 16–18 of Appendices 2–5. Let us consider first the most difficult interval $40 < P_t^{\gamma} < 50\ GeV/c$. From the tables of Appendix 2 one can see that this selection leads to approximately 30% further reduction of the number of selected events as compared with Selection 2. A combined usage of all three jetfinders in this P_t^{γ} interval (Tables 16–18) does not improve the balance values. A requirement of simultaneous jet finding by two of them, namely UA1 and LUCELL algorithms (that use fixed value of $R^{jet} = 0.7$), gives values of the $(P_t^{\gamma} - P_t^{Jet})/P_t^{\gamma}$ balance and other variables, presented in Tables 19, 20, close to the case of Selection 2 and leads to a better result (from point of view of the $(P_t^{\gamma} - P_t^{Jet})/P_t^{\gamma}$ balance values as well as from point of view of the number of selected events) as compared with the case of combined usage of all three jetfinders for this aim (compare also plots A and B in Fig. 21). This fact stresses a good compatibility of UA1 and LUCELL jetfinders. For other high P_t^{γ} intervals considered here the UA1, UA2 and LUCELL algorithms give more or less close results.

Let us mention that Selections 2 and 3, besides improving the $P_t^{\gamma} - P_t^{Jet}$ balance value, are also important for selecting events with a clean jet topology and for rising the confidence level of a jet determination and events selection.

Up to now we have been studying the influence of the P_{tCUT}^{clust} parameter on the balance. Let

[32] The same is true for Selection 3, see [11] – [15]. In those papers the Selection 2 criterion was considered for a more severe cut $\epsilon^{jet} = 2\%$.

us see, in analogy with Fig. 15, what effect is produced by P_{tCUT}^{out} variation [33]. If we vary this variable from 30 to 5 GeV/c, keeping ${P_t}^{clust}$ slightly restricted by $P_{tCUT}^{clust} = 30\,GeV/c$ (practically unbound), then, as can be seen from Fig. 22, the mean and RMS values of the disbalance $({P_t}^{\gamma} - Pt^J)/{P_t}^{\gamma}$ measure in the case of the LUCELL algorithm for $40 < {P_t}^{\gamma} < 50\,GeV/c$ decrease as follows: mean from 3.7% to 1.0% and RMS from 16.8% to 9.6%. For $300 < {P_t}^{\gamma} < 360\,GeV/c$ practically for all events the mean and RMS values of $({P_t}^{\gamma} - {P_t}^J)/{P_t}^{\gamma}$ turn out to be less than 0.5% and 4%, respectively starting from the cut $P_{tCUT}^{out} = 20\,GeV/c$. From these plots we also conclude that variation of P_{tCUT}^{out} improves the disbalance, in fact, in the same way as the variation of P_{tCUT}^{clust}. It is not surprising as the cluster P_t activity is a part of the ${P_t}^{out}$ activity.

The influence of the P_{tCUT}^{out} variation (with the fixed value $P_{tCUT}^{clust} = 10\,GeV/c$) on the distribution of $({P_t}^{\gamma} - {P_t}^J)/{P_t}^{\gamma}$ is shown in Fig. 23 for Selection 1. In this case the mean value of $({P_t}^{\gamma} - {P_t}^J)/{P_t}^{\gamma}$ drops from 2% to 0.9% for LUCELL and UA2 algorithms (and to even less value for UA1) for the $40 < {P_t}^{\gamma} < 50\,GeV/c$ interval. At the same time the RMS value improves from 13% to 9% for all algorithms. For interval $300 < {P_t}^{\gamma} < 360\,GeV/c$ the mean value and RMS of $({P_t}^{\gamma} - {P_t}^J)/{P_t}^{\gamma}$ are less then 0.4% and 3.3% for all three jetfinders.

So, we conclude basing on the analysis of PYTHIA (as a model) simulation that the new cuts P_{tCUT}^{clust} and P_{tCUT}^{out} introduced in Section 3 as well as introduction of a new object, the "isolated jet", are found as those that may be very efficient tools to improve the jet calibration accuracy [34]. Their combined usage for this aim and for the background suppression will be a subject of a further more detailed study in Section 8.

[33] This variable enters into the expression $P_t(O + \eta > 5.0)/{P_t}^{\gamma}$, which makes a dominant contribution to the right-hand side of P_t balance equation (28), as we mentioned above.

[34] We plan to continue this study on the level of the full event reconstruction after CMSIM simulation.

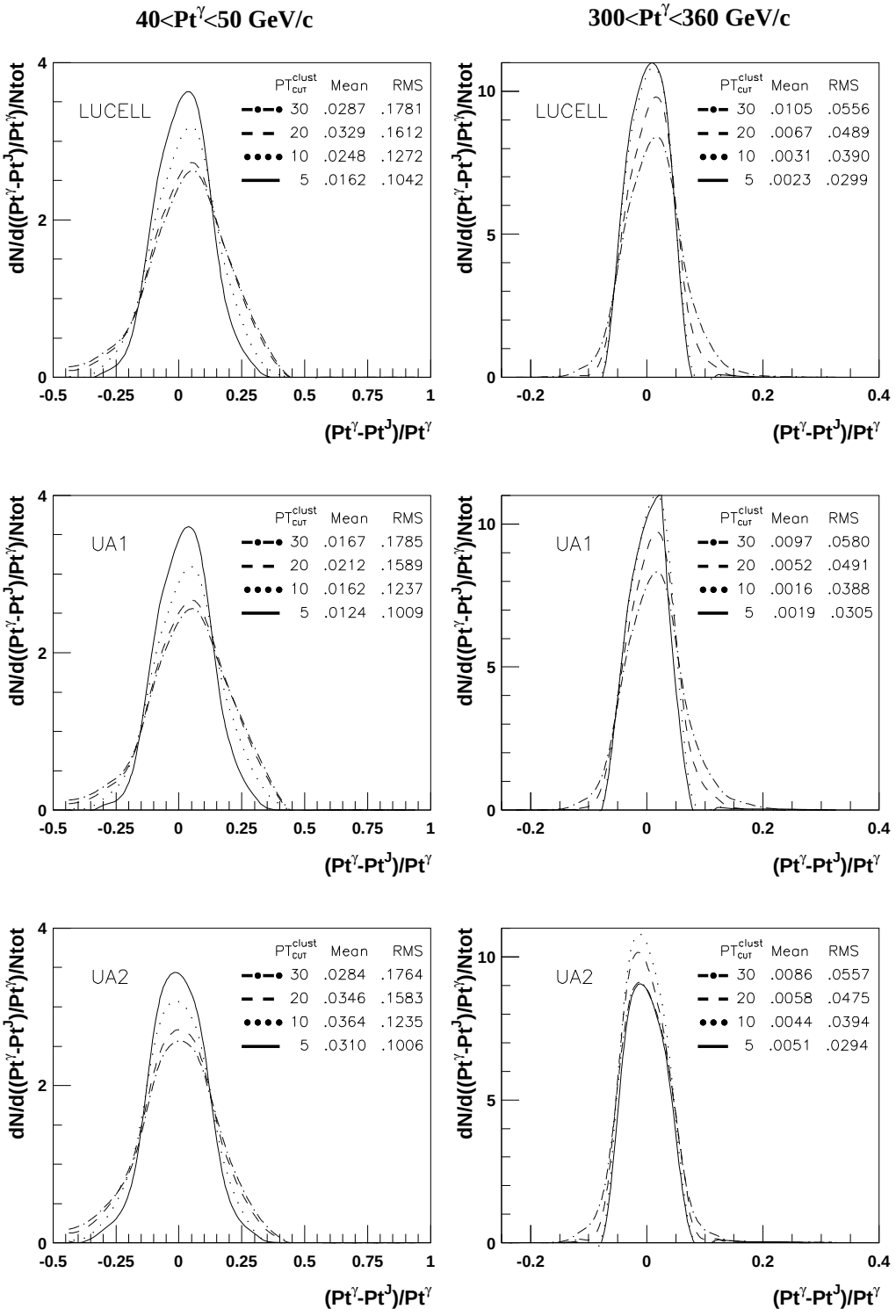

Fig. 15: A dependence of $(P_t{}^{\gamma} - P_t{}^{J})/P_t{}^{\gamma}$ on P_{tCUT}^{clust} for LUCELL, UA1 and UA2 jetfinding algorithms and two intervals of $P_t{}^{\gamma}$. The mean and RMS of the distributions are displayed on the plots. $\Delta\phi < 15^{\circ}$. $P_t{}^{out}$ is not limited. Selection 1.

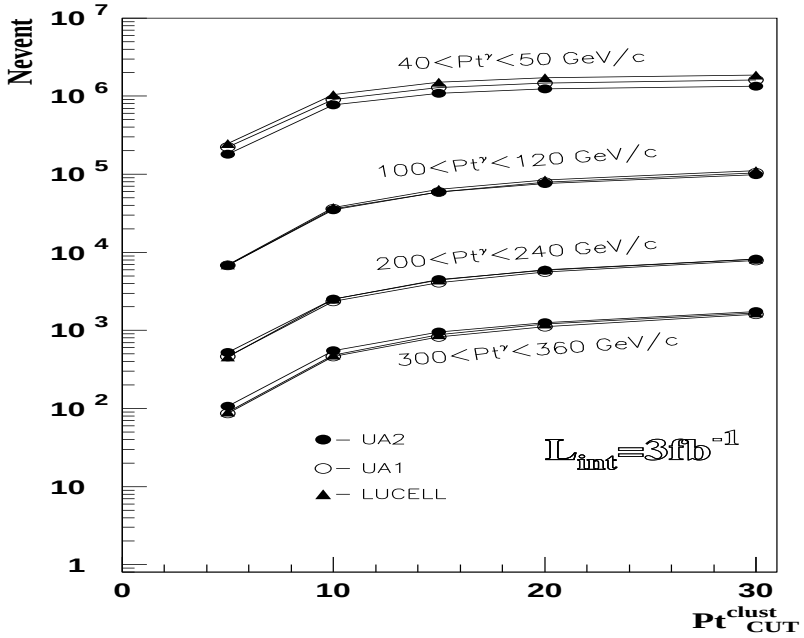

Fig. 16

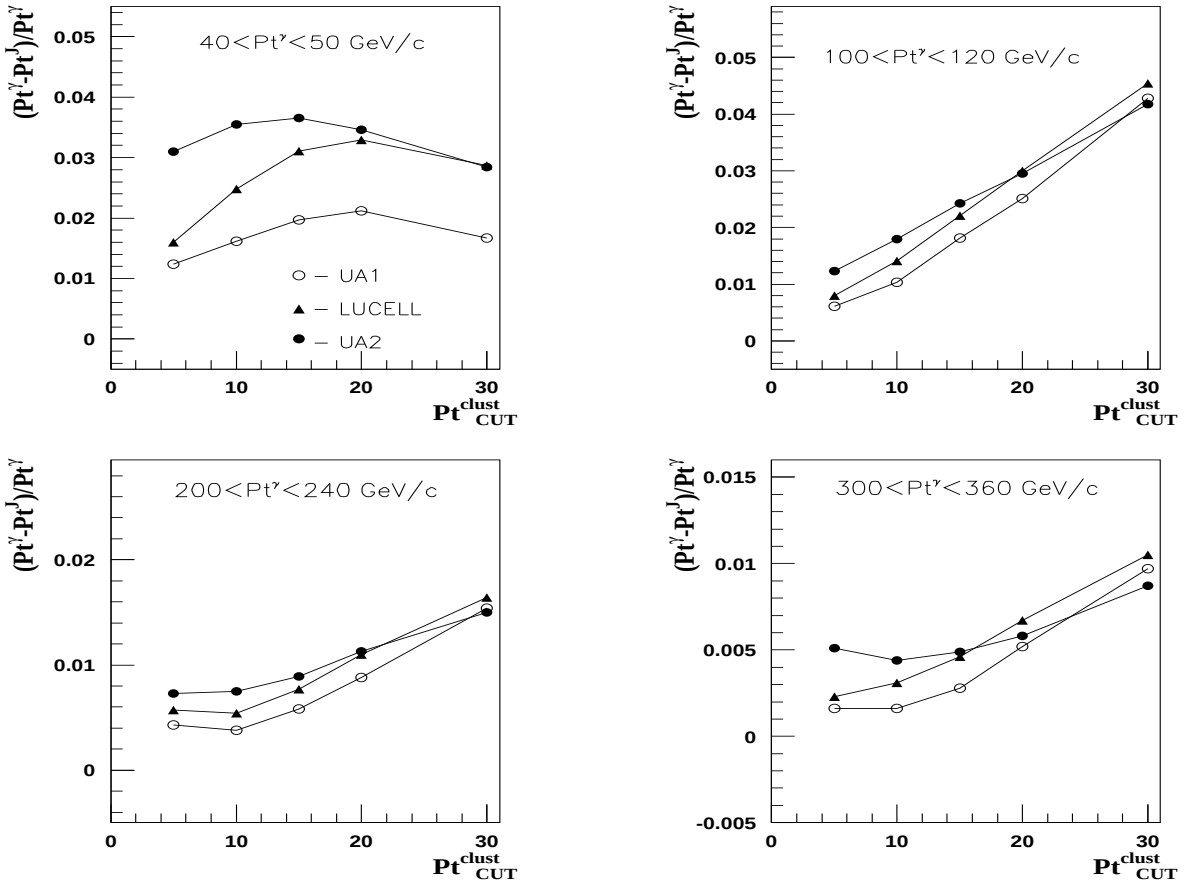

Fig. 17

Selection 1. Dependence of the number of events for $L_{int} = 3fb^{-1}$ (Fig. 16, top) and $(P_t{}^{\gamma} - P_t{}^{J})/P_t{}^{\gamma}$ (Fig. 17, bottom) on P_{tCUT}^{clust} in cases of LUCELL, UA1 and UA2 jetfinding algorithms. $\Delta\phi = 15^{\circ}$. $P_t{}^{out}$ is not limited.

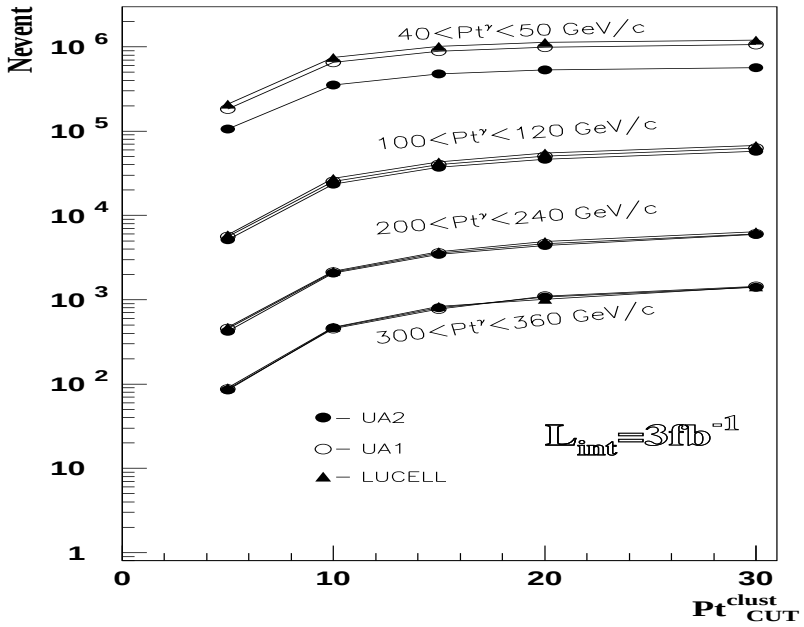

Fig. 18

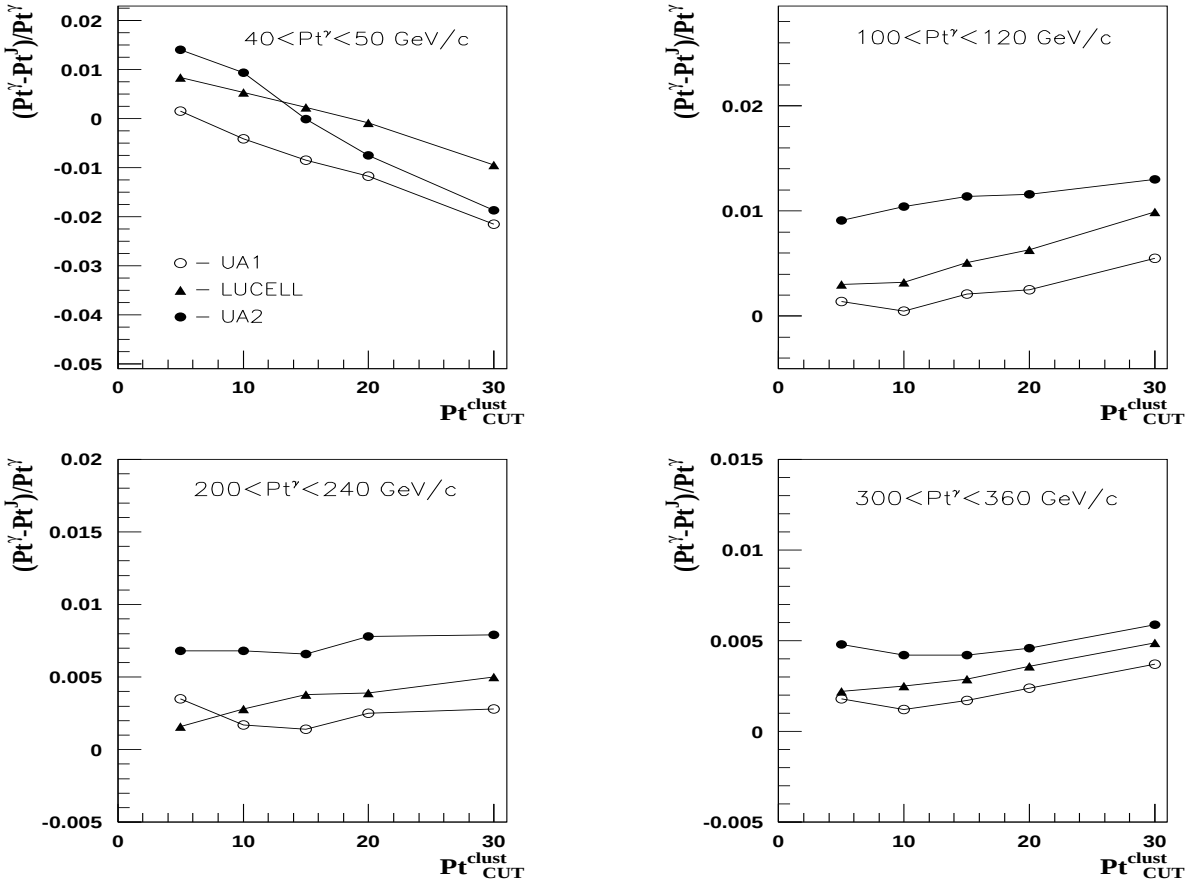

Fig. 19

Selection 2. Dependence of the number of events for $L_{int} = 3fb^{-1}$ (Fig. 18, top) and $(P_t{}^{\gamma} - P_t{}^{J})/P_t{}^{\gamma}$ (Fig. 19, bottom) on P_{tCUT}^{clust} in cases of LUCELL, UA1 and UA2 jetfinding algorithms. $\Delta\phi = 15^{\circ}$. $P_t{}^{out}$ is not limited. $\epsilon^{jet} < 6-8\%$ $(40 < P_t{}^{\gamma} < 50)$,$< 4\%$ $(100 < P_t{}^{\gamma} < 120)$,$< 3\%$ $(200 < P_t{}^{\gamma} < 240)$,$< 3\%$ $(300 < P_t{}^{\gamma} < 360)$.

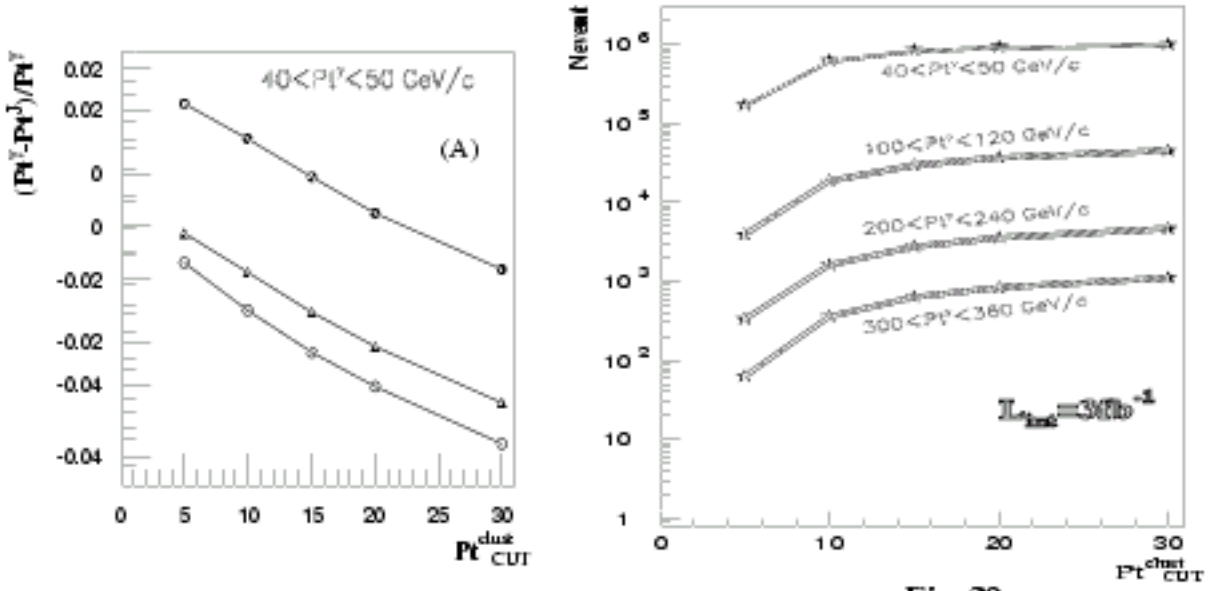

Fig. 20

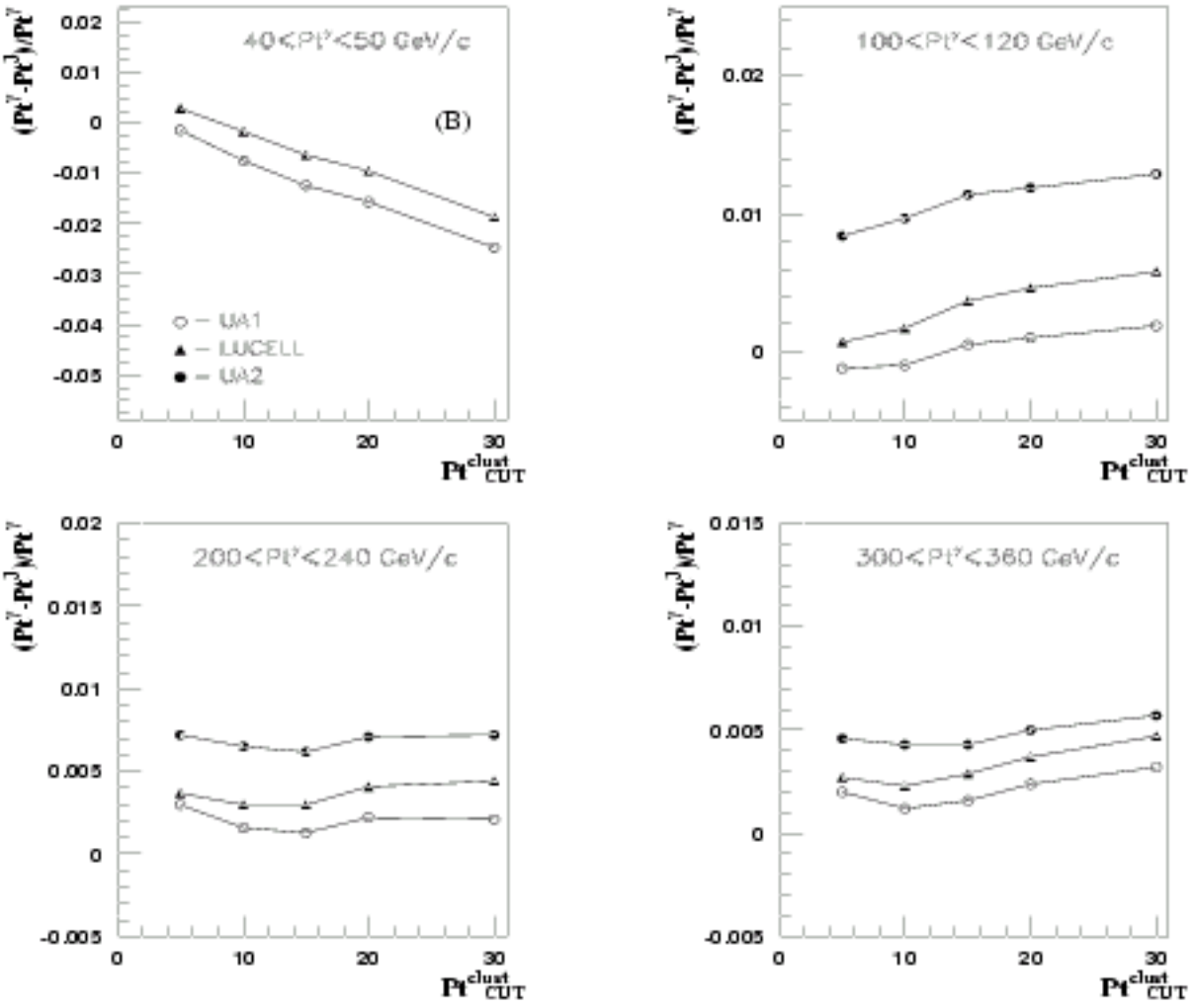

Fig. 21

Selection 3. Dependence of the number of events for $L_{int} = 3fb^{-1}$ (Fig. 20, right-hand top) and $(P_t{}^{\gamma} - P_t{}^{J})/P_t{}^{\gamma}$ (Fig. 21, left-hand top and bottom) on $P_t{}^{clust}_{CUT}$ in cases of LUCELL, UA1 and UA2 jetfinding algorithms. $\Delta\phi = 15°$. $P_t{}^{out}$ is not limited. $\epsilon^{jet} < 6 - 8\%$ $(40 < P_t{}^{\gamma} < 50)$,$< 4\%$ $(100 < P_t{}^{\gamma} < 120)$,$< 3\%$ $(200 < P_t{}^{\gamma} < 240)$,$< 3\%$ $(300 < P_t{}^{\gamma} < 360)$. The $P_t{}^{\gamma}$ and $P_t{}^{Jet}$ balances for simultaneous jet finding by UA1, UA2 and LUCELL for $40 < P_t{}^{\gamma} < 50$ are plotted in Fig. 21A and for simultaneous jet finding by only UA1 and LUCELL for $40 < P_t{}^{\gamma} < 50$ are plotted in Fig. 21B (see also text of Section 7).

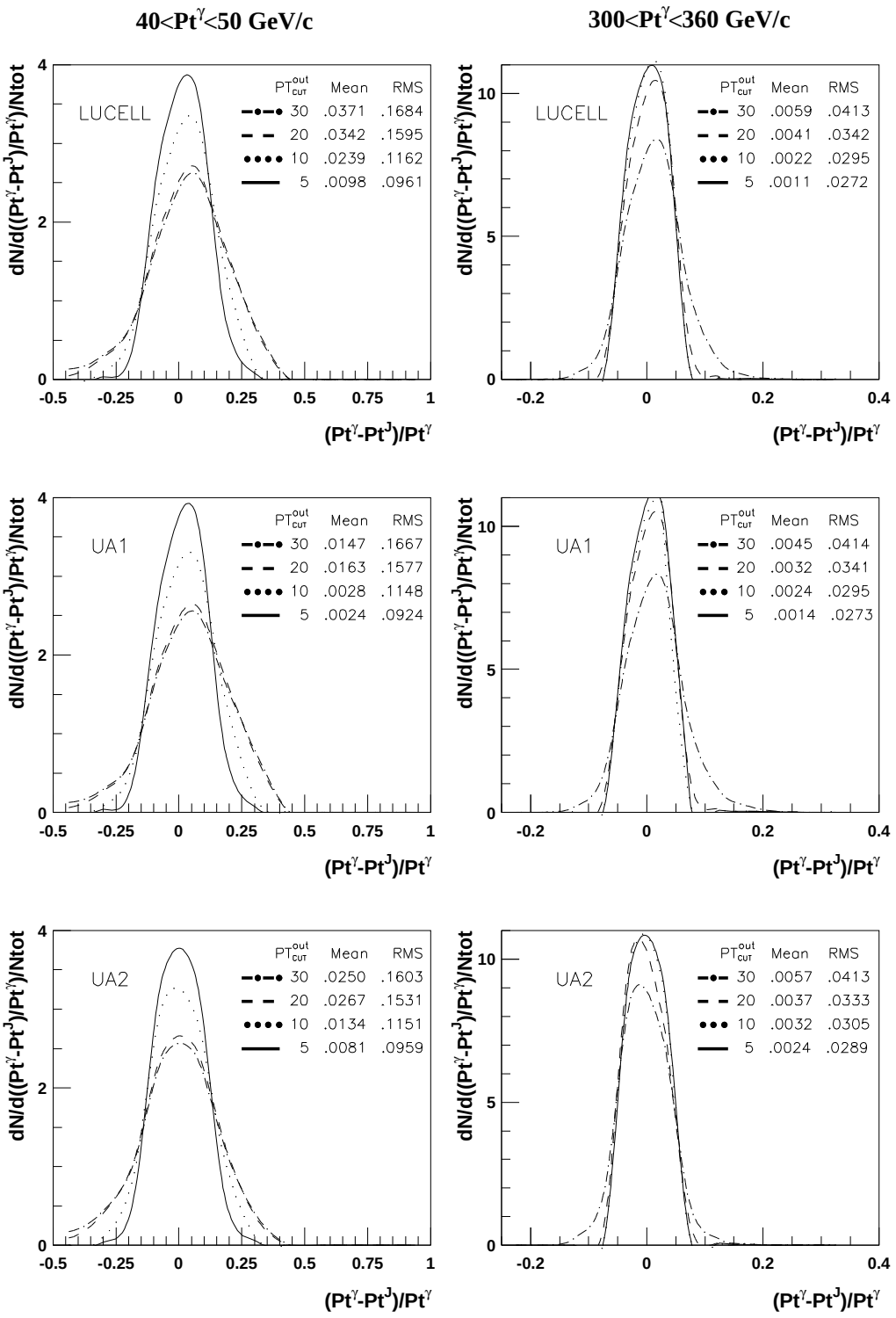

Fig. 22: A dependence of $(P_t{}^{\gamma} - P_t{}^{J})/P_t{}^{\gamma}$ on P_{tCUT}^{out} for LUCELL, UA1 and UA2 jetfinding algorithms and two intervals of $P_t{}^{\gamma}$. The mean and RMS of the distributions are displayed on the plots. $\Delta\phi \leq 15°$, $P_{tCUT}^{clust} = 30\ GeV/c$. Selection 1.

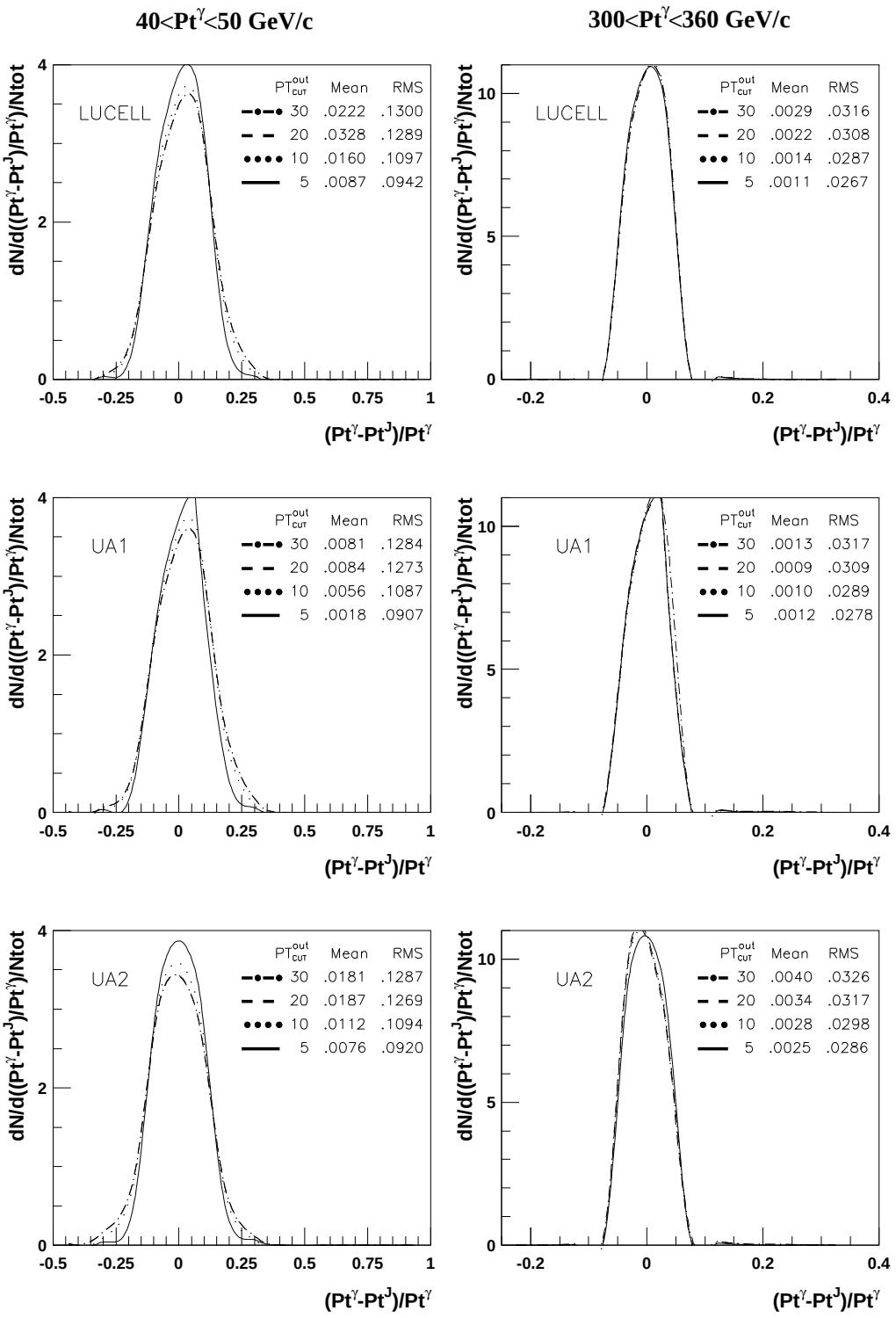

Fig. 23: A dependence of $(P_t{}^{\gamma} - P_t{}^{J})/P_t{}^{\gamma}$ on P_{tCUT}^{out} for LUCELL, UA1 and UA2 jetfinding algorithms and two intervals of $P_t{}^{\gamma}$. The mean and RMS of the distributions are displayed on the plots. $\Delta\phi \leq 15°$, $P_{tCUT}^{clust} = 10\ GeV/c$. Selection 1.

8. ESTIMATION OF BACKGROUND SUPPRESSION CUTS EFFICIENCY.

The relative efficiency of "hadronic" cuts that are added to "photonic" ones, used to suppress the background in the case of inclusive photon measurement, is estimated at the particle level.

It is also shown that the simultaneous use of P_{tCUT}^{out}, P_{tCUT}^{clust} together with imposing jet isolation criterion would lead to a substantial improvement of signal-to-background ratio and $P_t{}^{\gamma} - P_t{}^{Jet}$ balance (see Tables 14–21 and Appendix 6).

The potentially dangerous role of a new source of background to the signal "$\gamma^{dir} + jet$" events caused by hard bremsstrahlung photons ("$\gamma - brem$") is demonstrated. It is shown that at LHC energy this new "$\gamma - brem$" irreducible background may be compatible at low $P_t{}^{\gamma}$ intervals with the π^0 contribution and it may grow faster with $P_t{}^{\gamma}$ increasing than the latter one.

To estimate the efficiency of the cuts proposed in Section 3.2 we carried out the simulation [35] with a mixture of all QCD and SM subprocesses with large cross sections existing in PYTHIA (namely, in notations of PYTHIA, with ISUB=1, 2, 11–20, 28–31, 53, 68). The events caused by this set of the subprocesses may give a large background to the "$\gamma^{dir} + jet$" signal events defined by the subprocesses (1a) and (1b) [36] (ISUB=29 and 14) that were also included in this simulation.

Three generations with the above-mentioned set of subprocesses were done. Each of them was performed with a different value of PYTHIA parameter $CKIN(3) \equiv \hat{p}_{\perp}^{min}$ that defines the minimal value of P_t appearing in the final state of a hard $2 \to 2$ parton level fundamental subprocess in the case of ISR absence. These values were $\hat{p}_{\perp}^{min} = 40, 100$ and $200\ GeV/c$. By 80, 50 and 80 million events were generated for three $\hat{p}_{\perp}^{min}$ values respectively. The cross sections of the above-mentioned subprocesses define the rates of the corresponding physical events and, thus, serve in simulation as weight factors.

We selected "γ^{dir}-candidate +1 Jet" events containing one γ^{dir}-candidate (denoted in what follows as $\tilde{\gamma}$) and one jet (found by LUCELL) with $P_t{}^{Jet} > 30\ GeV/c$. Here and below, as we work at the PYTHIA particle level of simulation, speaking about the γ^{dir}-candidate, we actually mean, apart from the γ^{dir}, a set of particles like electrons, bremsstrahlung photons and also photons from neutral meson decays that may be registered in the 5×5 ECAL crystal cell window having the cell with the highest P_t (γ/e) in its center.

Below we consider a set of 17 cuts that are separated into 2 subsets: a set of the "photonic" cuts and a set of the "hadronic" ones. The first set consists of five cuts used to select an isolated photon candidate in some $P_t^{\tilde{\gamma}}$ interval. The second one includes twelve cuts applied after the "photonic" cuts. These "hadronic" cuts deal mostly with jets and clusters and are used to select events having one "isolated jet" and limited P_t activity out of "$\tilde{\gamma} + jet$" system.

The used cuts are listed in Table 13. To give an idea about their physical meaning and importance we have done an estimation of their possible influence on the signal-to-background ratios S/B. The letter were calculated after application of each cut. Their values are presented in Table 14 for a case of the most illustrative intermediate interval of event generation with $\hat{p}_{\perp}^{min} = 100\ GeV/c$. In Table 14 the number in each line corresponds to the number of the cut in Table 13 (the important lines of Table 14 are darkened because they will be often referenced to while discussing the following Tables 15–17).

Line number 1 of Table 13 contains four primary preselection criteria. It includes and specifies our first general cut (17) of Section 3.2 as well as the cut connected with ECAL geometry

[35] PYTHIA 5.7 version with default CTEQ2L parameterization of structure functions is used here.

[36] A contribution of another possible NLO channel $gg \to g\gamma$ (ISUB=115 in PYTHIA) was found to be still negligible even at LHC energies.

Table 13: List of the applied cuts (will be used also in Tables 14 – 17).

0. No cuts;	
1. $a)\ P_t^{\tilde{\gamma}} \geq 40\ GeV/c,\ \ b)\ \|\eta^{\tilde{\gamma}}\| \leq 2.61,\ \ c)\ P_t^{jet} \geq 30\ GeV/c,\ \ d) P_t^{hadr} < 5\ GeV/c$ * ;	
2. $\epsilon^{\tilde{\gamma}} \leq 15\%$;	**11**. $P_t^{clust} < 20\ GeV/c$;
3. $P_t^{\tilde{\gamma}} \geq \hat{p}_\perp^{min}$;	**12**. $P_t^{clust} < 15\ GeV/c$;
4. $\epsilon^{\tilde{\gamma}} \leq 5\%$;	**13**. $P_t^{clust} < 10\ GeV/c$;
5. $P_t^{isol} \leq 2\ GeV/c$;	**14**. $P_t^{out} < 20\ GeV/c$;
6. $Njet \leq 3$;	**15**. $P_t^{out} < 15\ GeV/c$;
7. $Njet \leq 2$;	**16**. $P_t^{out} < 10\ GeV/c$;
8. $Njet = 1$;	**17**. $\epsilon^{jet} \leq 5\%$.
9. $\Delta\phi < 15^\circ$;	
10. $P_t^{miss} \leq 10\ GeV/c$;	

$*$ P_t of a hadron in the 5x5 ECAL cell window containing the γ^{dir}-candidate in the center.

and the cut (21) that excludes γ^{dir}-candidates accompanied by hadrons.

Line number 2 of Table 13 fixes the values of ϵ^{γ}_{CUT} that, according to (19), define the isolation parameters of $\tilde{\gamma}$.

The third cut selects the events with γ^{dir}-candidates having P_t higher than $CKIN(3) \equiv \hat{p}_\perp^{min}$ threshold. We impose the third cut to select the samples of events with $P_t^{\tilde{\gamma}} \geq 40, 100$ and $200\ GeV/c$ as ISR may smear the sharp kinematical cutoff defined by $CKIN(3)$ [20]. This cut reflects an experimental viewpoint when one is interested in how many events with γ^{dir}-candidates are contained in some definite interval of $P_t^{\tilde{\gamma}}$.

The restriction $\epsilon^{\gamma}_{CUT} < 5\%$, realized in the fourth line, acts already on the events having a rather clean surrounding space near γ^{dir}-candidate and makes the fractional isolation cut in line 2 to be tighter.

The fifth cut makes stronger the isolation criterion of γ^{dir}-candidate (within $R = 0.7$) than it was required by the second line of Table 13. It should be noted that this cut includes the restriction of "infrared" cut (20) of Section 3.2 which was not included to this reason into Table 13.

The cuts considered up to now, apart from general preselection cut $P_t^{jet} \geq 30\ GeV/c$ used in the first line of Table 13, were connected with photon selection ("photonic" cuts). Before we go further, some words of caution must be said here. Firstly, we want to emphasize that the starting numbers of the signal (S) and background (B) events (first line of Table 14) may be specific only for PYTHIA generator and for the way of preparing primary samples of the signal and background events described above. So, we want to underline here that the starting values of S and B in the first columns of Table 14 are model dependent

Nevertheless, for our aim of investigation of efficiencies of new hadronic cuts 6–17 (see [9]–[15]) the important thing here is that we can use these starting model numbers of S- and B-events for studying the further relative influence of these cuts on S/B ratio, choosing the conventional normalization to 100% of the cut efficiencies [37] for S- and B-events in line 1.

In spite of self-explaining notations of the cuts 6–9 let us mention, before passing to cuts 10–17, that the cuts 6–9 are connected with the selection of events having only one jet and the definition of jet-photon spatial orientation. Usage of these four cuts leads to the almost three-fold

[37] In Table 14 the efficiencies $Eff_{S(B)}$ (with their errors) are defined as a ratio of the number of signal (background) events that passed under a cut (1–17) to the number of the preselected events (1st cut of this table).

Table 14: Values of significance and efficiencies for $\hat{p}_\perp^{\,min}$=100 GeV/c

Cut	S	B^*	$Eff_S(\%)$	$Eff_{B^*}(\%)$	S/B^*	$e^\pm$
0	19420	5356.E+6			0.00	3.9E+6
1	19359	1151425	100.00 ± 0.00	100.000 ± 0.000	0.02	47061
2	18236	65839	94.20 ± 0.97	5.718 ± 0.023	0.28	8809
3	15197	22437	78.50 ± 0.85	1.949 ± 0.013	0.71	2507
4	14140	9433	73.04 ± 0.81	0.819 ± 0.008	1.50	2210
5	8892	4618	45.93 ± 0.59	0.401 ± 0.006	1.93	1331
6	8572	3748	44.28 ± 0.57	0.326± 0.005	2.29	1174
7	7663	2488	39.58 ± 0.53	0.216± 0.004	3.08	921
8	4844	813	25.02 ± 0.40	0.071± 0.002	5.96	505
9	4634	709	23.94 ± 0.39	0.062 ± 0.002	6.54	406
10	4244	650	21.92 ± 0.37	0.056 ± 0.002	6.53	87
11	3261	345	16.84 ± 0.32	0.030 ± 0.002	9.45	53
12	2558	194	13.21 ± 0.28	0.017 ± 0.001	13.19	41
13	1605	91	8.29 ± 0.22	0.008 ± 0.001	17.64	26
14	1568	86	8.10 ± 0.21	0.007 ± 0.001	18.23	26
15	1477	77	7.63 ± 0.21	0.007 ± 0.001	19.18	25
16	1179	52	6.09 ± 0.18	0.005 ± 0.001	22.67	22
17	1125	46	5.81 ± 0.18	0.004 ± 0.001	24.46	21

$*$ The background B^* is considered here with no account of contribution from the "$e^\pm$ events" in which $e^\pm$'s appear as γ^{dir}-candidates, separated into the column "$e^\pm$".

relative improvement of model S/B ratio (compare lines 5 and 9 of Table 14).

In line 10 we used the P_{tCUT}^{miss} cut, applied in Section 4, to reduce an uncertainty of P_t^{Jet} due to a possible neutrino contribution to a jet. Here it also reduces the contribution to background from the decay subprocesses $q\,g \to q' + W^\pm$ and $q\,\bar{q}' \to g + W^\pm$ with the subsequent decay $W^\pm \to e^\pm\nu$ that leads to a substantial P_t^{miss} value. It is clear from the distributions over P_t^{miss} for two P_t^e intervals presented in Fig. 24. From the last column ($e^\pm$) of Table 14 one can see that P_{tCUT}^{miss} cut (see line 10) reduces strongly (5 times) the number of events containing $e^\pm$ as direct photon candidates. So, P_{tCUT}^{miss} would make a noticeable improvement of the total S/B ratio.

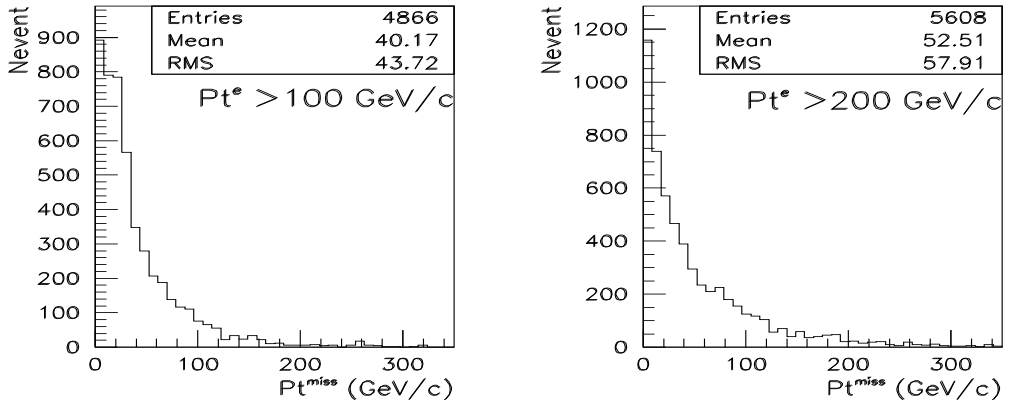

Fig. 24: Distribution of events over P_t^{miss} in events with energetic $e^\pm$'s appearing as direct photon candidates for the cases $P_t^e \geq 100\,GeV/c$ and $P_t^e \geq 200\,GeV/c$ (here events satisfying cuts 1–3 of Table 13 are used).

Moving further we see from Table 14 that the cuts 10–16 of Table 13 reduce the values of P_t^{clust} and P_t^{out} down to the values less than $10\ GeV/c$. The 17-th cut of Table 13 imposes

the jet isolation requirement. It leaves only the events with jets having the sum of P_t in a ring surrounding a jet to be less than 5% of ${P_t}^{Jet}$. From comparison of the numbers in 9-th and 17-th lines we make the important conclusion that all these new cuts (10–17), despite of model dependent nature of starting S/B value in line 10, may, in principle, lead to the following about four-fold improvement of S/B ratio. This improvement is reached by reducing the P_t activity out of "$\tilde{\gamma} + 1\ jet$" system.

It is also rather interesting to mention that the total effect of "hadronic cuts" 6–17 at ${P_t}^{\gamma} > 100\ GeV/c$ consist of decrease of background contribution by 2 orders (!) at the cost of eight-fold loss of signal events. So, in this sense, we may conclude that from the viewpoint of S/B ratio the study of "$\gamma + jet$" events may be more preferable as compared with a case of inclusive photon production.

Below we shall demonstrate in some plots how new selection criteria 10–17 work to choose the events with further almost four-fold improvement of S/B ratio. For this reason we have built the distributions that correspond to the three above-mentioned values of $\hat{p}_{\perp}^{\,min}$ and for the "$\tilde{\gamma} + 1\ jet$" events that have passed the set of cuts 1–8 defined in Table 13. Thus, no special cuts were imposed on $\Delta\phi$, ${P_t}^{out}$ and ${P_t}^{clust}$ (the values of ${P_t}^{clust}$ are automatically bounded from above since we select "$\tilde{\gamma} + 1\ jet$" events with ${P_t}^{jet} > 30\ GeV/c$).

These distributions are given here to show the dependence of the number of events on the physical observables $\Delta\phi$, ${P_t}^{out}$ and ${P_t}^{clust}$ introduced in Sections 3.1 and 3.2. We present them separately for the signal "γ-dir" and background events contained in each of three generated samples. The distributions are given for three different ${P_t}^{\tilde{\gamma}}$ intervals in Figs. 25, 27, 29 and are accompanied by scatter plots 26, 28, 30. So, each pair of a figure and a scatter plot does correspond to one ${P_t}^{\tilde{\gamma}}$ interval. Thus, Fig. 25 and scatter plot 26 correspond to ${P_t}^{\tilde{\gamma}} \geq 40\ GeV/c$ and so on.

The first columns in these figures, denoted by "γ - dir", show the distributions in the signal events, i.e. in the events corresponding to processes (1a) and (1b). The second columns, denoted as "γ - brem", correspond to the events in which the photons were emitted from quarks (i.e. bremsstrahlung photons). The distributions in the third columns were built on the basis of the events containing "γ-mes" photons, i.e. those photons which originate from multiphoton decays of mesons (π^0, η, ω and K_S^0).

First, we see that in the case of ${P_t}^{\tilde{\gamma}} \geq 100\ GeV/c$ (see Figs. 27, 29) practically all "signal events" are within $\Delta\phi < 15^{\circ}$. It is seen from Fig. 25 that for ${P_t}^{\tilde{\gamma}} \geq 40\ GeV/c$ there is still a large number of signal events (about 70%) belonging to the $\Delta\phi < 15^{\circ}$ interval. From here and from the comparison of plots in the "γ-dir" and "γ-brem" columns (showing the $\Delta\phi$ dependence) in the same figures 25–30 we conclude that the upper cut $\Delta\phi < 15^{\circ}$, used in previous sections, is reasonable, and moreover, it does discard a lot of "γ-brem" background events in the intervals with ${P_t}^{\tilde{\gamma}} < 100\ GeV/c$.

From the second "γ-brem" columns of Figs. 25, 27 and 29 one can also see that ${P_t}^{clust}$ spectra of the events with bremsstrahlung photons look different from the analogous ${P_t}^{clust}$ distributions of the signal "γ-dir" photons. The latter distributions have the most of the events in the region of small ${P_t}^{clust}$ values

Since the bremsstrahlung ("γ-brem") photons give the most sizeable background [38], (compare the numbers of entries in the second "γ-brem" and the third "γ-mes" columns of Figs. 24–29) the observed difference of the spectra prompts an idea of using an upper cut for the value of ${P_t}^{clust}$

[38]The numbers in Table 15 below supports this remark. But it is also necessary to keep in mind the results obtained in [39] that the PYTHIA/JETSET fragmentation may underestimate the π^0, η contribution to the isolated photon background.

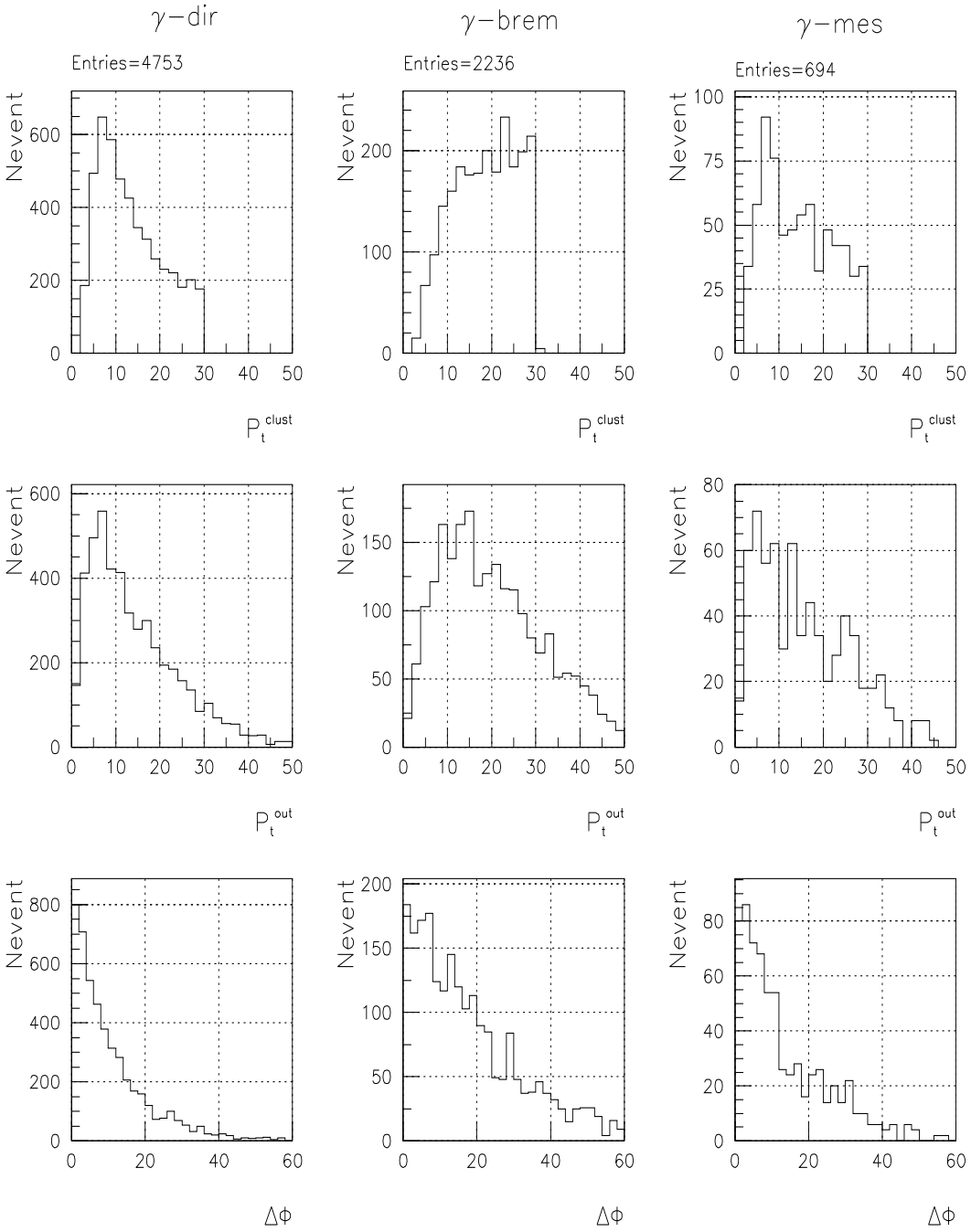

Fig. 25: Signal/Background: Number of events distribution over $P_t{}^{clust}$, $P_t{}^{out}$, $\Delta\phi$ ($P_t{}^{\tilde{\gamma}} \geq 40\ GeV/c$).

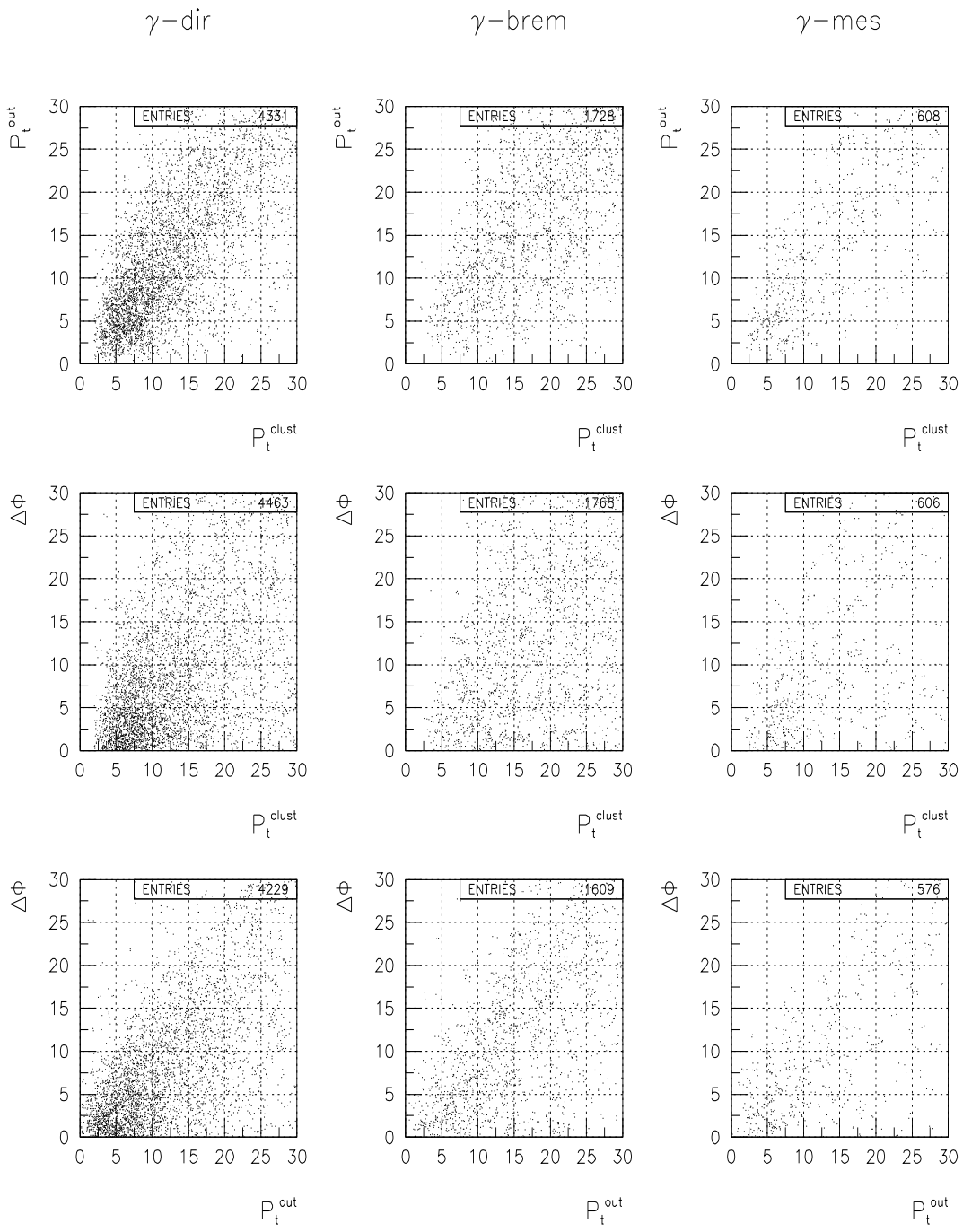

Fig. 26: Signal/Background: $P_t{}^{clust}$ vs. $P_t{}^{out}$, $P_t{}^{clust}$ vs.$\Delta\phi$, $P_t{}^{out}$ vs. $\Delta\phi$ ($P_t{}^{\tilde{\gamma}} \geq 40\ GeV/c$).

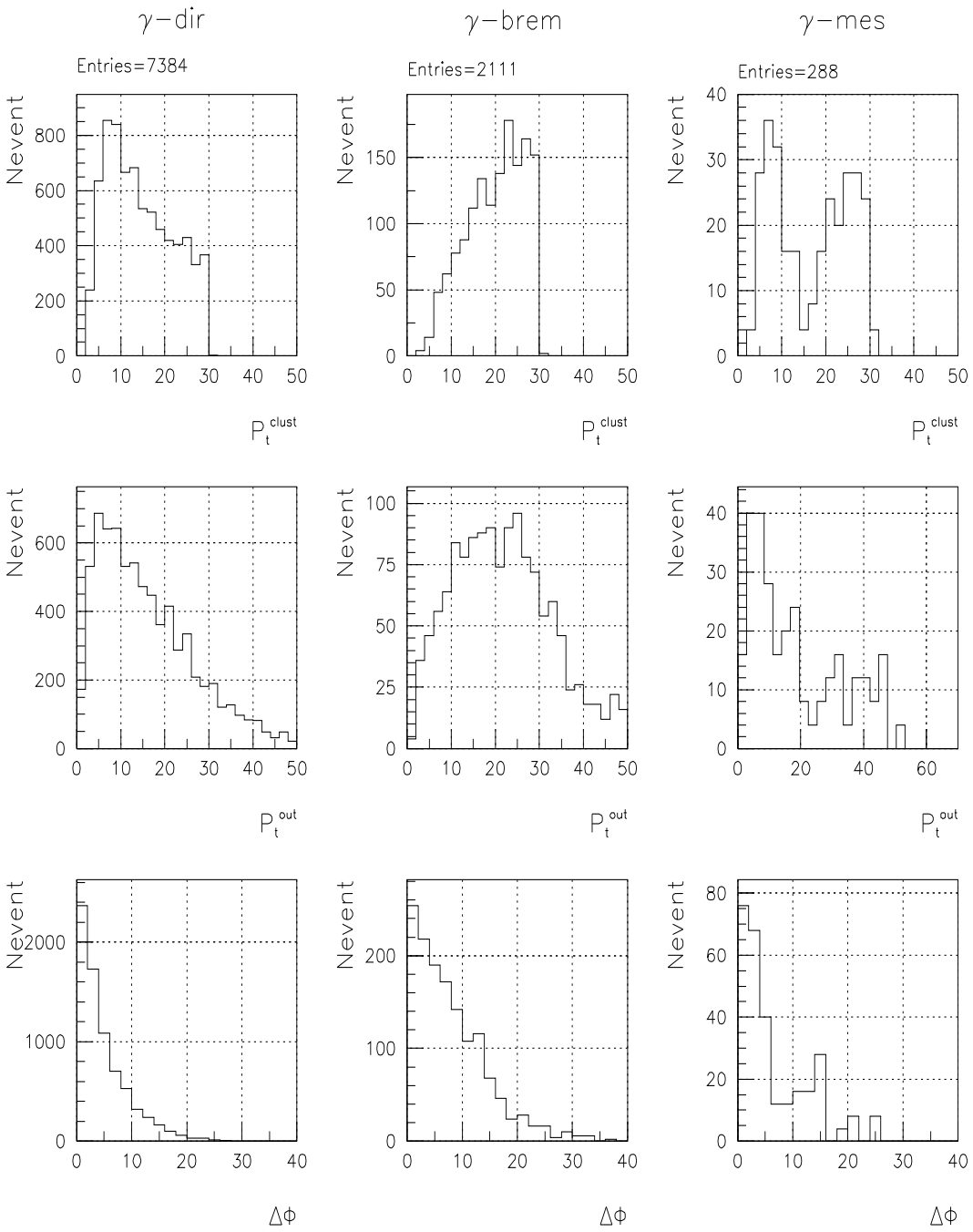

Fig. 27: Signal/Background: Number of events distribution over P_t^{clust}, P_t^{out}, $\Delta\phi$ ($P_t^{\tilde{\gamma}} \geq 100\, GeV/c$).

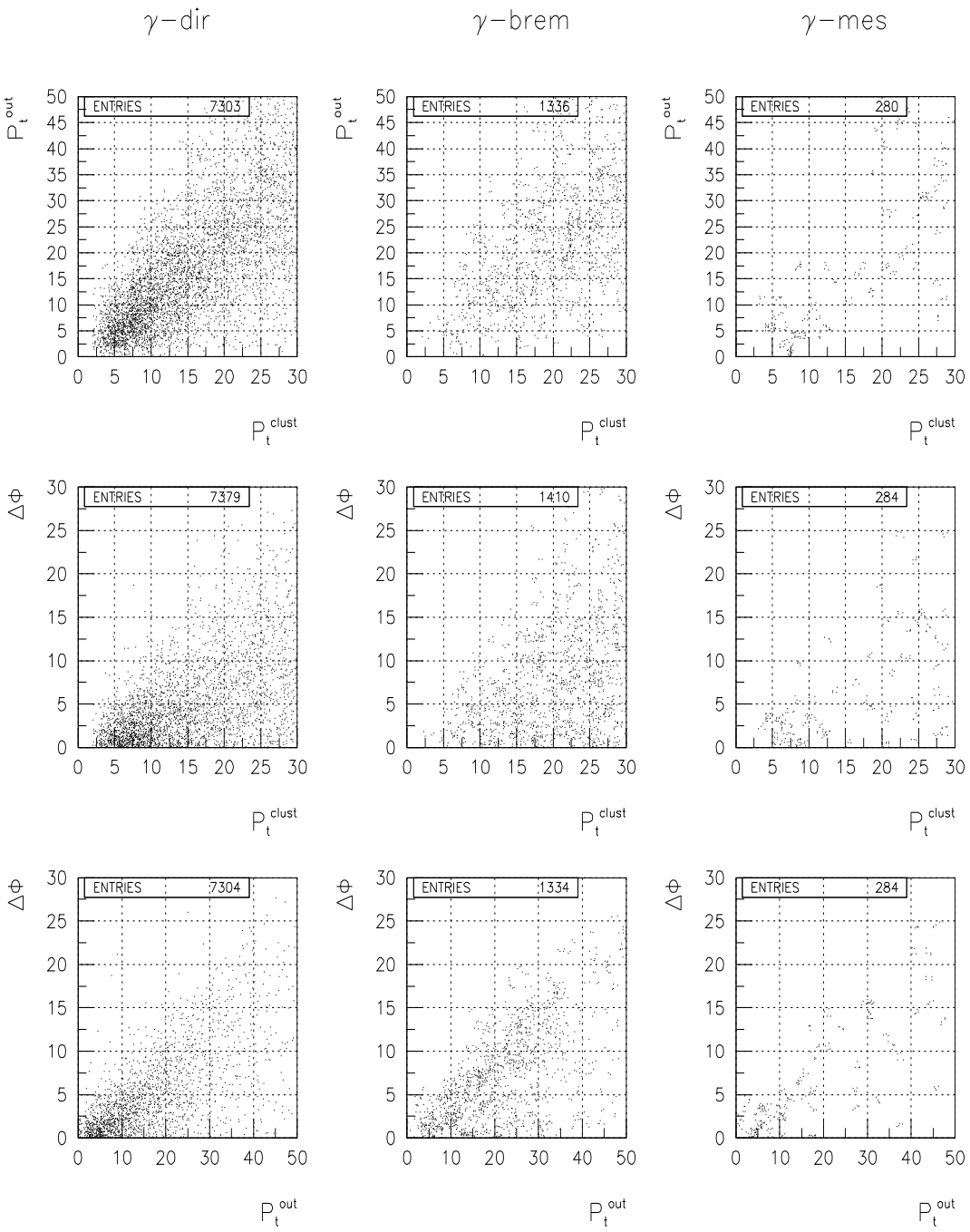

Fig. 28: Signal/Background: $P_t{}^{clust}$ vs. $P_t{}^{out}$, $P_t{}^{clust}$ vs.$\Delta\phi$, $P_t{}^{out}$ vs. $\Delta\phi$ ($P_t{}^{\tilde{\gamma}} \geq 100\ GeV/c$).

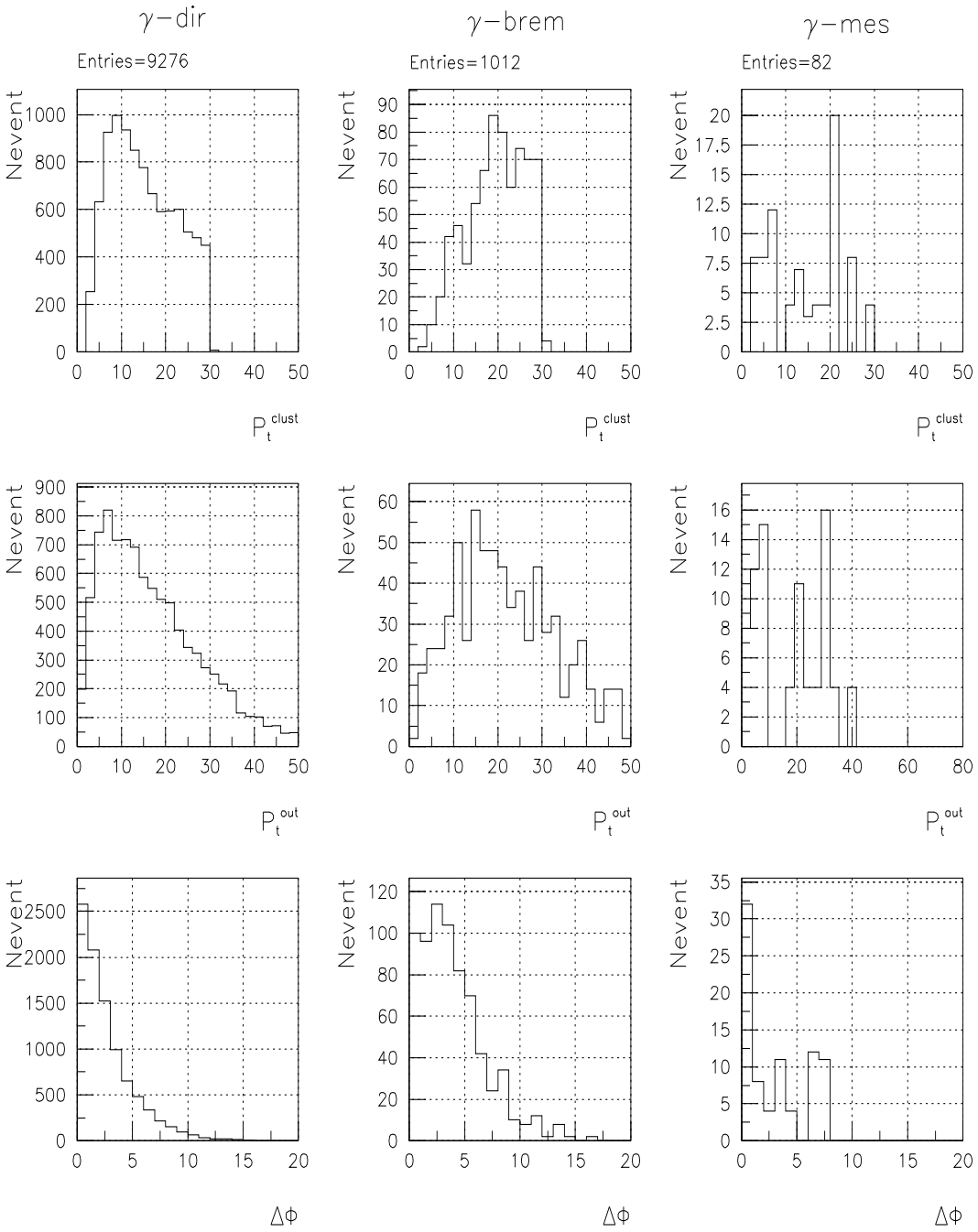

Fig. 29: Signal/Background: Number of events distribution over $P_t{}^{clust}$, $P_t{}^{out}$, $\Delta\phi$ ($P_t{}^{\tilde{\gamma}} \geq 200\ GeV/c$).

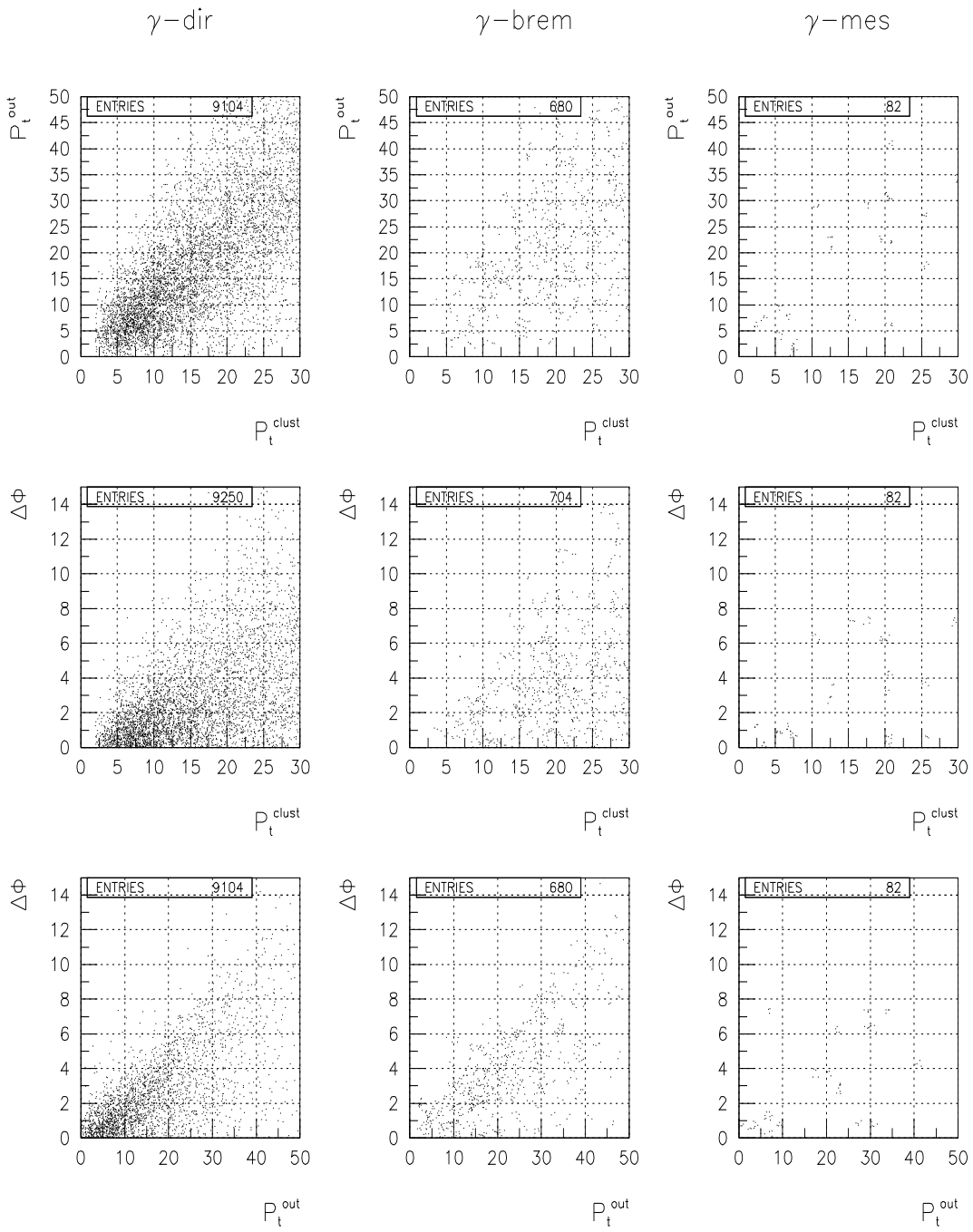

Fig. 30: Signal/Background: $P_t{}^{clust}$ vs. $P_t{}^{out}$, $P_t{}^{clust}$ vs.$\Delta\phi$, $P_t{}^{out}$ vs. $\Delta\phi$ ($P_t{}^{\tilde{\gamma}} \geq 200\ GeV/c$).

to reduce the "γ-brem" background which dominates at large P_t^{clust} values (that was not a primary guideline for introduction of P_t^{clust} in Sections 2 and 3 as a physical variable and a cut on it).

The analogous difference of P_t^{out} spectra of signal "γ-dir" events (which are concentrated at low P_t^{out} values) from those of background "γ-brem" events having longer tails at high P_t^{out} enables us to impose an upper cut on the P_t^{out} value.

Now from the scatter plots in Figs. 26, 28 and 30 as well as from Figs. 25, 27 and 29 we can conclude that the use of cuts [39]: $\Delta\phi < 15^\circ$, $P_{tCUT}^{clust} = 10\ GeV/c$, $P_{tCUT}^{out} = 10\ GeV/c$ would allow to keep a big number of the signal "γ-dir" events and to reduce noticeably the contribution from the background "γ-brem" and "γ-mes" events in all intervals of $P_t^{\tilde{\gamma}}$. At the same time the Figs. 25–30 give the information about what parts of different spectra are lost with the imposed cuts.

So, Figs. 25–30 illustrate well that the new physical variables P_t^{clust} and P_t^{out} [9]–[15], described in Sections 3.1 and 3.2 may be useful for separation of the "$\gamma^{dir} + jet$" events from the background ones (the latter, in principle, are not supposed to have the well-balanced $P_t^{\tilde{\gamma}}$ and P_t^{Jet}).

Table 15 includes the numbers of signal and background events left in three generated event samples after application of cuts 1–16 and 1–17. They are given for all three intervals of $P_t^{\tilde{\gamma}}$. Tables 15 and 14 are complementary to each other. The summary of Table 14 is presented in the middle section ($\hat{p}_\perp^{\,min} = 100\ GeV/c$) of Table 15 where the line "Preselected" corresponds to the cut 1 of Table 13 and, respectively, to the line number 1 of Table 14 presented above. The line "After cuts" corresponds to the line 16 of Table 14 and line "+jet isolation" corresponds to the line 17 of Table 14.

Table 15 is done to show in more detail the origin of γ^{dir}-candidates. The numbers in the "$\gamma - direct$" column correspond to the respective numbers of signal events left in each of $P_t^{\tilde{\gamma}}$ intervals after application of the cuts defined in lines 1, 16 and 17 of Table 13 (and in column "S" of Table 14). Analogously the numbers in the "$\gamma - brem$" column of Table 15 correspond to the numbers of events with the photons radiated from quarks participating in the hard interactions. Their P_t^{clust} and P_t^{out} distributions were presented in the central columns of Figs. 25 – 30. Columns 5 – 8 of Table 15 illustrate the numbers of the "$\gamma - mes$" events with photons originating from $\pi^0,\ \eta,\ \omega$ and K_S^0 meson decays. Their distributions were shown in the right-hand columns of Figs. 25 – 30. In a case of $P_t^{\tilde{\gamma}} > 100\ GeV/c$ the total numbers of background events, i.e. a sum over the numbers presented in columns 4 – 8 of Table 15, are shown in the lines 1, 16 and 17 of column "B^*" of Table 14. The other lines of Table 15 for $\hat{p}_\perp^{\,min} = 40$ and $200\ GeV/c$ have the meaning analogous to that described above for $\hat{p}_\perp^{\,min} = 100\ GeV/c$.

The last column of Table 15 shows the number of preselected events with $e^\pm$ (see our notes above while discussing the tenth cut of Table 13).

The numbers in Tables 16 (without jet isolation cut) and 17 (with jet isolation cut) accumulate in a compact form the final information of Tables 13 – 15. Thus, for example, the columns S and B of the line that corresponds to $\hat{p}_\perp^{\,min} = 100\ GeV/c$ contain the total numbers of the selected signal and background events taken at the level of 16-th (for Table 16) and 17-th (for Table 17) cuts from Table 14.

It is seen from Table 16 that in the case of Selection 1 the ratio S/B grows from 3.9 to 48.4 while $P_t^{\tilde{\gamma}}$ increases from $P_t^{\tilde{\gamma}} \geq 40\ GeV/c$ to $P_t^{\tilde{\gamma}} \geq 200\ GeV/c$ interval.

The jet isolation requirement (cut 17 from Table 13) noticeably improves the situation at

[39] rather soft here, but the results of their further restriction were already shown in tables of Appendices 2–5 and Figs. 12–20 and will be discussed below

Table 15: Number of signal and background events remained after cuts **(I)**

$\hat{p}_\perp^{min}$ (GeV/c)	Cuts	γ direct	γ brem	photons from the mesons				$e^\pm$
				π^0	η	ω	K_S^0	
40	Preselected	12394	20952	166821	66533	17464	23942	6684
	After cuts	1718	220	146	56	2	15	10
	+ jet isol.	1003	102	59	26	2	7	8
100	Preselected	19359	90022	658981	247644	69210	85568	47061
	After cuts	1179	34	13	4	1	0	22
	+ jet isol.	1125	32	9	4	1	0	21
200	Preselected	55839	354602	1334124	393880	141053	167605	153410
	After cuts	1837	30	4	6	0	0	17
	+ jet isol.	1828	30	4	6	0	0	17

Table 16: Efficiencies and significance values in events without jet isolation cut **(I)**

$\hat{p}_\perp^{min}$ (GeV/c)	S	B^*	$Eff_S(\%)$	$Eff_B^*(\%)$	S/B^*	$S/\sqrt{B^*}$
40	1718	439	13.86 ± 0.36	0.149 ± 0.007	3.9	82.0
100	1179	52	6.09 ± 0.18	0.005 ± 0.001	22.7	163.5
200	1837	40	3.29 ± 0.08	0.002 ± 0.000	45.9	290.5

Table 17: Efficiencies and significance values in events with jet isolation cut **(I)**

$\hat{p}_\perp^{min}$ (GeV/c)	S	B^*	$Eff_S(\%)$	$Eff_B^*(\%)$	S/B^*	$S/\sqrt{B^*}$
40	1003	196	8.09 ± 0.27	0.066 ± 0.005	5.1	71.6
100	1125	46	5.81 ± 0.18	0.004 ± 0.001	24.5	165.9
200	1828	40	3.28 ± 0.08	0.002 ± 0.000	45.7	289.0

low $P_t^{\tilde{\gamma}}$ (see Table 17). After application of this criterion the value of S/B increases from 3.9 to 5.1 at $P_t^{\tilde{\gamma}} \geq 40\ GeV/c$ and from 22.7 to 24.5 at $P_t^{\tilde{\gamma}} \geq 100\ GeV/c$. Remember on this occasion the conclusion that the sample of events selected with our criteria has a tendency to contain more events with an isolated jet as $P_t^{\tilde{\gamma}}$ increases (see Sections 5–7 and Appendices 2–5). Thus, from Appendices 4 and 5 it can be seen that the main part of jets with $P_t^{jet} \geq 100\ GeV/c$ appears to be isolated (compare also the last two lines in each $\hat{p}_\perp^{min}$ section of Table 15).

Let us underline here that, in contrast to other types of background, "$\gamma - brem$" background has an irreducible nature. So, the number of "$\gamma - brem$" events should be carefully estimated for each $P_t^{\tilde{\gamma}}$ interval using the particle level of simulation in the framework of event generator like PYTHIA. They are also have to be taken into account in experimental analysis of the prompt photon production data at high energies.

Table 18 shows the relative contributions of fundamental QCD subprocesses (having the largest cross sections) with ISUB=11, 12, 28, 53 and 68 (see [20]) which define the main production of "$\gamma - brem$" background in event samples selected with criteria 1–13 of Table 13 in three $P_t^{\tilde{\gamma}}$ intervals.

We found from the PYTHIA event listing analysis that in the main part of selected "$\gamma - brem$" events these photons are produced in the final state of the fundamental $2 \to 2$ subprocess [40]. Namely, they are mostly radiated from the outgoing quarks in the case of the first three sets of subprocesses (ISUB=28, 11, 12 and 53). They may also appear as a result of string breaking in a final state of $gg \to gg$ scattering (ISUB=68). But this subprocess, naturally, gives a small

[40] i.e. from lines 7, 8 in Fig. 3

contribution into "$\tilde{\gamma} + jet$" events production.

Table 18: Relative contribution (in per cents) of different QCD subprocesses into the "$\gamma - brem$" events production.

P_t^{γ} (GeV/c)	fundamental QCD subprocess			
	ISUB=28	ISUB=11,12	ISUB=53	ISUB=68
40–71	70.6± 8.7	21.7± 3.8	5.1± 1.6	2.6± 1.0
71–141	67.5± 7.3	25.7± 3.5	4.2± 1.2	2.6± 0.9
141–283	58.7± 9.0	39.5± 5.7	1.8± 1.0	—

It may be noted also from the first two columns of Table 18 that the most of "$\gamma - brem$" background events originate from the ISUB=28 ($fg \rightarrow fg$) and ISUB=11, 12 ($f_i f_j \rightarrow f_i f_j$, $f_i \bar{f}_i \rightarrow f_j \bar{f}_j$) subprocesses ($90\%$ at least). Table 18 shows also a tendency of increasing the contribution from the sum of two subprocess "11+12" (given in the second column of Table 18) with growing $P_t^{\tilde{\gamma}}$.

Now let us discuss how the values in Tables 14–17 may change if one takes into account the real behaviour of processes in the detectors.

As for the photons from π^0 decays, the the rejection efficiencies were estimated for the Endcap [29], [31] and Barrel [29], [30] ECAL regions. They are of the order of 0.20 – 0.70 for the Barrel and 0.51 – 0.75 for the Endcap, depending on P_t^{γ} and slightly on η^{γ}, for the single photon selection efficiency 90%. As for the $e^{\pm}$ background, we take the electron track finding efficiency to be 85% (following [28] and after averaging over its η dependence) for $P_t^{e} \geq 40\ GeV/c$.

To study the η, ω, K_S^0 mesons contribution we carried out the CMSIM GEANT simulation of samples consisting of 4000 decay events for each source meson from Table 15. We looked for the difference between the profiles of showers produced by direct photons in the ECAL and the profiles of the showers produced by photons originating from meson decays. This search was performed in the $20 < P_t^{\tilde{\gamma}} < 100\ GeV/c$ interval. The results of studying neutral and charged decay channels are presented in [23]. It was found that the suppression factor of η, ω, K_S^0 mesons of the order of 0.3 – 0.8 can be achieved for $40 < P_t^{\tilde{\gamma}} < 100\ GeV/c$ with a selection efficiency of single photons taken to be 90%. As for charged decay channels of η, ω, K_s^0 mesons the results of [23] show that by chosing absolute isolation cut $E_t^{isol} \leq 2\ GeV/c$ in the isolation cone with $R_{isol}^{\gamma} = 0.7$ and upper cut on the transverse energy deposited in HCAL $E_{t\,dep}^{HCAL} \leq E_{t\,thr}^{HCAL}$ (where $E_{t\,thr}^{HCAL} = 2 - 5\ GeV$ depends on $P_t^{\tilde{\gamma}}$) one can suppress these decays with a very good efficiency (at least 98%).

The correction of Tables 15–17 with account of the above rejection efficiencies is presented in new Tables 19–21. Here the background (B) differs from the one in Tables 15–17 by including events with electron candidates with the discussed above efficiency. Comparing Tables 19–21 with Tables 15–17 we observe the $50 - 55\%$ growth of the S/B ratio for $P_t^{\tilde{\gamma}} \geq 40\ GeV/c$ and, in practice, very small changes of the S/B values at $P_t^{\tilde{\gamma}} \geq 100\ GeV/c$.

We have not discussed here the background that may appear due to possible γ/jet misidentification, because as was shown in [32], γ and jet can be discriminated with a high precision. Really, as was mentioned at the beginning of this section (see also Section 3.2), we defined the photon (or the candidate to be registered as the direct photon) as the signal in the 5×5 ECAL crystal cell window satisfying cut conditions (17) – (22) of Section 3.2. These conditions effectively discriminate the photons from jets (see [23]).

From Tables 15 – 17 we have seen that the cuts listed in Table 13 (having rather moderate values of P_{tCUT}^{clust} and P_{tCUT}^{out}) allow to suppress the major part of the background events.

The considered here samples of generated events with all QCD subprocesses were used to study the effect of simultaneous application of P_{tCUT}^{clust} and P_{tCUT}^{out} on:

Table 19: Signal vs. background **(II)**

$\hat{p}_\perp^{min}$ (GeV/c)	Cuts	γ direct	γ brem	photons from the mesons				$e^\pm$
				π^0	η	ω	K_S^0	
40	Preselected	12394	20952	166821	66533	17464	23942	6684
	After cuts	1546	198	54	16	1	2	2
	+ jet isol.	903	92	23	8	1	2	1
100	Preselected	19359	90022	658981	247644	69210	85568	47061
	After cuts	1061	31	9	3	1	0	3
	+ jet isol.	1013	29	6	3	1	0	3
200	Preselected	55839	354602	1334124	393880	141053	167605	153410
	After cuts	1653	27	3	5	0	0	3
	+ jet isol.	1645	27	3	5	0	0	2

Table 20: Values of efficiencies and significance **(II)**

$\hat{p}_\perp^{min}(GeV/c)$	S	B	$Eff_S(\%)$	$Eff_B(\%)$	S/B	$S/\sqrt{B}$
40	1546	276	12.47± 0.34	0.091 ± 0.006	5.6	93.1
100	1061	47	5.48 ± 0.17	0.004 ± 0.001	22.6	154.8
200	1653	38	2.96 ± 0.07	0.001 ± 0.000	43.5	268.2

Table 21: Values of efficiencies and significance with jet isolation cut **(II)**

$\hat{p}_\perp^{min}(GeV/c)$	S	B	$Eff_S(\%)$	$Eff_B(\%)$	S/B	$S/\sqrt{B}$
40	903	127	7.29 ± 0.25	0.042 ± 0.004	7.1	80.1
100	1013	42	5.23 ± 0.17	0.004 ± 0.001	24.1	156.3
200	1645	38	2.95 ± 0.07	0.001 ± 0.000	43.3	266.9

(a) the number of selected events (for $L_{int} = 3\ fb^{-1}$);
(b) the signal-to-background ratio S/B;
(c) the mean value of $(P_t^{\tilde{\gamma}} - P_t^{Jet})/P_t^{\tilde{\gamma}} \equiv F$ and its standard deviation value $\sigma(F)$.

The results are presented in Tables 1 – 12 of Appendix 6 for Selection 1 and Tables 13–24 for Selection 2.

Let us emphasize that the tables of Appendix 6 include, in contrast to Appendices 2–5, the results obtained after analyzing three generated samples (described in the beginning of this section) of *signal and background* events. These events were selected with the cuts of Table 13.

Namely, the cuts (1) – (10) of Table 13 were applied for preselection of "$\tilde{\gamma} + 1\ jet$" events. The jets in these events as well as clusters were found by use of only one jetfinder LUCELL (for the whole η region $|\eta^{jet}| < 5.0$).

Tables 1 – 4 of Appendix 6 correspond to the simulation with $\hat{p}_\perp^{min} = 40\ GeV/c$. Analogously, the values of $\hat{p}_\perp^{min} = 100\ GeV/c$ and $\hat{p}_\perp^{min} = 200\ GeV/c$ were used for Tables 5 – 8 and Tables 9 – 12 respectively. The events used for analysis in Tables 1 – 12 have passed the cuts defined by Selection 1. The rows and columns of Tables 1 – 12 illustrate, respectively, the influence of P_{tCUT}^{clust} and P_{tCUT}^{out} on the quantities mentioned above (in the points (a), (b), (c)).

First of all, we see from Tables 2, 6 and 10 that a noticeable reduction of the background take place while moving along the table diagonal from the right-hand bottom corner to the left-hand upper one, i.e. with reinforcing P_{tCUT}^{clust} and P_{tCUT}^{out}. So, we see that for $\hat{p}_\perp^{min} = 40\ GeV/c$ the value of S/B ratio changes in the table cells along the diagonal from $S/B = 2.9$ (in the case

of no limits on these two variables), to $S/B = 5.6$ for the cell with $P_{tCUT}^{clust} = 10\ GeV/c$ and $P_{tCUT}^{out} = 10\ GeV/c$. Analogously, for $\hat{p}_{\perp}^{min} = 200\ GeV/c$ the value of S/B changes in the same table cells from 13.6 to 43.5 (see Tables 2, 10 of Appendix 6).

The second observation from Appendix 6. The restriction of P_{tCUT}^{clust} and P_{tCUT}^{out} improves the calibration accuracy. Table 3 shows that in the interval $P_t{}^{\tilde{\gamma}} > 40\ GeV/c$ the mean value of the fraction $F(\equiv (P_t{}^{\tilde{\gamma}} - P_t{}^{Jet})/P_t{}^{\tilde{\gamma}})$ decreases from 0.031 (the bottom right-hand corner) to 0.009 for the table cell with $P_{tCUT}^{clust} = 10\ GeV/c$ and $P_{tCUT}^{out} = 10\ GeV/c$. At the same time, the both cuts lead to a noticeable decrease of the gaussian width $\sigma(F)$ (see Table 4 and also Tables 8 and 12). For instance, for $\hat{p}_{\perp}^{min} = 40\ GeV/c$ $\sigma(F)$ drops by about a factor of two: from 0.163 to 0.085. It should be also noted that Tables 4, 8 and 12 demonstrate that for any fixed value of P_{tCUT}^{clust} further improvement in $\sigma(F)$ can be achieved by limiting $P_t{}^{out}$ (e.g. in line with $P_{tCUT}^{clust} = 15\ GeV/c$ $\sigma(F)$ drops by a factor of 2 with variation of $P_t{}^{out}$ from 1000 to $5\ GeV/c$).

The explanation is simple. The balance equation (28) contains 2 terms on the right-hand side ($1 - cos\Delta\phi$) and $P_t(O{+}\eta > 5.0)/P_t{}^{\tilde{\gamma}}$. The first one is negligibly small in a case of Selection 1 and tends to decrease with growing $P_t{}^{\tilde{\gamma}}$ (see tables in Appendices 2–5). So, we see that in this case the main source of the disbalance in equation (28) is the term $P_t(O{+}\eta > 5.0)/P_t{}^{\tilde{\gamma}}$. This term can be diminished by decreasing P_t activity beyond the jet, i.e. by decreasing $P_t{}^{out}$.

The behavior of the number of selected events (for $L_{int} = 3\ fb^{-1}$), the mean values of $F = (P_t{}^{\tilde{\gamma}} - P_t{}^{Jet})/P_t{}^{\tilde{\gamma}}$ and its standard deviation $\sigma(F)$ as a function of P_{tCUT}^{out} (with fixed $P_{tCUT}^{clust} = 10\ GeV/c$) are also displayed in Fig. 31 for events with non-isolated (left-hand column) and isolated jets (right-hand column, see also Tables 13–24 of Appendix 6).

Thus, we can conclude that application of two criteria introduced in Section 3.2, i.e. P_{tCUT}^{clust} and P_{tCUT}^{out}, results in two important consequences: significant background reduction and essential improvement of the calibration accuracy.

The numbers of events for different P_{tCUT}^{clust} and P_{tCUT}^{out} are given in the cells of Tables 1, 5 and 9 of Appendix 6. One can see that even with such strict P_{tCUT}^{clust} and P_{tCUT}^{out} values as $10\ GeV/c$ for both, for example, we would have a sufficient number of events (3 million, about 80 000 and 4 000 for $P_t{}^{\tilde{\gamma}} \geq 40\ GeV/c$, $P_t{}^{\tilde{\gamma}} \geq 100\ GeV/c$ and $P_t{}^{\tilde{\gamma}} \geq 200\ GeV/c$, respectively) with low background contamination ($S/B = 5.6,\ 22.6,\ 43.5$) and a good accuracy of the absolute jet energy scale setting during one month of continuous LHC running (i.e. $L_{int} = 3\ fb^{-1}$).

In addition, we also present in Appendix 6 Tables 13–24 obtained with Selection 2. They contain the information analogous to that in Tables 1 – 12 but for the case of isolated jets with $\epsilon^{jet} < 5\%$. From these tables we see that with the same cuts $P_{tCUT}^{clust} = P_{tCUT}^{out} = 10\ GeV/c$ one can expect about 1 700 000, 80 000 and 4 000 events for $P_t{}^{\tilde{\gamma}} \geq 40\ GeV/c$, $P_t{}^{\tilde{\gamma}} \geq 100\ GeV/c$ and $P_t{}^{\tilde{\gamma}} \geq 200\ GeV/c$, respectively, with a much more better fractional $P_t{}^{\tilde{\gamma}} - P_t{}^{Jet}$ balance, less than $F = 0.5\%$ for all.

Let us mention that all these PYTHIA results give us an indication of a tendency and may serve as a guideline for further full GEANT simulation that would allow to come to a final conclusion.

To conclude this section we would like to stress, firstly, that, as is seen from Tables 15, the "$\gamma - brem$" background defines a dominant part of the total background. Its contribution is about 1.5 – 3 times larger (see Tables 15, 19) than the combined background from neutral meson decays. Thus, one can see from Table 17 that π^0 contribution being about a half of "$\gamma - brem$" background at $\hat{p}_{\perp}^{min} > 40\ GeV/c$ becomes one order less than "$\gamma - brem$" background at $\hat{p}_{\perp}^{min} > 200\ GeV/c$. We would like to emphasize here that this is a strong prediction of the PYTHIA generator that has to be compared with predictions of another generator like HERWIG, for example.

Secondly, we would like to underline also that as it is seen from Table 14, 17 the photon

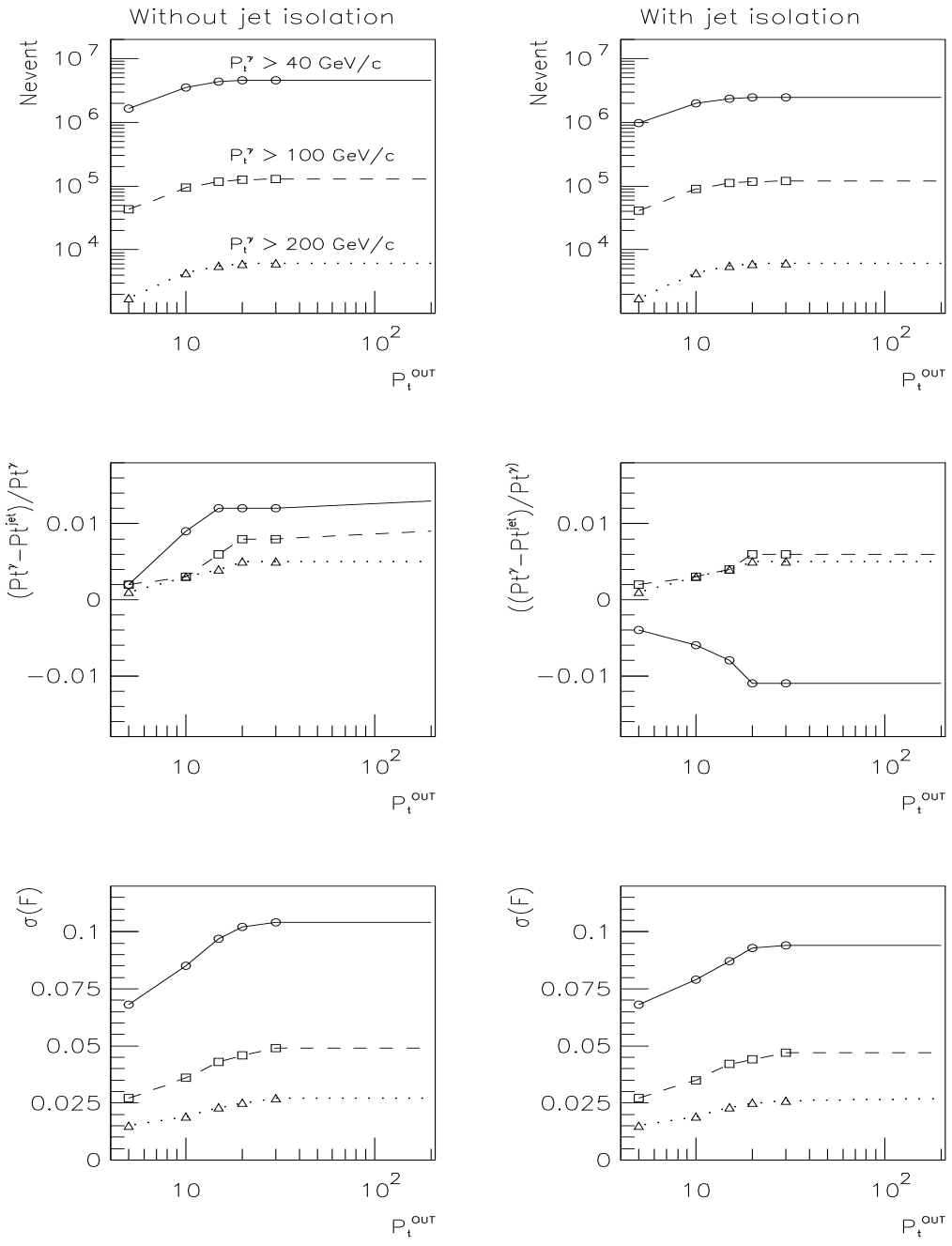

Fig. 31: Number of events (for $L_{int} = 3\ fb^{-1}$), mean value of $(P_t{}^{\tilde{\gamma}} - P_t{}^{Jet})/P_t{}^{\tilde{\gamma}}$ ($\equiv F$) and its standard deviation $\sigma(F)$ distributions over $P_t{}^{out}$ for the cases of nonisolated (left-hand column) and isolated (right-hand column) jet and for three intervals: $P_t{}^{\tilde{\gamma}} > 40, 100$ and $200\ GeV/c$. $P_{tCUT}^{clust} = 10\ GeV/c$.

isolation and selection cuts 1–5, usually used in the study of inclusive photon production (see, for instance, [36], [37], [38]), increase the S/B ratio (for $\hat{p}_{\perp}^{min} > 100\ GeV/c$) up to 1.93 only while the other cuts 6–17, that select events with a clear "$\gamma + jet$" topology and limited P_t activity beyong a chosen single jet, lead to a significant improvement of S/B by about one order of magnitude to 24.46.

The numbers in the tables of Appendix 6 were obtained with inclusion of the contribution from the background events. The tables show that their account does not spoil the ${P_t}^{\gamma} - {P_t}^{Jet}$ balance in the event samples preselected with the cuts 1–10 of Table 13. The estimation of the number of these background events would be important for the gluon distribution determination (see Section 10).

9. STUDY OF DEPENDENCE OF THE ${P_t}^{\gamma}$ and ${P_t}^{Jet}$ BALANCE ON PARTON k_t.

It is shown that in the case of ISR presence the value of fractional disbalance $({P_t}^{\gamma} - {P_t}^{Jet})/{P_t}^{\gamma}$ depends weakly on the variation of the average value of intrinsic parton transverse momentum $\langle k_{\,t} \rangle$.

This section is dedicated to the study (within PYTHIA simulation) of a possible influence of the intrinsic parton transverse momentum $k_{\,t}$ on the P_t balance of the "$\gamma + jet$" system. For this aim we consider two samples of signal events gained by simulation with subprocesses (1a) and (1b) in two different ranges of $\hat{p}_{\perp}^{min}$: $\hat{p}_{\perp}^{min} \geq 40\ GeV/c$ and $\hat{p}_{\perp}^{min} \geq 200\ GeV/c$. For these two $\hat{p}_{\perp}^{min}$ intervals Tables 22 and 23 demonstrate the average values of $P_t 56$ and $\langle {P_t}^{5+6} \rangle$ (defined by (3)) for two different cases of generation: without initial state radiation ("ISR is OFF") and with it ("ISR is ON"). Five different generations were done for each $\hat{p}_{\perp}^{min}$ interval. They correspond

Table 22: Effect of k_t on the ${P_t}^{\gamma}$ - ${P_t}^{Jet}$ balance with $\hat{p}_{\perp}^{min}$=40 GeV/c. $F = ({P_t}^{\gamma} - {P_t}^{Jet})/{P_t}^{\gamma}$

$\langle k_T \rangle$	ISR is OFF				ISR is ON			
(GeV/c)	$\langle P_t 56 \rangle$	$\langle {P_t}^{5+6} \rangle$	$\langle F \rangle$	$\sigma(F)$	$\langle P_t 56 \rangle$	$\langle {P_t}^{5+6} \rangle$	$\langle F \rangle$	$\sigma(F)$
0.0	0.0	0.0	-0.002	0.029	8.8	6.9	0.007	0.065
1.0	1.8	1.3	-0.001	0.036	9.1	7.0	0.009	0.069
2.5	4.5	3.2	0.001	0.054	9.6	7.4	0.010	0.074
5.0	8.7	6.1	0.014	0.089	10.4	7.2	0.015	0.088
7.0	11.2	7.7	0.020	0.107	11.0	8.2	0.022	0.101

Table 23: Effect of k_t on ${P_t}^{\gamma}$ -${P_t}^{Jet}$ balance with $\hat{p}_{\perp}^{min}$=200 GeV/c. $F = ({P_t}^{\gamma} - {P_t}^{Jet})/{P_t}^{\gamma}$

$\langle k_T \rangle$	ISR is OFF				ISR is ON			
(GeV/c)	$\langle P_t 56 \rangle$	$\langle {P_t}^{5+6} \rangle$	$\langle F \rangle$	$\sigma(F)$	$\langle P_t 56 \rangle$	$\langle {P_t}^{5+6} \rangle$	$\langle F \rangle$	$\sigma(F)$
0.0	0.0	0.0	0.000	0.010	11.1	8.4	-0.001	0.027
1.0	1.8	1.3	0.000	0.013	11.2	8.6	0.000	0.028
2.5	4.5	3.1	0.000	0.019	11.8	8.8	0.001	0.028
5.0	8.7	6.1	0.001	0.022	12.7	9.3	0.001	0.031
7.0	11.2	7.8	0.001	0.029	13.9	10.4	0.002	0.034

$*$ All numbers in the tables above are given in GeV/c.

to five values of parton $\langle k_t \rangle$ [41]: $\langle k_t \rangle = 0.0, 1.0, 2.5, 5.0$ and $7.0\ GeV/c$ (the values $\langle k_t \rangle > 1\ GeV/c$ are given here only for illustration of a tendency).

Let us consider firstly the case with ISR switched off during the simulation. The numbers in Tables 22 and 23 (obtained from the set of events selected by the cuts $\Delta\phi < 15^{\circ}$, $P_{tCUT}^{out} =$

[41] $\equiv$ PARP(91) parameter in PYTHIA

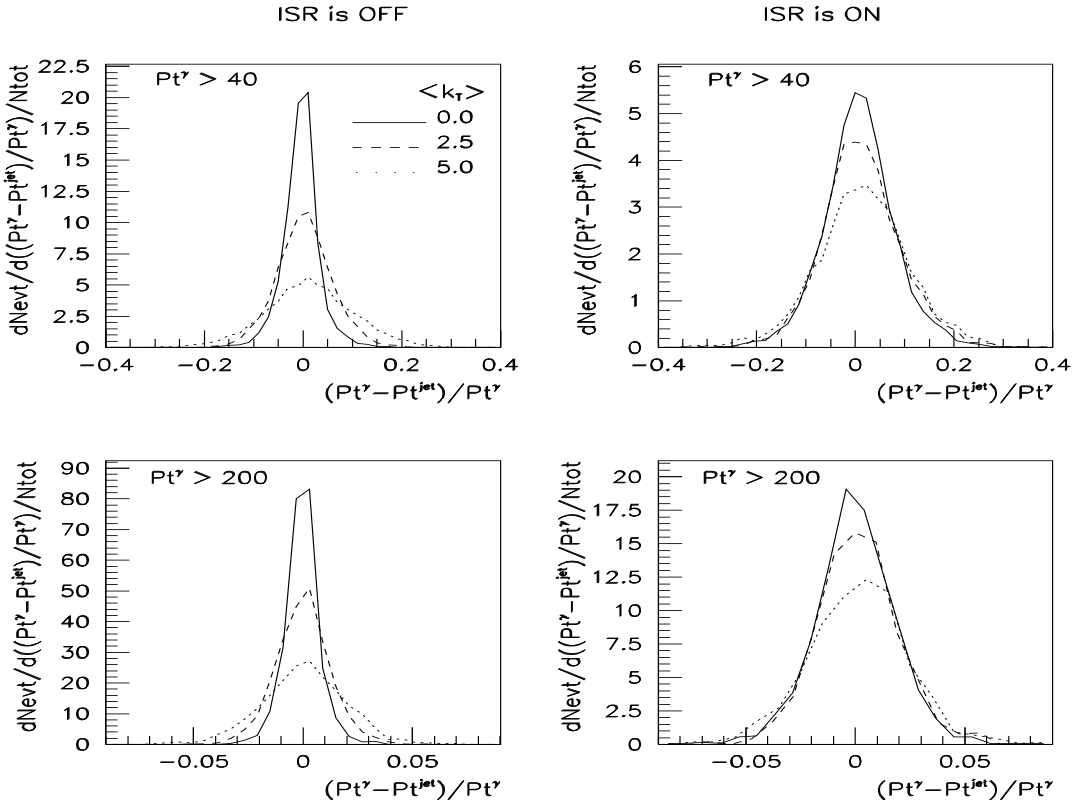

Fig. 32: $(P_t{}^{\gamma} - P_t{}^{Jet})/P_t{}^{\gamma} \equiv F(\gamma, jet)$ as a function of primordial k_t value for the cases of switched off (left column) and switched on (right column) initial radiation for $\hat{p}_\perp^{\,min} = 40$ and $\hat{p}_\perp^{\,min} = 200\ \ GeV/c$.

$5\ GeV/c$ and $P_{tCUT}^{clust} = 10\ GeV/c$) show that in the case when "ISR is OFF" the values of $\langle P_t 56\rangle$ and $\langle P_t{}^{5+6}\rangle$ grows rapidly with increasing $\langle k_t\rangle$ and does not depend on $P_t{}^{\gamma}$(or $\hat{p}_\perp^{\,min}$). In fact, the values of $\langle P_t 56\rangle$ are proportional to the values of $\langle k_t\rangle$ in this case.

The picture changes when ISR is taken into accound. In this case the variables $\langle P_t 56\rangle$ and $\langle P_t{}^{5+6}\rangle$ initially get large value at $\langle k_t\rangle = 0$, e.g. $\langle P_t 56\rangle = 8.8\ GeV/c$ and $11.1\ GeV/c$ for $\hat{p}_\perp^{\,min} = 40\ GeV/c$ and $200\ GeV/c$, respectively. But at the same time, in contrast to the case "ISR is OFF", the values of $\langle P_t 56\rangle$ grow more slowly with $\langle k_t\rangle$ when "ISR is ON". Indeed, they grow up from $8.8\ (11.1)$ at $\langle k_t\rangle = 0.0$ to $11.0\ (13.9)$ at $\langle k_t\rangle = 7\ GeV/c$ for $\hat{p}_\perp^{\,min} = 40\ GeV/c\ (200\ GeV/c)$.

The most remarkable thing, as it follows from Tables 22 and 23, that $\langle P_t 56\rangle$ depends weakly on $\langle k_t\rangle$ in the range of its reasonable values $\langle k_t\rangle \leq 1\ GeV/c$.

The variations of the fractional disbalance $F \equiv (P_t{}^{\gamma} - P_t{}^{Jet})/P_t{}^{\gamma}$ and its standard deviation $\sigma(F)$ with $\langle k_t\rangle$ are also shown in Tables 22 and 23 and in plots of Fig. 32. One can see that for reasonable values $\langle k_t\rangle \leq 1\ GeV/c$ and for the case "ISR is ON" the changes in the fractional disbalance F with k_t variation are very small. They are of order of 0.2% for $\hat{p}_\perp^{\,min} = 40\ GeV/c$ and of order of 0.1% for $\hat{p}_\perp^{\,min} = 200\ GeV/c$ [42].

[42] Recall that the numbers in Tables 22 and 23 may be compared with those in the tables of Appendix 6, where the same $\hat{p}_\perp^{\,min}$ cuts are used, rather than with the results of the tables of Appendices 2 – 5, where $\hat{p}_\perp^{\,min}$ cuts were taken to be two times smaller (see for explanation the beginning of Section 7).

10. "$\gamma + jet$" EVENT RATE ESTIMATION FOR GLUON DISTRIBUTION $f_g(x, Q^2)$ DETERMINATION AT THE LHC.

The number of "$\gamma+jet$" events suitable for measurement of gluon distribution $f_g(x, Q^2)$ in different x and Q^2 intervals is estimated. It is shown that with $L_{int} = 20\ fb^{-1}$ it would be possible to collect about ten million of these events. This number would allow to cover a new kinematical area not studied in any previous experiment ($2 \cdot 10^{-4} < x < 1.0$ with $1.6 \cdot 10^3 \leq Q^2 \leq 8 \cdot 10^4\ (GeV/c)^2$). This area in the region of small $x \geq 10^{-4}$ has Q^2 by about two orders of magnitude higher than reached at HERA now.

Many of theoretical predictions on the production of new particles (Higgs, SUSY) at the LHC are based on model estimations of the gluon density behaviour at low x and high values of square of transfered momentum Q^2. Therefore a measurement of the proton gluon density for this kinematic region directly in LHC experiments would be obviously useful. One of the promising channels for this measurement, as was shown in [33], may be a high P_t direct photon production $pp(\bar{p}) \rightarrow \gamma^{dir} + X$. The region of high P_t, reached by UA1 [34], UA2 [35], CDF [36] and D0 [37] extends up to $P_t \approx 80\ GeV/c$ and recently moved up to $P_t = 105\ GeV/c$ [38]. These data together with the later ones (see references in [40]–[49]) and recent E706 [50] and UA6 [51] results give an opportunity for studying deeply the gluon distribution in proton (for data analysis see [41], [46], [52]). The rates and estimated cross sections of inclusive direct photon production at the LHC were given in [33] (see also [53]).

Here for the same aim we shall consider the process $pp \rightarrow \gamma^{dir} + 1\ jet + X$ defined in the leading order by two QCD subprocesses (1a) and (1b) (for experimental results see [55], [56]).

Apart from the advantages, discussed in Section 8 in connection with the background suppression (see also [57]–[71]), the "$\gamma^{dir} + 1\ jet$" final state may be easier for physical analysis than inclusive photon production process "$\gamma^{dir} + X$" if we shall look at this problem from the viewpoint of extraction of information on the gluon distribution in a proton. Indeed, in the case of inclusive direct photon production the cross section is given as an integral over the products of a fundamental $2 \rightarrow 2$ parton subprocess cross sections and the corresponding parton distribution functions $f_a(x_a, Q^2)$ (a = quark or gluon), while in the case of $pp \rightarrow \gamma^{dir} + 1\ Jet + X$ for ${P_t}^{Jet} \geq 30\, GeV/c$ (i.e. in the region where "k_t smearing effects" [43] are not important, see [47]) the cross section is expressed directly in terms of these distributions (see, for example, [44]):

$$\frac{d\sigma}{d\eta_1 d\eta_2 d{P_t}^2} = \sum_{a,b}\ x_a\, f_a(x_a, Q^2)\, x_b\, f_b(x_b, Q^2) \frac{d\sigma}{d\hat{t}}(a\, b \rightarrow c\, d), \tag{35}$$

where

$$x_{a,b}\ =\ P_t/\sqrt{s} \cdot\ (exp(\pm\eta_1)\ +\ exp(\pm\eta_2)). \tag{36}$$

The designation used above are as the following: $\eta_1 = \eta^{\gamma}$, $\eta_2 = \eta^{Jet}$; $P_t = {P_t}^{\gamma}$; $a, b = q, \bar{q}, g$; $c, d = q, \bar{q}, g, \gamma$. Formula (35) and the knowledge of $q,\ \bar{q}$ distributions allow the gluon distribution $f_g(x, Q^2)$ to be determined after account of selection efficiencies for jets and $\gamma^{dir}-$candidates as well as after subtraction of the background contribution (as it was discussed in Section 8 keeping in hand this physical application).

The earlier estimations of "$\gamma + jet$" events suitable for jet energy calibration, and thus for determination the gluon distribution inside a proton [9], [10], showed that there would be many events with well-isolated photons and suppressed cluster activity beyond the "$\gamma + jet$" system. In the previous sections a lot of details connected with the structure and topology of these events

[43] This terminology is different from ours, used in Sections 2 and 9, as we denote by "k_t" only the value of parton intrinsic transverse momentum.

and the features of objects appearing in them were discussed. Now with this information in mind we are in position to discuss an application of the "$\gamma + jet$" event samples, selected with the previously proposed cuts, for estimating the rates of gluon-based subprocess (1a) in different x and Q^2 intervals. We shall use here the cuts $1-13$ of Table 13 with the following values of parameters [44]:

$$P_t{}^{\gamma} > 40\ GeV/c, \quad |\eta^{\gamma}| < 2.61, \quad P_t{}^{jet} > 30\ GeV/c, \quad |\eta^{jet}| < 5.0, \quad P_t{}^{hadr} > 5\ GeV/c,$$
$$P_{tCUT}^{isol} = 5\ GeV/c,\ \epsilon_{CUT}^{\gamma} = 7\%,\ \Delta\phi < 15^{\circ},\ P_{tCUT}^{clust} = 5\ GeV/c \qquad (37)$$

Table 24 shows percentage of "Compton-like" subprocess (1a) (amounting to 100% together with (1b)) in the samples of events selected with cuts (17) – (23) of Section 3.2 for $P_{tCUT}^{clust} = 10\ GeV/c$ for different $P_t{}^{\gamma}$ and η^{jet} intervals: Barrel (HB) part ($|\eta^{jet}| < 1.4$, see also tables of Appendix 1) and Endcap+Forward (HE+HF) part ($1.4 < |\eta^{jet}| < 5.0$). We see that the contribution of Compton-like subprocess drops with $|\eta^{jet}|$ enlarging and with growing $P_t{}^{jet} (\approx P_t{}^{\gamma}$ in the sample of the events collected with the cuts $1-13$ of Table 13).

Table 24: The percentage of "Compton-like" process $q\,g \to \gamma + q$.

Calorimeter part	$P_t{}^{Jet}$ interval (GeV/c)		
	40–50	100–120	200–240
HB	90	85	80
HE+HF	86	82	74

In Table 25 we present the $Q^2 (\equiv (P_t{}^{\gamma})^2)$ [45] and x (defined according to (36))distribution of the number of events (divided by 10^3) that are caused by the $q\,g \to \gamma + q$ subprocess and passed the following cuts ($P_t{}^{out}$ was not limited).

Table 25: Number of $g\,q \to \gamma^{dir} + q$ events (divided by 10^3) at different Q^2 and x values for $L_{int} = 20\ fb^{-1}$.

Q^2	x values of a parton				All x	$P_t{}^{\gamma}$
$(GeV/c)^2$	10^{-4}–10^{-3}	10^{-3}–10^{-2}	10^{-2}– 10^{-1}	10^{-1}–10^{0}	10^{-4}–10^{0}	(GeV/c)
1600-2500	735.7	2319.2	2229.0	236.9	5521.0	40–50
2500-5000	301.6	1323.3	1402.7	207.4	3235.1	50–71
5000-10000	33.7	361.3	401.0	97.7	893.8	71–100
10000-20000	1.5	80.8	99.4	38.0	219.9	100–141
20000-40000	0	15.6	24.4	12.4	52.5	141–200
40000-80000	0	2.1	4.2	2.5	8.8	200–283
				Sum =	**9 931** $\times\ 10^3$	

The analogous information for events with the charmed quarks in the initial state $g\,c \to \gamma^{dir} + c$ is presented in Table 26 (see also tables of Appendix 1). The simulation of the process $g\,b \to \gamma^{dir} + b$ has shown that the rates for the b-quark are 8 – 10 times smaller than for the c-quark (these event rates are also given in tables of Appendix 1 for different $P_t{}^{\gamma}$ intervals). [46]

Thus one can expect on total of about 10 millions events with clean "$\gamma + jet$" topology (in a sense of reduced Pt cluster or mini-jet activity in addition to a leading jet) at $L_{int} = 20\ fb^{-1}$ and among them of about 1.5 million of events with c-quark jets. Fig. 33 includes the widely used (x, Q^2) kinematic plot (see [72] and also [47]) to show what area can be covered by $q\,g \to \gamma + q$

[44] An application of cuts 14–17, as it is seen from Table 2, leads only to 20%-30% improvement of S/B ratio and they are essential mostly for improvement of disbalance $(P_t{}^{\gamma} - P_t{}^{J})/P_t{}^{\gamma}$ value.

[45] see [20]

[46] See also the estimations of heavy quarks production in "$\gamma + jet$" events at LHC energy that were done in [54], [66], [67], [11] and [16].

Table 26: Number of $g\,c \to \gamma^{dir} + c$ events (divided by 10^3) at different Q^2 and x values for $L_{int} = 20\ fb^{-1}$.

Q^2	x values for c-quark				All x	P_t^{γ}
$(GeV/c)^2$	10^{-4}–10^{-3}	10^{-3}–10^{-2}	10^{-2}– 10^{-1}	10^{-1}–10^{0}	10^{-4}–10^{0}	(GeV/c)
1600-2500	109.4	360.5	329.6	34.7	834.4	40–50
2500-5000	35.1	189.7	202.7	25.4	453.2	50–71
5000-10000	3.9	51.5	58.6	12.1	126.3	71–100
10000-20000	0.1	9.0	12.4	3.4	25.0	100–141
20000-40000	0	1.4	3.2	1.0	5.6	141–200
40000-80000	0	0.1	0.4	0.1	0.7	200–283
				$Sum =$	**1 446** $\times\ 10^3$	

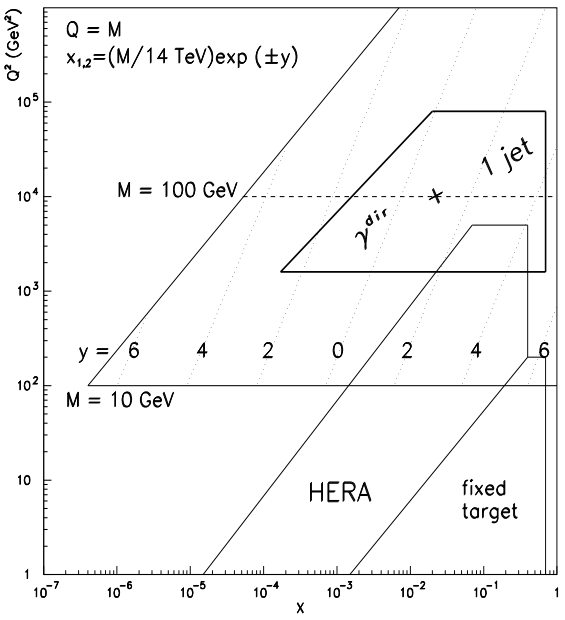

events selected with the discussed above cuts. The number of events in this area is given in Table 25. From this figure and Table 25 it becomes clear that even at low LHC luminosity it would be possible (after gaining of $L_{int} = 20\ fb^{-1}$) to study with a good statistics of "$\gamma + jet$" events the gluon distribution of in the region of small x , attainable now at HERA, but in a new interval of Q^2 that may be about 2–3 orders of magnitude higher than now reached at HERA. It is worth emphasising that extension of the experimentally reachable region at the LHC to the region of lower Q^2, overlapping with the area covered by HERA, would also be of great interest.

Figure 33: (x, Q^2) kinematic region that can be covered at LHC in first few months of low luminosity operation by $pp \to \gamma + Jet$ events selected for gluon distribution measurement.

11. SUMMARY.

We have done an attempt here to consider, following [9]–[16], the physics of high P_t direct photon and jet associative production in proton-proton collisions basing on the predictions of PYTHIA generator and the models implemented there. This work may be useful for two practical goals: for absolute jet energy scale determination and for gluon distribution measurement at LHC energy.

The detailed information provided in the PYTHIA event listings allows to track the origin of different particles (like photons) and of objects (like clusters and jets) that appear in the final state. So, the aim of this work was to explore at the particle level of simulation this information as much as possible for finding out what effect may be produced by new variables, proposed in [9]–[15] for describing "$\gamma + jet$" events, and the cuts on them for solution of the mentioned above practical tasks.

For the first problem of the jet energy scale determination an important task is find a way to select the events that may be caused (with a high probability) by the $q\bar{q} \to g + \gamma$ and $qg \to q + \gamma$ fundamental parton subprocesses of direct photon production. To take into account a possible effect of initial state radiation (which spectra are presented in different P_t^{γ} intervals in Tables 2–7 of Section 5) we used here the P_t-balance equation, see (16), written for an event as

a whole. It allows to express $P_t^{\gamma} - P_t^{Jet}$ fractional disbalance (see (28)) through new variables [9]–[15] that describe the P_t activity *out* of "$\gamma + jet$" system. They are P_t^{out} and P_t^{clust}, i.e. P_t of mini-jets or clusters that are additional to the main jet in event. The latter are the most "visible" part of P_t^{out}.

It is shown that the limitation of P_t of clusters, i.e. P_t^{clust}, can help to decrease this disbalance (see Figs. 15–21 and Tables 4–12 of Appendices 2–5).

Analogously, the limitation of P_t activity of all detectable particles ($|\eta_i| < 5.0$) beyond the "$\gamma + jet$" system, i.e. P_t^{out}, also leads to a noticeable $P_t^{\gamma} - P_t^{Jet}$ disbalance reduction (see Figs. 22 and 23).

It is demonstrated that in the events, selected by means of simultaneous restriction from above of the P_t^{clust} and P_t^{out} activity, the values of P_t^{γ} and P_t^{Jet} are well balanced with each other while considering the PYTHIA particle level of simulation. The samples of these "$\gamma + jet$" events, gained in this way, are expected to be of a large enough volume for jet energy scale determination in the interval $40 < P_t^{\gamma} < 360\ GeV/c$ (see Tables 1–12 of Appendix 6).

It is worth mentioning that the most effect of improvement of P_t^{γ} and P_t^{Jet} balance can be reached by applying additionally the jet isolation criterion defined in [9]–[15]. As it can be seen from Figs. 18, 19 (Selection 2) as well as from Figs. 20, 21 (Selection 3) and also from Tables 13–18 of Appendices 2–5 and Tables 13–24 of Appendix 6, the application of this criterion allows to select the events having the $(P_t^{\gamma} - P_t^{Jet})/P_t^{\gamma}$ disbalance at the particle level less than 1% [47].

Definitely, the detector effects may worsen the balance determination due to the limited accuracy of the experimental measurement. We are planning to present the results of full GEANT simulation with the following digitization and reconstruction of signals by using the corresponding CMS packages (like CMSIM) in the forthcoming papers.

We present also PYTHIA predictions for the dependence of the distributions of the number of selected "$\gamma + jet$" events on P_t^{γ} and η^{jet} (see Tables 8–12 of Section 5 and also tables of Appendices 2–5 with account of P_t^{clust} variation). The features of "$\gamma + jet$" events in the barrel region of the CMS detector ($|\eta^{jet}| < 1.4$) are exposed (see Figs. 8, 10). The P_t structure of the region in the $\eta - \phi$ space inside and beyond a jet is established (see Figs. 11–14).

The corrections to the measurable values of P_t^{jet} that take into account the contribution from neutrinos belonging to a jet are presented for different $P_t^{Jet} (\approx P_t^{\gamma}$ for the selected events) intervals in the tables of Appendix 1. It is shown in Section 4 that a cut on $P_t^{miss} < 10\ GeV/c$ allows to reduce this contribution down to the value of $\Delta_{\nu} = \langle P_{t(\nu)}^{Jet} \rangle_{all\ events} = 0.2\ GeV/c$. At the same time, as it is shown in Section 8 (see also [15]), this cut noticeably decreases the number of the background $e^{\pm}$-events in which $e^{\pm}$ (produced in the $W^{\pm} \to e^{\pm}\nu$ weak decay) may be registered as direct photon.

The study of the fractional disbalance $(P_t^{\gamma} - P_t^{Jet})/P_t^{\gamma}$ dependence on an intrinsic parton transverse momentum $\langle k_t \rangle$, performed in Section 9, has shown its weak impact on the disbalance in the case of initial state radiation account.

The possibility of the background events (caused by QCD subprocesses of qg, gg, qq scattering) suppression was studied in Section 8. Basing on the introduced selection criteria that include 17 cuts (see Table 13 of Section 8), the background suppression relative factors and the values of signal event selection efficiencies are estimated (see Table 14).

It is shown that after applying the first 5 "photonic" cuts (that may be used, for example, for

[47] The achieved disbalance value at the particle level of simulation shows the most optimistic value of $(P_t^{\gamma} - P_t^{Jet})/P_t^{\gamma}$.

selecting events with inclusive photon production and lead to signal-to-background ratio $S/B = 1.9$ in the interval $P_t^{\gamma} > 100\ GeV/c$, see Table 14) the use of the next 12 "hadronic" cuts of Table 13 may lead to further essential improvement of S/B ratio (by a factor of 12 for the same $P_t^{\gamma} > 100\ GeV/c$ thus S/B becomes equal to 24.5, see Table 14).

It is important to underline that this improvement is achieved by applying "hadronic" cuts that select the events having clear "$\gamma + jet$" topology at the particle level and also having rather "clean" area (in a sense of limited P_t activity) beyond a "$\gamma + jet$" system. The consideration of the cuts, connected with detector effects (e.g., based on an electromagnetic shower profile), may lead to further improvement of S/B ratio (see [23] and [24]). In this sense and taking into account also the fact that these "hadronic" cuts lead to an essential improvement of $P_t^{\gamma} - P_t^{Jet}$ balance, we conclude that the cuts on P_t^{clust} and P_t^{out}, considered here, are quite effective for selection of the events caused by leading order diagrams (see Fig. 1) and they do suppress the contribution of NLO corrections shown by diagrams of Figs. 2, 4.

Another interesting predictions of PYTHIA is about the dominant contribution of "γ-brem" events into the total background at LHC energy, as in was already mentioned in Section 8 (see also [15]). As the "γ-brem" background has an irreducible nature its careful estimation is an important task and we plan to make the analogous estimation with other generators (HERWIG, for instance).

To finish the discussion of the jet calibration study let us mention that the main results on this subject are summed up in tables 1–12 (Selection 1) and in tables 13–24 (Selection 2 with jet isolation criterion) of Appendix 6 and in Fig. 31.

It should be emphasized that numbers presented in all mentioned tables and figures were found within the PYTHIA particle level of simulation. They may depend on the used generator and on the particular choice of a long set of its parameters [48] as well as they may change after account of the results of the full GEANT-based simulation.

It is shown that the samples of the "$\gamma + jet$" events, gained with the cuts used for the jet energy calibration, can provide an information suitable also for determining the gluon distribution inside a proton in the kinematic region (see Fig. 33) that includes x values as small as accessible at HERA [73], [74], but at much higher Q^2 values (by about two orders of magnitude): $2 \cdot 10^{-4} \leq x \leq 1.0$ with $1.6 \cdot 10^3 \leq Q^2 \leq 8 \cdot 10^4\ (GeV/c)^2$. The number of events, based on the gluonic process (1a), that may be collected with $L_{int} = 20\ fb^{-1}$ in different x- and Q^2- intervals of this new kinematic region for extraction of the information about gluon distribution are presented in Table 25 (all quarks included) and in Table 26 (only for charm quarks) [49]

ACKNOWLEDGMENTS.

We are greatly thankful to D. Denegri who initiated our interest to study the physics of "$\gamma + jet$" processes, for his permanent support and fruitful suggestions. It is a pleasure for us to express our deep recognition for helpful discussions to P. Aurenche, M. Dittmar, M. Fontannaz, J.Ph. Guillet, M.L. Mangano, E. Pilon, H. Rohringer, S. Tapprogge, H. Weerts and J. Womersley. Our special gratitude is to J. Womersley also for supplying us with the preliminary version of paper [1], interest in the work and encouragements.

[48] The comparison of predictions of different generators (PYTHIA, HERWIG, etc.) with the experimental results is a part of a work in any experiment.

[49] see also tables of Appendix 1.

References

[1] D0 Collaboration, F. Abachi *et al.*, NIM **A424** (1999)352 (Its ealier prototype: B. Abbot *et al.*, "Jet Energy Scale at D0"; D0 Note #3287, D0, FNAL, 1997 contains some more detailed discussions of different physical aspects of the calibration).

[2] CDF Collaboration. F. Abe *et al.*, Phys.Rev. **D50** (1994)2966; F. Abe *et al.*, Phys.Rev.Lett. **73** (1994)225.

[3] D. Denegri, R. Kinnunen, A. Nikitenko, CMS Note 1997/039 "Study of calorimeter calibration with τ's in CMS".

[4] R. Kinnunen, A. Nikitenko, CMS Note 1997/097 "Study of calorimeter calibration with pions from jets in CMS".

[5] J. Womersley. A talk at CMS Week meeting, Aachen, 1997.

[6] J. Freeman, W. Wu, **draft** "In situ calibration of CMS HCAL calorimeter".

[7] R. Mehdiyev, I. Vichou, ATLAS Note ATL-COM-PHYS-99-054 (1999) "Hadronic jet energy scale calibration using Z+jet events".

[8] ATLAS Detector and Physics Performance, Technical Design Report, Volumes **1, 2**, 1999. CERN/LHCC 99-14.

[9] N.B. Skachkov, V.F. Konoplyanikov D.V. Bandourin, "Photon – jet events for calibration of HCAL". Second Annual RDMS CMS Collaboration Meeting. CMS-Document, 1996–213. CERN, December 16-17, 1996, p.7-23.

[10] N.B. Skachkov, V.F. Konoplyanikov D.V. Bandourin, "γ-direct + 1 jet events for HCAL calibration". Third Annual RDMS CMS Collaboration Meeting. CMS-Document, 1997–168. CERN, December 16-17, 1997, p.139-153.

[11] D.V. Bandourin, V.F. Konoplyanikov, N.B. Skachkov. "Jet energy scale setting with "$\gamma + jet$" events at LHC energies. Generalities, selection rules." JINR Preprint E2-2000-251, JINR, Dubna, hep-ex/0011012.

[12] D.V. Bandourin, V.F. Konoplyanikov, N.B. Skachkov. "Jet energy scale setting with "$\gamma + jet$" events at LHC energies. Event rates, P_t structure of jet." JINR Preprint E2-2000-252, JINR, Dubna, hep-ex/0011013.

[13] D.V. Bandourin, V.F. Konoplyanikov, N.B. Skachkov. "Jet energy scale setting with "$\gamma + jet$" events at LHC energies. Minijets and cluster suppression and $P_t^{\gamma} - P_t^{Jet}$ disbalance." JINR Preprint E2-2000-253, JINR, Dubna, hep-ex/0011084.

[14] D.V. Bandourin, V.F. Konoplyanikov, N.B. Skachkov. "Jet energy scale setting with "$\gamma + jet$" events at LHC energies. Selection of events with a clean "$\gamma + jet$" topology and $P_t^{\gamma} - P_t^{Jet}$ disbalance." JINR Preprint E2-2000-254, JINR, Dubna, hep-ex/0011014.

[15] D.V. Bandourin, V.F. Konoplyanikov, N.B. Skachkov. "Jet energy scale setting with "$\gamma + jet$" events at LHC energies. Detailed study of the background suppression." JINR Preprint E2-2000-255, JINR, Dubna, hep-ex/0011017.

[16] D.V. Bandourin, V.F. Konoplyanikov, N.B. Skachkov, " "$\gamma + jet$" events rate estimation for gluon distribution determination at LHC", Part.Nucl.Lett.103:34-43,2000, hep-ex/0011015.

[17] D.V. Bandourin, V.F. Konoplyanikov, N.B. Skachkov, "Jet energy scale setting with "gamma+jet" events for a hadronic calorimeter of CMS." Fifth Annual RDMS CMS Collaboration Meeting "Physics Program with the CMS Detector". CMS Document 2000-058. pp. 422-427.

[18] D.V. Bandurin, N.B. Skachkov. " "$\gamma + jet$" process application for setting the absolute scale of jet energy and determining the gluon distribution at the Tevatron Run II." D0 Note 3948, 2002, hep-ex/0203003.

[19] S. Abdullin, A. Khanov, N. Stepanov, CMS Note CMS TN/94–180 "CMSJET".

[20] T. Sjostrand, Comp.Phys.Comm. **82** (1994)74.

[21] GEANT3 - Detector Description and Simulation Tool, R. Brun *at al*, GEANT3 CERN DD/EE/84-1, revised 1987.

[22] GEANT-3 based simulation package of CMS detector CMSIM. CMS TN/93-63, C. Charlot *et al*, "CMSIM–CMANA. CMS Simulation facilities", CMSIM User's Guide at WWW: http://cmsdoc.cern.ch/cmsim/cmsim.html.

[23] D.V. Bandurin, V.F. Konoplyanikov, N.B. Skachkov. "On the possibility of $\pi^0, \eta, \omega, K_s^0$ mesons and a photon discrimination basing on the calorimeter information in the CMS detector", JINR Communication E1-2001-261, JINR, Dubna, hep-ex/0108050.

[24] D.V. Bandurin, N.B. Skachkov. "Separation of a signle photon and products of the π^0, η, K_s^0 mesons neutral decay channels in the CMS electromagnetic calorimeter using neural network", JINR Communication E2-2001-259, JINR, Dubna, hep-ex/0108051.

[25] I.A. Bertram *et al.*, "Single jet energy resolutions at D0 for Run I", D0 Note 3414, 1998.

[26] S. Frixione, Phys.Lett. **B429** (1998)369.

[27] S. Catani, M. Fontannaz and E. Pilon, Phys.Rev. **D58** (1998)094025

[28] CMS Tracker Project, Technical Design Report, CERN/LHCC 98–6, CMS TDR 5, CERN, 1999.

[29] CMS Electromagnetic Calorimeter Project, Technical Design Report, CERN/LHCC 97–33, CMS TDR 4, CERN, 1997.

[30] S. Shevchenko et al., CMS Note 1997/050, "Neutral pion rejection in the CMS $PbWO_4$ crystal calorimeter using a neural network".

[31] A. Kyriakis, D. Loukas, J. Mousa, D. Barney, CMS Note 1998/088, "Artificial neural net approach to $\gamma - \pi^0$ discrimination using CMS Endcap Preshower".

[32] F. Gianotti, I. Vichou, ATLAS Note PHYS-No-78, 1996, γ/jet separation with the ATLAS detector".

[33] P. Aurenche *et al.* Proc. of "ECFA LHC Workshop", Aachen, Germany, 4-9 Oktob. 1990, edited by G. Jarlskog and D. Rein (CERN-Report No 90-10; Geneva, Switzerland 1990), Vol. **II**

[34] UA1 Collaboration, C. Albajar *et al.*, Phys.Lett, **209B** (1998)385.

[35] UA2 Collaboration, R. Ansari *et al.*, Phys.Lett. **176B** (1986)239.

[36] CDF Collaboration. F. Abe *et al.*, Phys.Rev.Lett. **68** (1992)2734; F. Abe *et al.*,Phys.Rev. **D48** (1993)2998; F. Abe *et al.*,Phys.Rev.Lett., **73** (1994)2662.

[37] D0 Collaboration, F. Abachi *et al.*, Phys.Rev.Lett, **77** (1996)5011;

[38] D0 Collaboration, B. Abbott *et al.* , Phys.Rev.Lett. **84** 2786-2791,2000.

[39] L3 Collaboration, D. Kirkby, CALT-69-1992, hep-ex/9505012.

[40] T. Ferbel and W.R. Molzon, Rev.Mod.Phys. **56** (1984)181.

[41] P. Aurenche, *et al.* Phys.Lett. **169B** (1986)441.

[42] E.N. Argyres, A.P. Contogouris, N. Mebarki and S.D.P. Vlassopulos, Phys.Rev, **D35** (1987)1534–1589.

[43] P. Aurenche, *et al.* Phys.Rev. **D39** (1989)3275.

[44] J.F. Owens, Rev.Mod.Phys. **59** (1987)465.

[45] J. Huston *et al.*, Phys.Rev. **D51** (1995)6139.

[46] W. Vogelsang and A. Vogt, Nucl.Phys. **B453** (1995)334.

[47] J. Huston ATLAS Note ATL-Phys-99-008, CERN,1999.

[48] W. Vogelsang and M. Whally, J.Phys. **G23** (1997)A1.

[49] S. Frixione and W. Vogelsang, CERN-TH/99-247 hep-ph/9908387.

[50] E706 Collaboration, L. Apanasevich *et al.*, Phys.Rev.Lett., **81** (1997)2642.

[51] UA6 Collaboration, G. Ballocchi *et al.*, Phys.Lett.,**B436** (1998)222.

[52] A.D. Martin *et al.*, Eur.Phys.J. **C4** (1998)463.

[53] P. Aurenche, M. Fontannaz, S. Frixione Proc. of "CERN Workshop on Standard Model Physics (and more) at the LHC", QCD, Section 6.1 "General features of photon production", Yellow Report CERN-2000-004, 9 May 2000, CERN, Geneva.

[54] M. Dittmar, F. Pauss, D. Zurcher, Phys.Rev.D56:7284-7290,1997; hep-ex/9705004.

[55] ISR–AFS Collaboration, T.Akesson *et al.*, Zeit.Phys. **C34** (1987)293;

[56] CDF Collaboration, F. Abe *et al.*,Phys.Rev. **D57** (1998)67.

[57] E.L. Berger and J. Qiu, Phys.Rev. **D44** (1991)2002.

[58] M. Fontannaz, S. Frixione, S. Tapprogge Proc. of "CERN Workshop on Standard Model Physics (and more) at the LHC", QCD, Section 6 "Prompt photon production", Yellow Report CERN-2000-004, 9 May 2000, CERN, Geneva.

[59] L. Borissov, A. Kirkby, H. Newman, S. Shevchenko, CMS-Note 1997/050, "Neutral pion rejection in the CMS $PbWO_4$ crystal calorimeter using a neural network"

[60] A. Kyriakis, D. Loukas, J. Mousa, D. Barney, CMS Note 1998/088, "Artificial neural net approach to $\gamma - \pi^0$ discrimination using CMS Endcap Preshower".

[61] D. Barney, P. Bloch, CMS-TN/95-114, "π^0 rejection in the CMS endcap electromagnetic calorimeter - with and without a preshower.'

[62] G.P. Skoro, M.V. Tokarev, "Asymmetry of jet production in polarized pp collisions and sign of ΔG", Proc. of the XIV International Seminar on High Energy Physics Problems "Relativistic Nuclear Physics and QCD", Vol.II, p.120., hep-ph/0009028

[63] G.P. Skoro, M.V. Tokarev, "Asymmetry of jet production in polarized pp collisions at RHIC and sign of ΔG", Nuov. Cim. **A111** (1998) 353.

[64] G.P. Skoro, M. Zupan, M.V. Tokarev, "Asymmetry of Prompt Photon Production in $\vec{p} - \vec{p}$ Collisions at RHIC" Nuov. Cim. **A112** (1999) 809.

[65] P. Chiapetta, G.J. Gounaris, J. Layssac and F.M. Renard "Glue constraining asymmetries in W, γ or Z production at CERN LHC", hep-ph/9807563.

[66] See, for example, the presentations of M. Dittmar and K.Mazumdar at http://cmsdoc.cern.ch/doc/ph/agendas/990518-1 "gamma+c-jets" and http://cmsdoc.cern.ch/doc/ph/agendas/000607-1 "Constraining structure functions of s, c, b quarks at LHC".

[67] M. Dittmar, K.Mazumdar, "Measuring the parton distribution functions of charm, beauty and strange quarks and antiquarks at the LHC", CMS Note 2001/002.

[68] M. Dittmar, K.Mazumdar, N. Skachkov, Proc. of "CERN Workshop on Standard Model Physics (and more) at the LHC", QCD, Section 2.7 "Measuring parton luminosities ...", Yellow Report CERN-2000-004, 9 May 2000, CERN, Geneva.

[69] D.V. Bandourin, V.F. Konoplyanikov, N.B. Skachkov, "Events rate estimation for gluon distribution determination at LHC", Proc. of the XV ISHEPP "Relativistic Nuclear Physics and Quantum Chromodynamocs", Dubna 2000. Eds.A.M.Baldin, V.V.Burov, A.I. Malakhov. Dubna, 2001, v.I, pp.375-283.

[70] D.V. Bandourin, N.B. Skachkov, " "$\gamma + jet$" event rate estimation for gluon distribution determination at the Tevatron RUN II", hep-ex/0206040.

[71] J. Huston *et al.* "Study of the uncertainty of the gluon distribution", hep-ph/9801444.

[72] R. Ball, M. Dittmar, W.J. Stirling, Proc. of "CERN Workshop on Standard Model Physics (and more) at the LHC", QCD, Section 2 "Parton distribution functons", Yellow Report CERN-2000-004, 9 May 2000, CERN, Geneva.

[73] H1 Collaboration, S. Aid *et al.*, Nucl.Phys. **B470** (1996)3; C. Adloff *et al.* Nucl.Phys. **B497** (1997)3.

[74] ZEUS Collaboration, M. Derrick *et al.*, Zeit.Phys. **C69** (1996)607; M. Derrick *et al.*, Zeit.Phys. **C72** (1996)399.

[75] Particle Data Group, D.E. Groom *et al.*, The European Physical Journal C15 (2000) 1.